Search for the Wh Production Using High-p_T Isolated Like-Sign Dilepton Events in 1.96-TeV Proton-Antiproton Collisions

A dissertation submitted
in partial fullfillment of the requirements
for the Degree of Doctor of Philosophy in Science
in the Graduate School of Science of
Osaka City University

by
Takayuki Wakisaka

April 2009

Abstract

The thesis describes search for the neutral Higgs production associated with the W boson using high-p_T isolated like-sign (LS) dilepton events in proton-antiproton collisions at a center-of-mass energy of 1.96 TeV. The search is performed on a data collected by the Collider Detector at Fermilab (CDF) between March 2002 and April 2008 corresponding to an integrated luminosity of 2.7 fb^{-1}.

Although The Higgs boson is predicted in Standard Model (SM) which is most successful particle physics theory, its existence is not verified yet experimentally. And the SM does not tell us the Higgs mass, so it need to be measured by experiments.

The physics objective in this thesis is to search for the low-mass fermiophobic higgs and the high-mass SM Higgs boson using LS dilepton events such as the below process,

$$qq' \rightarrow W^{\pm}h \rightarrow W^{\pm}W^{*}W^{*} \rightarrow \ell^{\pm}\ell^{\pm} + X, \quad (1)$$

where the same charged W boson decay to leptonic, after that, the process have a final state with LS dilepton. The LS dilepton event requirement is quite effective to suppress QCD and known electroweak process, however the fake-lepton backgrounds and residual photon-conversions still remain at a considerable level in the events of the higgs signature. The fake electron backgrounds are for instance interactive $\pi^{\pm}$, overlap of π^{0} and a track, and residual photon-conversions, but in this analysis, the residual photon-conversion are separately estimated from fake lepton backgrounds. The fake muon backgrounds are punch-through hadrons and decay-in-flight muons from $\pi^{\pm}$ and $K^{\pm}$. The backgrounds are estimated by data-driven methods. While other backgrounds such as WZ and ZZ production events, that is containing prompt real lepton, are estimated by Monte Carlo (MC) data.

The number of expected signal events passing LS dilepton event requirement are 1.31 for the fermiophobic higgs of the mass 110 GeV/c^2 assuming the SM production cross-section and 0.38 for the SM higgs of 160 GeV/c^2. And the expected number of backgrounds events are 188 $\pm$ 24, while the actual number of observed events are 172.

The Boosted Decision Tree (BDT) are employed to get more search sensitivity in this analysis. The BDT is based on a multivariate analysis technique and used to separate the signal and background events in the final sample passing LS dilepton requirement.

There are no significant disagreements in the BDT results, then, the upper limits on the production cross-section times the branching fraction for the higgs with masses in

the region from 110 to 200 GeV/c^2 at 95% confidence level. The expected limit is 1.54 pb for 120 GeV/c^2 higgs and 0.98 pb for 160 GeV/c^2 higgs, while the observed limits are 2.42 and 1.23 pb, respectively. The expected limit on the ratio to the theoretical prediction for the cross-section is 8.2 for the fermiophobic higgs of the mass 120 GeV/c^2 and 20.1 for the SM higgs of the mass 160 GeV/c^2, while the observed limits are 12.9 and 25.1, respectively.

Acknowledgments

I would like to thank everyone who supported and encouraged me until this thesis is completed for a few years. This thesis could have been not completed without the numerous supports and encouragements.

I would like to thank Prof. Toru Okusawa. He gave me the opportunity to join to the CDF experiment and supported the working during my doctoral program. I am sure that my physical basement ideas are constructed by him wisdom. I am deeply thankful to Prof. Yoshihiro Seiya. He gave me unparalleled suggestions and comments for this analysis. And it is happy and blessing for me to study this analysis with him. I am specially grateful to Prof. Kazuhiro Yamamoto. He alway elegantly advised me the physical ideas and supported me technical aspects. My pleasant working atmosphere was provide by his trouble-free working. I also would like to thank Dr. Hirokazu Kobayashi who is the pioneer for this study. This advanced study is enabled by his great working.

I would like to thank to CDF Higgs group conveners, Prof. Tom Junk, Prof. Anton Anasassov. Prof. Matthew Herndon, and Prof. Mark Kruse. They supported my analysis and empathetically discussed with me to polish the analysis.

CDF silicon detector group members, Prof. Ulrich Husemann, Prof. Jose Enrique Garcia, Prof. Ignacio Redondo, Prof. Oscar Gonzalez, and other staffs, I was happy and did valuable experience by working with them.

I would like to express thanks to Ms. Carol Picciolo, Ms. Kyoko Kunori, and Ms. Kazuko Kumashiro. They supported me by a lot of their secretary works and I could concentrate on my working by them.

I would like to thank the other staff members of CDF, DØ, and Fermilab, Prof. Shyuichi Kunori, Prof. Nobuaki Oshima, Prof. Kaori Maeshima, Prof. Kiyomi Seiya, Dr. Kenichi Hakakeyama, Dr. Koji Sato, Dr. Yuji Enari, Dr. Masato Aoki, I also would like to thank the staff members and the students of CDF Japan group, Prof. Kunitaka Kondo, Prof. Shinhong Kim, Prof. Fumihiko Ukegawa, Prof. Kazuhiko Hara, Prof. Yuji Takeuchi, Prof. Reisaburo Tanaka, Prof. Ituo Nakano, Prof. Makoto Shimojima, Prof. Yukihiro Kato, Prof. Kohei Yorita Dr. Tomonobu Tomura, Dr. Hideki Miyake, Dr. Masakazu Kurata, Dr. Junji Naganoma, Dr. Tatsuya Masubushi, Dr. Taichi Kubo, Dr. Kimura Naoki, Dr. Ai Nagano, Dr. Koji Nakamura, Mr. Yoshiaki Nagai, and Mr. Astunari Hamaguchi. It was greatest delight and full of happiness for me to get through same times with them.

I wish to express my appreciation to the staff members and the students of other

experiments, Prof. Takasumi Maruyama, Prof. Masashi Yokoyama, Dr. Hidekazu Tanaka, Mr. Katsuki Hiraide, Mr. Yasuhiro Nakajima, Mr. Yoshinori Kurimoto, and Mr. Hideyuki Takei. It's my replaceable asset that I met them.

And, I thank the Fermilab staffs and the technical staffs of the participating institutions for their vital contributions. This work was supported by the U.S. Department of Energy and National Science Foundation; the Italian Istituto Nazionale di Fisica Nucleare; the Ministry of Education, Culture, Sports, Science and Technology of Japan; the Natural Sciences and Engineering Research Council of Canada; the National Science Council of the Republic of China; the Swiss National Science Foundation; the A.P. Sloan Foundation; the Bundesministerium fuer Bildung und Forschung, Germany; the Korean Science and Engineering Foundation and the Korean Research Foundation; the Particle Physics and Astronomy Research Council and the Royal Society, UK; the Russian Foundation for Basic Research; the Comision Interministerial de Ciencia y Tecnologia, Spain; and in part by the European Community's Human Potential Programme under contract HPRN-CT-20002, Probe for New Physics.

Finally, I would like to supreme thank to my family. They always supported my life and mental. I keep to express my gratitude to them during my life.

Thank you so much, everyone.

Contents

List of Figures

List of Tables

Chapter 1

Introduction

What's the origin of mass?

Isaac Newton said in his book "Philosophiae naturalis principia mathematica" [1] at 1687,

$$\boldsymbol{F} = m\boldsymbol{a}.$$

It means that mass (m) indicates a physical quantity which is degree of acceleration ($\boldsymbol{a}$) when a boby are applied a force ($\boldsymbol{F}$).

Albert Einstein said in his papers [2, 3] at 1905,

$$E = mc^2.$$

It shows mass-energy equivalence where c is the speed of light in a vacuum.

However now we have understood the mass in sense of physical quantity by their excellent achievements, we do not know why there is the mass. Particle physics have understood various fundamental physicial picutures in our world. The knowlege will extend the grasp of mass.

Now, Human may be in a ground they can know the origin of mass.

1.1 The Standard Model

Standard Model (SM) is one of particle physics theories based on gauge field theory which is invariance under the gauge transformation, and extremely well describes the phenomena and properties of the elementary particles which was tested by various experiments. The SM can form three gauge field theories in the framework, the three gauge field theories are "Quantum Electrodynamics (QED)", "Quantum Chromodynamics (QCD)" and "Weak theory". The QED describes the electromagnetic

interaction between charged particles based on $U(1)$ gauge group, the QCD describes the strong interaction between quarks and gluons based on $SU(3)_C$ gauge group, and the Weak theory describes weak interaction where in the nuclei based on $SU(2)$ gauge group. In particular, the QED and the Weak theory are unified in the SM framework as $SU(2)_L \otimes U(1)_Y$ gauge theory. In addition, the "Higgs Mechanism" amazingly plays to give "Mass" to a particle with keeping the gauge invariance in the theory. However, a particle is needed for the mechanism, which is called Higgs boson, the Higgs boson is undiscovered yet experimentally.

1.1.1 Elementary Particles in the Standard Model

In the SM, there are mainly 2 types elementary particles, so-called "Fermion" and "Boson", respectively. The Fermions construct matters in the universe, while the Bosons mediate forces between the elementary particles. The visible complex matters in this world are made up of them. This following section describes the elementary particles in some detail.

Fermion

A particle called Fermion obeys the "Pauli Exclusion Principle", i.e. it has half-integral spin. In the SM, the Fermions are classified into six leptons and six quarks. The three of the six leptons are charged lepton, which are "electron", "muon", and "tau", they have different mass, respectively, however its spin, weak isospin, and electric charge are same. The remaining three leptons have no electric charge so-called "neutrino", they have a lepton flavor (lepton number) same as corresponding charged lepton, when electron has $+1$ electron number, the corresponding neutrino so-called "electron neutrino" has $+1$ electron number.

The three of the six quarks have $2/3$ electric charge, so-called "up", "charm", and "top" quark respectively, they are collectively called "up-type quark" while the other three quarks is $-1/3$ electric charge called "down", "strange", and "bottom", collectively "down-type quark". They also have color charge which is source of the strong interaction.

In addition, there are antiparticle for each fermion, which have opposite quantum numbers corresponding to the each fermion. Table 1.1 shows the list of the leptons and the quarks.

Boson

The Bosons play a role in mediating force between the elementary particles corresponding to type of forces. Such bosons are especially called "gauge boson". In the present, it is believed that there are at least 4 kind of force, "Electromagnetic", "Weak", "Strong", and "Gravity", however the Gravity force is excluded in the SM due to normalization problem, and its extremely small affect in the particle world. The electromagnetic forces are propagated via "photon" by feeling electric charge which is gauge boson in

the electromagnetic field. The photon has spin 1, and massless means that the force caries to infinity. The weak force interactions are mediated by $W^{\pm}$ and Z^0 bosons have 80 and 91 GeV/c^2 mass, respectively, unlike electromagnetic force, it can effect within short range ($\sim 10^{-16}$ cm). The strong force interactions are occurred by exchanging gauge boson so-called "gluon" via color charge, which can propagate within finite range due to "asymptotic freedom". The color charge are conventionally expressed as 3 colors, "red (r)", "blue (b)", and "green (g)", which is introduced by taking Pauli Exclusion Principle in Hadrons (Baryons and Mesons) into account, for example Δ^{++} particle is constructed by 3 up-quarks, it can be expressed as (u_r, u_b, u_g). The force mediating particles, i.e. gauge bosons, are shown in Table 1.2 [4].

Name	Symbol	Mass		Charge ($Q/\|e\|$)	Spin	Weak Isospin
Leptons						
electron	e	0.509	MeV/c^2	-1	1/2	$+1/2$
electron neutrino	ν_e	<225(95%CL)	eV/c^2	0	1/2	$-1/2$
muon	μ	105.7	MeV/c^2	-1	1/2	$+1/2$
muon neutrino	ν_μ	<0.19(90%CL)	MeV/c^2	0	1/2	$-1/2$
tau	τ	1776.8	MeV/c^2	-1	1/2	$+1/2$
tau neutrino	ν_τ	<18.2(95%CL)	MeV/c^2	0	1/2	$-1/2$
Quarks						
up	u	$2.55^{+0.75}_{-1.05}$	MeV/c^2	$+2/3$	1/2	$+1/2$
down	d	$5.04^{+0.96}_{-1.54}$	MeV/c^2	$-1/3$	1/2	$-1/2$
charm	c	$1.27^{+0.07}_{-0.11}$	GeV/c^2	$+2/3$	1/2	$+1/2$
strange	s	104^{+26}_{-34}	MeV/c^2	$-1/3$	1/2	$-1/2$
top	t	171.2 ± 2.1	GeV/c^2	$+2/3$	1/2	$+1/2$
bottm	b	$4.20^{+0.17}_{-0.07}$	GeV/c^2	$-1/3$	1/2	$-1/2$

Table 1.1: List of the leptons and quarks and its properties in the Standard Model [4].

Interaction	Gauge boson (symbol)	Mass (GeV/c^2)	Effective coupling	Range [cm]	Typical time [s]
Electromagnetic	photon (γ)	0	1/137	∞	10^{-20}
Weak	$W^{\pm}$, Z^0	80.4, 91.2	10^{-5}	10^{-16}	10^{-10}
Strong	gluon (g)	0	~ 1	10^{-13}	10^{-23}

Table 1.2: Summry of the forces and gauge bosons in the Standard Model.

1.1.2 Quantum Electrodynamics: $U(1)$

Quantum Electrodynamics (QED) is relativistic quantum field theory of the classical electromagnetism [5]. QED has the structure of an Abelian gauge theory with a $U(1)$ gauge group. The gauge field, which mediates the interaction between the charged 1/2 spin fields, is the electromagnetic field. An electron is described by a complex field and the Lagrangian is written as follows,

$$\mathscr{L} = i\bar{\psi}\gamma_\mu\partial^\mu\psi - m\psi\bar{\psi}. \tag{1.1}$$

The Lagrangian is invariant under the phase transformation,

$$\psi \to e^{i\alpha}\psi, \tag{1.2}$$

where α is a real constant. The family of phase transformations $U(\alpha) \equiv e^{i\alpha}$ forms a unitary Abelian group known as the $U(1)$ group. Using Neother's theorem, this invariant implies the existence of a conserved current and charge,

$$\partial_\mu j^\mu = 0,\ j^\mu = -e\bar{\psi}\gamma^\mu\psi,\ Q = \int d^3x j^0. \tag{1.3}$$

In addition, the local gauge transformation is generalized as

$$\psi \to e^{i\alpha(x)}\psi, \tag{1.4}$$

where $\alpha(x)$ depends on space and time in a completely arbitrary way. Now, the Lagrangian (1.1) is not invariant under such phase transformation. Using (1.4),

$$\bar{\psi} \to e^{-i\alpha(x)}\bar{\psi}, \tag{1.5}$$

the last term of the Lagrangian is invariant, however the term of derivative ψ is not as follows,

$$\partial_\mu\psi \to e^{i\alpha(x)}\partial_\mu\psi + ie^{i\alpha(x)}\psi\partial_\mu\alpha, \tag{1.6}$$

and the $\partial_\mu\alpha$ term breaks the invariant of the Lagrangian. To impose invariance of the Lagrangian under local gauge transformation, the derivative ∂_μ is modified as D_μ, the treatment covariantly transforms the Lagrangian under the phase transformation,

$$D_\mu\psi \to e^{i\alpha(x)}D_\mu\psi, \tag{1.7}$$

$$D_\mu \equiv \partial_\mu - ieA_\mu, \tag{1.8}$$

where a vector field A_μ is introduced to cancel the unwanted term in (1.6), and the vector field transforms as,

$$A_\mu \to A_\mu + \frac{1}{e}\partial_\mu\alpha. \tag{1.9}$$

Invariance of the Lagrangian (1.1) under the local gauge transformation (1.4) is achieved by replacing ∂_μ by D_μ,

$$\begin{aligned}\mathscr{L} &= i\bar{\psi}\gamma_\mu D^\mu\psi - m\psi\bar{\psi} \\ &= \bar{\psi}(i\gamma^\mu\partial_\mu - m)\psi + e\bar{\psi}\gamma^\mu\psi A_\mu. \end{aligned} \tag{1.10}$$

By demanding local phase invariance, it forces to introduce a vector field A_μ, i.e. gauge field in QED. If the additional field is regarded as the physical photon field, the Lagrangian is added a term corresponding to its kinetic energy. Since the kinetic term must be invariant under (1.9), it can only involve the gauge invariant field strength tensor

$$F_{\mu\nu} = \partial_\mu A_\nu - \partial_\nu A_\mu. \tag{1.11}$$

Finally, the Lagrangian of QED is expressed as follows,

$$\mathscr{L} = \bar{\psi}(i\gamma^\mu\partial_\mu - m)\psi + e\bar{\psi}\gamma^\mu\psi A_\mu - \frac{1}{4}F_{\mu\nu}F^{\mu\nu}. \tag{1.12}$$

The addition of a mass term $(1/2)m^2 A_\mu A^\mu$ is prohibited by gauge invariance. The gauge particle must be massless and the gauge field can propagate to an infinite range.

1.1.3 Quantum Chromodynamics: $SU(3)_C$

Quantum Chromodynamics (QCD) is the gauge theory for strong interactions [5]. QCD is based on the extension of the QED idea, however it has a gauge transformation invariant under $SU(3)$ group on quark color fields. The Lagrangian is written in the following,

$$\mathscr{L} = \bar{q}_j(i\gamma^\mu\partial_\mu - m)q_j, \tag{1.13}$$

where $q_j (j = 1, 2, 3)$ denotes the three color fields. The Lagrangian (1.13) is to be invariant under local phase transformations as follows,

$$q(x) \to Uq(x) \equiv e^{i\alpha_a(x)T_a}q(x), \tag{1.14}$$

where U is an arbitrary 3×3 unitary matrix, it has the summation over the repeated suffix a. $T_a (a = 1, \cdots, 8)$ is a set of linearly independent traceless 3×3 matrices, and α_a are the group parameters. The group is non-Abelian since the generators T_a do not commute with each other,

$$[T_a, T_b] = if_{abc}T_c, \tag{1.15}$$

where f_{abc} are real constants called the structure constants of the group. To impose $SU(3)$ local gauge invariance on the Lagrangian (1.13), the infinitesimal phase transformation is introduced,

$$q(x) \to [1 + i\alpha_a(x)T_a]q(x), \tag{1.16}$$

$$\partial_\mu q \to (1 + i\alpha_a T_a)\partial_\mu q + iT_a q\partial_\mu\alpha_a. \tag{1.17}$$

The last term spoils the invariance of Lagrangian. The 8 gauge fields G^a_μ are constructed by requiring the invariance of the Lagrangian under the local gauge transformation,

$$G^a_\mu \to G^a_\mu - \frac{1}{g}\partial_\mu \alpha_a - f_{abc}\alpha_b G^c_\mu, \tag{1.18}$$

and form a covariant derivative,

$$D_\mu = \partial_\mu + igT_a G^a_\mu. \tag{1.19}$$

The gauge invariant QCD Lagrangian is formed by the replacement $\partial_\mu \to D_\mu$ in the Lagrangian (1.13), and adding a gauge invariant kinetic energy term for each of the G^a_μ fields,

$$\mathscr{L} = \bar{q}(i\gamma^\mu \partial_\mu - m)q - g(\bar{q}\gamma^\mu T_a q)G^a_\mu - \frac{1}{4}G^a_{\mu\nu}G^{\mu\nu}_a, \tag{1.20}$$

$$G^a_{\mu\nu} = \partial_\mu G^a_\nu - \partial_\nu G^a_\mu - g f_{abc} G^b_\mu G^c_\nu, \tag{1.21}$$

(1.20) is the Lagrangian for interacting colored quarks q and vector gluons G_μ, with coupling specified by g. The local gauge invariance requires the gluons to be massless. The field strength $G^a_{\mu\nu}$ has a remarkable new property as shown in the last term in (1.21). Imposing the gauge symmetry has required that the kinetic energy term in Lagrangian is not purely kinetic but includes an induced self-interaction between the gauge bosons and reflects the fact that gluons themselves carry color charge.

1.1.4 Electroweak Theory: $SU(2)_L \otimes U(1)_Y$

The electroweak theory is a gauge theory unified the electromagnetic $U(1)$ and weak interactions $SU(2)$. The weak interaction typically occurs in β decay in nuclei ($n \to p + \ell + \nu_\ell$) via a W boson which is weak gauge boson. The weak interaction acts only left-handed fermions, so-called $V-A$ structure, and based on $SU(2)$ isospin group with three vector bosons. The electroweak theory is suggested by Glashow [6], Weinberg [7], and Salam [8].

By demanding weak interaction, the quark fields are expressed as follows,

$$\psi_L = \begin{pmatrix} q_u \\ q_d \end{pmatrix}_L, \ \psi_R = q_R. \tag{1.22}$$

The left-handed quark fields can be expressed in doublets, while the right-handed quark fields in singlets, where q_u is up-type quarks (u, c, t), q_d is down-type quarks (d, s, b), and q_R is six quark flavours (u, d, c, s, t, b). The lepton fields are also expressed by,

$$\psi_L = \begin{pmatrix} \nu_\ell \\ \ell^- \end{pmatrix}_L, \ \psi_R = \ell_R, \tag{1.23}$$

where ℓ means three lepton flavours i.e. e, μ, and τ. Note that there are no right-handed neutrino fields due to satisfying $V-A$ structure in the weak interaction. Here, the free Lagrangian for the lepton and the quark fields is written in,

$$\mathscr{L} = \sum_{j=L,R} i\bar{\psi}_j \gamma^\mu \partial_\mu \psi_j. \tag{1.24}$$

The Lagrangian (1.24) is invariant under global transformation,

$$\psi_L \to e^{i\alpha_a T^a + i\beta Y}\psi_L, \tag{1.25}$$
$$\psi_R \to e^{i\beta Y}\psi_R, \tag{1.26}$$

where the parameter Y is hypercharge for $U(1)_Y$ phase transformation, the T^a is defined by using Pauli matrices as follows,

$$T^a = \frac{\tau^a}{2},\ \tau^1 = \begin{pmatrix} 0 & 1 \\ 1 & 0 \end{pmatrix},\ \tau^2 = \begin{pmatrix} 0 & -i \\ i & 0 \end{pmatrix},\ \tau^3 = \begin{pmatrix} 1 & 0 \\ 0 & -1 \end{pmatrix}, \tag{1.27}$$

and it is under $SU(2)_L$ transformation. The Lagrangian should be invariant under local $SU(2)_L \otimes U(1)_Y$ gauge transformation,

$$\psi_L \to e^{i\alpha_a(x) T^a + i\beta(x) Y}\psi_L, \tag{1.28}$$
$$\psi_R \to e^{i\beta(x) Y}\psi_R. \tag{1.29}$$

To achieve the local gauge invariance in the Lagrangian, the derivative is replaced by covariant derivatives,

$$D_{\mu L} \equiv \partial_\mu + igT_a W^a_\mu, + i\frac{g'}{2}B_\mu Y \tag{1.30}$$

$$D_{\mu R} \equiv \partial_\mu + i\frac{g'}{2}B_\mu Y, \tag{1.31}$$

$D_{\mu L}(D_{\mu R})$ is for the left(right)-handed fermion fields, g is the coupling constant of $SU(2)_L$ and g' is of $U(1)_Y$. The covariant derivatives have gauge fields, $W^a_\mu (a = 1, 2, 3)$ for $SU(2)_L$, and B_μ for $U(1)_Y$. The gauge fields also transform as,

$$B_\mu \to B_\mu - \frac{1}{g'}\partial_\mu \beta, \tag{1.32}$$

$$\boldsymbol{W}_\mu \to \boldsymbol{W}_\mu - \frac{1}{g}\partial_\mu \boldsymbol{\alpha} - \boldsymbol{\alpha} \times \boldsymbol{W}_\mu. \tag{1.33}$$

In addition, the gauge field strength tensors are introduced by requiring the local gauge invariant,

$$B_{\mu\nu} \equiv \partial_\mu B_\nu - \partial_\nu B_\mu, \tag{1.34}$$
$$W^a_{\mu\nu} \equiv \partial_\mu W^a_\nu - \partial_\nu W^a_\mu - g\varepsilon_{abc} W^b_\mu W^c_\nu. \tag{1.35}$$

Finally, the Lagrangian under local gauge invariant in electroweak interaction can be written as,

$$\mathscr{L} = \sum_{j=L,R} i\bar{\psi}_j \gamma^\mu D_{\mu,j} \psi_j - \frac{1}{4} W^a_{\mu\nu} W^{\mu\nu}_a - \frac{1}{4} B_{\mu\nu} B_{\mu\nu}, \tag{1.36}$$

Although the weak and electromagnetic interactions coexist in the $SU(2)_L \otimes U(1)_Y$ gauge symmetry, it describes no realistic world, because there are no mass terms for fermions and weak gauge bosons which are known that they are massive, and weak interaction only affects in short range. However introducing the mass terms such as $\frac{1}{2} M_W^2 W_\mu W^\mu$ in the Lagrangian breaks the gauge symmetry. The fermion terms also break due to different transformation between the left-handed and right-handed fermion fields,

$$m_f \bar{f} f = m_f (\bar{f}_R f_L + \bar{f}_L f_R), \tag{1.37}$$

using the left-handed and right handed relation equations,

$$f_L = \frac{1}{2}(1 - \gamma^5) f, \;\; f_R = \frac{1}{2}(1 + \gamma^5) f. \tag{1.38}$$

Fortunately, the nature have a solution(mechanism) to be invariant under gauge transformation when the Lagrangian has a mass terms for fermion and weak gauge boson, so-called "Spontaneous symmetry breaking".

1.1.5 Spontaneous Symmetry Breaking

To give mass to the gauge bosons and fermions, the electroweak gauge symmetry are hidden. Here let us start by introducing the scalar real field ϕ as simple example, and its Lagrangian is written by,

$$\mathscr{L} = \frac{1}{2} \partial_\mu \phi \partial^\mu \phi - V(\phi), \tag{1.39}$$

$$V(\phi) = \frac{1}{2} \mu^2 \phi^2 + \frac{1}{4} \lambda \phi^4, \tag{1.40}$$

where $\lambda > 0$, the Lagrangian is invariant under the symmetry operation: $\phi \to -\phi$.

If $\mu^2 > 0$, it can be regarded that the Lagrangian describes a scalar fields with mass μ, the ϕ^4 terms means self-interaction with coupling λ, and the minimum of the potential $V(\phi)$ is,

$$\langle 0|\phi|0\rangle \equiv \phi_0 = 0, \tag{1.41}$$

as shown in the left side of Figure 1.1. On the other hand, if $\mu^2 < 0$, the potential $V(\phi)$ has a minimum when,

$$\frac{\partial V}{\partial \phi} = \mu^2 \phi + \lambda \phi^3 = 0, \tag{1.42}$$

$$\langle 0|\phi^2|0\rangle \equiv \phi_0^2 = -\frac{\mu^2}{\lambda} \equiv v^2, \tag{1.43}$$

as shown in the right side of Figure 1.1. The value $v = \sqrt{\mu^2/\lambda}$ is called "vacuum expectation value" of the scalar field ϕ. Here the field ϕ is expanded around the minimum value v with the quantum fluctuation η,

$$\phi = v + \eta. \tag{1.44}$$

From this, the Lagrangian (1.40) becomes

$$\mathscr{L} = \frac{1}{2}\partial_\mu\eta\partial^\mu\eta - \lambda v^2\eta^2 - \lambda v\eta^3 - \frac{1}{4}\eta^4 + \text{const}, \tag{1.45}$$

where a scalar field η with mass $m_\eta = \sqrt{-2\mu^2}$ appears in the Lagrangian (1.45), and there are self-interaction terms η^3 and η^4, in particular, the cubic term breaks the symmetry in the Lagrangian without external operation, it is called "Spontaneous Symmetry Breaking (SSB)". Next step, let us introduce the SSB to electroweak symmetry to get the true world picture, that is, the weak bosons and the fermions are massive.

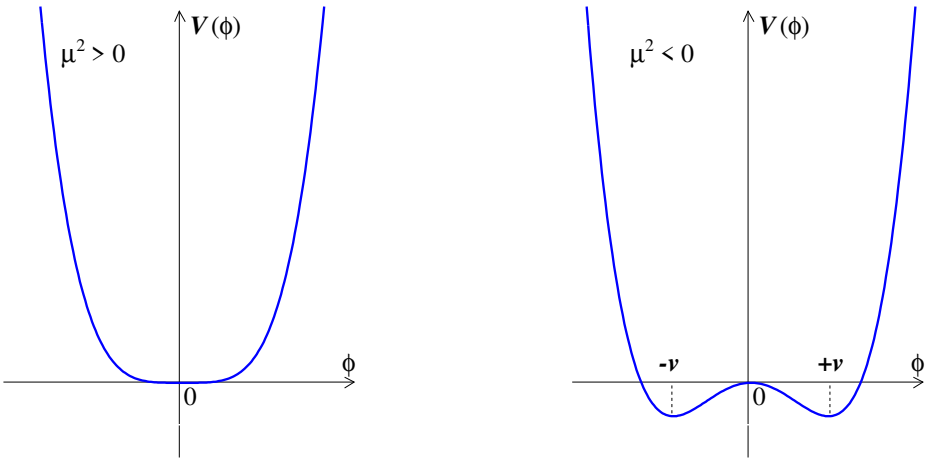

Figure 1.1: The potential $V(\phi)$ of the scalar field ϕ in the case $\mu^2 > 0$ (left) and $\mu^2 < 0$ (right).

1.1.6 Higgs Mechanism

As described in §1.1.4, however the Lagrangian (1.36) is invariant under local gauge invariant, the Lagrangian describes the no real world picture because the weak gauge bosons and fermions have no mass in the Lagrangian. But the Lagrangian is broken by including the mass terms. Now, let us show that the Lagrangian becomes the real

world Lagrangian by using the symmetry breaking [9, 10, 11]. By introducing complex scalar doublet,

$$\phi = \begin{pmatrix} \phi^+ \\ \phi^0 \end{pmatrix} = \frac{1}{\sqrt{2}} \begin{pmatrix} \phi_1 + i\phi_2 \\ \phi_3 + i\phi_4 \end{pmatrix}, \; Y_\phi = +1, \tag{1.46}$$

where the hypercharge is 1 for the scalar fields, the Lagrangian can be written by

$$\mathscr{L} = (\partial_\mu \phi)^\dagger (\partial^\mu \phi) - \mu^2 \phi^\dagger \phi - \lambda (\phi^\dagger \phi)^2. \tag{1.47}$$

In this case, if $\mu^2 < 0$, the vacuum expectation value and the scalar field after the symmetry breaking with the real scalar field h become as follows,

$$\phi^\dagger \phi = \frac{\phi_1^2 + \phi_2^2 + \phi_3^2 + \phi_4^2}{2} = \frac{-\mu^2}{2\lambda} \equiv \frac{v^2}{2}, \tag{1.48}$$

$$\phi = \frac{1}{\sqrt{2}} \begin{pmatrix} 0 \\ v + h \end{pmatrix}, \tag{1.49}$$

where the scalar fields are chosen as $\phi^1 = \phi^2 = \phi^4 = 0$, and $\phi^3 = v$. Let us expand the first term of the Lagrangian (1.47), i.e. the kinematical terms,

$$\begin{aligned} |D_\mu \phi|^2 &= \left| \left(\partial_\mu - igT^a W_\mu^a + i\frac{g'}{2} B_\mu \right) \phi \right|^2 \\ &= \frac{1}{2}(\partial_\mu h)^2 + \frac{g^2 v^2}{4} \left| \frac{W_\mu^1 + iW_\mu^2}{2} \right|^2 + \frac{v^2}{8} |gW_\mu^3 - g' B_\mu|^2 + \text{interaction terms} \end{aligned} \tag{1.50}$$

where the derivative is replaced to covariant derivative (1.31), and define the field $W_\mu^\pm$, Z_μ and A_μ written as follows,

$$W_\mu^\pm = \frac{1}{\sqrt{2}}(W_\mu^1 \pm iW_\mu^2), \tag{1.51}$$

$$Z_\mu = W_\mu^3 \cos\theta_W - B_\mu \sin\theta_W, \tag{1.52}$$

$$A_\mu = W_\mu^3 \sin\theta_W + B_\mu \cos\theta_W, \tag{1.53}$$

where weak mixing angle θ_W is defined as $g' = g \tan\theta_W$, the A_μ field is the orthogonal field to the Z_μ field, and the masses of fields can be expressed as respectively,

$$M_W = \frac{1}{2} v g, \; M_Z = \frac{1}{2} v \sqrt{g^2 + g'^2}, \; M_A = 0. \tag{1.54}$$

Note that the W_μ and the Z_μ fields become massive, while the A_μ field is still massless, that is, the weak gauge bosons can have desirable mass by introducing the SSB, in particular, it is called "Higgs Mechanism". By using the weak mixing angle θ_W, the W_μ field is related to Z_μ field as follows,

$$M_W = M_Z \cos\theta_W. \tag{1.55}$$

The fermion fields should be massive to achieve the true world in the electroweak Lagrangian. The Higgs mechanism also gives a mass to the fermions under the local gauge invariant. The Lagrangian with fermion fields is written by,

$$\mathscr{L}_{Yukawa} = -G_f \bar{\psi}_L \phi \psi_R - G_f \bar{\psi}_R \phi^\dagger \psi_L, \tag{1.56}$$

where G_f is arbitrary constant for each fermion. First, the lepton sector Lagrangian becomes,

$$\begin{aligned}
\mathscr{L}_{\text{lepton}} &= -G_\ell \left[(\bar{\nu}_\ell, \bar{\ell})_L \begin{pmatrix} \psi^+ \\ \psi^0 \end{pmatrix} \ell_R + \bar{\ell}_R (\psi^-, \bar{\psi}^0) \begin{pmatrix} \nu_\ell \\ \ell \end{pmatrix}_L \right] \\
&= -\frac{G_\ell}{\sqrt{2}} v (\bar{\ell}_L \ell_R + \bar{\ell}_R \ell_L) - \frac{G_\ell}{\sqrt{2}} (\bar{\ell}_L \ell_R + \bar{\ell}_R \ell_L) h \\
&= -m_\ell \bar{\ell}\ell - \frac{m_\ell}{v} \bar{\ell}\ell h,
\end{aligned} \tag{1.57}$$

using (1.38) and $m_\ell = G_\ell v/\sqrt{2}$ is defined as the lepton mass. The lepton sector Lagrangian (1.57) then keeps the gauge symmetry under the local transformation. Let us show that the quark sector Lagrangian also becomes the invariant. In the quark sector, the new higgs doublet must be introduced by using ϕ to give the the up-type quark mass,

$$\phi_c = i\tau_2 \phi = \begin{pmatrix} -\bar{\phi}^0 \\ \phi^- \end{pmatrix}, \tag{1.58}$$

the higgs doublet is chosen the following after the symmetry breaking,

$$\phi_c = \frac{1}{\sqrt{2}} \begin{pmatrix} v + h \\ 0 \end{pmatrix}. \tag{1.59}$$

The quark sector Lagrangian is formed by

$$\begin{aligned}
\mathscr{L}_{\text{quark}} &= -G_d (\bar{u}, \bar{d})_L \begin{pmatrix} \psi^+ \\ \psi^0 \end{pmatrix} d_R - G_u (\bar{u}, \bar{d})_L \begin{pmatrix} -\bar{\psi}^0 \\ \psi^- \end{pmatrix} u_R + h.c. \\
&= -m_d \bar{d}d - m_u \bar{u}u - \frac{m_d}{v} \bar{d}dh - \frac{m_u}{v} \bar{u}uh,
\end{aligned} \tag{1.60}$$

where the down-type and the up-type quark masses are defined as $m_d = G_d v/\sqrt{2}$ and $m_u = G_u v/\sqrt{2}$ respectively. The quark sector Lagrangian also preserves the gauge invariant after the symmetry breaking.

The Higgs Mechanism gives us the electroweak Lagrangian with relevant field mass terms under the gauge symmetry. However the fermions masses are not predicted in the Lagrangian because of general fermion coupling G_f's are arbitrary constant, and the Higgs mass and its potential structure are also unknown. They need to be revealed by a experiment.

1.1.7 Two Higgs Doublet Model

In the previous section, the minimal SM higgs is considered, however the scalar field doublet can be introduced as two, and more doublets to break the electroweak symmetry. Then, Let us introduce the two complex doublet scalar fields ϕ_1 and ϕ_2 so-called "Two Higgs Doublet Model (2HDM)",

$$\phi_1 = \begin{pmatrix} \phi_1^+ \\ \phi_1^0 \end{pmatrix}, \ \phi_2 = \begin{pmatrix} \phi_2^+ \\ \phi_2^0 \end{pmatrix}, \tag{1.61}$$

The 2HDM have mainly two scenarios, named "Type-I" and "Type-II", respectively. In the "Type-I", the scalar fields ϕ_1 do not couple to any quarks and leptons, while the other scalar fields ϕ_2 couple to them. In the "Type-II", the first scalar fields ϕ_1 couple only to down-type quarks and leptons, while the second scalar fields ϕ_2 couple only to up-type quarks. In this thesis, the Type-I scenario is noticed [13, 14].

First, let us start to introduce the most general potential written as,

$$\begin{aligned} V(\phi_1,\phi_2) =& \lambda_1(\phi_1^\dagger\phi_1 - v_1^2)^2 + \lambda_2(\phi_2^\dagger\phi_2 - v_2^2)^2 \\ &+ \lambda_3\left[(\phi_1^\dagger\phi_1 - v_1^2) + (\phi_2^\dagger\phi_2 - v_2^2)\right]^2 \\ &+ \lambda_4\left[(\phi_1^\dagger\phi_1)(\phi_2^\dagger\phi_2) - (\phi_1^\dagger\phi_2)(\phi_2^\dagger\phi_1)\right] \\ &+ \lambda_5\left[\mathrm{Re}(\phi_1^\dagger\phi_2) - v_1v_2\cos\xi\right]^2 + \lambda_6\left[\mathrm{Im}(\phi_1^\dagger\phi_2) - v_1v_2\sin\xi\right]^2 \\ &+ \lambda_7\left[\mathrm{Re}(\phi_1^\dagger\phi_2) - v_1v_2\cos\xi\right]\left[\mathrm{Im}(\phi_1^\dagger\phi_2) - v_1v_2\sin\xi\right] \end{aligned} \tag{1.62}$$

where λ_i are real parameters, and the potential has a discrete symmetry, $\phi_1 \to -\phi_1$, only broken softly. The last term with λ_7 can be eliminated by defining the phases of the scalar fields or demanding the CP-conservation which is assumed in this section.

The vacuum expectation values for the two scalar fields after symmetry breaking are formed as follows,

$$\langle\phi_1\rangle = \begin{pmatrix} 0 \\ v_1 \end{pmatrix}, \ \langle\phi_2\rangle = \begin{pmatrix} 0 \\ v_2 \end{pmatrix}, \tag{1.63}$$

where $v_{1,2}$ are real, in addition, the vacuum expectation values are defined by,

$$\tan\beta \equiv \frac{v_2}{v_1}, \ v^2 \equiv v_1^2 + v_2^2 = \frac{2m_W^2}{g^2} = (173\ \mathrm{GeV})^2, \tag{1.64}$$

as discussed below, the parameter β serves as key role in the model. In this model, there are five Higgs boson (h^0, H^0, A^0, and $H^\pm$) and three Goldstone bosons (G^0 and $G^\pm$) which give a mass to weak bosons. The charged Goldstone boson $G^\pm$ is orthogonal to the charged Higgs boson $H^\pm$, and the charged sector are expressed by,

$$G^\pm = \phi_1^\pm\cos\beta + \phi_2^\pm\sin\beta, \tag{1.65}$$

$$H^\pm = -\phi_1^\pm\sin\beta + \phi_2^\pm\cos\beta. \tag{1.66}$$

By demanding the CP-conservation, the imaginary parts and the real parts of the neutral scalar fields decouple. The neutral Goldstone boson is orthogonal to the one of the neutral higgs bosons, the imaginary sector (CP-odd) are obtained as,

$$G^0 = \sqrt{2}\left[\mathrm{Im}(\phi_1^0)\cos\beta + \mathrm{Im}(\phi_2^0)\sin\beta\right], \tag{1.67}$$

$$A^0 = \sqrt{2}\left[-\mathrm{Im}(\phi_1^0)\sin\beta + \mathrm{Im}(\phi_2^0)\cos\beta\right], \tag{1.68}$$

while the real sector (CP-even) are expressed by as follows,

$$H^0 = \sqrt{2}\left[(\mathrm{Re}(\phi_1^0) - v_1)\cos\alpha + (\mathrm{Re}(\phi_2^0) - v_2)\sin\alpha\right], \tag{1.69}$$

$$h^0 = \sqrt{2}\left[-(\mathrm{Re}(\phi_1^0) - v_1)\sin\alpha + (\mathrm{Re}(\phi_2^0) - v_2)\cos\alpha\right], \tag{1.70}$$

where the neutral higgs scalars are related with the mixing angle α which is defined as,

$$\sin 2\alpha = \frac{2\mathcal{M}_{12}}{\sqrt{(\mathcal{M}_{11} - \mathcal{M}_{22})^2 + 4\mathcal{M}_{12}^2}}, \tag{1.71}$$

$$\cos 2\alpha = \frac{\mathcal{M}_{11} - \mathcal{M}_{22}}{\sqrt{(\mathcal{M}_{11} - \mathcal{M}_{22})^2 + 4\mathcal{M}_{12}^2}}, \tag{1.72}$$

then, the scalar masses can be obtained by diagonalizing the Higgs boson matrix, $M_{ij}^2 = \frac{\partial^2 V}{\partial\phi_i\partial\phi_j}$, the Higgs masses are respectively written as,

$$M_{H^0,h^0}^2 = \frac{1}{2}\left[\mathcal{M}_{11} + \mathcal{M}_{22} \pm \sqrt{(\mathcal{M}_{11} - \mathcal{M}_{22})^2 + 4\mathcal{M}_{12}^2}\right], \tag{1.73}$$

$$M_{H^\pm}^2 = \lambda_4(v_1^2 + v_2^2),\ M_{A^0}^2 = \lambda_6(v_1^2 + v_2^2), \tag{1.74}$$

where using the mass matrices defined as follows,

$$\mathcal{M} = \begin{pmatrix} \mathcal{M}_{11} & \mathcal{M}_{12} \\ \mathcal{M}_{12} & \mathcal{M}_{22} \end{pmatrix} = \begin{pmatrix} 4v_1^2(\lambda_1 + \lambda_3) + v_2^2\lambda_5 & (4\lambda_3 + \lambda_5)v_1v_2 \\ (4\lambda_3 + \lambda_5)v_1v_2 & 4v_2^2(\lambda_2 + \lambda_3) + v_1^2\lambda_5 \end{pmatrix}. \tag{1.75}$$

The neutral Higgs boson couplings relate to the vacuum expectation value ratio β and the mixing angle α, the coupling can be repressed by,

$$\frac{g_{h^0VV}}{g_{\phi^0VV}} = \sin(\beta - \alpha),\ \frac{g_{H^0VV}}{g_{\phi^0VV}} = \cos(\beta - \alpha), \tag{1.76}$$

where ϕ^0 is minimal SM Higgs boson, and $V = W^\pm, Z$. Note that the remaining neutral Higgs boson A^0 couples to no gauge boson.

Next, let us show the Higgs-fermion interaction in the Type-I. The interaction is formed as,

$$\begin{aligned}\mathscr{L}_{\text{fermion}} = &-\frac{g}{2M_W\sin\beta}\bar{D}M_DD(H^0\sin\alpha + h^0\cos\alpha) - \frac{ig\cot\beta}{2M_W}\bar{D}M_D\gamma^5DA^0 \\ &-\frac{g}{2M_W\sin\beta}\bar{U}M_UU(H^0\sin\alpha + h^0\cos\alpha) + \frac{ig\cot\beta}{2M_W}\bar{U}M_U\gamma^5UA^0 \\ &+\frac{g\cot\beta}{2\sqrt{2}M_W}(\bar{U}[M_UK(1-\gamma^5) - KM_D(1+\gamma^5)]DH^+ + h.c.) + \text{leptonic sector}.\end{aligned} \tag{1.77}$$

where M_U and M_D are diagonal quark matrices, K is Kobayashi-Maskawa mixing matrix. The Higgs-lepton couplings can be expressed by replacing U, D and the quark mass matrices with the corresponding lepton fields and lepton matrices and setting $K = 1$. The neutral Higgs boson couplings to gauge bosons and fermions are shown in Table 1.3. In particular, the "fermiophobic Higgs (h_F)" appears in the 2HDM Type-I by setting the mixing angle,

$$\alpha = \frac{\pi}{2}, \tag{1.78}$$

as seen in (1.77), so-called "fermiophobia". The "fermiophobic Higgs" becomes only coupling to the bosons.

ϕ	H^0	h^0	A^0
$g_{\phi VV}$	$\cos(\beta-\alpha)$	$\sin(\beta-\alpha)$	0
$g_{\phi\bar{u}u}$	$\frac{\sin\alpha}{\sin\beta}$	$\frac{\cos\alpha}{\sin\beta}$	$\cot\beta$
$g_{\phi\bar{d}d}$	$\frac{\sin\alpha}{\sin\beta}$	$\frac{\cos\alpha}{\sin\beta}$	$\cot\beta$
$g_{\phi\bar{e}e}$	$\frac{\sin\alpha}{\sin\beta}$	$\frac{\cos\alpha}{\sin\beta}$	$\cot\beta$

Table 1.3: The neutral Higgs boson couplings to gauge bosons ($V = W^{\pm}, Z$) and fermions in 2HDM Type-I.

1.2 Production of The Higgs Boson at Tevatron

As mentioned before, the SM Higgs boson is that particle give a mass to any particles except for weak gauge boson photon and neutrinos, that is, the higgs boson couples to the massive particles with its production and decay. The strength of the process depend on higgs mass and relevant particle masses.

The main production mechanisms for the SM Higgs at hadron collider uses coupling to the heavy particles, i.e. W, Z bosons, and top quark. There are 4 dominant SM Higgs boson production modes in the Tevatron, the gluon-gluon fusion production, the associated production with the weak boson, the vector boson fusion (VBF) production, and the associated production with top quark, as shown in Figure 1.2. However there are also several mechanisms for the pair Higgs boson production, the mechanism is not useful production in the Tevatron because the production cross-section will extremely become small by the additional coupling.

In this section, the production mechanisms are described, and also its cross-sections in the Tevatron are mentioned which are taken QCD correction on NLO into account [15, 16].

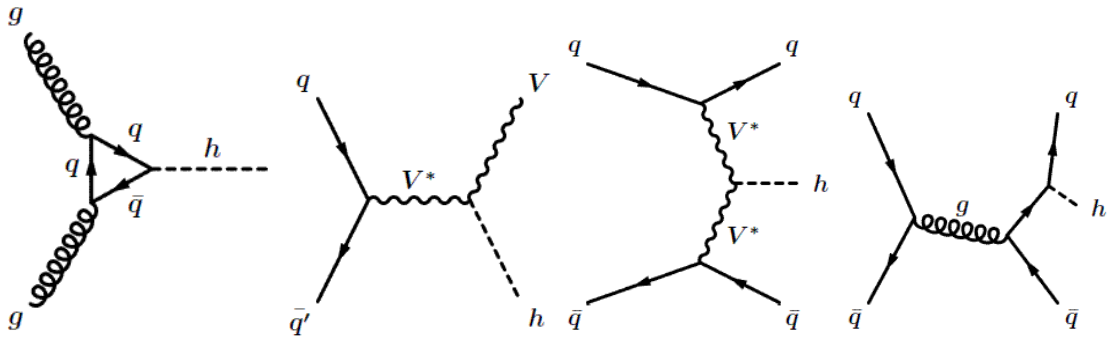

Figure 1.2: Feynman diagrams for the Higgs boson production mechanism (from left to right: the gluon-gluon fusion, the associated production with vector boson, the vector boson fusion, and the associated production with heavy quarks).

1.2.1 The gluon-gluon Fusion Production

The Higgs boson production in the gluon-gluon fusion mechanism is mediated by triangular loop of the heavy quarks, in the SM, the top quarks mostly contribute the process, while the bottom quark loop is also non-negligible contribution. In the single Higgs production, the two loop QCD radiative corrections enhance the cross-section 60-100%. The production process is the largest cross-section in the Tevatron, as shown in Figure 1.3, 1.0-0.2 pb from 100 to 200 GeV/c^2.

1.2.2 The Associated Production with Vector Boson

The associated production process goes on with $q\bar{q}$ annihilation into a virtual vector boson V^*, and then, do the "Higgs-strahlung". The QCD corrections increases the cross-section 30%. The cross-section for a virtual W^* process, $q\bar{q} \to Wh$, is roughly a factor of two higher than for a virtual Z ones, as shown in Figure 1.3. The cross-section for Wh mechanism is 0.3-0.02 pb from 100 to 200 GeV/c^2, and for Zh, 0.2-0.01 pb. The production mechanism is most promising discovery ones for $M_h < 130$ GeV/c^2.

1.2.3 The Vector Boson Fusion Production

The vector boson fusion mechanism is that the quark and anti-quark both radiate virtual bosons, and then the bosons annihilate to produce the Higgs boson. The QCD corrections enhance the cross-section by about 10%. The cross-section is 0.1-0.02 pb from 100 to 200 GeV/c^2. In this production process, there are two forward jets, it can somewhat suppress the QCD backgrounds by using the distinct kinematics.

1.2.4 The Associated Production with Heavy Quarks

The production process where Higgs is produced association with heavy quark pairs with the final state quarks being either the top or the bottom quark. At tree-level, it

originates from $q\bar{q}$ annihilation into heavy quarks with the Higgs boson emitted from the quarks lines which is the mains source at the Tevatron. Figure 1.3 shows of the top quark pairs, the QCD corrections are taken the limit of $M_h \ll M_t$ into account.

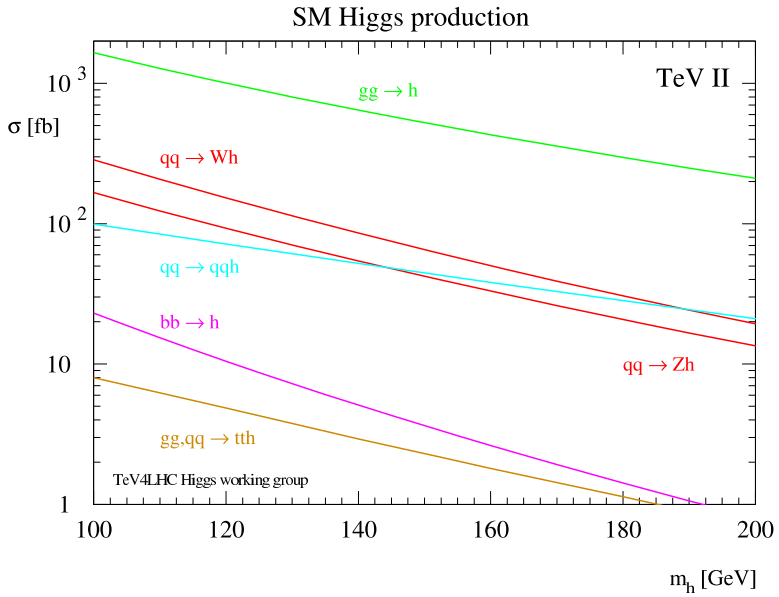

Figure 1.3: Production cross-section of the SM Higgs boson in several processes at the Tevatron.

1.3 Decay of The Higgs Boson at Tevatron

In the decay process, the Higgs boson has the tendency to decay into the heaviest particles allowed by phase space, because the Higgs couplings to gauge bosons and fermions are proportional to the masses of the particles.

The branching fractions for the dominant decay modes of the Higgs boson are varied by the Higgs-self mass. In the Tevatron, the Higgs hunters chose the best set of the Higgs decay mode and production mechanism as mentioned previous section to maximally get the discovery chance.

In this below section, the several decay modes are discussed, which are used in the Higgs search at the Tevatron. Figure 1.4 shows the branching fraction of the dominant decay modes of the minimal Standard Model Higgs boson and the fermiophobic Higgs in 2HDM Type-I.

1.3.1 $h \to f\bar{f}$ Mode

The decay mode $h \to b\bar{b}$ dominates for the minimal SM Higgs boson below about 130 GeV/c^2. The $b\bar{b}$ decay mode is ubiquitous employed in the Higgs search at the Tevatron, in particular, in the associated production with vector boson channel, because there are distinctive signatures in the final state, i.e. leptons plus two-bjets, which lead to not too large backgrounds, and the valid feature can reconstructs the $b\bar{b}$ invariant mass peak using flavour tagging (b-tagging) to reject the background such as $Wb\bar{b}$ and $t\bar{t}$ production event. The decay mode $h \to \tau\tau$ also is somewhat valid with respect to its high branching fraction for low mass minimal SM Higgs boson if enough luminosity is available, however needs a significant improvement of τ identification.

1.3.2 $h \to WW^{(*)}$ Mode

The decay mode has one of the most promising detection and the potential discovery final state $\ell^+\nu\ell^-\nu$ for the minimal SM Higgs boson $M_h > 135$ GeV/c^2 combination using gluon-gluon fusion production in the Tevatron. The dominant background source is WW and $t\bar{t}$ production. The decay process in the latter involves $t \to bW$, i.e. become 2-lepton plus 2-bjets final state, although 2-bjets non-requirement can greatly removes the background. The former can be removed by using the characteristic spin-correlations in the Higgs channel. With associated production with vector boson, the decay mode will be significance detection channel using like-sign dilepton event in the final state, which excellently remove the QCD and electroweak backgrounds. The combination channel are employed in this thesis, and also useful to search for the fermiophobic Higgs from its low mass region due to its feature, as shown in the right-hand side of Figure 1.4.

1.3.3 $h \to \gamma\gamma$ Mode

Although the two photon decay mode is extremely rare for the minimal SM Higgs boson at the Tevatron, for low mass fermiophobic Higgs will be useful, which will be dominant mode, as shown in Figure 1.4. And the mode give a narrow mass peak which can effectively reject the backgrounds.

1.4 Higgs Boson Mass Constraints

As mentioned before, the Higgs boson mass are not given in the SM framework while predicted the existence of the Higgs boson. However the Higgs boson mass can be constraint by taking into account adaptive limit for perturbation theory. In additional, the passed experiment results have constrained the Higgs boson mass. In this section, the constraints on the Higgs boson mass are discussed in both theoretical and experimental point of view.

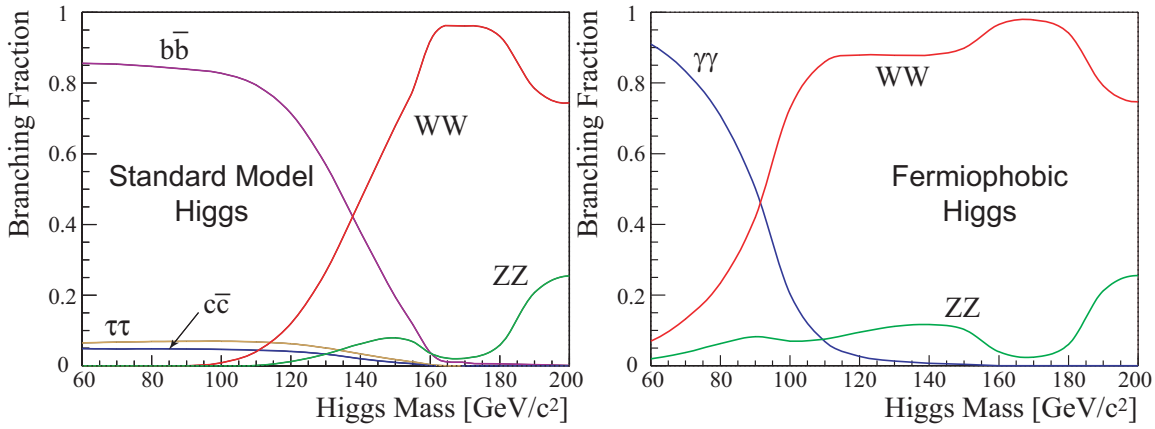

Figure 1.4: The branching fraction on the minimal SM Higgs boson (left-side) and the Fermiophobic Higgs boson in 2HDM Type-I (right-side).

1.4.1 Theoretical Higgs Boson Mass Constraints

The Higgs mass and its coupling depend on the considered energy because of quantum (radiative) corrections. The Higgs mass can be limited by taking into account the energy scale from upper side (triviality bound) and lower side (vacuum stability bound) where the SM is valid within perturbation theory. In this section, let us see the theoretical constraint of the Higgs boson mass. Figure 1.7 shows the upper bound and the lower bound on the Higgs boson mass as a function of the energy scale Λ_c.

Triviality Bound

First, let us take the one-loop radiative correction to the Higgs boson quartic coupling for the contributions to the Higgs boson. The Feynman diagrams for the tree-level and the one-loop corrections to the Higgs boson self-coupling are shown in Figure 1.5. The variation of the quartic Higgs coupling with the energy scale Q is described by the Renormalization Group Equation (RGE),

$$\frac{d\lambda(Q^2)}{dQ^2} = \frac{3}{4\pi^2}\lambda^2(Q^2) + \text{higher order}. \tag{1.79}$$

The solution of the equation by selecting a energy point to be the electroweak symmetry breaking scale $Q_0 = v$ can be written by,

$$\lambda(Q^2) = \lambda(v^2)\left[1 - \frac{3}{4\pi^2}\lambda(v^2)\log\frac{Q^2}{v^2}\right]^{-1}. \tag{1.80}$$

The quartic couplings varies logarithmically with the squared energy Q^2. From (1.80), if the energy is much smaller than the electroweak breaking scale, $Q^2 \ll v^2$, the quartic coupling becomes extremely small and eventually vanishes, i.e. the theory is trivially

non-interacting, $\lambda(Q^0) \sim 0$. While when the energy is much higher than electroweak scale, $Q^2 \gg v^2$, the quartic coupling grows and eventually becomes infinite $\lambda(Q^2) \gg 1$ which is called Landau Pole, i.e. the coupling becomes infinite at the energy,

$$\Lambda_c = v \exp\left(\frac{4\pi^2 v^2}{M_h^2}\right). \tag{1.81}$$

The energy point Λ_c is corresponding to the Higgs mass upper limit to avoid the Landau pole as seen in (1.81). For instance, if the energy $\Lambda_c \sim 10^{16}$, the Higgs boson mass need to be light, $M_h < 200$ GeV/c^2, while when the energy $\Lambda_c \sim 10^3$, the Higgs boson mass is allowed to be the order of 1 TeV/c^2.

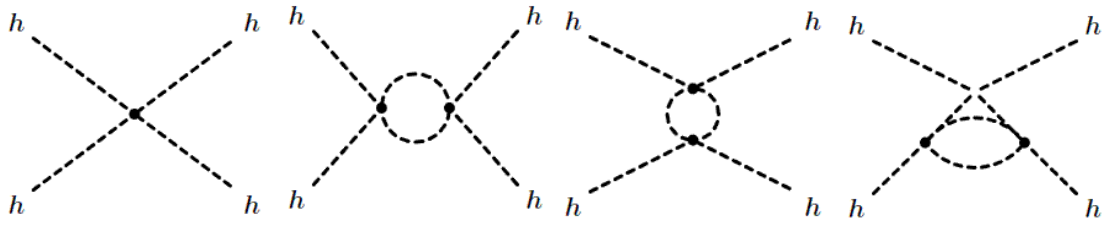

Figure 1.5: Feynman diagrams for the tree-level and one-loop Higgs self-coupling.

Stability Bound

Next, the Higgs boson coupling needs to also include the contribution from fermion and gauge bosons. In this case, only the contribution of top quark and massive gauge bosons are taken into account because the Higgs boson coupling are proportional to the particle masses. The Feynman diagrams for the top quark and gauge boson contribution are shown in Figure 1.6. The one-loop RGE for the quartic coupling including the additional contribution can be obtained by,

$$\frac{d\lambda}{d\log Q^2} \simeq \frac{1}{16\pi^2}\left[12\lambda^2 - \frac{12M_t^4}{v^4} + \frac{3}{16}(2g_2^4 + (g^2 + g^1)^2)\right], \tag{1.82}$$

where the top quark Yukawa coupling is $\lambda_t = \sqrt{2}m_t/v$. The solution taking the electroweak breaking scale same as the case of Higgs self-coupling,

$$\lambda(Q^2) = \lambda(v^2) + \frac{1}{16\pi^2}\left[-\frac{12M_t^4}{v^4} + \frac{3}{16}(2g_2^4 + (g_2^2 + g_1^2)^2)\right]\log\frac{Q^2}{v^2}. \tag{1.83}$$

If the coupling λ is too small, the top quark contribution can be dominant and could result a negative value $\lambda(Q^2) < 0$ which is eventually leading to a scalar potential $V(Q^2) < V(v)$, and it can say that the vacuum is stable since it has no minimum. From the stability perspective, that is, to keep $\lambda(Q^2) > 0$, the Higgs boson mass need to be larger than a value as written in the following,

$$M_h^2 > \frac{v^2}{8\pi^2}\left[-\frac{12M_t^4}{v^4} + \frac{3}{16}(2g_2^4 + (g_2^2 + g_1^2)^2)\right]\log\frac{Q^2}{v^2}. \tag{1.84}$$

The lower constraint on Higgs boson mass depends on the value of the energy scale Λ_c, if the value $\Lambda_c \sim 10^3$, the Higgs boson mass should be larger than 70 GeV/c^2, and if $\Lambda_c \sim 10^{16}$, the Higgs boson mass is larger than 130 GeV/c^2.

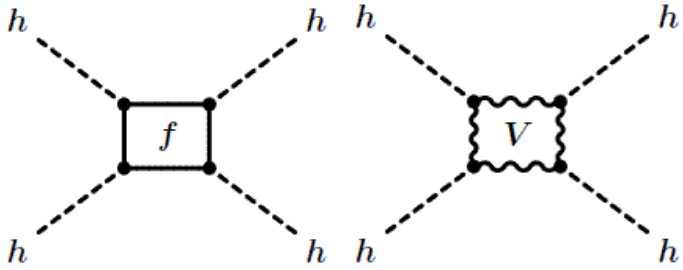

Figure 1.6: Feynman diagrams for the one-loop contribution of fermion and gauge boson to the Higgs coupling λ.

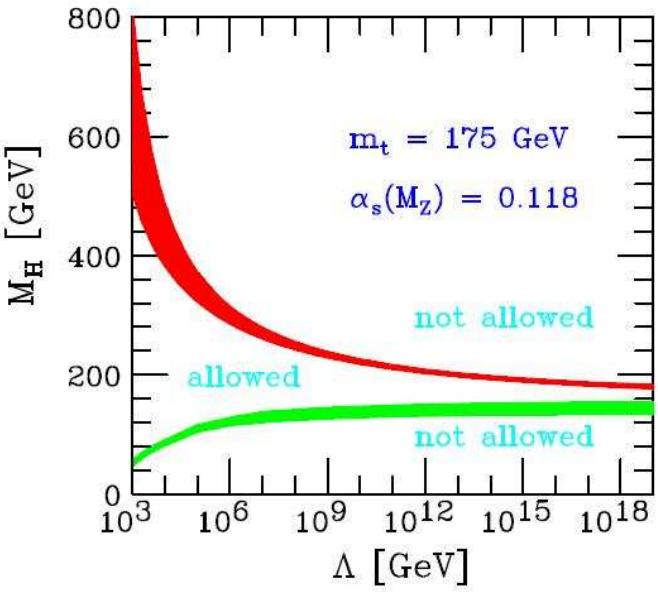

Figure 1.7: The triviality (upper) bound and the vacuum stability (lower) bound on the Higgs boson mass as a function of the cut-off scale Λ for a top quark mass $M_t = 175 \pm 6$ GeV/c^2 and $\alpha_s(M_Z) = 0.118 \pm 0.002$.

1.4.2 Experimental Higgs Boson Mass Constraints

The Higgs searches have performed and are going on with the various experiments in the whole world. The experiments results give us the constraint of the Higgs mass, directly and indirectly. The letter constraints are set by using precision electroweak measurements taking top quark and Higgs boson radiative correction into account. The

four LEP collaborations performed the Higgs direct searches at LEP1 and LEP2 from 1989 to 2000. The collaborations reported the combined lower limits on the mass of SM Higgs boson, also set the lower limit on the mass of the fermiophobic Higgs boson. In this section, The experimental Higgs mass constraints are discussed.

The Electroweak Precision Measurements

The electroweak parameters, the vector boson and top quark mass and its width, forward-backward asymmetry, and so on, are precisely measured by various experiments (ALEPH, DELPHI, L3, OPAL, SLD, CDF, DØ and NuTeV) in the world. The precision electroweak results have the sensitivity to the masses of the top and the Higgs boson through radiative (loop) corrections as shown in Figure 1.8. The parameter indicating the relation of the W boson and the Z boson mass with weak mixing angle at one loop is,

$$\rho = \frac{M_W^2}{M_Z^2(1-\sin^2\theta_W)} \equiv 1 + \Delta r, \tag{1.85}$$

and a radiative correction are written by,

$$\Delta r = \frac{3G_F}{8\pi^2\sqrt{2}} m_t^2 + \frac{\sqrt{2}G_F}{16\pi^2} M_W^2 \left[\frac{11}{3}\ln\left(\frac{M_h^2}{M_W^2}\right) + \cdots\right] + \cdots, \tag{1.86}$$

which is quadratic in the top quark mass, while the dependence on the mass of the Higgs boson is only logarithmic, therefore the top quark mass, especially if large, is the dominant parameter in the correction to electroweak processes [17].

The electroweak precision measurements allow the constraint on the SM Higgs boson mass [18]. The Figure 1.9 shows the $\Delta\chi^2$ of the fit to all electroweak measurements as a function of SM Higgs Mass. From the fitting, the constraint SM Higgs mass with the experiment uncertainties are obtained as,

$$M_h = 84^{+34}_{-26}\ \mathrm{GeV}/c^2, \tag{1.87}$$

the shaded band represents the uncertainty due to uncalculated higher-order corrections. And the 95% one-sided confidence level upper limits on the SM Higgs mass is,

$$M_h < 154\ \mathrm{GeV}/c^2, \tag{1.88}$$

when the 95% confidence level lower limits on the SM Higgs mass 114.4 GeV/c^2 from direct searches as discussed in the following section is included, the upper limit increases to 185 GeV/c^2.

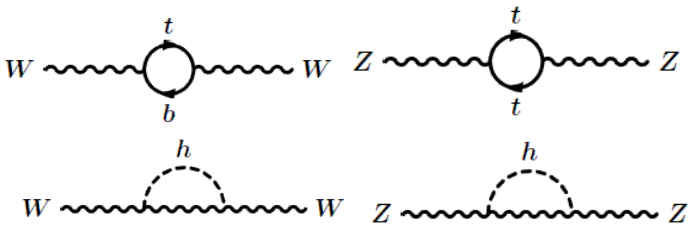

Figure 1.8: Radiative loop correction for electroweak processes.

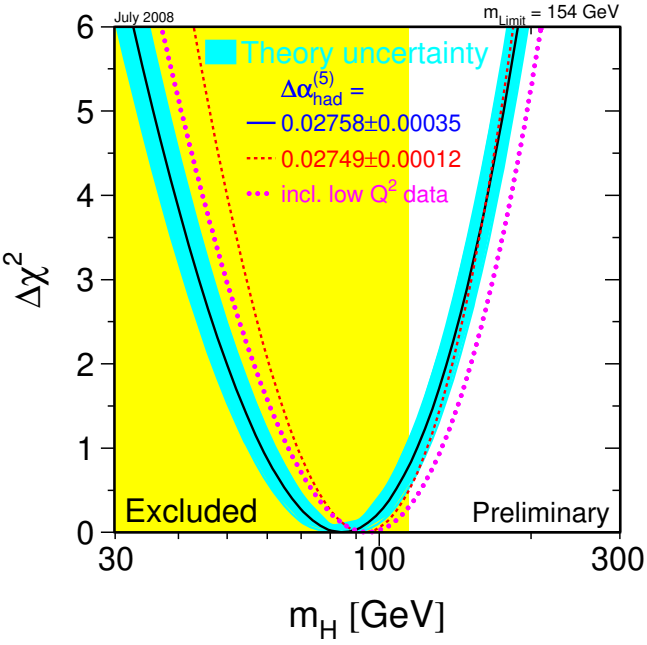

Figure 1.9: The $\Delta\chi^2$ of the fit to the electroweak precision data as a function of SM Higgs mass. The solid line results by including all data, and the blue band is the estimated theoretical error from missing higher-order corrections.

The SM Higgs Boson Searches at LEP

The four LEP collaborations, ALEPH, DELPHI, L3, and OPAL set a lower bound of the SM Higgs bosons at 95% confidence level using the combined result [19]. The LEP collaborations have collected a total of 2461 pb^{-1} of e^+e^- collision data at $\sqrt{s} = 189 - 209$ GeV which are used to search for the SM Higgs boson. The four results are combined and examined in a likelihood test for their consistency with two hypotheses, the background hypothesis and the signal plus background hypothesis.

The SM Higgs boson is expected to be produced mainly in association with Z as $e^+e^- \to Zh$, and the SM Higgs boson is expected to decay mainly into $b\bar{b}$ pairs. The target final state are the 4-jets event ($Zh \to q\bar{q}b\bar{b}$), the missing energy event

($Zh \to \nu\bar{\nu}b\bar{b}$), the leptonic event ($Zh \to \ell^+\ell^- b\bar{b}$, $\ell = e, \mu$), and the tau lepton event ($Zh \to \tau^+\tau^- b\bar{b}$).

The ratio $CL_s = CL_{s+b}/CL_b$ is used to drive a lower bound on the SM Higgs boson mass, where CL_{s+b} means the compatibility for the observation and signal + background hypothesis, and CL_b is the compatibility for the observation and background hypothesis. Using The quantity for setting exclusion limits by taken a mass hypothesis into account to be excluded at the 95% confidence level if the corresponding value of CL_s is less than 0.05. The combined the final results from the four LEP experiments is a lower bound of 114.4 GeV/c^2 on the mass of the SM Higgs boson at the 95% confidence level as shown in Figure 1.10.

The Fermiophobic Higgs Boson Searches at LEP

The LEP collaborations also set a lower bound on the "benchmark" fermiophobic Higgs boson at the 95% confidence level assuming Standard Model production rates [20]. The four experiments searched for hadronic, leptonic, and missing energy decay mode of the associated Z boson in the production Zh^0 with $h^0 \to \gamma\gamma$. For the combined data from the four experiments, the 95% confidence level lower mass limit for a benchmark fermiophobic Higgs boson is set at 109.7 GeV/c^2. Figure 1.11 shows the combined upper limit on $B(h^0 \to \gamma\gamma) \times \sigma(e^+e^- \to h^0 Z)/\sigma(\mathrm{SM})$ at 95% confidence level.

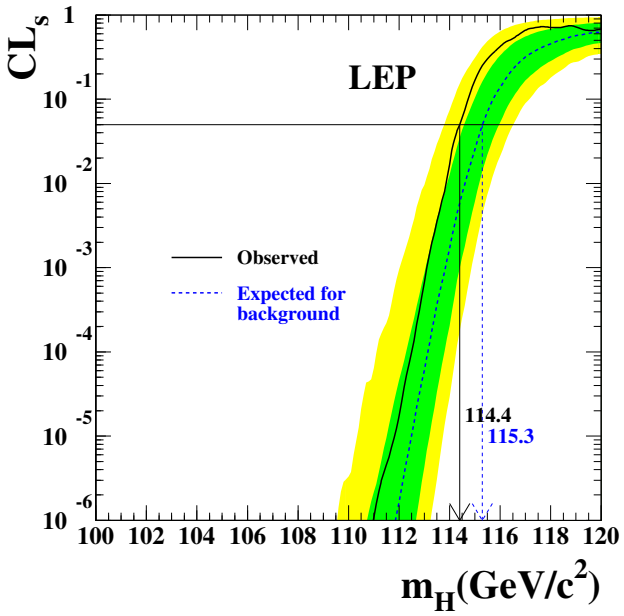

Figure 1.10: Confidence Level CL_s for the signal+background hypothesis in Higgs production at LEP2. The yellow green and yellow band around the median expected line correspond to the 68% and 95% probability bands, respectively.

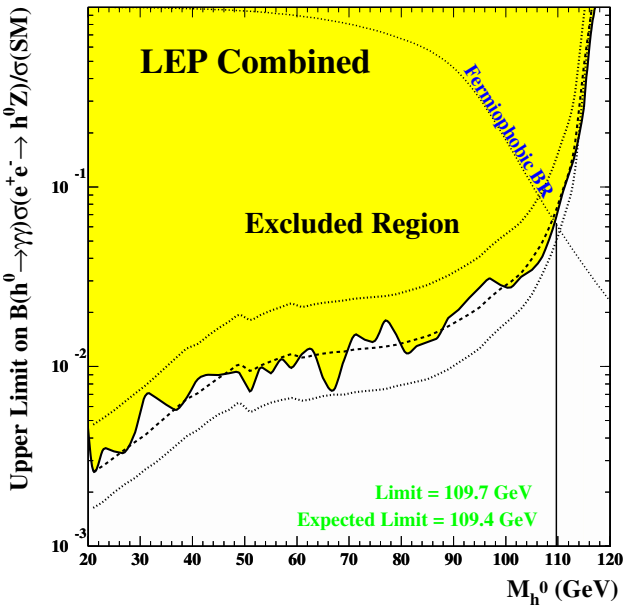

Figure 1.11: Combined LEP experiment upper limits for the Higgs bosons decaying into di-photons $B(h^0 \to \gamma\gamma) \times \sigma(e^+e^- \to h^0 Z)/\sigma(\mathrm{SM})$ as a function of Higgs mass at 95% confidence level.

1.5 Higgs Boson Searches at Tevatron

The two Tevatron collaboration, CDF and DØ, are performing not the SM Higgs boson searches but also the extended SM Higgs and the MSSM Higgs searches. At the present day, the Tevatron are already here that give us the new knowledge for the SM Higgs bosons for the first times in 5 years from the LEP result. In this section, let us discuss the performing SM Higgs searches and also fermiophobic searches at two Tevatron collaborations.

The SM Higgs Boson Searches

The CDF and the DØ collaborations are searching the SM Higgs boson by looking at several Higgs production and decay modes as described §1.2 and §1.3 with too efforts. The CDF experiment searches the SM Higgs Boson under mainly six channels [21, 22, 23, 24, 25, 26], the four of them are sensitive to low mass SM Higgs ($M_h < 135$ GeV/c^2) because of the looking for $H \to b\bar{b}$ and $\tau^+\tau^-$ decay mode ($WH \to \ell\nu b\bar{b}$, $ZH \to \ell\ell b\bar{b}$, $VH \to \nu\bar{\nu}b\bar{b}$, and $H \to \tau^+\tau^-$), while the remaining two channels are sensitive to the high mass SM Higgs ($M_h > 135$ GeV/c^2) because of the looking for $H \to WW$ ($gg \to H \to WW \to \ell^\pm\nu\ell^\mp\nu$ and $WH \to WWW \to \ell^\pm\nu\ell^\pm\nu$ that is this study channel), they contribute to the combined Tevatron (CDF and DØ) upper limits on the SM Higgs boson production. The latest result (2009 winter) will show in §8.

Also the several SM Higgs search channels (total 6 channels [27, 28, 29, 30, 31, 32]) in the DØ experiment contribute to the Tevatron limits, in this case, included channel $H \to \gamma\gamma$ instead of $H \to \tau^+\tau^-$ channel. It is necessary to emphasize that the Tevatron combined result using 2.0-3.0 fb^{-1}, at 2008 Summer, excluded the SM Higgs mass 170 GeV/c^2 at 95% confidence level. Figure 1.12 shows the Tevatron combined upper limit on the ratios to the SM Higgs boson production in the high Higgs mass region [33].

The Fermiophobic Higgs Boson Searches

The Tevatron experiments, CDF and DØ also search for the fermiophobic Higgs boson. In 1st period run, so-called Run-I, the CDF collaboration set a lower mass limit by looking at di-photon events ($h_f \to \gamma\gamma$) at $\sqrt{s} = 1.8$ TeV with 100 pb^{-1} data [34]. The Higgs boson production considers the associated production with W and Z boson. The lower limit on the mass of the fermiophobic Higgs is 82 GeV/c^2 at 95% confidence level. The DØ collaboration also reported the lower limit on the mass at Run-I [35]. The limit are set by using the associated production with vector boson and vector boson fusion production and looking at di-photon plus 2-jets final state ($h_f \to \gamma\gamma$, $Z/W \to jj$). The DØ collaboration set the lower limits on the fermiophobic Higgs mass of 85 GeV/c^2 at 95% confidence level. Now, in the Run-II, the CDF and the DØ collaborations are also searching for the fermiophobic Higgs boson by using several the Higgs production and decay modes, for instance di-photon channel [36] and 3 or 4-photons channel [37], and also $Wh \to WWW$ channel as discussed this thesis has discovery potential.

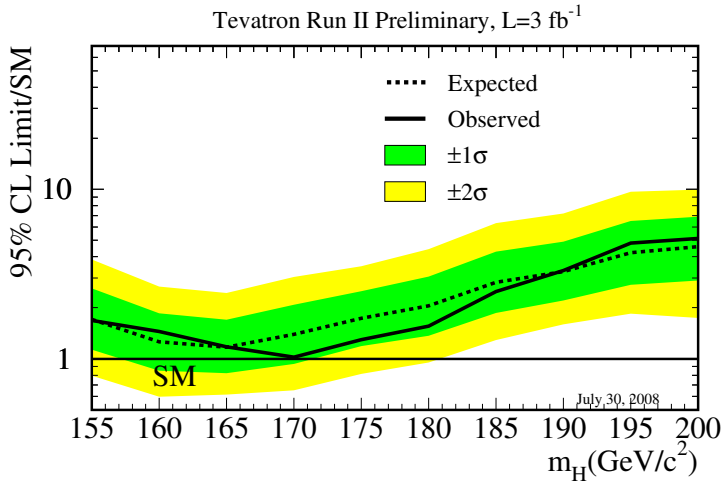

Figure 1.12: Tevatron combined upper limit on the ratios to the SM Higgs boson production as a function of the Higgs mass at 95% confidence level. The green and yellow bands indicate the 68% and 95% probability regions, respectively.

Chapter 2

Experimental Apparatus

The Tevatron Collider represents the high energy frontier accelerator in particle physics. The Tevatron is located at Fermilab in Batavia, Illinois USA. It is currently providing highest energy proton-antiproton with a center-of-mass energy of $\sqrt{s} = 1.96$ TeV. The collisions occur at two points in Tevatron ring which has a radius of about 1km. The collision points are instrumented with a detector in each which called The Collider Detector at Fermilab (CDF II) and DØ. This study uses data collected with the CDF II. The CDF II is a general purpose solenoidal detector which combines precision charged particle tracking, scintillator based calorimetry, and muon detection chambers and scintillators. This chapter describes the beam production and acceleration system, and the CDF II detector design.

2.1 The Accelerator Complex

The Tevatron is the last in a chain of accelerators that gradually increase the energy of protons and antiprotons. The protons are abundant and readily in nature, while antiprotons must be produced and stored. In addition, a single accelerator cannot bring particles from rest to very high energies because no magnets have the dynamic range necessary. Consideration of these requirements led to the design of a chain of accelerators at Fermilab. Figure 2.1 shows a diagram and aerial photograph of the Fermilab accelerator chain.

2.1.1 Proton Production and Boosting

The Cockcroft-Walton pre-accelerator provides the first stage of acceleration. The accelerator ionizes the hydrogen gas to H^+ ions, which are accelerated to 750 keV of kinetic energy.

The ionized hydrogen gases (H^+) enter a liner accelerator (Linac), approximately 150m long, and the ions are accelerated to 400 MeV. The acceleration in the Linac is done by a series of "kicks" from Radio Frequency (RF) cavities.

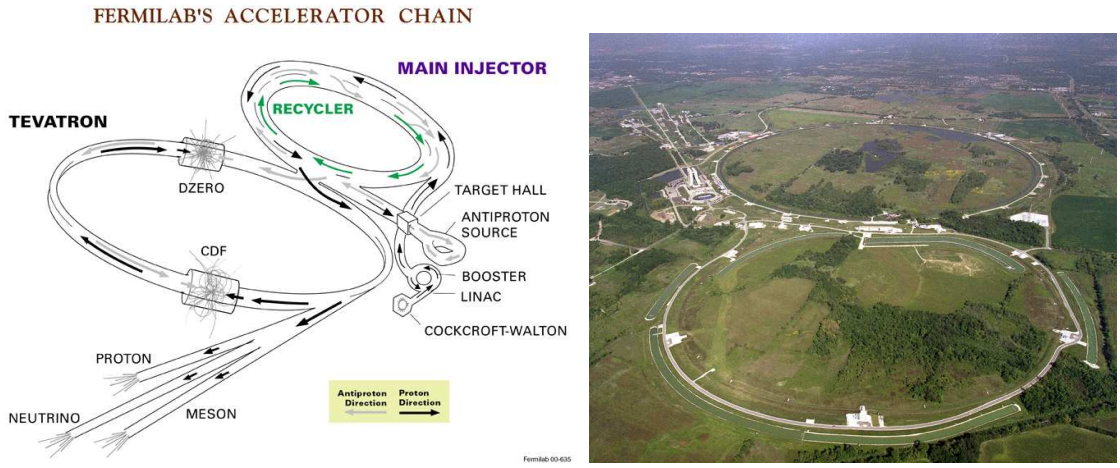

Figure 2.1: A diagram (left) and aerial photograph (right) of the Fermilab accelerator chain.

The H^+ ions with 400 MeV are injected into the Booster. The Booster is a circular synchrotron, approximately 150m in diameter. A carbon foil strips the electrons from the H^+ ions, leaving behind protons. The intensity of the protons beam is increased by injecting new protons into the same orbits as the circulating ones. The protons are accelerated from 400 MeV to 8 GeV with a series of magnets arranged around a 75m radius circle, with 18 RF cavities interspersed.

2.1.2 Main Injector

The Main Injector (MI) is a circular synchrotron seven times the circumference of the Booster and slightly more than half the circumference of the Tevatron. Main Injector has 18 accelerating cavities. It can accelerate 8 GeV protons from the Booster to either 120 GeV or 150 GeV, depending on their destination. When used to stack antiprotons, the final energy is 120 GeV. When used to inject into the Tevatron, the final beam energy is 150 GeV. As well as accepting protons from Booster, the Main Injector can accept antiprotons from the Antiproton Source. The Main Injector can accelerate beam as fast as every 2.2 seconds.

2.1.3 Antiproton Source

In order to produce antiprotons, the protons with 120 GeV are extracted from the MI and strike a nickel target at the Antiproton source. These high-energy protons striking the target produce a spray of all sorts of secondary particles. Using magnets to choose which momentum and charge we can collect 8 GeV antiprotons from this spray. Approximately one antiproton is produced per 10^5 protons. These antiprotons are directed into the Debuncher.

The Debuncher is a rounded triangular-shaped synchrotron with a mean radius of 90m. It can accept 8 GeV antiprotons from the target station, and maintain the beam at a energy of 8 GeV. Its primary purpose is to efficiently capture the high momentum spread antiprotons coming from the target using a RF manipulation called bunch rotation which reduce the antiproton momentum spread. The reduction is done to improve the Debuncher to Accumulator transfer because of the limited momentum aperture of the Accumulator at injection.

The Accumulator is also triangular-shaped synchrotron and is mounted in the same tunnel as the Debuncher. It is the storage ring for antiprotons, all of the antiprotons made are stored here at 8 GeV and cooled until need.

2.1.4 Recycler

The Recycler is an antiproton storage ring installed in the same tunnel as the MI. The proposed purpose of the Recycler was to recycle the antiproton from a Tevatron store, cooling them and storing them alongside those sent from the Antiproton Source. This was abandoned after early problems in RunII. The Recycler now accepts transfers only from the Antiproton Source and cools them further than the antiprotons Accumulator is capable. The Recycler uses both a stochastic cooling system and an electron cooling system. Stochastic cooling is used to cool the beam in Recycler, but loses its effectiveness with higher intensities. Once above 2×10^{12} antiprotons in the Recycler, Electron cooling is required. Electron cooling works on the principle of momentum transfer between electrons and antiprotons, a highly concentrated, cool beam of electrons is driven at the same energy as the antiprotons and laid overtop of the antiprotons. The resulting glancing collisions between electrons and antiprotons transfer some of the momentum from the "hot" antiprotons to the "cool" electrons. With enough electrons, a substantial longitudinal cooling force is produced by absorbing momenta from the antiprotons allowing for more compact, brighter bunches to send to the Tevatron.

2.1.5 Tevatron

The Tevatron is the largest of the Fermilab accelerators, with a circumference of approximately 6km long. It is a circular synchrotron with eight accelerating cavities. The Tevatron can accept both protons and antiprotons from MI and accelerate them from 150 GeV to 980 GeV. In Collider mode, the Tevatron can store beam for hours at a time. Because the Tevatron is a primarily storage ring, the length of time between acceleration cycles is widely variable. The Tevatron is the cryogenically cooled accelerator. The magnets used in the Tevatron are made up of a superconducting niobium/titanium alloy that needs to be kept extremely cold ($\sim$4 K) to remain a superconductor. The benefit of having superconducting magnets is the increased magnetic fields possible when high currents can be run through thin wires without fear of damage related to excessive resistive heating.

2.1.6 Luminosity

The luminosity of collisions can be expressed as:

$$\mathcal{L} = \frac{f N_B N_p N_{\bar{p}}}{2\pi(\sigma_p^2 + \sigma_{\bar{p}}^2)} F\left(\frac{\sigma_l}{\beta^*}\right), \tag{2.1}$$

where f is the revolution frequency, N_B is the number of bunched, $N_{p(\bar{p})}$ is the number of protons (antiprotons) per bunch, and $\sigma_{p(\bar{p})}$ is the protrons (antiprotons) RMS beam size at the interaction point. F is a form factor which corrects for the bunch shape and depends on the ratio of σ_l, the bunch length to β^*, the beta function, at the interaction point. The beta function is a measure of the beam width, and it is proportional to the beam's x and y extent in phase space. Table 2.1 shows the accelerator parameter in the current run (Run II). The current peak luminosity is $\sim 3.6 \times 10^{32}$ cm^{-2}s^{-1}. The delivered luminosity is 5.4 fb^{-1} and actual recorded luminosity is 4.5 fb^{-1}, which is collected between February 2002 and December 2008. Figure 2.2 shows integrated luminosity measured with CDF.

Parameter	Run II
Number of bunhes (N_B)	36
Bunch length [m]	0.37
Bunch spacing [ns]	396
Protons/bunch (N_p)	2.7×10^{11}
Antiprotons/bunch ($N_{\bar{p}}$)	3.0×10^{10}
Total antiprotons	1.1×10^{12}
β^* [cm]	35
Interactions/crossing	2.3

Table 2.1: Accelerator parameters for Run II configurations.

2.2 The Collider Detector at Fermilab

The CDF II detector [38] is a general purpose solenoidal detector which combines precision charged particle tracking with fast projective calorimetry and fine grained muon detection. Figure 2.3 and Figure 2.4 show a cut away view and elevation view of the CDFII detector for each. Tracking systems are made up Silicon Trackers, Central Outer Tracker (COT), and Superconducting Solenoid which to measure precise trajectories and momenta of charged particles and reconstruct vertices. The solenoid surround the Silicon Trackers and COT, has 1.5m in radius and 4.8m long, and generates a 1.4 T magnetic field parallel to the beam axis. Calorimetry Systems measure the energy of particles, surround the solenoid. Muon Chambers detect the particles penetrating both Tracking Systems and Calorimetry Systems. Muons deposit small amount of ionization

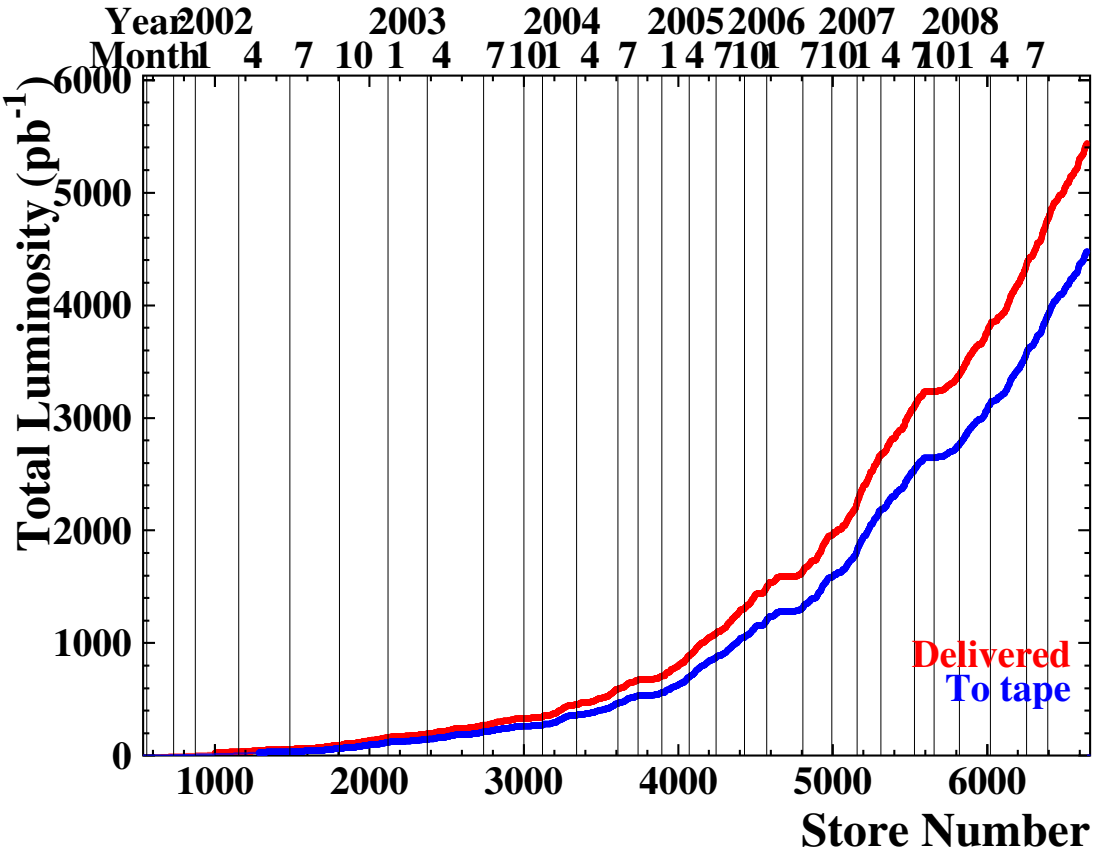

Figure 2.2: Integrated luminosity as a function of store number between February 2002 and December 2008.

energy in the material because they act as minimally ionizing particles (MIP), that is, the penetrating particles are mostly muons.

2.3 Coordinate System in the CDF

The standard coordinate system to be used in the CDF is the right-handed coordinate system. The z-axis is oriented the direction of the proton beam. The x-axis points horizontally away from the detector and the y-axis is vertical pointing up-wards. It is helpful to use the cylindrical coordinate. The azimuthal angle ϕ is $x-y$ plane angle around the beam line. The polar angle θ is measured starting from the z-axis. The rapidity of a particle is defined as,

$$y \equiv \frac{1}{2}\ln\left(\frac{E+p_z}{E-p_z}\right). \tag{2.2}$$

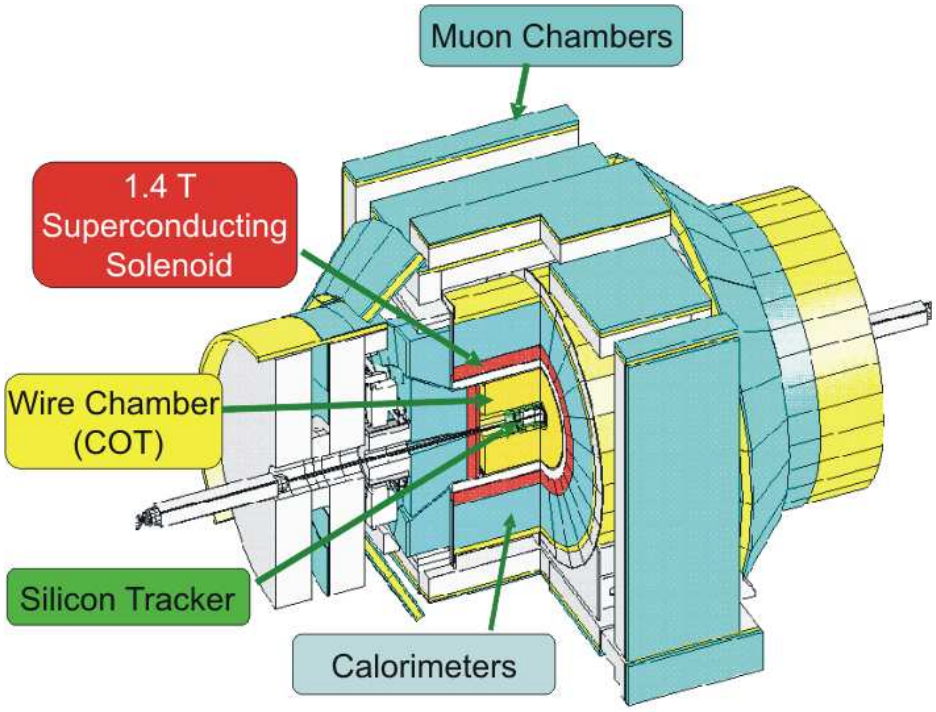

Figure 2.3: Cut away view of the CDF II detector.

where E is the energy of the particle and p_z is its longitudinal momentum. For highly boosted particles, $E \sim p$ and $p_z = p\cos\theta$, that is, the rapidity can be approximated by pseudorapidity,

$$\eta = -\ln\left(\tan\frac{\theta}{2}\right). \tag{2.3}$$

2.4 Tracking Systems

For CDF analysis technique, precision charged particle tracking is very important. CDF II detector has an open cell drift chamber, the Central Outer Tracker (COT) covers the region $|\eta| \leq 1.0$. Inside the COT, a silicon "inner tracker" is built from three components. Layer 00 (L00) is mounted on the beam pipe, very close to the beam line. Its primary purpose is to improve the impact parameter resolution. A micro-vertex detector at very small radii, so-called Silicon Vertex Detector (SVX-II), establishes the ultimate impact parameter resolution. Two additional silicon layers at intermediate radii, so-called Intermediate Silicon Layers (ISL), provides p_T resolution and b-tagging in the forward region $1.0 \leq |\eta| \leq 2.0$, and stand-alone silicon tracking over the full region $|\eta| \leq 2.0$. The stand-alone silicon segments allow integrated tracking algorithms which maximize tracking performance over the whole region $\eta \leq 2.0$. In the central region ($\eta \leq 1.0$), the stand-alone silicon segment can be linked to the fill

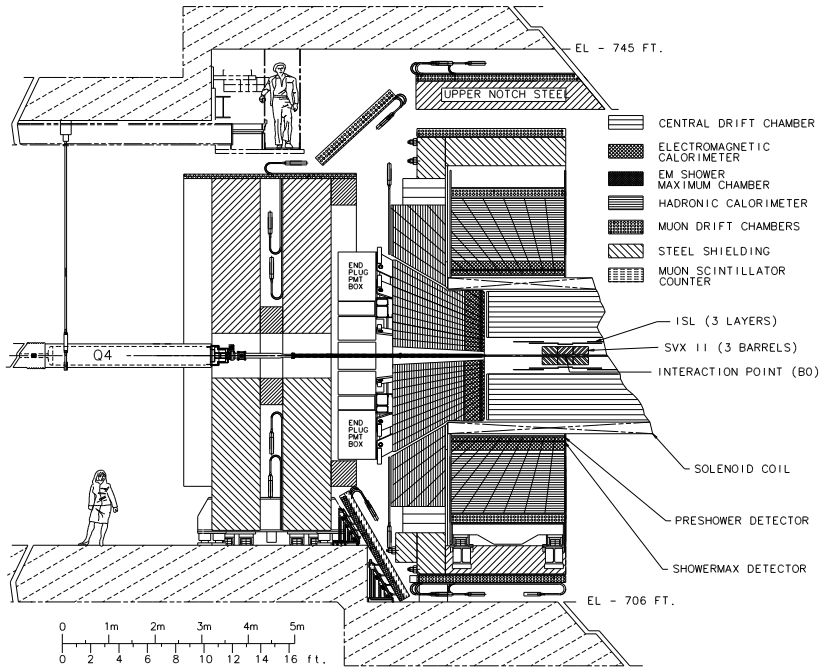

Figure 2.4: Elevation view of the CDF II detector.

COT track to give excellent p_T and impact parameter resolution.

2.4.1 Layer 00

Layer 00 [39, 40] is installed directly in the beam pipe. L00 was added at beginning of RunII for two reasons. Firstly to improve the impact parameter resolution of the CDF detector. Placement of a minimal material silicon layer at a smaller radius provides a precise measurement. Secondly, L00 was installed to extend the useful lifetime of the silicon system. The inner layers SVX-II will have a limited lifetime due to radiation damage. The design has six narrow (128 channels) and six wide (256 channels) groups in θ at $r = 1.35$cm and $r = 1.62$cm respectively. There are six readout modules in z, with two sensors bounded together in each module for a total length of 95cm. The sensors are single-sided p-in-n silicon with a 25(50)μm implant(readout) pitch. These have been produced by Hamamatsu Photonics (HPK), SGS-Thompson (ST) and Micron. These sensors can be biased up to 500V, limited by the maximum range of the power supplies. Figure 2.5 shows the end view of L00 and a part of SVX-II (L0 and L1).

2.4.2 Silicon Vertex Detector

Silicon Vertex Detector (SVX, SVX-II) [41] is the core detector for silicon tracking and for a trigger on tracks with large impact parameter with respect to the interaction

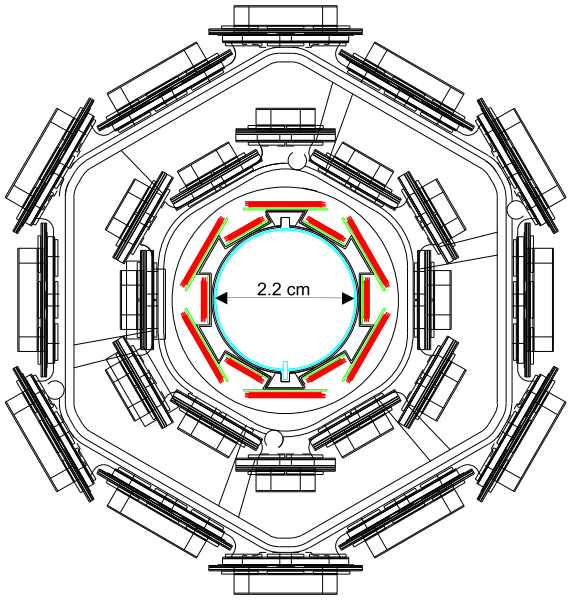

Figure 2.5: End view of Layer 00 (colored), also showing a part of SVX-II (un-colored).

point [42]. The SVX-II detector has 5 layers of double-sided sensors surround the L00 at radii from 2.5 to 10.6cm. Three layers (L0, L1, and L3) are made of Hamamatsu silicon with the n strips perpendicular to the p strips. The remaining two layers (L2 and L4) are Micron sensors with a stereo angle of 1.2° between the n and p strips. The strip pitch varies between 60 to 140μm, depending on the layer radius. The maximum bias voltages that can be applied to Hamamatsu and Micron sensors are 170 V and 70 V respectively, limited by the breakdown voltage of the integrated coupling capacitors and subtle sensor effects. The SVX-II can provide track information to $|\eta| < 2.0$. Table 2.2 shows the design parameters of the SVX-II. Figure 2.6 shows 3D view and $r - \phi$ view for SVX-II.

2.4.3 Intermediate Silicon Layers

Intermediate Silicon Layers (ISL) [43, 44] provides an extended forward coverage and links tracks between the COT and The SVX-II, and also can provide stand-alone 3D track information in the forward region. The ISL detector has one central layer at radius of 22cm covering $|\eta| < 1.0$, and two forward layers at radii of 22cm and 28cm covering $1 < |\eta| < 2$, with total length of 3m. It is made of double-sided silicon with strips at a stereo angle of 1.2°, and a strip of 112μm. The breakdown voltage of the sensors is 100V limited by the breakdown voltage of the coupling capacitors.

Parameter	Layer 0 (L0)	Layer 1 (L1)	Layer 2 (L2)	Layer 3 (L3)	Layer 4 (L4)
Number of ϕ strips	256	384	640	768	896
Number of z strips	512	576	640	512	896
stereo angle (degree)	90	90	+1.2	90	−1.2
ϕ strip pitch [μm]	60	62	60	60	65
z strip pitch [μm]	141	125.5	60	141	65
Total width [mm]	171.140	25.594	40.300	47.860	60.170
Total length [mm]	74.3	74.3	74.3	74.3	74.3
Active width [mm]	15.300	23.746	38.340	46.020	58.175
Active length [mm]	72.43	72.43	72.38	72.43	72.38
Number of sensors	144	144	144	144	144

Table 2.2: Design parameters of the Silicon Vertex Detector.

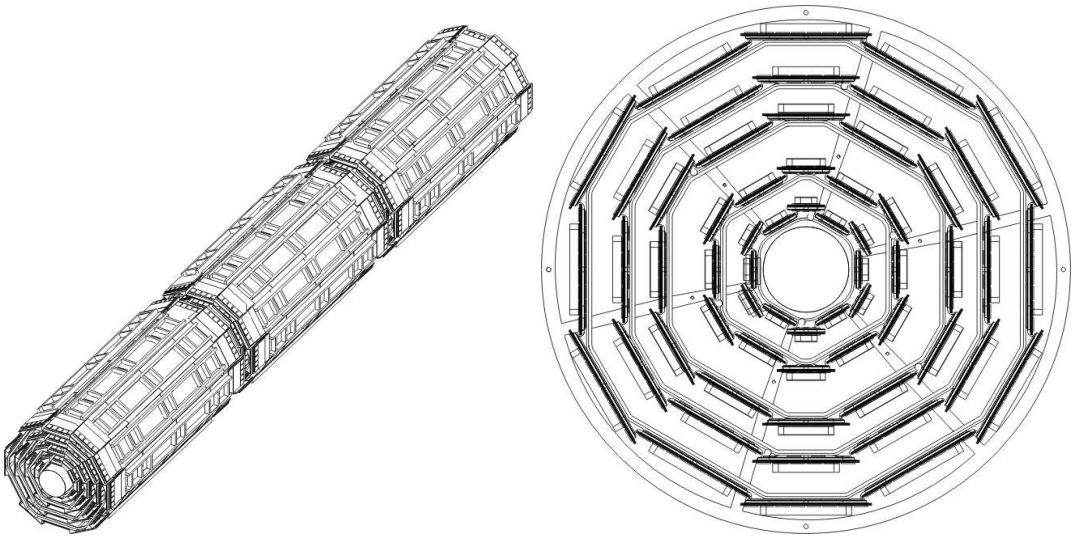

Figure 2.6: 3D view of the three barrels (left) and $r-\phi$ view of the barrel showing the 12 wedges with the 5 layers.

2.4.4 Central Outer Tracker

The Central Outer Tracker (COT) [45] is a cylindrical open-cell drift chamber spanning from 44 to 132cm in radii, and 310cm long. It operates inside a 1.4 Tesla solenoidal magnetic field and is designed to find charged tracks in the region $|\eta| \leq 1.0$. The hit position resolution is approximately 140μm and the momentum resolution $\sigma(p_T) = 0.0015\ (\mathrm{GeV}/c)^{-1}$. The COT is segmented into 8 super-layers alternating stereo and axial, with a stereo angle of $\pm 2°$. Each super-layer contains 12 sense wires alternated with 13 potential wires which provide the field shaping within the cell yielding a total

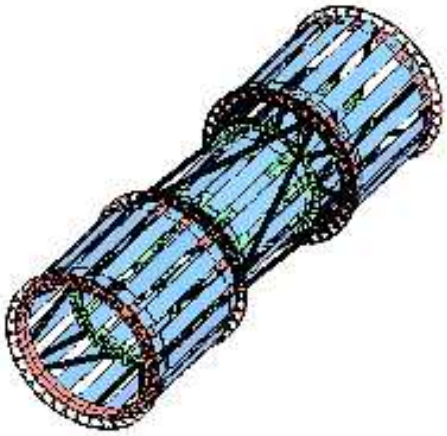

Figure 2.7: 3D veiw of the ISL spaceframe.

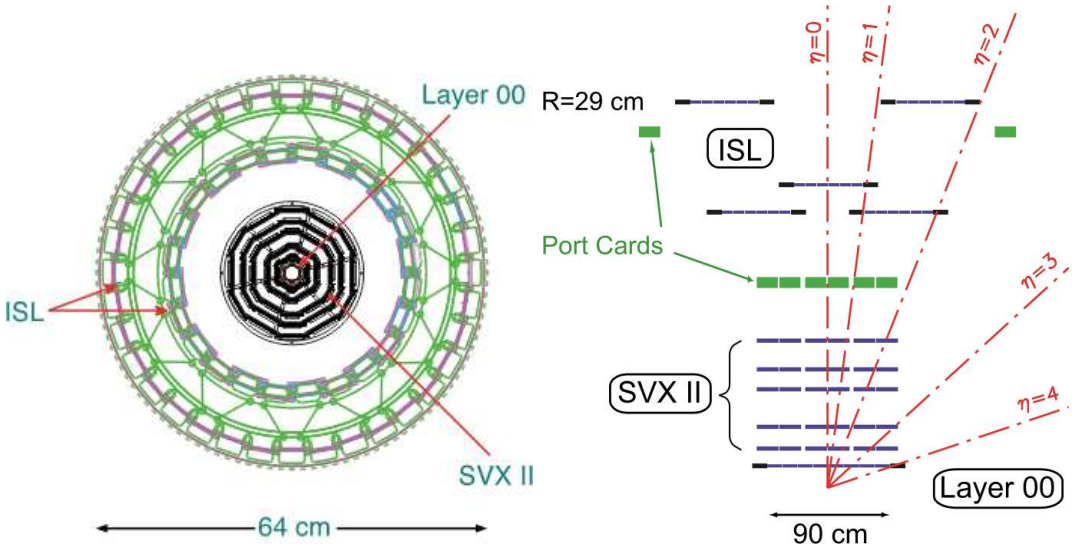

Figure 2.8: $r-\phi$ veiw (left) and $r-z$ view (right) of the silicon detectors.

of 96 measurement layers. For the entire cell chamber, there are 30,240 sense wires and 32,760 potential wires. Operating with an Argon-Ethane (50:50) gas mixture the maximum drift time is approximately 180 ns. The cells ate tilted at 35° to account for the Lorentz angle such that the drift direction is azimuthal. Tracks originating from the interaction point which have $|\eta| < 1$ pass through all 8 superlayers of the COT. Tracks which have $|\eta| < 1.3$ pass through 4 or more superlayers. Table 2.3 shows a mechanical summary of the COT. Figure 2.9 shows cell layout for super-layer 2 (SL2). Figure 2.10 shows the east endplate slots sense and field planes.

Parameter	
Gas (Argon:Ethane)	(50:50)
Number of Layers	96
Number of Super-layers	8
Stereo Angle (degree)	+2, 0, −2, 0, +2, 0, −2, 0
Cells/Layers	168, 192, 240, 288, 336, 384, 432, 480
Sense Wires/Cell	12, 12, 12, 12, 12, 12, 12, 12
Radius at Center of SL (cm)	46, 58, 70, 82, 94, 106, 117, 129
Tilt Angle	35°
Material Thickness	1.6% X_0
Drift Field	1.9 kV/cm
Maximum Drift Distance	0.88 cm
Maximun Drift Time	177 ns
Number of Channels	30,240

Table 2.3: Design parameters of the Central Outer Tracker.

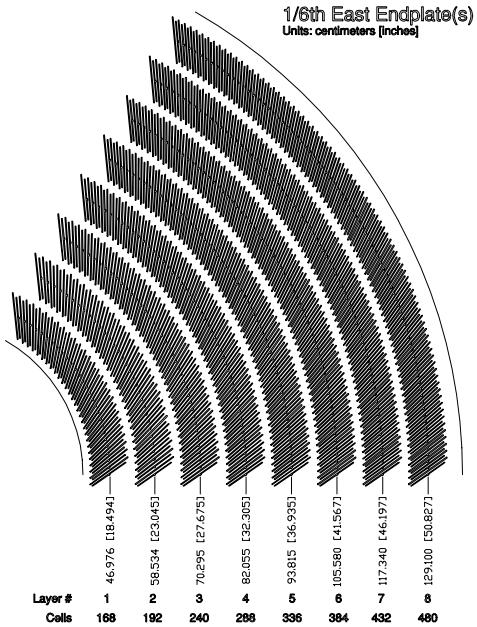

Figure 2.9: East endplate slots sense and field planes are at the clock-wise edge of each slot.

2.5 Calorimeter Systems

Segmented electromagnetic and hadron sampling calorimeters surround the tracking system and measure the energy flow of interacting particles in the $|\eta| < 3.6$. The

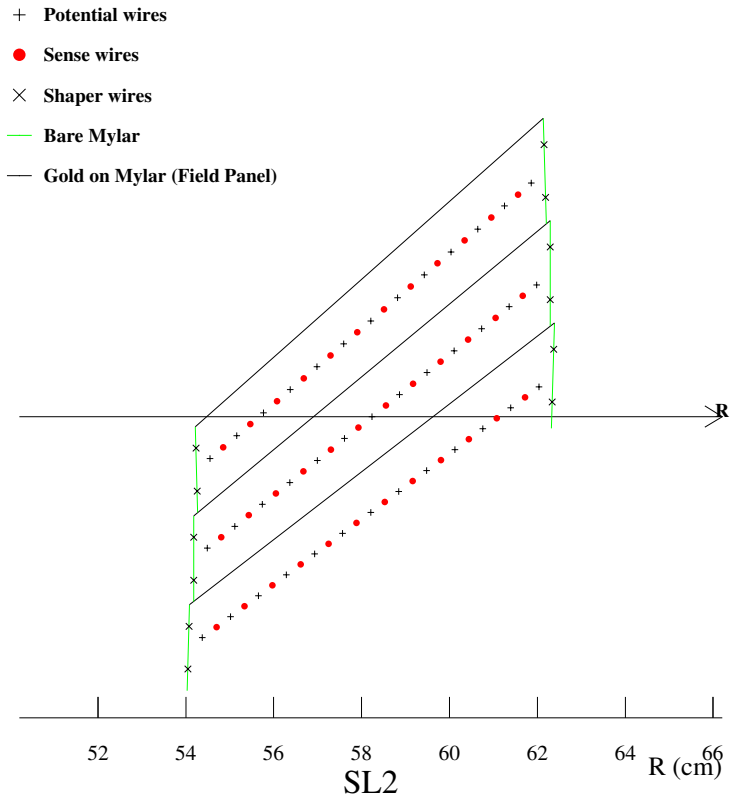

Figure 2.10: Nominal cell layout for SL2.

calorimeter systems are divided into 2 systems with respect to the pseudo-rapidity range, central and plug(forward) region. The Central Electromagnetic Calorimeter (CEM) covers the $|\eta| < 1.1$, which uses lead sheets interspersed with polystyrene scintillator as the active medium and employs phototube readout. The Central Hadronic Calorimeter (CHA) covers the $|\eta| < 0.9$, which uses steel absorber interspersed with acrylic scintillator as the active medium. The plug calorimeters, Plug Electromagnetic Calorimeter (PEM) and Plug hadron calorimeter (PHA), cover the $1.1 < |\eta| < 3.6$. They are sampling scintillator calorimeters which are read out with plastic fibers and phototubes.

2.5.1 Central Calorimeter

The Central Electromagnetic Calorimeter [46] detects electrons and photons and measures their energy. It is a lead-scintillator sampling system with tower segmentation, the each tower is 15° in $r - \phi$ plane. The CEM total thickness is 18 radiation length (32cm), to make sure that 99.7% of the electrons energy will be deposited. The CEM

energy resolution is

$$\frac{\sigma_E}{E} = \frac{13.5\%}{\sqrt{E_T}} \oplus 2\% \tag{2.4}$$

where E_T is the transverse energy in GeV, $\oplus$ symbol means that the constant term is added in quadrature to the resolution, and position resolution is typically 2mm for 50 GeV/c electrons.

The Central Electromagnetic Showermax Chamber (CES) is used to identify electrons and photons using the position measurement to match with tracks, the transverse shower profile to separate photon from π^0s, and pulse hight to help identify electromagnetic showers. The CES is located at approximately 6 radiation lengths deep at the expected shower maximum of particles in the EM calorimeter. The CES module is a multi-wire proportional chamber with 64 anode wires parallel to the beam axis.

The Central Preshower Detector (CPR) [48] is located at between the front face of the EM calorimeter and the magnet coil. The CPR can be useful in the $\pi-$photon separation and electron identification. The CPR was replaced the slow gas chamber with a faster scintillator version which has a better segmentation during RunII in 2004. The new CPR is used to improve the jet energy resolution.

The Central Hadronic Calorimeter [47] is an iron-scintillator sampling calorimeter, covering range $|\eta| < 0.9$, approximately 4.5 λ_0 interaction length, and the energy resolution is

$$\frac{\sigma_E}{E} = \frac{50.0\%}{\sqrt{E_T}} \oplus 3\%. \tag{2.5}$$

The Wall Hadronic Calorimeter (WHA) also an iron-scintillator sampling calorimeter, covering range $0.7 < |\eta| < 1.3$. The WHA is 4.5 λ_0 interaction length, and the energy resolution is

$$\frac{\sigma_E}{E} = \frac{75.0\%}{\sqrt{E_T}} \oplus 4\%. \tag{2.6}$$

2.5.2 Plug Calorimeter

The plug calorimeter covers $1.1 < |\eta| < 3.6$, corresponding to polar angles $3^\circ < \theta < 37^\circ$ as shown in Figure 2.11. Each plug wedge spans 15° in azimuth, however from $1.1 < |\eta| < 2.11$ (37° to 14°) the segmentation in ϕ is doubled, and each tower spans only 7.5°. There is an electromagnetic section (PEM) with a shower position detector (PES), followed by a hadronic section (PHA).

The PEM [49] is lead-scintillator sampling calorimeter, with unit layers composed of 4.5mm lead and 4mm scintillator. There are 23 layers in depth for a total thickness of about 21 X_0 radiation length at normal incidence. The PEM has an energy resolution is

$$\frac{\sigma_E}{E} = \frac{16\%}{\sqrt{E_T}} \oplus 1\%. \tag{2.7}$$

The PHA is an iron-scintillator sampling calorimeter, approximately 7 λ_0 in depth, and has an energy resolution of

$$\frac{\sigma_E}{E} = \frac{80\%}{\sqrt{E_T}} \oplus 5\%. \tag{2.8}$$

The PEM shower maximum detector is located about 6 λ_0 deep within the PEM, and is constructed of two layers of scintillating strips. The strips are 5mm wide, and roughly square in cross section. Position resolution of the PES is about 1mm. The summaries of design parameters for the calorimeter are shown in Table 2.4.

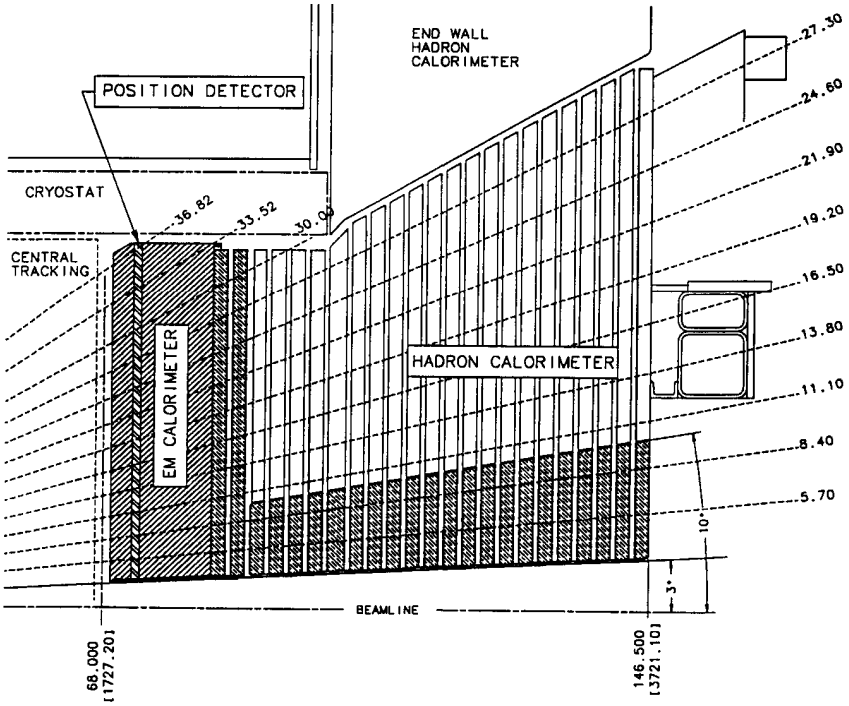

Figure 2.11: Cross section of the plug calorimeter (PEM and PHA).

2.6 Muon Detectors

Muons penetrate the tracking systems and the calorimeters leaving very little energy. The reason is muons produce much less bremsstrahlung than electrons and therefore do not produce electromagnetic showers, due to their larger mass. The CDF muon systems [38] use this property by placing detectors behind enough material. Muons deposit minimum ionizing energy in the calorimeters matched with a track in the

Calorimeter	Coverage	Energy Resolution (%)	Thickness	Absorber
CEM	$\|\eta\| < 1.1$	$13.5/\sqrt{E_T} \oplus 2$	18 X_0	3.18 mm lead
PEM	$1.1 < \|\eta\| < 3.6$	$16.0/\sqrt{E_T} \oplus 1$	21 X_0	4.5 mm lead
CHA	$\|\eta\| < 0.9$	$50.0/\sqrt{E_T} \oplus 3$	4.5 λ	2.5 cm iron
WHA	$0.7 < \|\eta\| < 1.3$	$75.0/\sqrt{E_T} \oplus 4$	4.5 λ	5.0 cm iron
PHA	$1.3 < \|\eta\| < 3.6$	$80.0/\sqrt{E_T} \oplus 5$	7.0 λ	5.08 cm iron

Table 2.4: Design parameters of the calorimeter.

COT. The momentum of these muons is measured by their bend in the solenoidal field using the COT. The central muon system is capable of detecting with transverse momentum $p_T \geq 1.4$ GeV, through their interaction with the gas and subsequent drift on the produced electrons toward the anode wires. The muon detectors consist of four separate subsystems: the central muon chambers (CMU), the central upgrade (CMP), the central muon extension (CMX), and the barrel muon detector (BMU). Table 2.5 shows design parameters of the muon detector. Figure 2.12 shows the effective muon detector coverage in $\eta - \phi$ plane.

The CMU detector locates directly outside of the central hadron calorimeter, 35 m from the interaction point, and covers the region of $|\eta| \leq 0.6$. It is divided into 24 east and 24 west 15° wedges. Each wedge contains three muon chambers and each muon chamber consists of four layers of four rectangular drift cells staggered in order to eliminate hit position ambiguities. A stainless steel sense wire a diameter of 50μm is located in the center of each cell. A muon object is created by forming a "stub" from hits in the muon chambers matching it to an extrapolated COT tracks.

The CMP consists of a second set of muon chambers behind additional 60cm of steel in the region $55° \leq \phi \leq 90°$. The chambers are fixed length in z and form box around the central detector. The pseudorapidity coverage thus varies with azimuth as shown in Figure 2.12.

The central extension consist of conical section of drift tubes (CMX) in polar angle from 42° to 55° ($0.6 \leq |\eta| \leq 1.0$). The top two wedges (Wedge 5 and 6) of the west CMX is called the "Keystone". There are no top 2 wedge on the east CMX due to cryogenic utilities servicing the solenoid. The bottom 6 wedges (Wedge 15-20) are called "Miniskirt". The design parameters of the muon detector are shown in Table 2.5.

2.7 Luminosity Monitor

The beam luminosity has been measured using the process of inelastic $p\bar{p}$ scattering. The cross section is $\sigma_{\rm in} \sim 60$ mb. The rate of inelastic $p\bar{p}$ interaction is given by

$$\mu f_{\rm BC} = \sigma_{\rm in} L \tag{2.9}$$

Muon detector	CMU	CMP	CMX
Coverage	$\|\eta\| < 0.6$	$\|\eta\| < 0.6$	$0.6 < \|\eta\| < 1.0$
Drift tube length [cm]	226	640	180
Max drift time [μs]	0.8	1.4	1.4
Total drift tubes	2304	1076	2208
Pion interation length (λ)	5.5	7.8	6.2
Minimum detectable muon p_T (GeV/c)	1.4	2.2	1.4

Table 2.5: Design parameters of the moun detector.

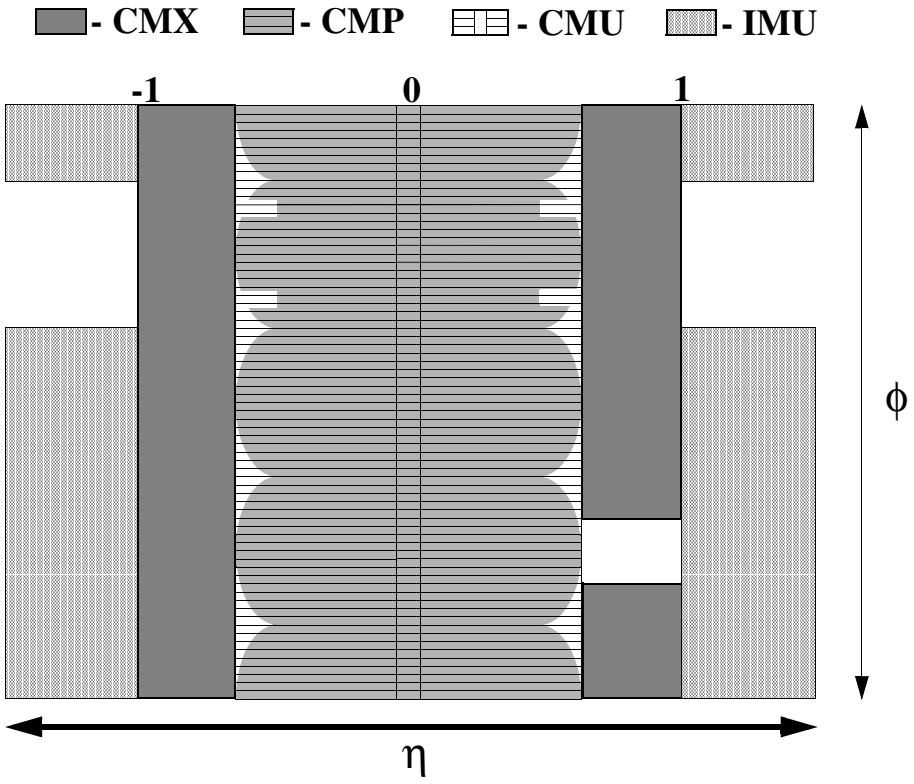

Figure 2.12: Muon detector coverage in $\eta - \phi$ plane.

where L is the instantaneous luminosity, $f_{\rm BC}$ is the rate of bunch crossing in the Tevatron and μ is the average number of $p\bar{p}$ interaction per bunch crossing. In CDF Run II, Cherenkov luminosity counters (CLC) [50, 51] is used to measure the luminosity by counting number of $p\bar{p}$ interaction μ accurately.

The detector consists of two modules which are located in the "3 degree holes" inside the end-plug calorimeter in the forward and backward region and which cover $3.7 < |\eta| < 4.7$ range. Each CLC detector module consists of 48 thin, long, conical,

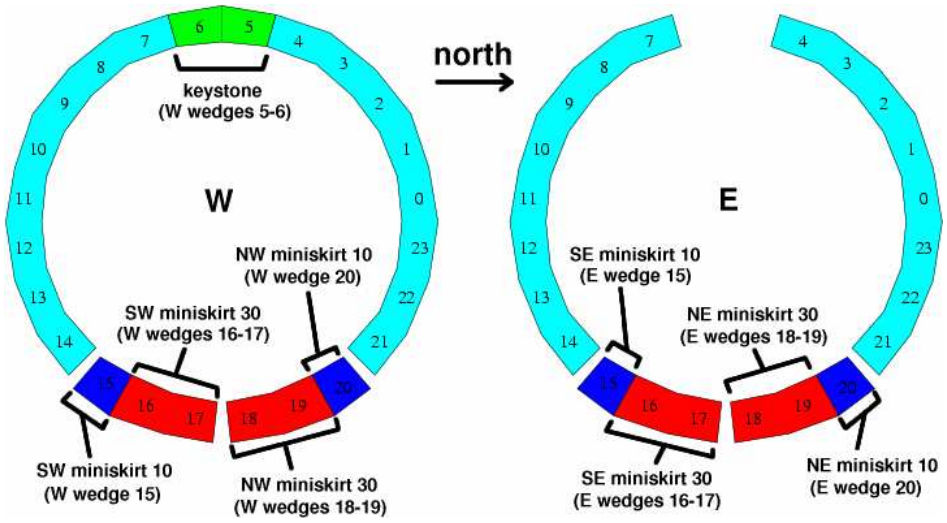

Figure 2.13: CMX detector in $r - \phi$ plane.

gas-filled Cherenkov counters. The counters arranged around the beam pipe in three concentric layers, with 16 counters each, and pointing to the center of the interaction region. They are built with reflective aluminized mylar sheets of 0.1mm thick and have a conical shape. The cones in two outer layers are about 180cm long and the inner layer counters have the length of 110cm. The Cherenkov light is detected with fast, 2.5cm diameter, photomultiplier tubes. The tubes have a concave-convex, 1mm thick, quartz window for efficient collection of the ultra-violet part of Cherenkov spectra and operate at a gain of 2×10^5. The counters are mounted inside a thin pressure vessel made of aluminum and filled with isobutane. The systematic uncertainty of the luminosity measurement is dominantly coming from the uncertainty of the inelastic $p\bar{p}$ cross section ($\sim 3\%$), the CLC acceptance ($\sim 2\%$), and the non-lineality of the CLC acceptance due to CLC occupancy saturates as growing luminosity due to the finite number of counters ($< 2\%$).

2.8 Trigger Systems

The trigger plays an important role on hadron collider experiment because the collision rate is much higher than the rate as which data can be stored on tape. The crossing rate of the Tevatron under 36 on 36 bunch operation is 7.6MHz, corresponding to 396 ns collision separation. The role of the trigger is to effectively extract the most interesting physics events from the large number of minimum bias events. For Run II, CDF employs a three-level trigger system to selectively capture interesting events. The levels are denoted simply as "L1", "L2" and "L3", with each subsequent level making more complicated decisions and requiring successively longer processing times. Figure 2.14 shows schematic of the CDF trigger system.

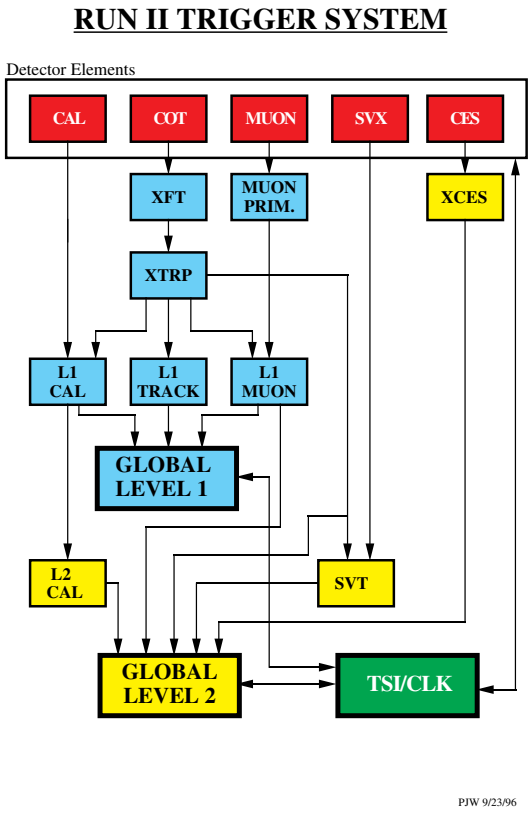

Figure 2.14: Book diagram of the trigger pass for Level 1 and Level 2.

2.8.1 Level-1

The first level of trigger selection Level-1 (L1) uses custom designed hardware to find physics objects based on a subset of the detector information and then makes a decision based on simple counting of these objects. The input to the L1 hardware comes from the calorimeters, tracking chambers and muon detectors. The decision to retain an event for further processing is based on the number and energies of the electron, jet and muon candidates as well as the missing energy in the event, or on the kinematic properties of few of these objects. The L1 hardware consists of three parallel synchronous processing streams which feed inputs of the single Global Level-1 decision unit. One stream finds calorimeter objects, another finds muons and the third finds tracks in the central region. The L1 trigger can be formed using these streams singularly as well as AND or OR combinations of them. All elements of the L1 trigger are synchronized to the same 132ns clock, with a decision made every 132ns by Global L1. In the period of the data taking considered in this analysis the accelerator was the two intermediate clock cycles automatically rejected. The maximum L1 accept rate is 20kHz, while the typical one is 12kHz.

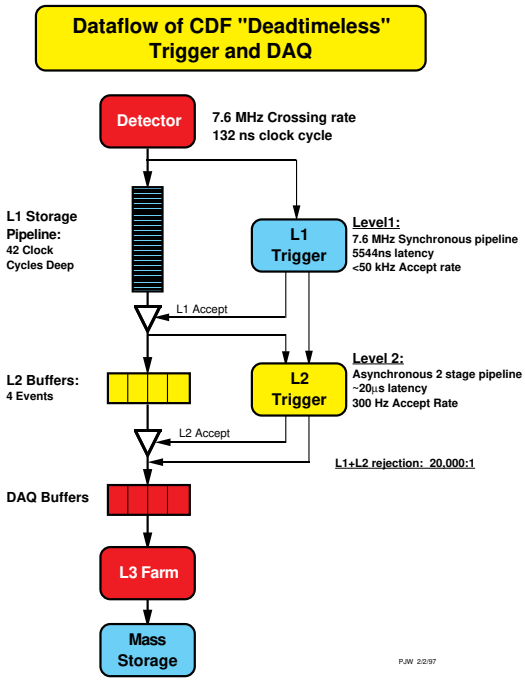

Figure 2.15: Schamatic diagram of the trigger and DAQ.

2.8.2 Level-2

Events accepted by L1 are processed by the second level of trigger Level-2 (L2), which is composed of several asynchronous subsystems. These provide input data to programmable L2 processors on the Global L2 crate, which determine if any of the L2 trigger are satisfied. Processing for L2 trigger decision starts after the event written into one of the four L2 buffers by a L1 accept. When L2 is analyzing the event in one of the buffers, that buffer cannot be used additional L1 accept. If all the four are full, the deadtime of the data acquisition is increased. It follows that the time required for a L2 decision needs to be less than about 80% of the average time between L1 accepts in order to keep the deadtime as low as possible. For this purpose L2 has been pipelined into two stages each taking approximately 10μs, which is sufficient to keep the deadtime at a minimum, even if L1 had an accept-rate of 50kHz. The L2 buffers perform a limited event reconstruction using essentially all the information used in L1, but with higher precision. In addition, at L2, data from the central shower-max detector and the SVX are available, which improve respectively the identification of electrons and photons and the reconstruction of the secondary vertices. Furthermore, a jet reconstruction algorithm is provided by the L2 cluster finder. After all of the data are stored in the processors, the event is examined to check if the criteria of any of the L2 triggers have been satisfied. This operation can be performed while the new events are being loaded into memory, thus not affecting the dead time. The typical L2 accept rate, as of this writing, is between 100 and 300Hz, depending on the initial luminosity.

2.8.3 Level-3

The Level-3 (L3) trigger subsystem is composed of two main components, the Event Builder (EVB) and the Level-3 Farm. Level-1 and Level-2 systems need to make their decisions at very high rate which makes it impossible to fully reconstruct each event. While Level-1 and Level-2 algorithms use small predefined pieces of event data to make their decision, the event pieces are stored in the buffers of the 140 Front End crates which constitute the EVB. After a L2 decision is made, the Event Builder assembles all event fragments from the Front End crates into one data block.

The 16 subfarms which compose the L3 Farm receive event fragments from the EVB and build complete events into the appropriate data structure for analysis. Since it takes about one second for one computer unit to make a trigger decision on one event, it takes a large farm of 250 Dual Pentiun Linux personal 5computers (called "processors") to ensure the required input rate. Each subfarm contains between 14 and 18 processor nodes and one "converter" node, which acts as "farm input" distributing the data flow coming from the EVB.

The events are then passed to a trigger algorithm (a different one for each processor) that categorizes the event and makes the decision as to whether or not to permanently store it. The selected event are passed to the Data Logger subsystem. During the building processing, the event integrity is checked. The L3 algorithms take advantage of the full detector information and improved resolution unavailable to lower trigger levels. This includes full three-dimensional track reconstruction and tight matching of tracks to calorimeter and muon-system information. Results from the lower level are used or drive the algorithms, which are based on the off-line analysis packages. This is a modular and separated filter modules for specific triggers. L3 accept events with a rate of approximately 75Hz.

Chapter 3

Dataset and Event Selection

Physics objective in this thesis is to search for the neutral higgs boson associated W boson using high-p_T like-sign dilepton events (ee, $e\mu$, and $\mu\mu$), such event occurs in the following process,

$$qq' \to W^{\pm} h \to W^{\pm} W^{*+} W^{*-} \to \ell^{\pm}\ell^{\pm} + X. \tag{3.1}$$

The desirable events are collected by using trigger systems as described in previous chapter and series of lepton selection criteria in efficiently.

First, the trigger system collects the events roughly, however removes the undesirable events, i.e. background events, for example the event coming from inelastic $p\bar{p}$ collisions.

In second step, the event collected by trigger system are imposed the series of lepton selection criteria to reject the backgrounds as possible. The selection criteria are constructed by taken the lepton properties and the detector response for the leptons into account.

3.1 Dataset and Triggers

To collect the events efficiently, the data collected by inclusive high-p_T lepton (electron and muon) trigger is used.

The inclusive high-p_T electron trigger requires at least a electron satisfied the series of electron selection and some large E_T requirement. Some concretely speaking, the trigger selects the events have a object which deposit its some large energy to electromagnetic calorimeter ($E_T > 18$ GeV) and the energy deposition ratio (HAD/EM) is less than 0.124 and the lateral shower profile ($L_{\rm shr}$), and the position matching on z direction between CES and extrapolated track ($\Delta z_{\rm CES} < 8$cm). The criteria is applied to events in step by step, i.e. Level 1, Level 2, and Level 3, to reduce the data taking rate due to the capability limit for the trigger system. The trigger path are named `ELECTRON_CENTRAL_18_v`$*$, the asterisk symbol means the version number because of the trigger criteria are changed in run by run due to the performance and condition of CDF detector and Tevatron accelerator.

The inclusive high-p_T muon trigger requires at least a muon satisfied the series of muon selection and some large p_T requirement. The muon trigger are mainly categorized into CMUP moun trigger and CMX muon trigger, CMUP muon means a track object points to both CMU and CMP detector, while CMX muon points to CMX detector. The CMUP muon trigger is named `MUON_CMUP18_*`, which requires CMUP muon with XFT track $p_T > 18$ GeV/c and the position matching in x direction between the position on muon detectors, both CMU and CMP, and track. And the CMX muon trigger (named `MUON_CMX18_*`) requires CMX muon with $p_T > 18$ GeV/c and the position matching same as CMUP muon trigger however CMX detector.

The collected data are achieved during from 4th Feb. in 2002 to 16th Apr. in 2008 corresponding to an integrated luminosity 2.7 fb^{-1} data after run filtering for good detector condition and desirable, so-called "good run filtering". In CDF Run-II, the data is categorized to some dataset with respect to data taking span, ex. `0d`, or Period 0, to calibrate the data take into account the varying taking data condition due to long range operation. The categorized dataset and the run range are shown in Table 3.1 in detail, also shows used trigger paths in each dataset in Table 3.2 and the main features of the triggers in Tables 3.3, 3.4, and 3.5.

Dataset	Period	Run range	Data taking time
`0d`	0	138425 – 186598	04/Feb/02 – 22/Aug/04
`0h`	1	190697 – 195408	07/Dec/04 – 18/Mar/05
	2	195409 – 198379	19/Mar/05 – 20/May/05
	3	198380 – 201349	21/May/05 – 19/Jul/05
	4	201350 – 203799	20/Jul/05 – 04/Sep/05
`0i`	5	203819 – 206989	05/Sep/05 – 09/Nov/05
	6	206990 – 210011	10/Nov/05 – 14/Jan/06
	7	210012 – 212133	14/Jan/06 – 22/Feb/06
	8	217990 – 222426	09/Jun/06 – 01/Sep/06
	9	222529 – 228596	01/Sep/06 – 22/Nov/06
`0j`	10	228664 – 233111	24/Nov/06 – 31/Jan/07
	11	233133 – 237795	31/Jan/07 – 30/Mar/07
	12	237845 – 241664	01/Apr/07 – 13/May/07
	13	241665 – 246231	13/May/07 – 04/Aug/07
`0k`	14	252836 – 254683	28/Oct/07 – 03/Dec/07
	15	254800 – 256824	05/Dec/07 – 27/Jan/08
	16	256840 – 258787	27/Jan/08 – 27/Feb/08
	17	258880 – 261005	28/Feb/08 – 16/Apr/08

Table 3.1: List of the datasets.

	0d	0h				0i					0j				0k			
Period =	0	1	2	3	4	5	6	7	8	9	10	11	12	13	14	15	16	17
ELECTRON_CENTRAL_18_v*	○	○	○	○	○	○	○	○	○	○	○	○	○	○	○	○	○	○
		The total number of good runs																
		1499				2128					4578				4577			
MUON_CMUP18_v*	○	○ (1121)	○	○							○ (4406)	○	○	○	○ (4577)	○	○	○
MUON_CMUP18_L2_PT15_v*				○ (378)	○	○	○	○ (2128)	○	○	○ (1502)	○						
MUON_CMUP18_L2_LOOSE_LUMI_260_v*											○ (34)	○						
MUON_CMUP18_L2_LOOSE_LUMI_240_v*												○ (839)	○					
MUON_CMUP18_L2_LOOSE_DPS_v*												○	○ (2203)	○	○ (4577)	○	○	○
MUON_CMUP18_L2_PS10_L3TAG_v*														○ (294)				
MUON_CMX18_v*	○	○ (1121)	○	○													○ (2466)	○
MUON_CMX18_L2_PT15_v*				○ (378)	○	○	○	○ (1653)	○	○								
MUON_CMX18_L2_PT15_LUMI_200_v*										○ (249)								
MUON_CMX18_L2_LOOSE_LUMI_200_v*										○ (226)	○ (2375)	○	○					
MUON_CMX18_L2_LOOSE_DPS_v*												○	○ (2203)	○	○ (4577)	○	○	○
MUON_CMX18_LUMI_250_v*										○ (226)	○ (2375)	○	○					
MUON_CMX18_DPS_v*												○	○ (2203)	○	○ (2111)	○	○	
MUON_CMX18_L2_PS100_L3TAG_v*														○ (294)				
MUON_CMX18_L2_PS10_v*														○ (294)	○ (1930)	○		
MUON_CMX18_L2_PS100_v*																	○ (2466)	○

Table 3.2: Datasets and selected triggers. The total number of runs containing correponding muon triggers are indicated.

ELECTRON_CENTRAL_18_v*	L1_CEM8_PT8 · Tower $E_T > 8$ GeV · HAD/EM < 0.125 · XFT $p_T > 8.34$ GeV/c	L2_AUTO_L1_CEM8_PT8 · Auto accept. L2_CEM16_PT8 · Cluster $E_T > 16$ GeV · HAD/EM < 0.125 · XFT $p_T > 8$ GeV/c Added during the 0j. · $\lvert\eta\rvert < 1.317$ L2_CEM18_PT8 · Cluster $E_T > 18$ GeV	L3_ELECTRON_CENTRAL_18 · $E_T > 18$ GeV · HAD/EM < 0.125 · $p_T > 9$ GeV/c Added during the 0d. · $L_{\rm shr} < 0.4$ · $\lvert\Delta z_{\rm CES}\rvert < 8$ cm

Table 3.3: Main features of the ELECTRON_CENTRAL_18_v* triggers.

3.2 Event Selection

As described before, the desirable events are high-p_T LS dilepton events to search for the higgs boson. CDF-II has well-defined algorithm to identify electrons or muons by using track reconstruction, energy clustering, and other particle proper reaction to

MUON_CMUP18_v*	L1_CMUP6_PT4 · CMU $p_T > 6$ GeV/c · CMP $p_T > 3$ GeV/c → CMP stub (0d) · XFT $p_T > 4$ GeV/c → 4.09 GeV/c (0d)	L2_AUTO_L1_CMUP6_PT4 · Auto accept. L2_TRK8_L1_CMUP6_PT4 (0d) · XFT $p_T > 8.34$ GeV/c L2_CMUP6_PT8 (0d) L2_CMUP6_PT15_3D (0j) · XFT $p_T > 14.77$ GeV/c · Stereo XFT = 1 L2_CMUP6_PT15_3DMATCH (0k) · Stereo XFT = 3	L3_MUON_CMUP_18 · $\lvert d_x \rvert_{\mathrm{U}} < 10$ cm · $\lvert d_x \rvert_{\mathrm{P}} < 10$ cm → 20 cm (0d) · $p_T > 18$ GeV/c
MUON_CMUP18_L2_PT15_v*	L1_CMUP6_PT4	L2_CMUP6_PT15 · XFT $p_T > 14.77$ GeV/c	L3_MUON_CMUP_18
MUON_CMUP18_L2_LOOSE_LUMI_260_v*	L1_CMUP6_PT4	L2_CMUP6_PT15_LUMI_260 · XFT $p_T > 14.77$ GeV/c · $\mathcal{L} < 260 \times 10^{30}$ cm^{-2}s^{-1}	L3_MUON_CMUP_18
MUON_CMUP18_L2_LOOSE_LUMI_240_v*	L1_CMUP6_PT4	L2_CMUP6_PT15_LUMI_240 · XFT $p_T > 14.77$ GeV/c · $\mathcal{L} < 240 \times 10^{30}$ cm^{-2}s^{-1}	L3_MUON_CMUP_18
MUON_CMUP18_L2_LOOSE_DPS_v*	L1_CMUP6_PT4	L2_CMUP6_PT15_DPS · XFT $p_T > 14.77$ GeV/c · DPS 1–30	L3_MUON_CMUP_18
MUON_CMUP18_L2_PS10_L3TAG_v* (p13 only)	L1_CMUP6_PT4	L2_CMUP6_PT15_3D_ROLXFT_PS10 · XFT $p_T > 14.77$ GeV/c · Stereo XFT = 1 · PS = 10	L3_NULL

Table 3.4: Main features of the CMUP_MUON18_$*$ triggers.

detectors. The particle identifications are not used to effectively picking up desirable events, but reduce the background such as fake lepton. To further pick up the good events, there are more event selection criteria, as mentioned after sections.

3.2.1 Pre-Event Selection

The Pre-Event Selections are first used in several studies and estimations described in this thesis, for instance background estimations. One of them is used to ensure well-defined measurement of collisions with the detector. The selection requires the vertex with the highest p_T-sum of associated tracks, so-called "primary vertex", within the region in z plane, i.e. $|z_{\mathrm{pv}}| < 60$cm.

The Cosmic ray veto is also required as the Pre-Event Selection. The cosmic rays contaminate the physics event, coming from collision, by mimicking muons or electrons. While the cosmic rays are coming from outside of the detector, the muon with collisions are coming from center of detector. And the Cosmic rays cross the detector at any time with respect to the beam crossing. The cosmic ray veto is achieved to look at the direction of the trajectory and crossing timing.

3.2.2 Lepton Identification

The Electron Identification is achieved by using series of selection criteria, tracking and energy clustering, validated using test beam. Central electron (CEM), Central muon

MUON_CMX18_v*	L1_CMX6_PT8_PS1 · CMX $p_T > 6$ GeV/c · XFT $p_T > 8$ GeV/c L1_CMX6_PT8_CSX_PS1 (0d) · CMX $p_T > 6$ GeV/c · XFT $p_T > 8.34$ GeV/c · CSX muon L1_CMX6_PT8_CSX (0d)	L2_AUTO_L1_CMX6_PT8 · Auto accept. L2_AUTO_L1_CMX6_PT8_CSX L2_CMX6_PT10 (0d) · XFT $p_T > 10.1$ GeV/c L2_CMX6_PT15_3DMATCH · XFT $p_T > 14.77$ GeV/c · Stereo XFT = 3	L3_MUON_CMX18 · $\lvert d_x \rvert_{\rm X} < 10$ cm · $p_T > 18$ GeV/c
MUON_CMX18_L2_PT15_v*	L1_CMX6_PT8_CSX	L2_CMX6_PT15 · XFT $p_T > 14.77$ GeV/c	L3_MUON_CMX18
MUON_CMX18_L2_PT15_LUMI_200_v* ⇓ (0i) MUON_CMX18_L2_LOOSE_LUMI_200_v*	L1_CMX6_PT8_CSX	L2_CMX6_PT15_LUMI_200 · XFT $p_T > 14.77$ GeV/c · $\mathcal{L} < 200 \times 10^{30}$ cm^{-2}s^{-1}	L3_MUON_CMX18
MUON_CMX18_L2_LOOSE_DPS_v*	L1_CMX6_PT8_CSX	L2_CMX6_PT15_DPS · XFT $p_T > 14.77$ GeV/c · DPS 1–80	L3_MUON_CMX18
MUON_CMX18_LUMI_250_v*	L1_CMX6_PT8_CSX	L2_CMX6_PT15_3D_LUMI_250 · XFT $p_T > 14.77$ GeV/c · Stereo XFT · $\mathcal{L} < 250 \times 10^{30}$ cm^{-2}s^{-1}	L3_MUON_CMX18
MUON_CMX18_DPS_v*	L1_CMX6_PT8_CSX	L2_CMX6_PT15_3D_DPS · XFT $p_T > 14.77$ GeV/c · Stereo XFT · DPS 1–10	L3_MUON_CMX18
MUON_CMX18_L2_PS100_L3TAG_v*	L1_CMX6_PT8_CSX	L2_CMX6_PT15_3D_ROLXFT_PS100 · XFT $p_T > 14.77$ GeV/c · Stereo XFT = 1 · PS = 100	L3_MUON_CMX18
MUON_CMX18_L2_PS10_v*	L1_CMX6_PT8_CSX	L2_CMX6_PT15_3D_PS10 · XFT $p_T > 14.77$ GeV/c · Stereo XFT = 1 · PS = 10	L3_MUON_CMX18
MUON_CMX18_L2_PS100_v*	L1_CMX6_PT8_CSX	L2_CMX6_PT15_3D_PS100 · XFT $p_T > 14.77$ GeV/c · Stereo XFT = 1 · PS = 100	L3_MUON_CMX18

Table 3.5: Main features of the CMX_MUON18_* triggers.

(CMUP and CMX) are only desirable object in the thesis, i.e. $|\eta|$ <1.2. The selections are categorized into 3 parts, "geometrical and kinematics cuts", "track quality cuts", and "identification cuts (ID cuts)".

Geometrical and kinematical cuts

- Electron Fiducial:
  This variable ensures that the electron is reconstructed in a region of the detector which well instrumented. The electron position in the CEM is determined using either the value determined by the CES shower or by the extrapolated track, and it must satisfy the following requirements.
  - The electron must lie within 21cm of the tower center in the $r - \phi$ view in order for the shower to be fully contained in the active region $|z_{\rm CES}| < 21$cm.
  - The electron should not be in the regions $|z_{\rm CES}| < 9$cm, where the two halves

of the central calorimeter meet, and $|z_{\rm CES}| > 230$cm, which corresponds to outer half of the last CEM tower. This region is prone to leakage into the hadronic part of the calorimeter.

- The electron should not be in the region immediately closest to the point penetration of the cryogenic connections to the solenoidal magnet, which is uninstrumented. This corresponds to $0.77 < \eta < 1.0$, $75 < \phi < 90$ degree, and $|z_{\rm CES}| < 193$cm.

- Muon Fiducial:
  Muons are identified by matching hits in the muon chambers with a reconstructed track and energy in the calorimeter on the trajectory of the particle. The muons pass through the moun chambers, then the muon tracking is formed using the hit information and fitting algorithm (Muon (stub) reconstruction). The muon stub has at least three hits associated to it.

  - The fiducial distance of the tracks extrapolated to muon chambers in the $r-\phi$ plane and z-direction.
  - COT exit radius ρ:
    To ensure that CMX muon pass through all eight COT superlayers, CMX muons require COT exit radius ρ of the track. ρ is defined as,

$$\rho = \frac{\eta}{|\eta|} \cdot \frac{z_{\rm COT} - z_0}{\tan(\pi/2 - \theta)} \tag{3.2}$$

    where $z_{\rm COT}$ is used for the length of the COT (155cm).

- High transverse energy (E_T):
  The transverse electromagnetic energy deposited by electron is calculated as the electromagnetic cluster energy multiplied by $\sin\theta$, where θ is the polar angle provided by the best COT track pointing to the EM cluster.

- High transverse momentum (p_T):
  The transverse momentum of the COT track as measured by using the track curvature in the COT.

Track quality cuts

- COT hits requirement:
  To ensure that the track associated with the electron or muon is good quality reconstructed track, require that track has been reconstructed in the COT in 3 axial and 3 stereo superlayers with at least 7 hits in each.

- The relative position to primary vertex in z plane ($z_0 - z_{\rm pv}$):
  Separation between z coordinate of the closest approach point with respect to run average beam line (z_0) and primary vertex z position ($z_{\rm pv}$).

- Silicon hits requirement:
  The track is required hitting to some SVX layers (>3). The requirement critical plays to reject the residual photon conversion events which are considerable background in the LS dilepton events.

- Impact parameter (d_0):
  This variable is recalculated to take the x coordinate of the primary vertex. The cuts is the most powerfully for rejecting cosmic rays background.

Isolation cut

- Isolation ($\mathrm{ISO}^{\mathrm{cal}}_{0.4}$):
  The leptons are required to be isolated in terms of the calorimeter cone-isolation with cone size of $\Delta R = 0.4$ ($\Delta R = \sqrt{\Delta\eta^2 + \Delta\phi^2}$). The calorimeter isolation is defined for track objects. It is

$$\mathrm{ISO}^{\mathrm{cal}}_{0.4} = \sum_{\Delta R<0.4} E_T^{(i)} - (E_T^{(\mathrm{seed})} + E_T^{(\eta+1)} + E_T^{(\eta-1)}), \tag{3.3}$$

  where $E_T^{(i)}$ is the tower E_T summed over the electromagnetic and hadronic calorimeter, $E_T^{(\mathrm{seed})}$ is the E_T of the tower that the track is pointing, and $E_T^{(\eta\pm1)}$ is the same quantities for the towers in the same wedge but with the η index off by the 1 with respect to the seed tower.

Electron Identification cuts

- Ratio of hadronic and electromagnetic energy (HAD/EM):
  The ratio should be small, that is, energy deposition in electromagnetic calorimeter is much higher than energy deposition in hadronic calorimeter.

- EM shower shape (L_{shr}):
  The purpose of this quantity is to provide some discrimination of electrons and photons from hadronic showers faking these particles in the central electromagnetic calorimeter. This is done by comparing the observed the energy in CEM towers adjacent to the seed tower to expected electromagnetic shower taken with test beam data.

$$L_{\mathrm{shr}} = 0.14 \sum_i \frac{E_i^{(\mathrm{adj})} - E_i^{(\mathrm{exp})}}{\sqrt{(0.14\sqrt{E})^2 + (\Delta E_i^{\mathrm{exp}})^2}}, \tag{3.4}$$

  where E_i^{adj} is the measured energy in tower adjacent to the seed tower, E_i^{exp} is the expected energy in the adjacent tower from test beam data, $\Delta E_i^{\mathrm{exp}}$ is the error on the energy estimate.

- Ratio of the cluster energy to the momentum (E/p):
  If a object pointing calorimeter cluster is electron, its momentum measured by COT track matches to the energy in the calorimeter cluster, i.e. $E/p \sim 1$.

- The pulse height shape in CES ($\chi^2_{\rm strip}$):
  The pulse height shape in the CES detector in the $r-z$ view is compared to the test beam data using the χ^2 test.

- Track matching to CES cluster ($\Delta z_{\rm CES}$ and $Q \times \Delta x_{\rm CES}$):
  The extrapolated track is required to match a CES cluster in $r-\phi(x)$ and z plane. the $r-\phi$ plane requirement is asymmetry due to the trajectory of track in the detector. If the sign of charge and Δx is opposite, the track traverses a larger part of the calorimeter in adjacent towers, which results in more radiation and a less precise position.

- Conversion removal:
  A photon traveling through material converts into an electron-positron pair. However the electron is true electron, it not directly comes from hard scattering events (prompt electron). To remove the conversion electron, conversion tagging algorithm is used. The algorithm requires to opposite charge of electrons the following,
  $$|\Delta\cot\theta| < 0.04, \text{ and } |\delta_{xy}| < 0.2, \tag{3.5}$$
  $\cot\theta$ is the difference between the polar angle cotangents of the tracks. δ_{xy} is the separation between the tracks in the $r-\phi$ plane.

Muon Identification cuts

- Small calorimeter deposition (EM and HAD):
  Muons deposit small energy in the calorimeters due to minimum ionization. The energy deposition in the calorimeter increases linearity with moun momentum, and consequently the cut efficiency loss. To maintain good efficiency for high momentum muon, the cut is taken into account for the momentum dependence.

- Track-stub matching in $r-\phi$ plane ($r \times \Delta\phi$):
  The track is required to match the muon stub in $r-\phi$ plane.

3.2.3 Jet Reconstruction

Quark and gluon particles are observed as "jet" objects due to its fragmentation and radiation effects, as a results construct shower of particles. The energy of jet are calculated from the energy deposited in the calorimeter towers using a cone clustering algorithm with a fixed cone size in which the center of the jet is defined as (η^{jet}, ϕ^{jet}) and the size of the jet cone as $R = \sqrt{(\eta^{tower} - \eta^{jet})^2 + (\phi^{tower} - \phi^{jet})^2} = 0.4$. The jet clustering algorithm groups calorimeter towers with $E_{Ti} < 1$ GeV. The algorithm is

performed by first defining "Seed towers" has largest E_{Ti}. The seed tower are used to build "clusters" with size $R = 0.4$. The cluster transverse energy and its position is calculated as the follows,

$$E_T^{jet} = \sum_{i=0}^{N} E_{Ti},\ \phi^{jet} = \sum_{i=0}^{N} \frac{E_{Ti}\phi_i}{E_T^{jet}},\ \eta^{jet} = \sum_{i=0}^{N} \frac{E_{Ti}\eta_i}{E_T^{jet}} \tag{3.6}$$

where N is the number of towers inside the radius R with $E_{Ti} > 1$ GeV. This procedure is repeated until the cluster centroid is stable. Overlapping jets are merged if they overlap by more than 50%. If the overlap is smaller than 50%, each tower in the overlap region is assigned to the nearest jet. The measured jets are corrected to particle jet level or parent parton level by taking into account for the detector effects and for radiation and fragmentation effects. The collected jet transverse momentum is expressed as the follows,

$$\begin{aligned} p_T^{parton} &= (p_T^{jet} \times C_\eta - C_{\rm MI}) \times C_{\rm Abs} - C_{\rm UE} + C_{\rm OOC} \\ &= p_T^{particle} - C_{\rm UE} + C_{\rm OOC}, \end{aligned} \tag{3.7}$$

where p_T^{parton} is the transverse momentum of the parent parton, which is taken into account for all effects, p_T^{jet} is the transverse momentum measured in the calorimeter, $p_T^{particle}$ is the transverse momentum of the particle jet, which is corrected for detector effects, and

- C_η is "η-dependent" correction. The correction takes into account variations in calorimeter response and gain as a function of jet η
- $C_{\rm MI}$ is "Multiple Interaction" correction, which is the energy coming from multiple $p\bar{p}$ interaction in the same bunch crossing to subtract from the jet
- $C_{\rm Abs}$ is "Absolute correction", is the correction of the calorimeter response to the momentum of the particle jet
- $C_{\rm UE}$ is "Underlying Event correction", to remove energy coming from underlying event such as initial state radiation and beam-beam remnant
- $C_{\rm OOC}$ is "Out-of-Cone correction" is correction of parton radiation and hadronization effects due to the finite size of the jet cone algorithm

The collections are performed by using the generic jet samples and MC samples generated by several generators (Pythia and Herwig), and The systematic uncertainties coming from these collections also estimated. The systematic contribution mainly arise from the absolute jet energy collection due to difference between data and MC for calorimeter response (2%). The total systematic uncertanity is decreasing $\sim 8\%$ to $\sim 2\%$ as the jet energy increases (0 to >80 GeV) [59].

3.2.4 Missing Transverse Energy

However neutrinos cannot be detected with CDF detector, its energy will manifest as missing energy. The CDF uses "missing transverse energy ($\not\!\!E_T$)" taking into account for transverse energy imbalance because of the missing energy, the vector sum of transverse energies should be ideal null. The missing transverse energy is measured using the transverse energy imbalance,

$$\not\!\!E_T = -\sum_i E_T^{(i)}, \tag{3.8}$$

where $E_T^{(i)}$ is the transverse energy of ith calorimeter tower. It need to be corrected for the muon minimum ionization energy taking into account for muon momentum measured by tracking.

3.3 Like-Sign Dilepton Event Selection

The final desirable events in this thesis are like-sign dilepton events to search for the higgs boson. To collect the events, the series of selection as mentioned in § 3.2 are applied to the data corresponding to an integrated luminosity of 2.7 fb^{-1}. In the selection, the applied transverse energy or momentum requirement to dilepton is asymmetric. If the 1st lepton is

- electron, $E_T > 20$ GeV and $p_T > 10$ GeV/c
- muon, $p_T > 20$ GeV/c

while, if the 2nd lepton is

- electron, $E_T > 6$ GeV and $p_T > 6$ GeV/c
- muon, $p_T > 6$ GeV/c

where the 1st lepton type is required to match trigger path, that is, when the 1st lepton is electron, the trigger path should be `ELECTRON_CENTRAL_18_v*`. The event selections are listed in Table 3.6.

The selected dilepton events are applied more selection cuts to clean up the sample. The additional selections are listed in Table 3.7. The dilepton is required to be consistent with coming from the same vertex, which is an important requirement for dilepton and multi-lepton signatures. The dilepton mass cut is to reject onium events such as J/ψ or Υ. The Z removal ($81< M_{\ell\ell} <101$ GeV/c^2) introduce to reduce WZ and ZZ events which potentially can be like-sign dilepton events in the final state. The Z-leg candidates are not the lepton passing lepton selection but also other object listed in Table 3.8 to catch Z events as many as possible. Finally, of course, like-sign charge combination requires to the dilepton events.

The number of desirable LS-dilepton events passing all event selection cuts are 172 events using data with 2.7 fb^{-1}.

Event pre-selection	
$\lvert z_{\rm pv}\rvert < 60$ cm	
Cosmic-ray veto	
Electron selection	**Muon selection**
Geometrical and kinematical cuts	
CEM	CMUP or CMX
Fiducial	Fiducial (CMUP), $\rho_{\rm COT} > 140$ cm (CMX)
	Blue-beam veto, keystone veto, miniskirt veto
$E_T^{\ell_1} > 20$ GeV ($p_T > 10$ GeV/c)	$p_T^{\ell_1} > 20$ GeV/c
$E_T^{\ell_2} > 6$ GeV ($p_T > 6$ GeV/c)	$p_T^{\ell_2} > 6$ GeV/c
Track quality cuts	
Axial ≥ 3 and stereo ≥ 3 (≥ 7 hits)	
$\lvert z_0 - z_{\rm pv}\rvert < 2$ cm	
Silicon hits ≥ 3	
$\lvert d_0\rvert < 0.02$ cm	
Isolation cut	
$\mathrm{ISO}_{0.4}^{\rm cal} < 2$ GeV	
Identification cuts	
HAD/EM $< 0.055 + 0.00045 \times E$	EM $< \max(2, 2 + 0.0115 \times (p - 100))$ GeV
$L_{\rm shr} < 0.2$ ($E_T < 70$ GeV)	HAD $< \max(6, 6 + 0.0280 \times (p - 100))$ GeV
$E/p < 2$ ($E_T < 50$ GeV)	$\lvert r \times \Delta\phi\rvert < 3$, 5, 6 cm (CMU, P, X)
$\chi^2_{\rm strip} < 10$	
$\lvert \Delta z_{\rm CES}\rvert < 3$ cm	
$-3.0 < Q \times \Delta x_{\rm CES} < 1.5$ cm	
Other cuts	
Conversion removal	

Table 3.6: Event pre-selection and lepton selection cuts.

Exactly two leptons
$\lvert z_0^{\ell_1} - z_0^{\ell_2}\rvert < 2$ cm
Dilepton mass > 12 GeV/c^2
Z removal
At least one like-sign pair

Table 3.7: Dilepton selection cuts.

Track object
Opposite-sign
$p_T > 10$ GeV/c
track cone-isolation < 4 GeV/c
axial ≥ 3 and stereo ≥ 2 (≥ 5 hits)
$\lvert z_0 - z_{\rm pv}\rvert < 10$ cm
EM object
$E_T > 10$ GeV
HAD/EM < 0.12
fractional isolation $\mathrm{ISO}_{0.4}^{\rm cal}/E_T < 0.15$
Muon object
$p_T > 10$ GeV/c
EM < 5 GeV
HAD < 10 GeV
fractional isolation $\mathrm{ISO}_{0.4}^{\rm cal}/p_T < 0.15$
$\lvert z_0 - z_{\rm pv}\rvert < 10$ cm
$\lvert d_0\rvert < 0.5$ cm

Table 3.8: Physics objects used to identify and remove Z bosons.

Chapter 4

Background Estimation

Although the LS requirement is quite effective to suppress QCD and known electroweak processes, fake-lepton backgrounds including non-prompt leptons such as those from photon conversions or from heavy-flavor decays, as well as literal fake leptons, still remain at a considerable level in the events of our signature. They are estimated by using data and MC samples, and the contributions of residual photon-conversion which survived our conversion veto are separated from the rest of the fake-lepton backgrounds by knowing the conversion detection efficiency and the number of identified conversions. While other backgrounds which is containing prompt real lepton are estimated by using MC data.

4.1 Residual Photon-conversions

The residual photon-conversion events arise from an electron originating from the photon conversion with an unobserved partner track due to its low momentum. The amount and kinematical shape of the events are estimated by multiplying lepton + conversion events by residual photon-conversion rate ($R_{\rm res}$). The following sections are discussed the residual photon-conversion event estimation in detail.

4.1.1 Photon-Conversion Detection Efficiency

Once we know the detection efficiency, $\varepsilon_{\rm con}$, we can calculate a ratio of the residual conversions to the identified conversions, $R_{\rm res}$, by

$$R_{\rm res} = \frac{1-\varepsilon_{\rm con}}{\varepsilon_{\rm con}} \,. \tag{4.1}$$

The amount of residual conversions in samples of our interest can be basically estimated by multiplying $R_{\rm res}$ to the number of identified conversions. The detection efficiency is defined by taking the denominator to be the conversions with one leg passing our electron selection criteria except the isolation cut and conversion veto, which we refer to as the seed electron. The reason for turning off the isolation cut is rather technical.

We use fake-event Monte Carlo (MC) samples created by generating single γ or π^0 to compare conversions with those in the real data, and the isolation variable in such fake-events is not usable in this respect.

The base efficiency is estimated as a function of partner-track p_T and decomposed into two factors in our analysis as

$$\varepsilon_{\rm con}(p_T) = \varepsilon_{\rm rel}(p_T) \cdot \varepsilon_{\rm pla} \ , \tag{4.2}$$

where $\varepsilon_{\rm rel}(p_T)$ is the p_T dependent efficiency covering low-p_T regions and defined relative to the efficiency on the plateau, and $\varepsilon_{\rm pla}$ is the absolute efficiency on the plateau. These efficiencies could be further broken down to the track-finding efficiency and the efficiency of the identification criteria given by

$$|\delta_{xy}| < 0.2 \text{ cm} \quad \text{and} \quad |\Delta \cot\theta| < 0.04 \ , \tag{4.3}$$

where $|\delta_{xy}|$ is the distance of the closest approach points between a pair of tracks of conversion candidates.

The inefficiency of detecting conversions is dominated by that of reconstructing low momentum partner-tracks and manifests itself in $\varepsilon_{\rm rel}(p_T)$. It is not negligible even for high E_T seed-electrons because the kinematics of conversions relatively favors asymmetric energy sharing as shown in Figure 4.1 which is a theoretical calculation of the relative probability of energy sharing as a function of fractional electron (e^-) energy [52]. Its asymmetric nature enhances the residual conversion events.

Our first goal is to measure the base efficiency, $\varepsilon_{\rm rel}(p_T)$, by comparing observed p_T spectrum of identified conversions to a perfect, or generator-level, MC spectrum. It turns out, however, that direct uses of this efficiency would not be useful in actual applications because it includes very low values at low p_T. As we can easily imagine from the form of the residual ratio, $(1-\varepsilon)/\varepsilon$, too-low efficiencies in a certain parametrization results in a significant loss of statistical power of predicting residual conversions, namely, we are forced to estimate the most needed part of residual conversions from the identified conversions with the least statistics. In order to avoid this problem, we transform the base efficiency to a function of different parameter, and we choose the parent-photon p_T for such parametrization. The base efficiency as a function of partner-track p_T is convoluted with the perfect p_T spectra of the MC for a given p_T bin of the parent photon to get $\varepsilon^{\gamma}_{\rm rel}(p_T)$. More details are explained in §4.1.4.

The next is to measure the plateau efficiency, $\varepsilon_{\rm pla}$, by using conversions in the real data identified with a method independent from our nominal identification algorithm.

Finally, the $\varepsilon^{\gamma}_{\rm con}(p_T)$ is obtained by multiplying this absolute efficiency to the relative efficiency:

$$\varepsilon^{\gamma}_{\rm con}(p_T) = \varepsilon^{\gamma}_{\rm rel}(p_T) \cdot \varepsilon_{\rm pla} \ . \tag{4.4}$$

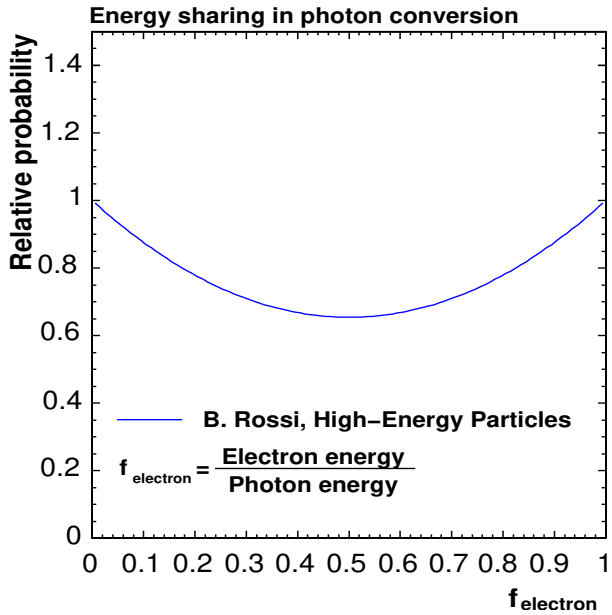

Figure 4.1: A theoretical calculation of the relative probability of energy sharing in the photon conversion as a function of fractional electron (e^-) energy [52].

4.1.2 Data samples

Real data

We use the `0d` dataset and a trigger bit selection of `ELECTRON_CENTRAL_18_v*`, called `bhel0d`. The sample corresponds to an integrated luminosity of 361.8 pb^{-1}. From this sample, we select events with at least one good electron satisfying our high-p_T electron selection ($E_T > 20$ GeV and $p_T > 10$ GeV/c) except the isolation cut and conversion veto. However, in first step, we not apply a electron selection requirement, silicon hit cut to the electron, to check its rejection performance which is usually used in LS dilpton selections, of course, finally we apply the requirement in the estimation of residual photon-conversion ratio.

Conversion Monte Carlo Samples

There are four MC-samples used in this study. The two of them are made by generating events of single π^0 using the `FAKE_EVENT` module: one with a flat p_T spectrum and the other with a certain p_T slope. The rest of the samples are made by generating single-γ events instead of π^0. The generation parameters are listed in Table 4.1. The "Good" in the table means that there is at least one high-p_T good electron in the event. Simulations of π^0 decays and succeeding conversions of γ themselves are left to the CDF detector simulation package. The simulated probability of conversion is about 18% per photon independent of its p_T.

Since p_T spectra of partner tracks are correlated with p_T of parent photons, we need to match MC slopes with those we observe in the data. In the MC tuning, we try to describe conversions found in the data with a mixture of the π^0 and γ MCs with optimized slopes. In order to improve the statistical power of the MCs in the optimization, the "flat samples" (the samples 1 and 3 in Table 4.1) are used to optimize the slopes, while the samples generated with the slopes in the table are combined appropriately, after re-weighting with the tuned slopes, to find out the optimum relative ratio γ/π^0.

Sample	Particle	min-p_T (GeV/c)	max-p_T (GeV/c)	Slope α ($p_T{}^{-\alpha}$)	max-$\|\eta\|$	Generated (events)	Good (events)
1.	π^0	3	150	0 (flat)	1.3	1520000	155651
2.	π^0	15	150	6.3	1.3	1600000	72500
3.	γ	3	150	0 (flat)	1.3	1580000	123470
4.	γ	15	150	4.8	1.3	1580000	112935

Table 4.1: Monte Carlo samples.

4.1.3 Monte Carlo tuning

Tuning the MC samples is done by using identified conversions collected with an additional requirement of partner-track $p_T > 2$ GeV/c which is expected to be high enough to avoid non-plateau region. The slope parameter α is optimized by matching the weighted p_T spectra of reconstructed photon with what is observed in the real data, where the photon p_T is formed by the scalar-p_T sum of the seed-electron track and the partner track. On the other hand, we use E/p distributions to constrain the mixture of the π^0 and γ. The actual optimization of the three parameters, two slopes for the π^0 and γ, and the relative ratio γ/π^0, is carried out by an iterative way. Namely, 1) find a relative ratio for a given set of two slopes; 2) by adding the π^0 and γ MCs with the obtained ratio, we look for the best set of two slopes that describes photon p_T of the data using the χ^2; 3) go back to the first step and iterate. The optimized parameters are

$$\alpha_{\pi^0} = 5.6 \pm 0.5\,, \qquad \alpha_\gamma = 4.9 \pm 0.5\,, \qquad \gamma/\pi^0 = 0.66 \pm 0.03\,. \tag{4.5}$$

Figure 4.2 shows the optimized E/p distribution compared to the data. The reduced χ^2 as a function of slope parameters is shown in Figure 4.3. Figure 4.4 shows a comparison of reconstructed photon-p_T spectra between the MC and the data. We also demonstrate that our MC sample simulates the conversion points reasonably well in Figure 4.5, and that the detailed p_T and E_T spectra of seed electrons are in good agreement with the data as shown in Figures 4.6 and 4.7. The jump at 50 GeV seen in Figure 4.7 is due

to the E/p cut turned off at this E_T. From these figures, we say that our MC events reproduce observed conversions well in a wide kinematical range.

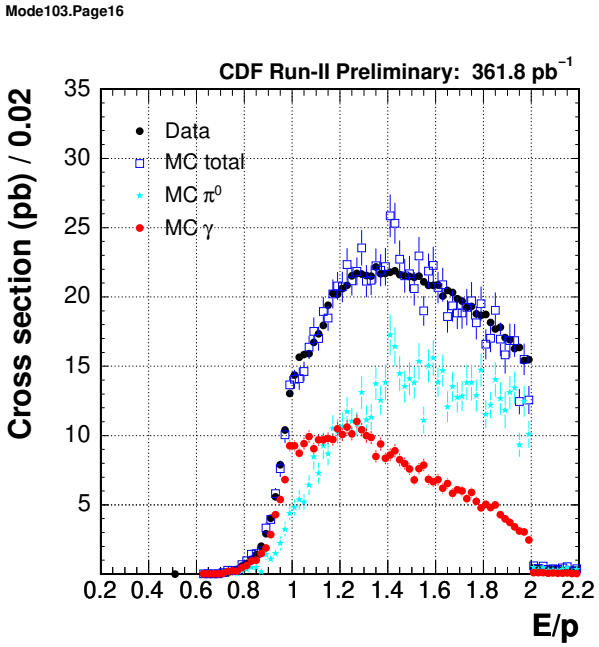

Figure 4.2: Distribution of E/p for the seed electron of conversions.

4.1.4 Relative efficiency in Low p_T Region

Figure 4.8 compares the p_T spectrum of conversion partner-tracks observed in the real data with the one obtained at the generator level of MC, where the MC spectrum is fit to the data in the region of $2 < p_T < 5$ GeV/c. We clearly see losses of tracks in very low-p_T region. The efficiency relative to the plateau, $\varepsilon_{\rm rel}(p_T)$, is obtained by dividing the observed partner-track distribution by the fitted MC distribution, and is shown in Figure 4.9, where the uncertainties in the figure are only statistical. The efficiency reaches its plateau at $p_T \simeq 1$ GeV/c. Figure 4.9 also shows the MC prediction of the efficiency. The MC performance is actually good in reproducing the p_T dependence of the conversion-detection efficiency.

We investigate systematic uncertainties of the relative efficiency coming from the MC tuning parameters. This is done by shifting the parameters by the quoted uncertainties given in (4.5), and the result is summarized in Figure 4.10 in terms of relative uncertainties. The uncertainty is dominated by MC statistics and at a level of 5%. The dependence on the MC tuning is small; only the slope dependence becomes non-negligible at very low p_T.

The relative efficiency as a function of partner-track p_T is an important and the most basic efficiency, but it is not useful in actual applications. Residual conversions

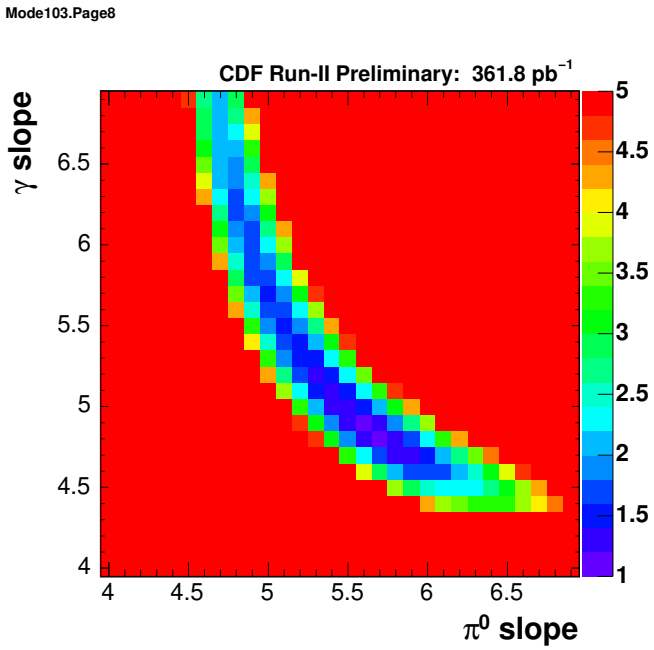

Figure 4.3: Reduced χ^2 between the data and the Monte Carlo distributions of reconstructed photon-p_T as a function of Monte Carlo slope-parameters.

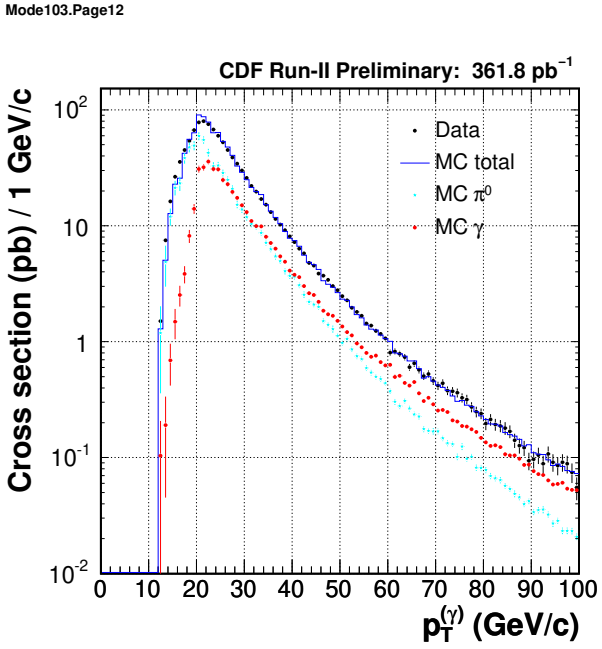

Figure 4.4: The reconstructed photon-p_T spectrum.

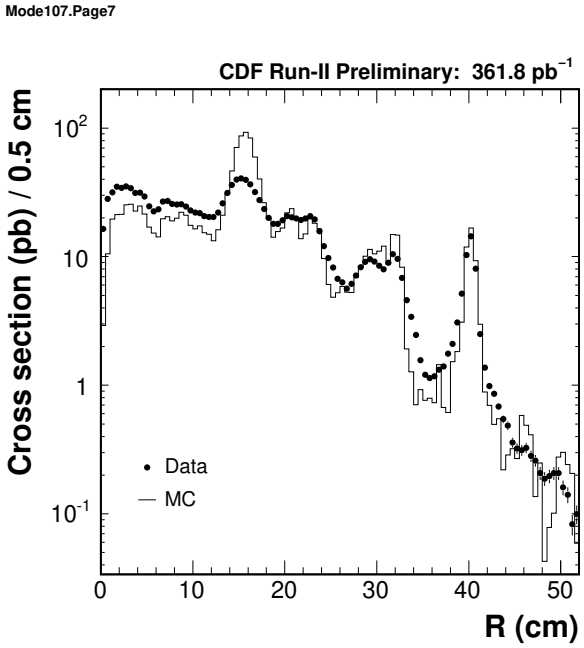

Figure 4.5: Distribution of the radius of conversion points from the beam line.

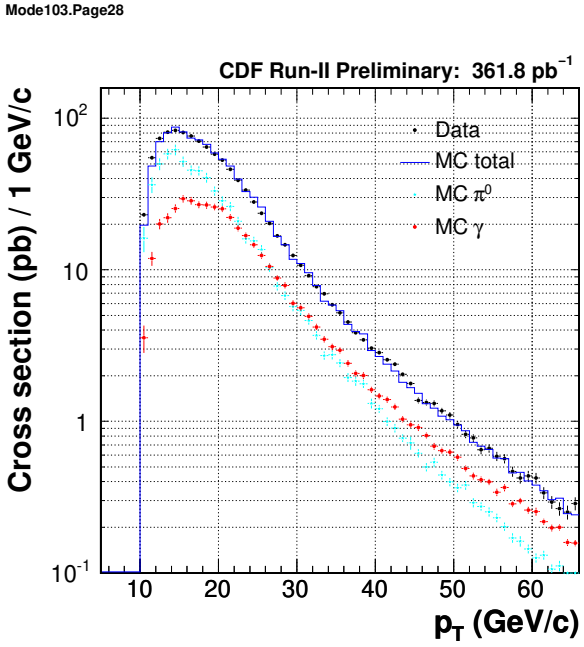

Figure 4.6: Conversion-electron p_T spectrum.

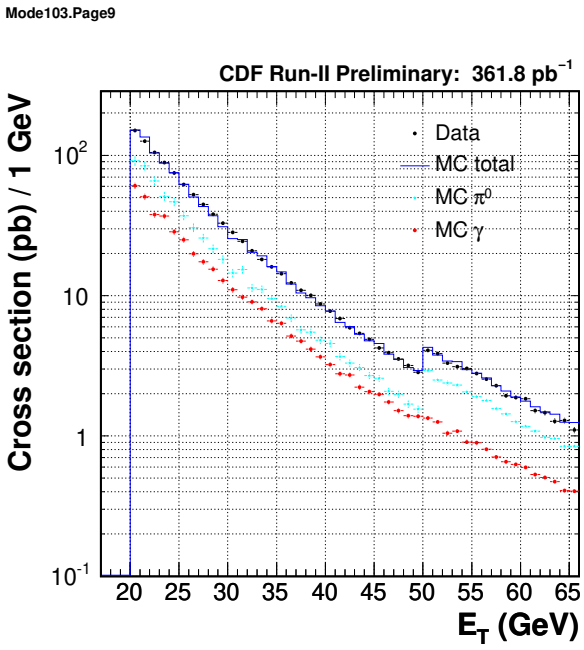

Figure 4.7: Conversion-electron E_T spectrum.

result from low efficiencies of detecting conversions, which in turn means that the statistical power of identified conversions is low as well. If we use the parametrization of the partner-track p_T, we would suffer from it to a considerable extent because there is an extremely low efficient point, and have to predict the most contributing residual conversions from the least statistics of identified conversions. A solution is to choose a different parametrization so that low and high efficiency regions are reasonably mixed and smeared out.

One might think that natural choices would be the E_T or p_T of seed electrons because the seed electron is a physics object we identify primarily in physics analyses. However, we found that such parameterizations had sample-to-sample dependences through different photon-p_T spectra. As an example, we consider the parametrization using the seed-electron E_T.

Before proceeding to an investigation of parametrization, we note that the transformation to a different parametrization is done by using only the base relative efficiency which has been just measured and the generator-level MC information regarding the partner-track p_T spectrum. The p_T cut on the seed-electron no longer has to be high in this situation because the generated MC particles cover low-p_T regions down to 3 GeV/c as given in Table 4.1. The kinematical cut in the actual LS dilepton analysis is asymmetric described as §3, where the low-p_T cut is defined to be $E_T > 6$ GeV and $p_T > 6$ GeV/c, and the primary estimation of residual conversion backgrounds in the LS dilepton analysis will be carried out for this low-p_T side of dilepton pairs. Given this, we mainly discuss the relative efficiency with different parameterizations

by imposing the low-p_T cut in what follows.

For getting the relative efficiency as a function of seed-electron E_T, we convolute the base efficiency as a function of partner-track p_T with the generator-level spectrum of partner-track p_T in a given seed-electron E_T bin. In this case, the partner-track p_T spectrum is inevitably dependent on the parent photon-p_T spectrum which has basically a sample dependence. In fact, a comparison of photon-p_T spectra between the MC that is tuned by the inclusive electron data and LS lepton + conversion events shown in Figure 4.11 demonstrates such a dependence. We see that a harder p_T spectrum is favored in the lepton + conversion events. Our analysis shows that the p_T spectrum of $\propto p_T^{-2.5}$ of the γ MC describes the observed spectrum better, which should be compared to $p_T^{-4.9}$ tuned by the inclusive electron sample. The relative efficiency as a function of electron E_T for each case is shown in Figure 4.12. There is a $\simeq 15\%$ difference at lower E_T regions, which translates to about a 40% change in terms of the residual ratio as calculated from

$$\frac{\Delta R_{\rm res}}{R_{\rm res}} = -\frac{1}{1-\varepsilon}\frac{\Delta\varepsilon}{\varepsilon}\,. \tag{4.6}$$

We could measure the slopes for samples of interest but it is not always possible due to, for example, limited statistics.

In order to obtain more stable efficiencies over different samples, we choose to use the parent-photon p_T itself to parametrize them. The convolution is expressed by

$$\varepsilon^{\gamma}_{\rm rel}(p_T) = \frac{\int f(\tilde{p}_T|p_T)\cdot\varepsilon_{\rm rel}(\tilde{p}_T)d\tilde{p}_T}{\int f(\tilde{p}_T|p_T)d\tilde{p}_T}\,, \tag{4.7}$$

where $f(\tilde{p}_T|p_T)$ represents the true (i.e. generator level) p_T spectrum of partner tracks for a given p_T of the parent photon. In actual calculation, the $\varepsilon_{\rm rel}(p_T)$ for the tracks with $p_T > 2$ GeV/c (normalization region) is set to 1. The obtained relative efficiency as a function of photon p_T is shown in Figure 4.13, where uncertainties are statistical only. The drop of the efficiency for the p_T less than 15 GeV/c is a threshold effect and it does not mean that the intrinsic efficiency is low in this p_T region. In the figure, efficiencies from γ and π^0 MCs are separately shown, and they are consistent with each other. This gives us an advantage that the application is not sensitive to the composition of γ and π^0 in samples. Related to this, we show a comparison of E/p distributions for conversions in the LS lepton+conversion events, the γ MC, and the π^0 MC in Figure 4.14, where the MC slope-parameters are tuned by the LS lepton+conversion events themselves and the MC distributions are normalized to the data. We comment that the conversions found in the LS lepton+conversion events are more likely to be originating from photons, not from π^0. In fact, if we try to fit the data with the two MC distributions, a fitter returns answers of negligible contributions from the π^0 MC. We use the efficiency obtained by using the γ MC from now on.

We mention here one complication in the calculation of statistical uncertainties included in Figure 4.13. For a given p_T bin of the parent photon, the denominator

shows a certain p_T distribution of partner tracks. This denominator is a sum of weights related to the MC slope. The numerator accepts another weight which is the relative efficiency $\varepsilon_{\rm rel}(p_T)$. The efficiency for a given p_T bin is thus symbolically written as

$$\varepsilon = \frac{\sum w_i' w_i x_i}{\sum w_i x_i}, \tag{4.8}$$

where x_i is actually 1 (event) for all i. The statistical uncertainty of ε is basically calculated by propagating the uncertainty of x_i, namely $\Delta x_i = 1$:

$$\Delta\varepsilon = \frac{\sum (w_i' w_i - \varepsilon w_i)\Delta x_i}{\sum w_i x_i} = \frac{\sum (w_i' w_i - \varepsilon w_i)}{D}, \tag{4.9}$$

where the $D = \sum w_i x_i$ is the integral of entries in the denominator. From this equation, we see that there arises a cross term proportional to $w'w^2$ when we compute $\langle(\Delta\varepsilon)^2\rangle$. We thus need to accumulate the square of weights of the form $\sqrt{w'w}$ in order to calculate the statistical uncertainty properly. As the systematic uncertainty of the relative efficiency as a function of photon p_T, we consider the input relative efficiency. Shifting them by $\pm\sigma$, we look at resulting changes of the final efficiency. A summary of the uncertainty calculations is shown in Figure 4.15, where the total uncertainty is obtained by adding all the uncertainties in quadrature.

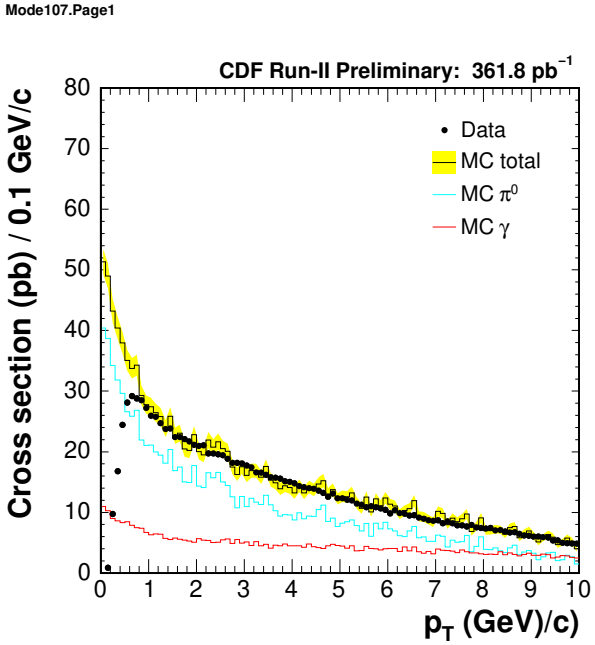

Figure 4.8: Partner-track p_T spectrum for conversions. The Monte Carlo spectrum is shown at the generator (OBSP) level and fitted to the data in the p_T region $2 < p_T < 5$ GeV/c.

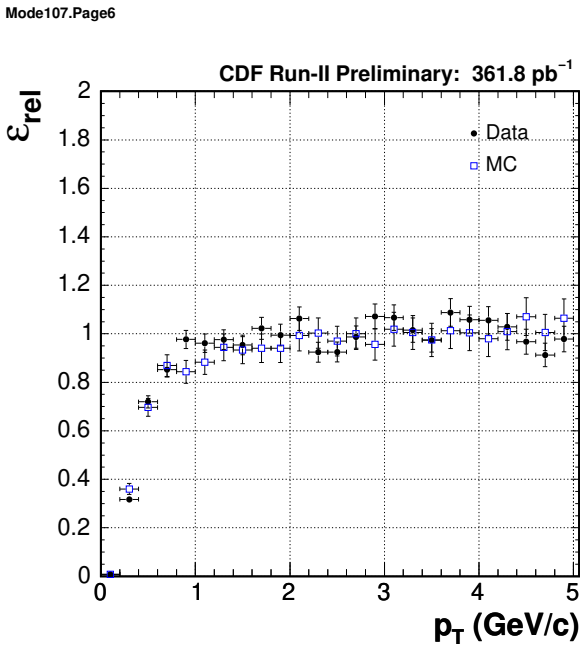

Figure 4.9: Relative conversion-detection efficiency as a function of partner-track p_T. Only statistical uncertainties are shown.

4.1.5 Absolute Efficiency on the Plateau

We need to identify conversions with a method independent from the nominal identification algorithm to measure the absolute efficiency on the plateau region. By the same way as the previous analysis, we use hit information of the CES strips for this purpose. It is based on a distinct feature of the conversion pair that the electron and the positron have approximately the same z position at any radius. When the electron and the positron separate enough so that they reach different ϕ wedges as illustrated in Figure 4.16, we can measure each z position of the electron and the positron on the CES plane, and will find that the z position difference, Δz, has a peak around zero in the "right" side (RS) wedge as expected from the charge combination. We refer to this identification of conversions as the CES method. In our analysis, we look for the highest energy CES cluster in the nearest three towers along the η direction of the wedges next to the seed electron (see Figure 4.16).

We go back to our initial electron sample (1195056 events) as described in §4.1.2 to measure the plateau efficiency. In order to make the geometrical configuration of conversions unambiguous, we here impose a set of "fiducial" cuts on the electrons, which essentially selects only the electrons located in the central region inside a tower. One requirement is that the local x coordinate of the extrapolated track at the CES plane satisfy $|x| < 15$ cm. Another cut is for the z direction to ensure that the partner track of a conversion is hitting the tower with the same η-index as the seed-electron tower.

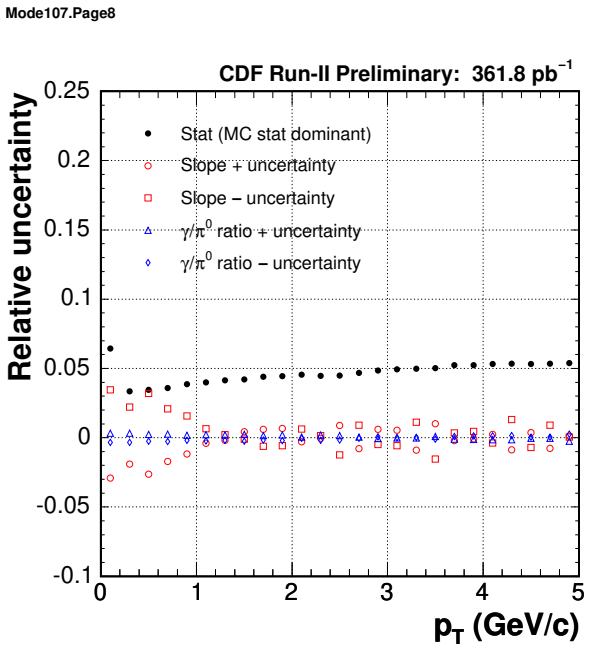

Figure 4.10: Relative uncertainty of the relative conversion-detection efficiency originating from different sources.

The appropriate definition of the z fiducial is obtained by looking again at identified conversions, but this time, only those with the η indices being different between the seed-electron tower and the tower the partner track is pointing. Figure 4.17 shows a distribution of the un-signed detector η for the seed electrons with such mismatching tower indices, where the partner-track p_T is required to be larger than 1 GeV/c, that is, in the plateau region. We avoid the η regions seen as peaks in this figure. Then, it is natural and relevant to require the CES cluster that we have found belong to the tower with the same η-index as the electron, i.e. exactly next to the electron tower and in the RS wedge. The last of our "fiducial" cuts is to require the number of tracks associated to the electron be just one in order to suppress the conversions with the partner track passing through the same tower as the seed electron, which better ensures the configuration we desire. Finally, as in the previous analysis, we demand a certain energy deposition in the RS tower to purify the sample: $E_{\rm strip}/p > 0.5$ and $E_{\rm CEM}/p > 0.7$, where the track momentum p is calculated from the assumed p_T of 2 GeV/c and the z position of the CES cluster. It is probably good to remember that the requirements introduced above are applied only to the information of the electrons and the RS tower, none is explicitly required on anything of partner tracks.

A demonstration of the Δz peaks for the RS and the wrong side (WS) wedge is given in Figure 4.18 in which we see a clear separation between what we observe in the RS and in the WS. The bremsstrahlung emitted off an electron could produce a false Δz peak in the RS tower but the probability of such cases is confirmed to be very

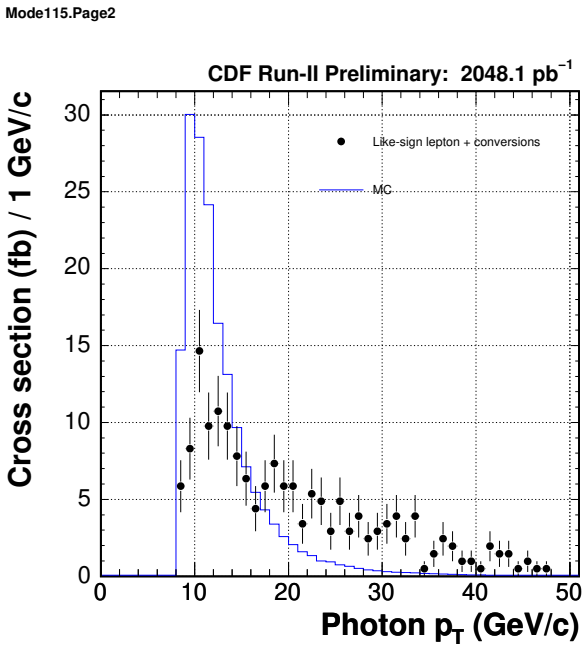

Figure 4.11: Comparison of photon-p_T spectra between like-sign lepton + conversion events and Monte Carlo tuned by conversions in inclusive electron data.

small, less than 0.1%, by using a large MC sample of single electrons.

The distribution is fit with Gaussian plus constant. The absolute efficiency is measured by looking at the reduction of the fitted Gaussian functions before and after our nominal conversion identification algorithm. The result is shown in Figure 4.19. For records, the ratio of the background to the signal (Gaussian) part is about 20% and 10% before and after conversion identification, respectively. The efficiency is obtained to be $\varepsilon_{\rm pla} = 0.935 \pm 0.006$. Instead of using the fitted Gaussian functions, we also try to count the excess events over the fitted background, which gives $\simeq 2\%$ larger counts. The efficiency in this case is, however, still stable and found to be 0.94 ± 0.01. The contamination of low-momentum partner-tracks with $p_T < 1$ GeV/c in the Δz peak is checked using the sample after the conversion tagging cut and found to be small ($< 1\%$). We do not observe any large systematics in the E_T dependence but just fluctuations due to statistics. From these, we believe that the systematic uncertainty is about 1% (absolute) at most, thus we quote

$$\varepsilon_{\rm pla} = 0.935 \pm 0.006({\rm stat}) \pm 0.010({\rm syst}) \; . \tag{4.10}$$

By performing the same analysis for the MC data, we obtain a MC prediction for the plateau efficiency which is found to be 0.966 ± 0.009.

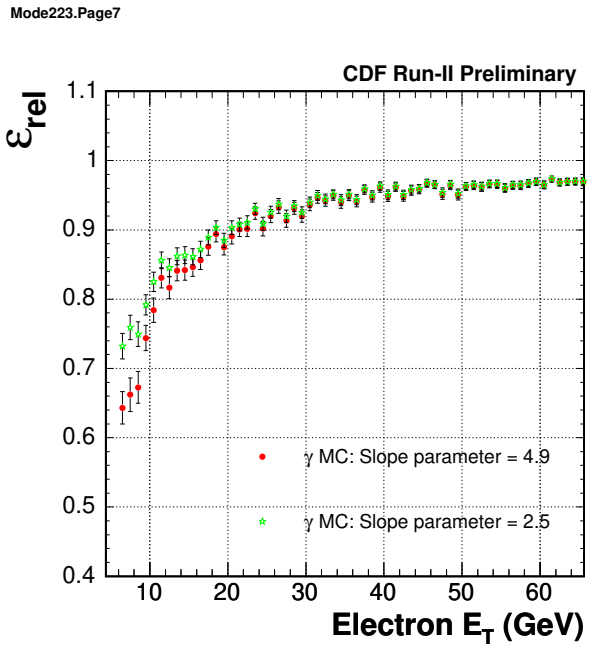

Figure 4.12: Relative conversion-detection efficiency as a function of seed-electron E_T for two cases of slope parameters in MC tuning.

4.1.6 Overall Efficiency and Residual-Conversion Ratio

We calculate the overall conversion-detection efficiency by $\varepsilon^{\gamma}_{\rm con}(p_T) = \varepsilon^{\gamma}_{\rm rel}(p_T) \cdot \varepsilon_{\rm pla}$. The result is shown in Figure 4.20. We see that the $\varepsilon^{\gamma}_{\rm con}(p_T)$ increases from 30% to 90% as the photon p_T increases. Figure 4.21 shows the $R_{\rm res}$ as a function of photon p_T.

Since the $\varepsilon^{\gamma}_{\rm con}(p_T)$ is obtained by merely rescaling $\varepsilon^{\gamma}_{\rm rel}(p_T)$, the relative uncertainty from MC statistics is the same as that of $\varepsilon^{\gamma}_{\rm rel}(p_T)$. We then propagate it according to (4.1) to the uncertainty of the $R_{\rm res}$. The other uncertainty of the $\varepsilon^{\gamma}_{\rm rel}(p_T)$ is separately propagated to the uncertainty of the $R_{\rm res}$. The systematic uncertainty originating from the plateau efficiency is obtained by a similar propagation which is straightforward. A summary of the relative uncertainties of the $R_{\rm res}$ is given in Figure 4.22. Figure 4.23 shows the result for the case of the high-p_T cut to be applied to conversions in the high-p_T side of dileptons.

4.1.7 Application of Residual-Conversion Ratio

We have obtained the primary result, the residual ratio as a function of photon p_T. In this section, we consider a couple of issues when we face in realistic applications.

For a given conversion, we reconstruct the parent-photon p_T from the seed-electron and its partner track, then obtain a residual ratio. By summing these ratios, or weights, over all the conversions found in a sample of interest, we obtain an expectation of the total number of residual conversions. However, we usually need the kinematical

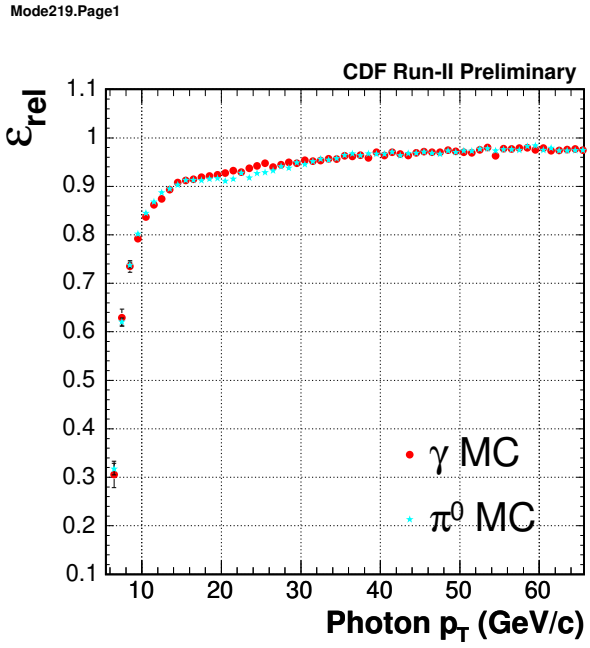

Figure 4.13: Relative conversion-detection efficiency as a function of photon p_T. The uncertainties are statistical only.

information of expected residual conversions such as p_T, while we only know the p_T of parent photons because the residual ratios is parametrized by the photon p_T. A handle of predicting kinematical information of residual conversions is the fact that they are most likely to have very low partner-track p_T, less than 1 GeV/c, as seen from the base relative efficiency shown in Figure 4.9. We, thus, approximate the partner-track p_T of residual conversions, expected from a given conversion, to be (0.5 ± 0.5) GeV/c, and re-assign the difference from the original partner-track p_T to the seed-electron p_T:

$$p_T{}^{(\mathrm{part})} \to 0.5 \text{ GeV}/c, \qquad p_T{}^{(\mathrm{seed})} \to (p_T{}^{(\mathrm{seed})} + p_T{}^{(\mathrm{part})} - 0.5) \text{ GeV}/c\,. \tag{4.11}$$

By this way, we can predict the kinematical information of residual conversions with an uncertainty of $\Delta p_T \simeq 0.5$ GeV/c. For the conversions that already have partner-track p_T less than 1 GeV/c, we do not perform this p_T re-assignment.

Yet we have a problem due to the fact that the plateau region is not fully efficient. It means that conversions with partner-track p_T of large values can still become residual conversions at small probabilities. Performing the above p_T re-assignment all the time is, thus, not really accurate, but using the original p_T is also a valid thing to do reflecting the overall inefficiency of conversion detection. Let us call residual conversions with the partner-track p_T less than 1 GeV/c "proper" and those with p_T larger than 1 GeV/c "non-proper". More precise predictions are then given by splitting residual conversions into the proper and non-proper part. The fraction of proper residual-conversions for each photon p_T bin, the "splitting" factor, can be constructed from the

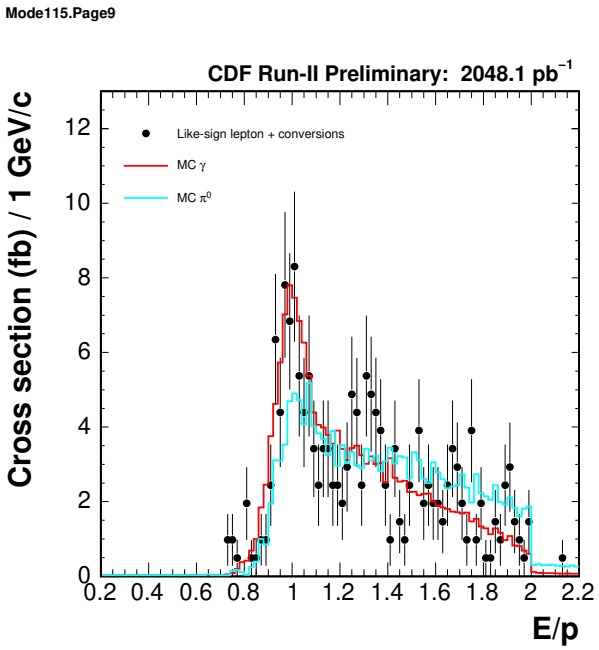

Figure 4.14: Comparison of E/p distributions for conversions in like-sign lepton+conversion events, the γ Monte Carlo, and the π^0 Monte Carlo. The p_T-slope parameters of the Monte Carlo data are tuned by the like-sign lepton+conversion events. The Monte Carlo distributions are normalized to the data. The uncertainties of the real data are statistical only.

MC by weighting the generator-level spectrum of partner-track p_T with $1 - \varepsilon_{\rm con}(p_T)$, where the $\varepsilon_{\rm con}(p_T)$ is the conversion detection efficiency as a function of parter-track p_T as given in (4.2). The result is shown in Figure 4.24. We form a function through fitting to the plot for the γ MC, which is given by

$$\min(1, f_L), \qquad f_L \equiv (2.6 \pm 0.1) \times p_T^{-(0.501 \pm 0.008)} \ , \tag{4.12}$$

where the L reminds us that the parametrization corresponds to the low-p_T cut. A similar fraction for the case of high-p_T cut is given in Figure 4.25. The parametrized function is

$$\min(1, f_H), \qquad f_H \equiv (5.0 \pm 0.1) \times p_T^{-(0.663 \pm 0.009)} \ . \tag{4.13}$$

The procedure for predicting residual conversions now includes one more step after obtaining the residual ratio w: we further get a splitting factor f using the functions above. Then the weight corresponding to the kinematics given by the p_T re-assignment is wf, while the weight $w(1-f)$ is applied when the original seed-electron p_T is used as the p_T of predicted residual conversion.

Finally, we consider another detail regarding the isolation cut. We impose a calorimeter isolation cut in the actual LS analysis. The residual conversions, therefore, must pass this cut too. But our conversion studies so far are carried out without

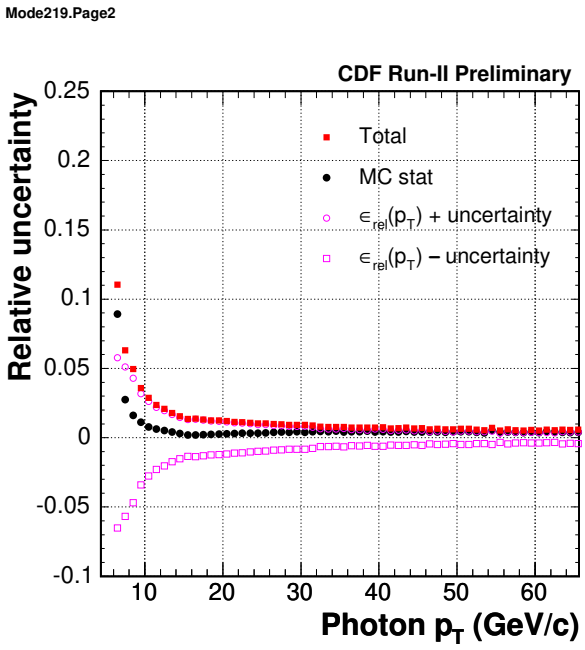

Figure 4.15: Relative uncertainty, shown for different sources, of the relative conversion-detection efficiency as a function of photon p_T.

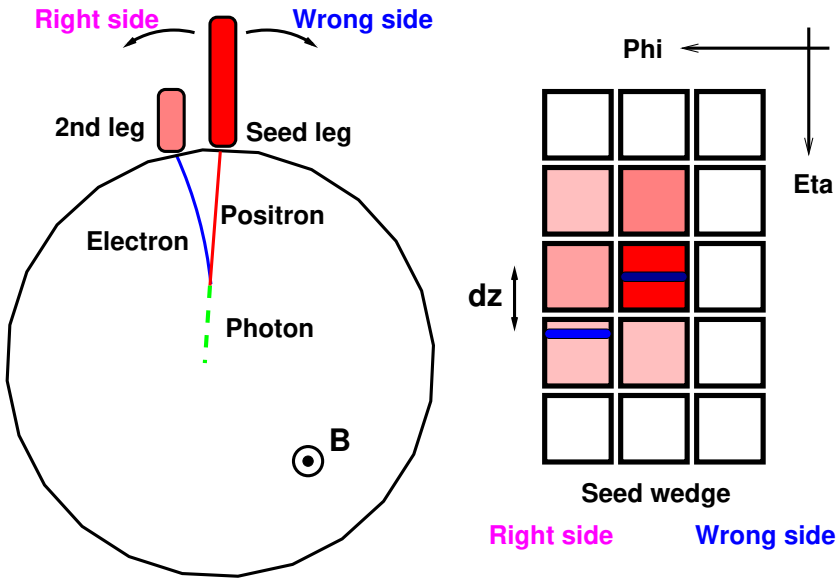

Figure 4.16: Illustration of the conversion tagging by means of CES strip information.

applying the isolation cut because the MC samples of fake-events are not sufficient to simulate such information. What we need here is to introduce effects of the isolation

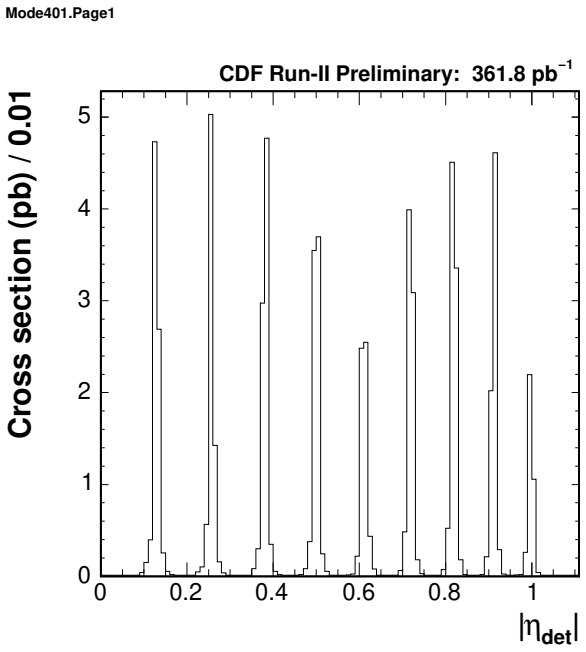

Figure 4.17: Distribution of absolute detector η for conversion electrons with the partner track hitting the tower with an η-index different from the electron.

cut specific to residual conversions that are not common to identified conversions. As we expect, residual conversions tend to pass the isolation cut more than identified conversions because the partner-track activity is less harmful. Our approach to introduce such effects is to subtract partner-track p_T from the original isolation value, then apply the nominal isolation cut. This subtraction is coordinated with the prediction of kinematic information for expected residual conversions just described in the previous paragraphs, i.e. when the partner-track p_T is assumed to be 0.5 GeV/c, the difference from the original value is subtracted from the isolation, and when the residual conversion is considered to be non-proper, we do not do anything to the isolation but just apply the cut as usual. Further we require the following conditions to trigger the subtraction in order to pick up only the case where the original isolation value is certainly affected by the partner track:

- the partner track is pointing a different wedge from the one of the seed electron;
- the partner track is within the isolation cone radius of 0.4;
- the partner track is passing through the local x coordinate at the CES plane in the region $|x| < 21$ cm to avoid ϕ cracks.

The contribution of partner-track p_T to the isolation is checked by looking at the ratio between the two (just like E/p for electron clusters but for the isolation cone in this case) and shown in Figure 4.26. We confirm a clear peak around unity in the plot.

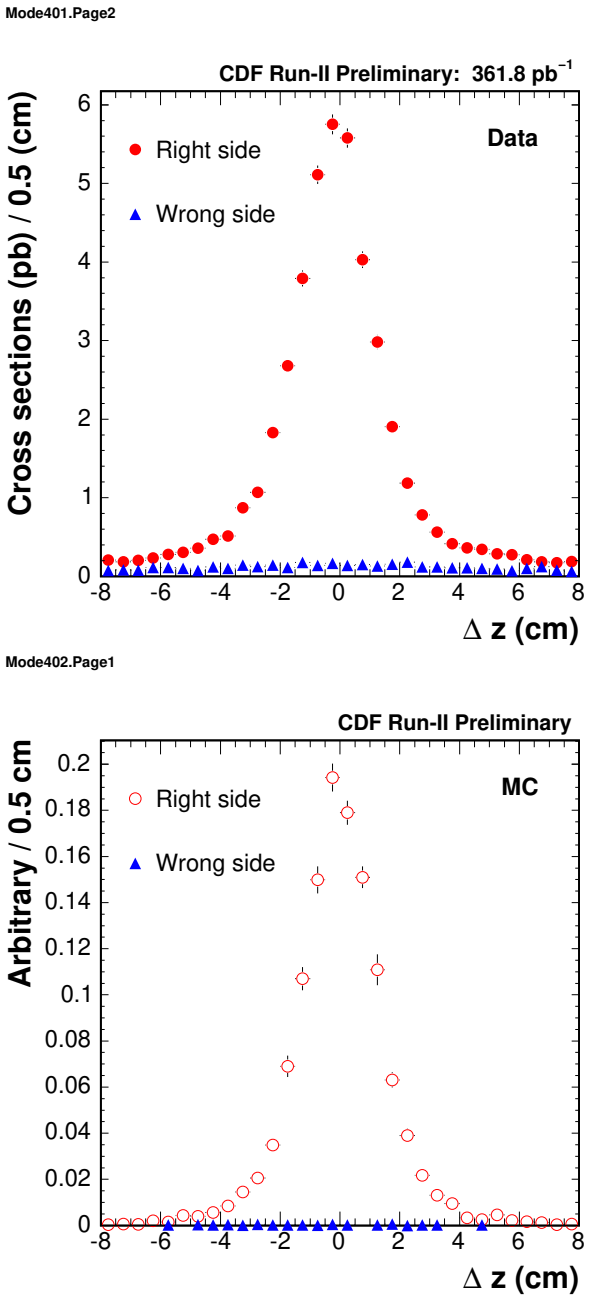

Figure 4.18: Distribution of z position difference on the CES plane between the seed electron and the highest-energy CES cluster in the nearest three towers of each ϕ side (right side and wrong side).

The left side of the peak can be considered to show detector-resolution effects, and the tail in the right side can be attributed to the effects from activities around the conversions, i.e. what the isolation is meant to measure. We argue that this scheme

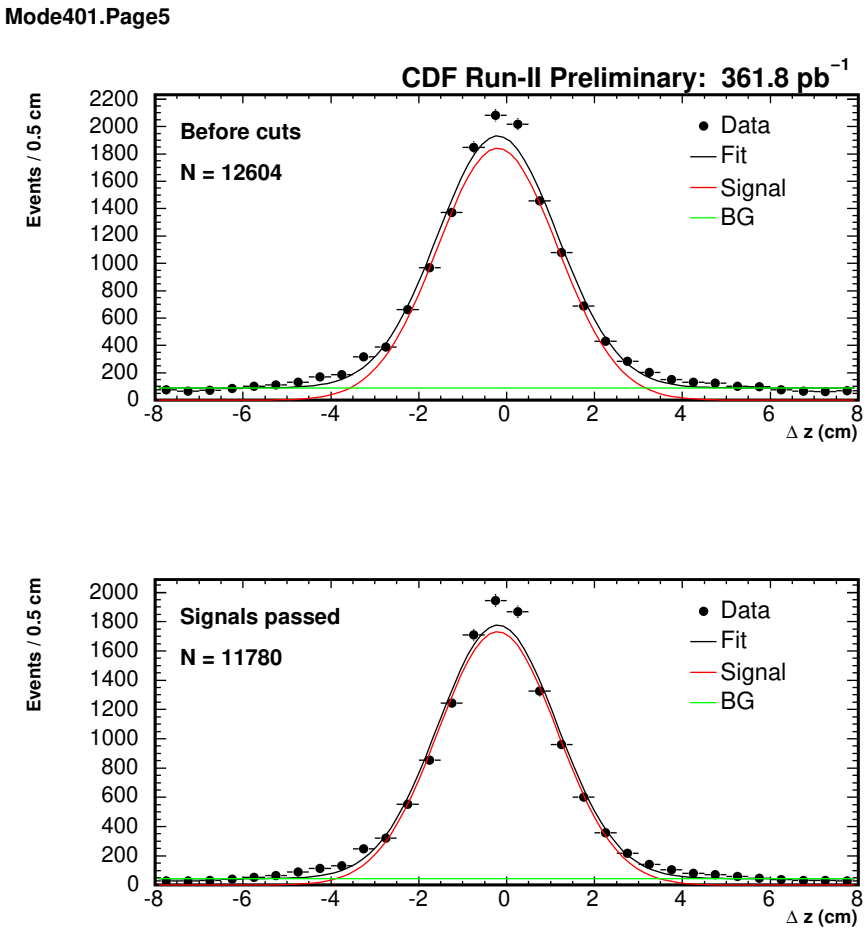

Figure 4.19: Distribution of z position difference before the conversion tagging cut (top) and after (bottom).

would be capable of respecting sample dependences of the isolation, if any, because what we are trying to subtract is the activity only from the conversion partner-track, while underlying events are intact.

4.1.8 Stability over different datasets

The conversion detection efficiency and residual ratio have been measured using the `bhel0d` dataset in the previous sections. We here check the stability of these numbers over the four datasets. Figure 4.27 compares the basic relative efficiencies as a function of partner-track p_T between four different datasets. A structure is common to all the datasets because the MC data used to obtain the efficiency are the same. We do not observe any significant changes among the datasets. The plateau efficiencies for all the datasets are listed in Table 4.2. The plateau efficiency is stable as well.

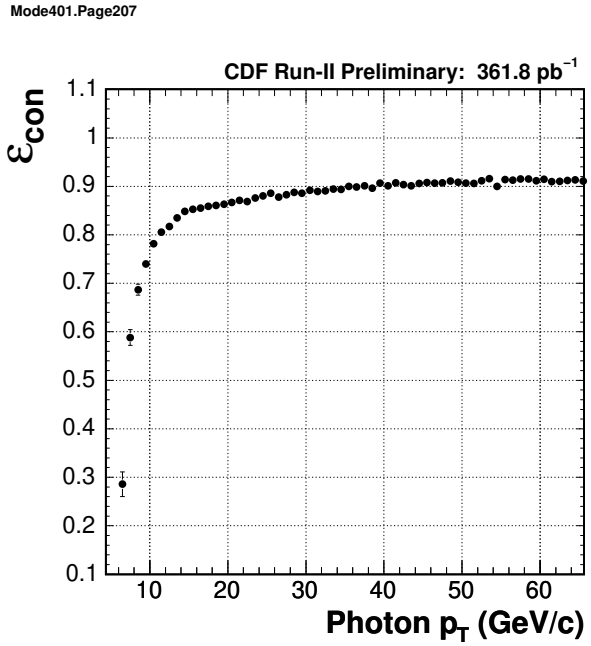

Figure 4.20: Conversion-detection efficiency as a function of photon p_T. The uncertainties are statistical only.

Dataset	$\varepsilon_{\rm pla}$
`bhel0d`	0.935 ± 0.006
`bhel0h`	0.945 ± 0.007
`bhel0i`	0.937 ± 0.006
`bhel0j`	0.933 ± 0.006

Table 4.2: Plateau efficiencies for the four datasets. The uncertainties are statistical.

4.1.9 Requiring silicon hits

In order to improve the signal to background ratio, we will eventually impose a cut requiring Si hits on lepton tracks. Correspondingly, we investigate the case of analyzing conversions with the seed-electron track satisfying our Si-hit cut

$$\text{the number of Si hits} \geq 3\ . \tag{4.14}$$

The results and discussions are mostly the same as what we described in the previous sections, thus we only briefly show the main points.

Figure 4.28 shows the base relative efficiency as a function of partner-track p_T. We see that the efficiency rise is slightly shifted toward the low p_T direction. The plateau efficiency is estimated to be

$$0.95 \pm 0.01\ (\text{stat}) \pm 0.01\ (\text{syst})\ , \tag{4.15}$$

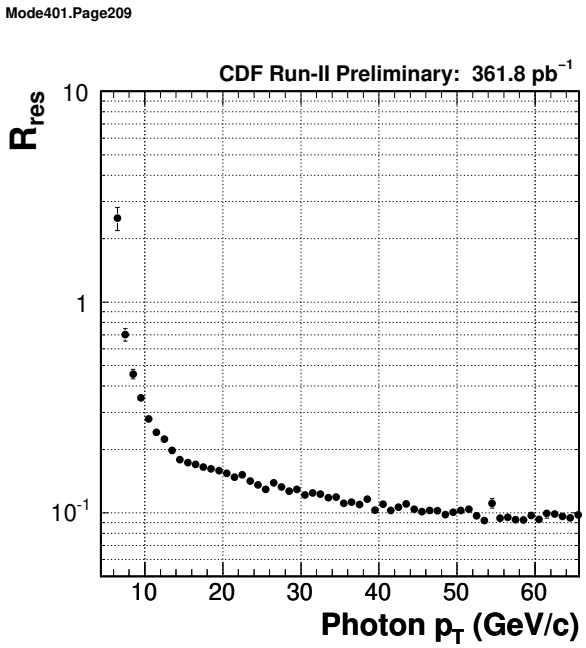

Figure 4.21: Residual ratio as a function of photon p_T. The uncertainties are statistical only.

which is virtually the same as the result without the Si cut. The overall detection efficiency and residual ratio are then shown in Figures. 4.29 and 4.30, respectively, for the case of the low-p_T cut. The relative uncertainty of the $R_{\rm res}$ is about 25% (not shown). The splitting functions are obtained to be

$$f_L = (3.5 \pm 0.2) \times p_T^{-(0.67 \pm 0.02)} , \tag{4.16}$$

and

$$f_H = (10.3 \pm 1.3) \times p_T^{-(0.94 \pm 0.04)} . \tag{4.17}$$

As the photon p_T increases, the factors decrease a little faster than those in the previous section, reflecting the slight extension of the plateau region of the detection efficiency toward the lower p_T.

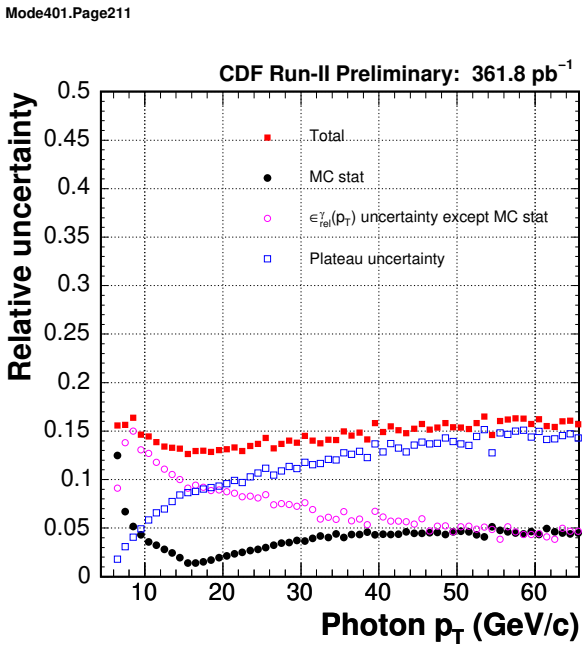

Figure 4.22: Relative uncertainty, shown for different sources, of the residual ratio as a function of photon p_T.

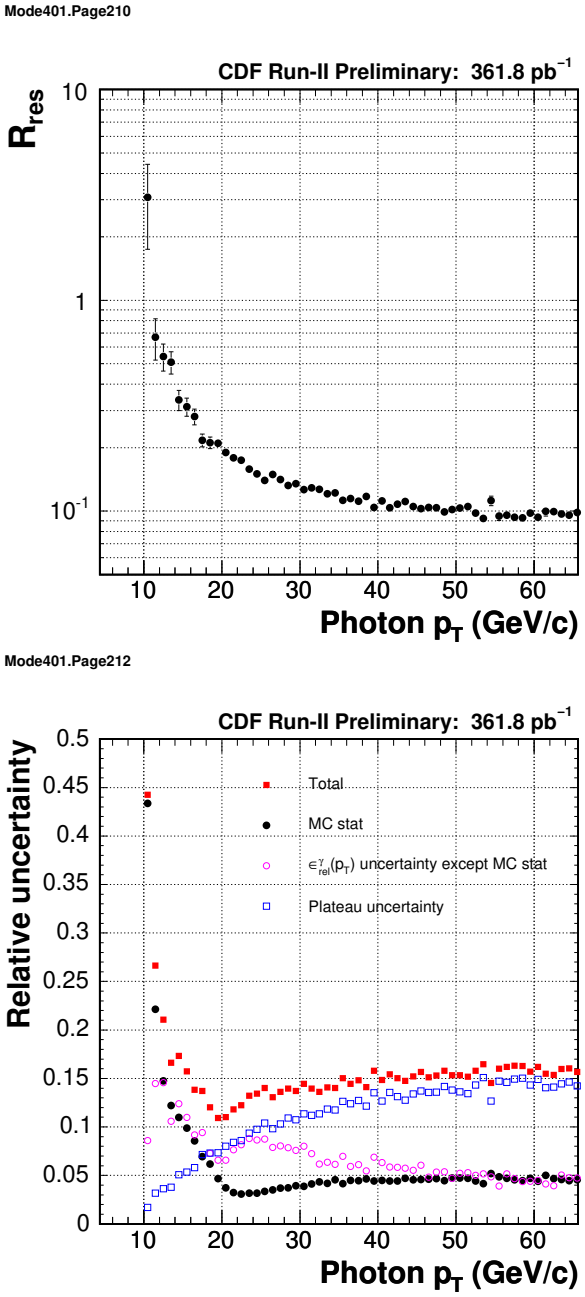

Figure 4.23: Residual ratio (top) and its relative uncertainties (bottom) as a function of photon p_T for the case of our high-p_T cut, $E_T > 20$ GeV and $p_T > 10$ GeV/c. The uncertainties in the top plot are statistical only.

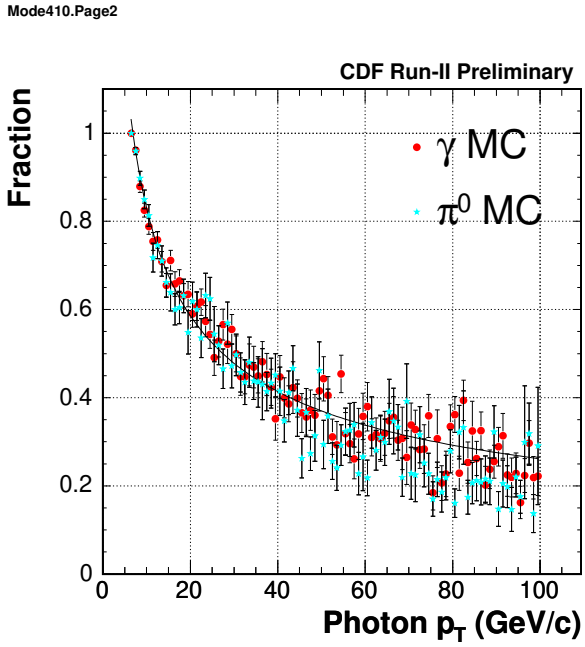

Figure 4.24: Fraction of residual conversions with partner-track p_T less than 1 GeV/c as a function of photon p_T for the case of low lepton-p_T cut.

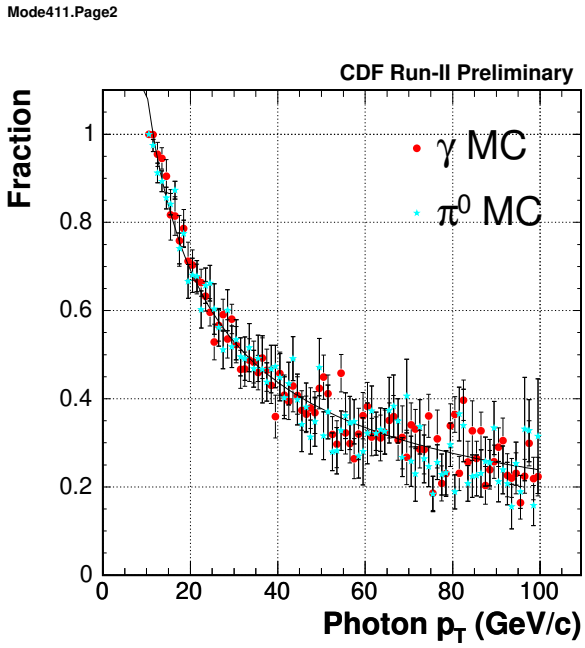

Figure 4.25: Fraction of residual conversions with partner-track p_T less than 1 GeV/c as a function of photon p_T for the case of high lepton-p_T cut.

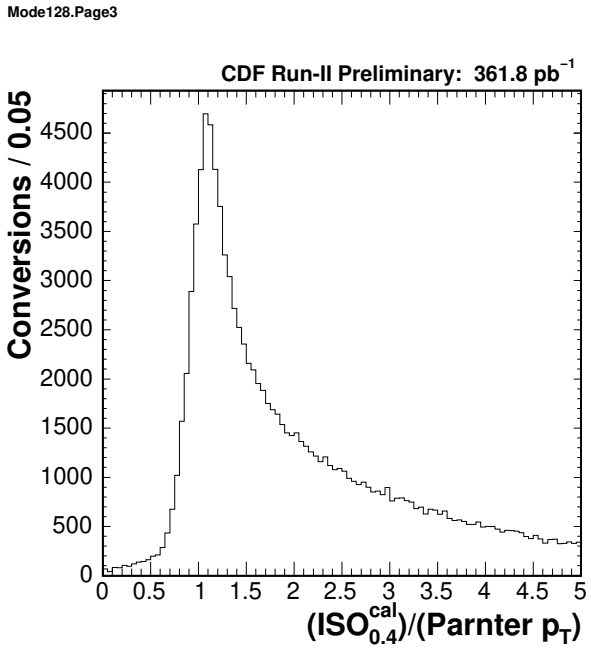

Figure 4.26: Ratio between the calorimeter isolation and the partner-track p_T for conversions.

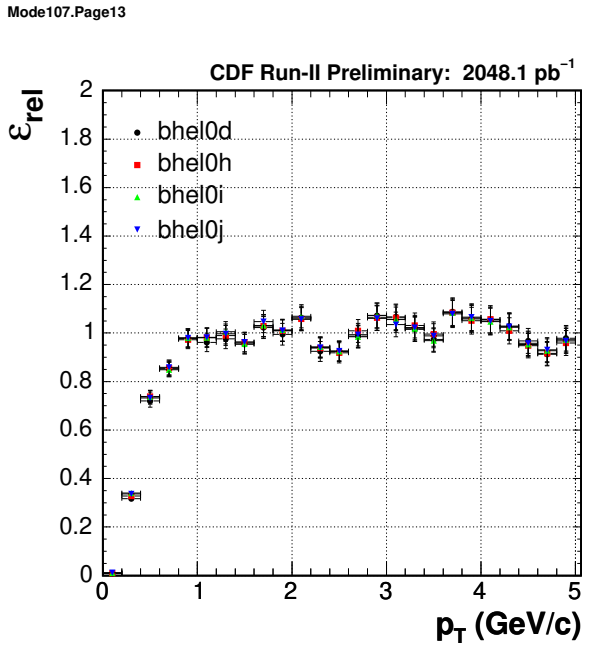

Figure 4.27: Comparison of relative conversion-detection efficiencies as a function of partner-track p_T between four datasets.

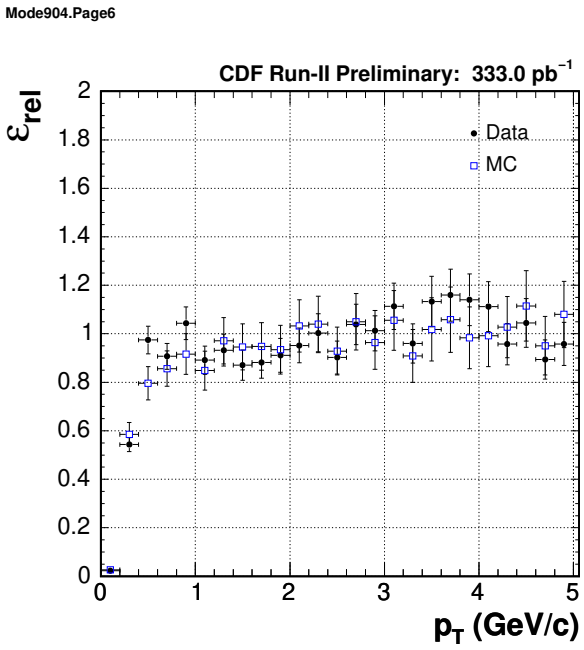

Figure 4.28: Relative conversion-detection efficiency as a function of partner-track p_T for the case that silicon hits are required for the seed-electron track. Only statistical uncertainties are shown.

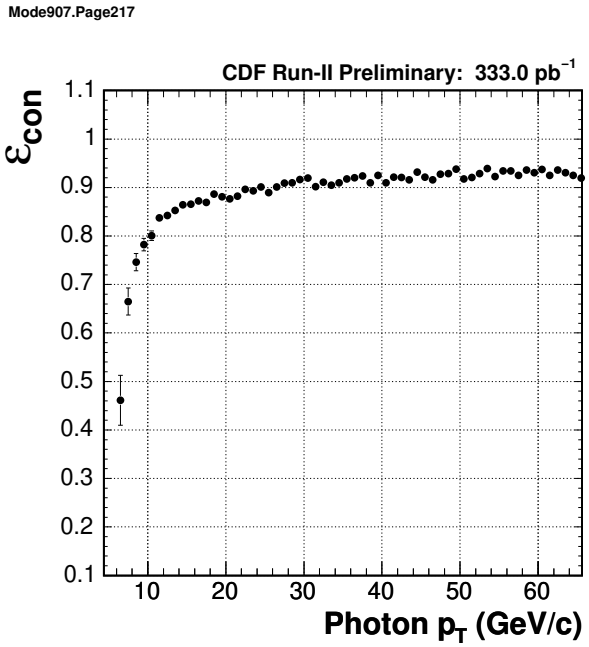

Figure 4.29: Conversion-detection efficiency as a function of photon p_T for the case that silicon hits are required for the seed-electron track. The uncertainties are statistical only.

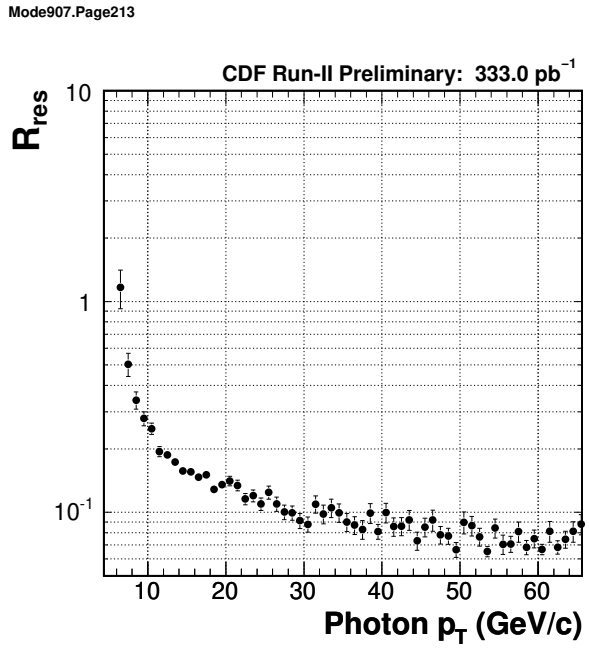

Figure 4.30: Residual ratio as a function of photon p_T for the case that silicon hits are required for the seed-electron track. The uncertainties are statistical only.

4.2 Fake Leptons

Fake leptons are one of major backgrounds in the like-sign (LS) dilepton events. They were estimated by weighting lepton + isolated track events with the expected fake-lepton yield for a given isolated track. These rates used to estimate fake-lepton backgrounds are called the fake-lepton rates, and are defined with respect to some reference rates, the rates of denominator objects. It is expected that the simple isolated-tracks in the OS combination are significantly contaminated by real leptons from Drell-Yan processes, which leads to overestimates of fake-lepton backgrounds. To avoid this problem and to establish a consistent scheme which can be applied to both the OS and LS cases, we choose isolated tracks that deposits certain energies in the electromagnetic (EM) and hadron (HA) calorimeters in the way such that they are not likely to be induced by real leptons.

4.2.1 Fake-lepton Backgrounds

The lepton plus fake-lepton backgrounds arise typically from a single lepton event such as $W \to \ell\nu$. This type of backgrounds consist of one trigger lepton and one fake lepton. The components of the "fake lepton" are

- Fake leptons
  1. Interactive $\pi^{\pm} \to$ fake electrons,
  2. Overlap of π^0 and a track $\to$ fake electrons,
  3. Punch-through hadrons $\to$ fake muons,
- Non-prompt leptons
  1. Residual photon conversions $\to$ electrons
  2. Decay-in-flight muons from $\pi^{\pm}$ and $K^{\pm} \to$ muons,
  3. (Semi-)Leptonic decay of heavy-flavor hadrons $\to$ leptons.

As noted here, we use "fake leptons" as a generic word to mean both the literal fake leptons and non-prompt leptons. Most of the components are considered to be non-isolated and quite common in generic QCD events, while the residual photon-conversions are not necessarily QCD specific, and they are separately estimated from identified conversions with a similar philosophy as the fake-lepton rates. Details of the estimation of residual photon-conversion backgrounds are discussed in §4.1. Correspondingly, contributions of residual conversions are subtracted from fake-electron rates in this study.

4.2.2 Measurement of Fake-lepton Rates

We define the fake rate R_{fake} as a rate of fake leptons relative to isolated tracks with certain energy depositions especially in the hadron calorimeters, which we call "hadronic"

tracks:

$$R_{\text{fake}} = \frac{\text{lepton objects passing nominal selections and considered to be fakes}}{\text{isolated tracks with required calorimeter energy depositions}}. \quad (4.18)$$

It is noted that we define the fake rate here per isolated track, not per jet. The event pre-selection and the isolated hadronic-track selection criteria are listed in Table 4.3. The kinematical cut is $p_T > 6$ GeV/c and we require the same track-quality cuts as shown in Table 3.6. The hadronic-track selection imposes cuts on the energy depositions in the calorimeter towers that a given track is pointing. The first cut in the table is thought to mainly reject real electrons and the other cuts are meant to reject real muons. As to the numerator, we apply the nominal lepton selection cuts to find fake-lepton objects.

We evaluate R_{fake} using inclusive jet samples. The data we use are the `Jet20`, `Jet50`, `Jet70`, and `Jet100` generic jet samples from the `0d` through the `0i` datasets. The "jet samples" means different types of jet data collected by different triggers. In order to remove real-leptons from the numerator side, we impose a W veto and a Z veto. The W veto rejects events with

- electrons with $E_T > 20$ GeV or muons with $p_T > 20$ GeV/c passing lepton selection shown in Table 3.6,
- $\not\!\!E_T > 30$ GeV or transverse mass > 40 GeV/c^2.

The $\not\!\!E_T$ is corrected for muons passing our muon selection with the $p_T > 6$ GeV/c cut. The Z veto rejects events with

- electrons with $E_T > 20$ GeV or muons with $p_T > 20$ GeV/c passing our lepton selection,
- invariant mass with the 2nd-leg objects is in the mass window of 81–101 GeV/c.

The definition of the 2nd-leg objects for the Z veto is given in Table 3.8. Note that the EM objects for the 2nd-leg are not necessarily in the central region. Finally, we require the hadronic tracks and fake-lepton objects be both separated from the trigger jet in the η-ϕ space by $R > 1.0$ to remove possible trigger biases.

Figure 4.31 shows the p_T distributions of isolated hadronic tracks, fake electrons, and fake muons for each jet sample combined over the datasets from the `0d` through the `0i`. The fake rates by combining jet samples with the RMS spread as a systematic uncertainty are shown in Figure 4.32 with breakdown of fake-muon rates into those of CMUP and CMX muons.

4.2.3 Subtraction of Residual Photon-Conversions

Residual photon-conversions in the fake-electron objects found in the jet samples are estimated from the amount of identified conversions multiplied with weights for residual

Event pre-selection
$\lvert z_{\rm pv}\rvert < 60$ cm
Cosmic-ray veto
Geometrical and kinematical cuts
CDF default tracks in the central region
$p_T > 6$ GeV/c
Track quality cuts
axial ≥ 3 and stereo ≥ 3 (≥ 7 hits)
$\lvert z_0 - z_{\rm pv}\rvert < 2$ cm
Silicon hits ≥ 3
$\lvert d_0\rvert < 0.02$ cm
Isolation cut
$\mathrm{ISO}^{\rm cal}_{0.4} < 2$ GeV
Hadronic-track selection
HA/EM > 0.2
EM > 1 GeV
HA > 4 GeV

Table 4.3: Event pre-selection and the denominator track selection.

photon-conversions inferred from them, which we refer to as residual conversion ratios. The details of the method itself is described in §4.1. We show only the results in this section. Figure 4.33 shows the p_T distributions of estimated residual conversions for each jet sample combined over the datasets. The combined fake-electron rates over the different type of jet samples, which is shown in Figure 4.34. In this case, the uncertainties shown in the figure include a systematic uncertainty from the residual conversion estimation, quantified by $\pm 1\sigma$ variations of the residual conversion ratios, as well as the RMS spread over the jet samples.

4.2.4 Real-lepton Contamination and Charge Correlation

In this section, we briefly check an implication of hadronic-track selection in applications to inclusive lepton data. Figure 4.35 shows effective cross sections of μ + track objects of a few types. For this plot, the track object search in a given event is performed only when there is exactly one good muon passing all the muon selection cut with the high p_T cut of $p_T > 20$ GeV/c. Also, the simple isolated tracks in this anal-

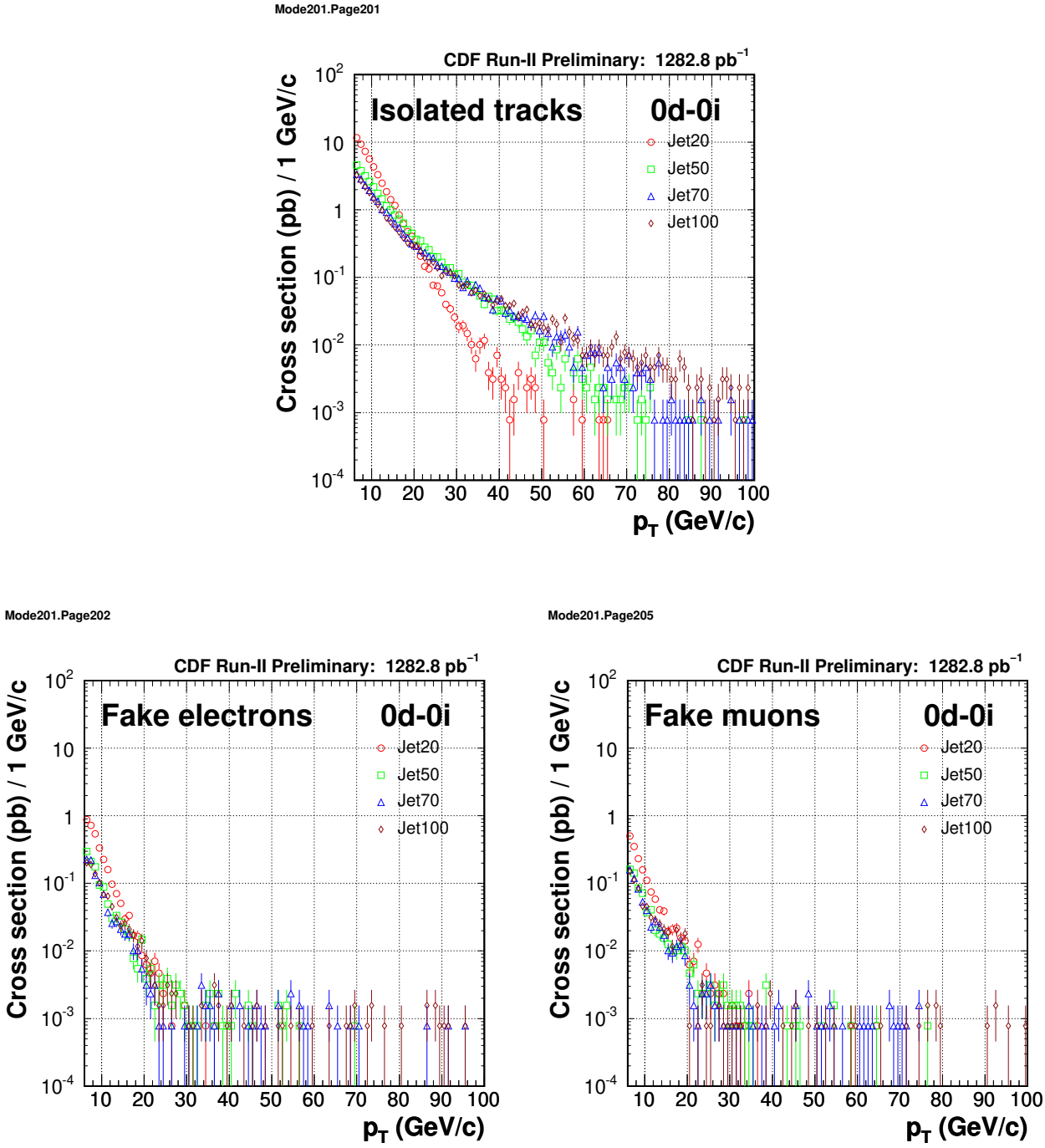

Figure 4.31: Track p_T distributions of isolated hadronic tracks (top), fake electrons (lower left), and fake muons (lower right) in the jet samples combined over the datasets.

ysis are checked if they are associated with any good leptons or any EM objects with conversion flags, and removed if so. The $\mu\mu$ events and the μ + isolated-track events are therefore mutually exclusive.

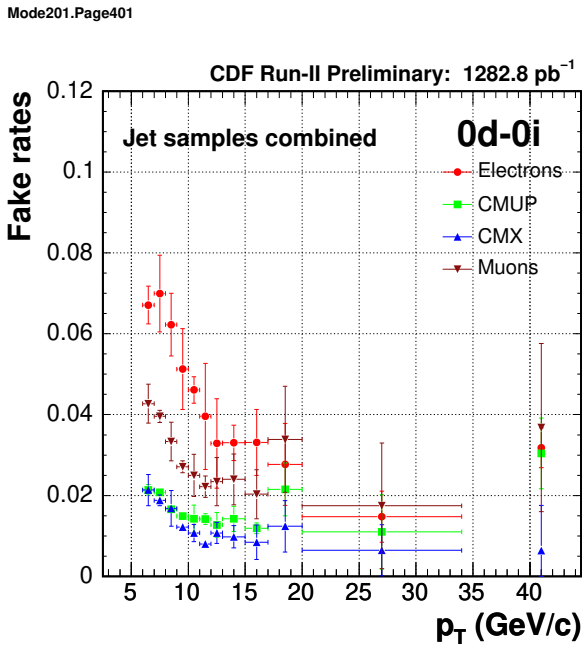

Figure 4.32: Fake rates as a function of track p_T obtained by combining all the datasets and jet samples. The uncertainties shown in the plots take into account of the RMS spread over jet samples as systematic uncertainties. The last data points in the plot correspond to the fake rates including overflow events.

First of all, we can confirm from a strong Z peak that simple isolated tracks of the OS case are significantly contaminated by real muons. Since the fake-muon rates are about at a few % level as obtained in the previous sections, the estimated fake backgrounds from the isolated tracks would be also a few % level of dimuon candidates. It is actually not a serious problem compared to the large contributions from real dimuon events, although the estimated value of fake backgrounds itself would be orders of magnitude larger than the correct answer. We also see that the isolated track rates get larger than those of the dimuon candidates toward low mass regions, which indicate more backgrounds at low masses as expected. For the case of isolated hadronic tracks, the situation is greatly improved. We are picking up relatively more backgrounds with suppressing real muon contamination. Remembering again the fake-muon rates are about a few %, the fake-lepton backgrounds are negligibly small in the OS dimuon events in rather a wide invariant mass range.

One of interesting thing is a comparison between the OS and LS combinations of μ + hadronic tracks (see Figure 4.35). The OS rates are larger than the LS rates even outside Z mass regions, which could be a sign of charge correlation besides the effects due to real dimuon events. In order to get a better measure, we investigate real-muon contamination in the hadronic tracks with helps of `PYTHIA` Monte Carlo (MC) events. We use inclusive $W\to\mu\nu$, $Z\to\mu\mu$, and $Z\to\tau\tau$ MC samples to collect μ + hadronic

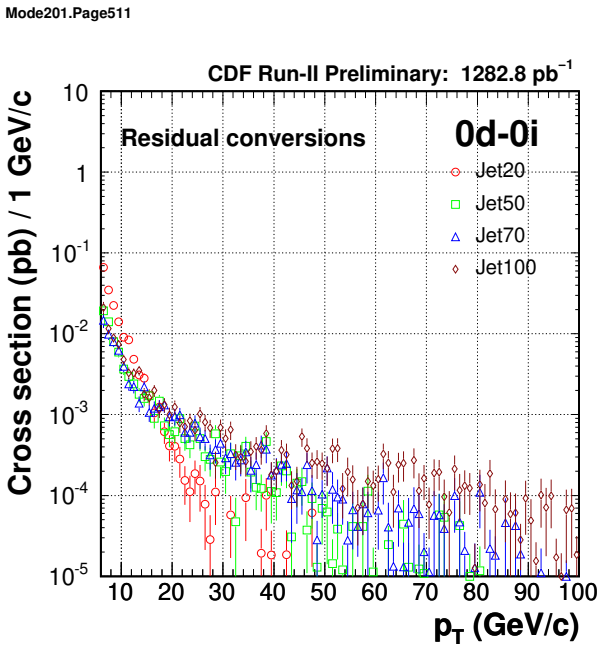

Figure 4.33: Track p_T distributions of residual photon-conversions in the jet samples combined over the datasets.

tracks, and compare with the data as given in Figure 4.36. We see that the observed μ + hadronic tracks are qualitatively described by MC events, and also see that contributing mass regions are different between the processes. The gradual rise of the rates toward low mass regions can be understood as coming mainly from contributions of W events. The MC predictions of the absolute value do not completely agree with the observed effective cross section due to some unknown reasons. We, however, try to obtain the fraction of real muons in these MC events by looking at `OBSP` information for which systematics would be canceled to some extent. The components of real muons in the MC events are shown in Figure 4.37. The real-muon contamination is due to $Z \to \mu\mu$ events and the small peak around Z mass regions are completely attributed to them as expected. Regarding this, we comment that Z mass regions will be eventually excluded from the final analysis, which provides us a certain safety factor against the problem of real-muon contamination. Real-muon fractions, f, as a function of invariant mass are estimated as shown in Figure 4.38, and a correction for real-muon contamination in the observed OS μ + hadronic tracks can be done by multiplying $1 - f$. The OS/LS ratios after the correction is shown in Figure 4.39. The result is not statistically powerful, but there seem to still remain indications of the charge correlation in the data which are as much as a factor of 2 in a mass region around 40–50 GeV/c^2. The MC predictions obtained by explicitly rejecting real-muons using `OBSP` information are also included in the figure. It shows a similar level of charge correlation, and further says that the correlation is originating from W events, not from $Z \to \mu\mu$ events. The $Z \to \tau\tau$ strongly

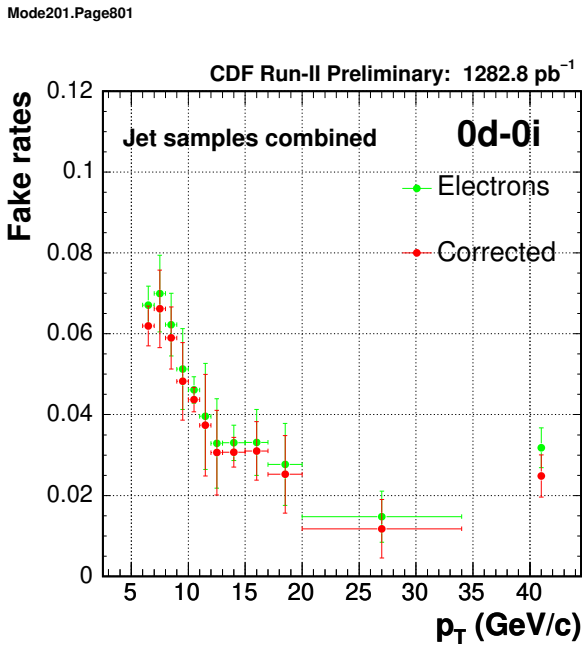

Figure 4.34: Fake-electron rates as a function of track p_T before and after subtracting residual photon-conversions, with combining all the datasets and jet samples. The uncertainties shown in the plots take into account of the RMS spread over jet samples as systematic uncertainties. The rates after correction also include a systematic uncertainty from the estimation of the residual photon-conversions. The last data points in the plot correspond to the fake rates including overflow events.

favors the OS combination as expected but the contribution itself is relatively small compared to the W events, thus the net effect is driven by the W events. From these investigation, we think that there may be charge correlations between leptons and additional track objects, thus the estimation of the fake-lepton backgrounds in the OS dilepton events using LS combinations is not necessarily ensured to lead to a correct answer. We can also say that the charge correlation may depend on the selection and on the kinematical space that we look at, and not always important especially when W events are not contributing much. For example, it might be reasonable to use LS combinations in the Z mass window. In general, we must always bear this in our mind when we analyze the OS dilepton events.

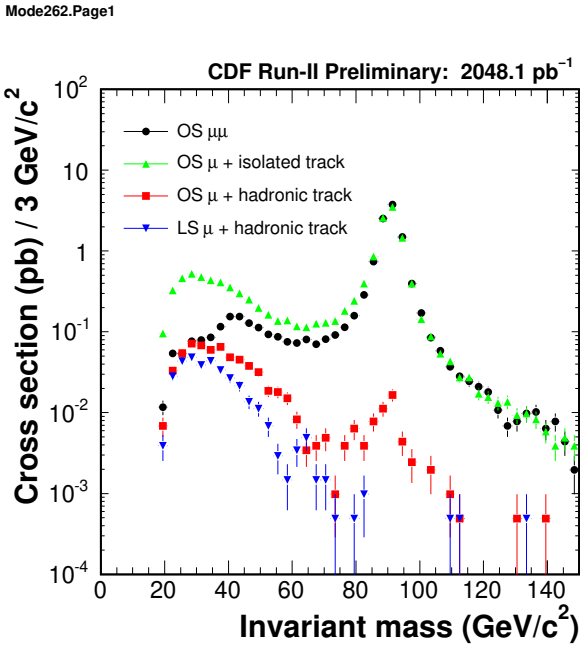

Figure 4.35: Comparison of the rates of μ + various objects from inclusive muon datasets.

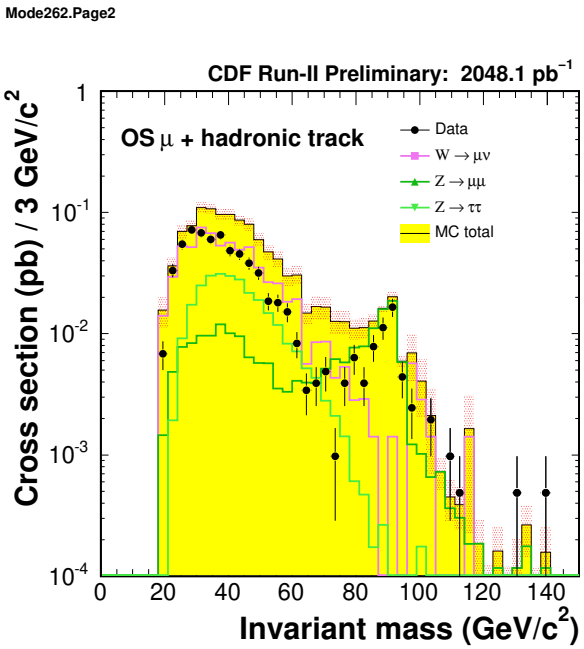

Figure 4.36: Comparison of the rates of μ + hadronic tracks between the data and the Monte Carlo predictions, where the hatch of the light red color represents statistical uncertainties of the Monte Carlo data.

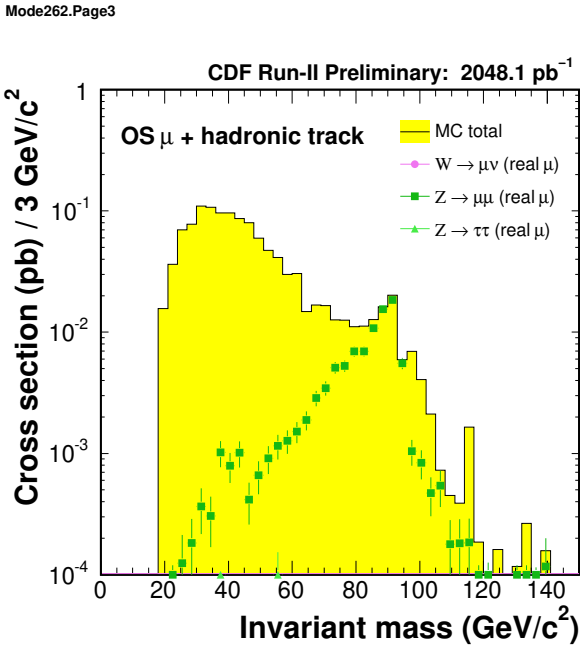

Figure 4.37: Real-muon components of hadronic tracks in the Monte Carlo events extracted by looking at OBSP information.

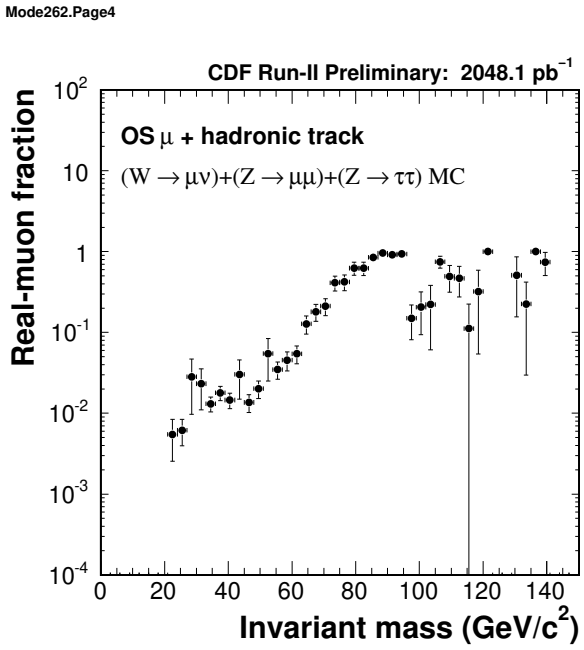

Figure 4.38: Fraction of real-muons of hadronic tracks for the Monte Carlo events.

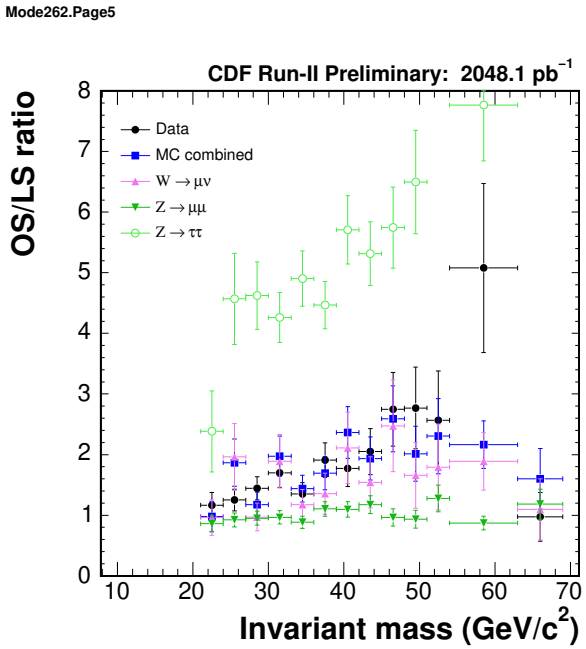

Figure 4.39: Opposite-sign and like-sign ratios of μ + hadronic track events for the data after subtracting real-muon fractions predicted by Monte Carlo events. The predictions of Monte Carlo events are also shown, which are obtained by explicitly removing real muons using the `OBSP` information.

4.3 Physics Background

The physics backgrounds can be classified into reducible and irreducible backgrounds:

- Reducible backgrounds
  1. $Z/\gamma^* \to \ell^+\ell^-$,
  2. W+(heavy-flavor hadrons)$\to \ell\ell + X$,
  3. $t\bar{t} \to (W^+b)(W^-\bar{b}) \to \ell\ell + X$,
  4. $W^+W^- \to (\ell^+\nu)(\ell^-\nu)$.
- Irreducible backgrounds
  1. $WZ \to (\ell^\pm\nu)(\ell^+\ell^-)$,
  2. $ZZ \to (\ell^+\ell^-)(\ell^+\ell^-)$.

The reducible backgrounds are reduced first of all by the LS requirement. When they contribute to LS dilepton events, the events are most likely due to residual conversions or fake leptons contained in these physics events, thus reduced also by the isolation cut. The irreducible backgrounds are suppressed mainly by a Z veto at the first order.

The MC samples were generated by PYTHIA generator. Table 4.4 lists the MC samples and related information of them. The MC data are all applied with the relevant scale factors that are discussed in the below. A rather important point regarding our MC prediction is that residual photon-conversions and fake-leptons including non-prompt leptons from (semi-)leptonic decays of heavy-flavor hadrons found in the MC events are explicitly removed from the MC contributions by looking at the `OBSP` information since their contributions are assumed to be directly estimated from the data-driven methods.

4.3.1 Monte Carlo Scale Factors

The scale factor (SF) is to be used in MC based events yield estimation. The event yield N is driven by

$$N = L \cdot \varepsilon \cdot \sigma, \tag{4.19}$$

where L is the integrated luminosity, ε is the total detection efficiency, and σ is the process cross section. The total detection efficiency includes several selection efficiency, can be expressed as,

$$\varepsilon = \sum_i A^{(i)} \cdot \varepsilon^{(i)}_{\rm trig} \cdot \varepsilon^{(i)}_{\rm pre} \cdot \varepsilon^{(i)}_{\rm ID} \tag{4.20}$$

where i means dilepton types such as CEM-CEM, CMUP-CMX and so on. $A^{(i)}$ is geometrical and kinematical acceptance, $\varepsilon^{(i)}_{\rm trig}$ is trigger efficiency, $\varepsilon^{(i)}_{\rm pre}$ is pre-selection efficiency, and $\varepsilon^{(i)}_{\rm ID}$ is lepton identification efficiency.

Process	Events	$\sigma \cdot B_F$	K factor (pb)	Filter-efficiency	Luminosity (fb^{-1})	Notes
Electron channels						
$W \to e\nu$	4036290	1960	1.4	—	1.47	
$Z/\gamma^* \to ee$	1594110	355 ± 3	1.4	—	3.21	$M > 20$ GeV/c^2
Muon channels						
$W \to \mu\nu$	1608588	1960	1.4	—	0.586	
$Z/\gamma^* \to \mu\mu$	6701700	355 ± 3	1.4	—	13.5	$M > 20$ GeV/c^2
Both channels						
$Z/\gamma^* \to \tau\tau$	6849882	238 ± 3	1.4	—	19.0	$M > 30$ GeV/c^2
$t\bar{t}$	1111652	7.3	—	—	152.3	
WW	1596781	1.27	—	—	1.26×10^3	
WZ	3598792	0.365	—	0.76	1.19×10^4	
ZZ	761342	2.01	—	0.23	1.65×10^3	$M > 15$ GeV/c^2

Table 4.4: Summary of the Monte Carlo samples.

The trigger efficiency is driven by using real data, while other efficiencies are driven by data and MC samples, respectively. The MC based event yield are scaled by the ratio of the efficiency in data and MC to more match MC yield to real data. In this thesis, the estimated scale factor are pre-selection efficiency and lepton identification efficiency.

4.3.2 Data Samples

As described in §3.1, the data collected by inclusive high-p_T lepton trigger is used to search in the higgs boson. The employed triggers are `ELECTRON_CENTRAL_18`, `MUON_CMUP18`, and `MUON_CMX18`, the trigger efficiencies is used in the total detection efficiency.

The triggers can effectively collect the electroweak process events such as Drell-Yan events. The Drell-Yan events are used to estimate the lepton identification efficiency. The Drell-Yan MCs are used to estimate the efficiency in MC, which are generated by PYTHIA. The higgs MC samples are also used to estimate the pre-selection efficiency, shown in Table 5.1.

4.3.3 Trigger Efficiency

The trigger efficiencies are estimated period by period from the period 0 through 17 to take the changes of trigger tables into account as much as possible.

High-p_T Electron Trigger Efficiency

The electron trigger efficiency is estimated for the parts of the tracking trigger and the calorimeter trigger, separately. We use the `W_NOTRAK` trigger to estimate tracking trigger efficiency. The `W_NOTRAK` trigger has the same calorimeter trigger path as the `ELECTRON_CENTRAL_18` trigger path, but does not have the tracking trigger path. For the tracking trigger efficiency, we pick up W candidate events which have good electrons passing our electron selections, missing $E_T > 25$ GeV, and `W_NOTRAK` trigger bits. These are the denominator of the efficiency. Then we require the tracking trigger at each level to estimate the efficiencies.

For the Level-1 calorimeter trigger efficiency, we use high-p_T muon samples as unbiased samples. In moun samples, we pick up good electrons passing our electron selections (the L1 denominator), then require the event to fire the `L1_EM8` trigger (the L1 numerator). The `L1_EM8` trigger is the same as the Level-1 trigger of `ELECTRON_CENTRAL_18` (`L1_CEM8_PT8`) for calorimeter trigger part. For the Level-2 calorimeter trigger efficiency, we use good lepton events which are triggered by the `ELECTRON_CENTRAL_18_NO_L2` and the Level-1 trigger of `ELECTRON_CENTRAL_18` (the L2 denominator), then we require the Level-2 trigger of `ELECTRON_CENTRAL_18` (the L2 numerator). For the Level-3 calorimeter trigger efficiency measurement, first we pick up good lepton events passing the `ELECTRON_CENTRAL_18_NO_L2` and the Level-2 trigger of `ELECTRON_CENTRAL_18` (the L3 denominator), moreover we require the Level-3 trigger (the L3 numerator). The efficiencies are shown in Table A.1.

High-p_T Muon Trigger Efficiency

We use $Z \rightarrow \mu\mu$ events which have the invariant mass between 81 to 101 GeV/c^2 and fire the `MUON_CMX18` (`MUON_CMUP18`) trigger to estimate the `MUON_CMUP18` (`MUON_CMX18`) trigger efficiency (the denominator events). Then we apply the `MUON_CMUP18`(`MUON_CMX18`) trigger. We just require dileptons in events, no jet objects, so this muon trigger efficiency is not including the `Jet10` trigger. The efficiencies are shown in Table A.2 and Table A.3.

4.3.4 Primary-vertex Cut Efficiency and Scale Factor

Primary-vertex cut is to select events within the detector region well-defined measurement of collisions. The region is confirmed as $|z_{\rm pv}| < 60$cm by using cosmic ray and simulation. The cosmic ray track z_0 and simulation z_0 finding efficiency both indicate that the finding efficiency within $|z_0| < 60$cm is flat. The acceptance with the $p\bar{p}$ beam luminous region of $|z_0| < 60$cm is determined by fitting to "Beam Luminosity Function" with $|z_0| < 60$cm. The beam luminosity function is the longitudinal profile of the luminous region, expressed by

$$\frac{dL(z)}{dz} = N_p N_{\bar{p}} \frac{1}{\sqrt{2\pi}\sigma_z} \frac{\exp(-z^2/2\sigma_z^2)}{4\pi\sigma_x(z)\sigma_y(z)} \tag{4.21}$$

where z is primary-vertex position, $N_{p,\bar{p}}$ are proton or antiproton beam fluxes, and $\sigma_{x,y,z}(z)$ are the beam widths. The efficiency is calculated from the fit to z of beam profile as follows,

$$\varepsilon(|z_0| < 60\text{cm}) = \frac{\int_{-60}^{+60} [dL(x)/dz]dz}{\int_{-\infty}^{+\infty} [dL(z)/dz]dz}. \tag{4.22}$$

We are using high-p_T lepton trigger samples, Drell-Yan Monte Carlo and higgs Monte Carlo samples. The efficiencies and scale factors are shown in Tables A.4-A.8.

4.3.5 Lepton Selection Efficiency and Scale Factor

We estimate lepton selection efficiency based on our like-sign dilepton analysis. Our base kinematical-cut is $p_T > 20$ GeV/c for the leading lepton and $p_T > 6$ GeV/c for the 2nd leading lepton, so we look at the efficiency and scale factor from $p_T > 6$ GeV/c. We use Drell-Yan events of the data and MC samples which are produced by PYTHIA to estimate the efficiency and scale factor. For the electron selection efficiency, we estimate it in 2 regions with respect to electron E_T, because the scale factor of electron identification cut depends on electron E_T. We decide to divide the efficiency and scale factor to 2 region at $E_T = 30$ GeV, while the scale factor does not show any clear dependence on the muon p_T. The estimated cut variables are shown in Table 3.6.

4.3.6 OSLS Fake Ratio

We use Drell-Yan events to estimate the efficiency and scale factor. The Drell-Yan events are opposite sign dilepton events which are passing $\Delta\phi_{\ell_1\ell_2} > 2.8$ (rad) cut. Such Drell-Yan events contain non-negligible amount fake backgrounds in the events, in particular when the 2nd leading lepton is low p_T. So, we subtract the backgrounds from the Drell-Yan events to get more pure Drell-Yan events using a ratio of opposite sign(OS) fake events and like sign(LS) fake events (R_{OSLS}). The Drell-Yan counting method is

$$N_{\text{DY}} = N_{\text{OS}} - N_{\text{LS}} \times R_{\text{OSLS}}, \tag{4.23}$$

$$R_{\text{OSLS}} = \frac{\text{The number of fake OS events}}{\text{The number of fake LS events}}, \tag{4.24}$$

where N_{OS} is the number of OS dilepton events, N_{LS} is the number of LS dilepton events. the dilepton events have the 1st leading lepton passing all lepton selection cut and the 2nd leading lepton passing geometrical, kinematical cut and any selection cut. we define the fake Drell-Yan event as the 1st leading object is passing all lepton selection criteria and the 2nd leading object is satisfied geometrical and kinematical cut and hadronic object criteria (HAD/EM > 0.2, HAD > 1.0 GeV and EM > 4 GeV). We regard such a diobject event as fake Drell-Yan event. If we simply regard the LS dilepton events as background, we go into underestimate the background, because real

dilepton events have charge correlation as mentioned in §4.2.4. We require the reading lepton passing all the lepton selection and the event fire the high-p_T lepton trigger. Then we apply our lepton selections to the 2nd lepton, as a probe, passing only the geometrical and kinematical selections. If the dilepton type contains the same type of lepton objects such as CEM-CEM, CMUP-CMUP, and CMX-CMX, the efficiency is calculated by

$$\varepsilon = \frac{2 \times N_{\text{after}}}{N_{\text{before}} + N_{\text{after}}}, \tag{4.25}$$

while if it consists of different types, the efficiency is given by

$$\varepsilon = \frac{N_{\text{after}}}{N_{\text{before}}}, \tag{4.26}$$

where the N_{before} is the number of events before a selection and the N_{after} is the number of events after a selection.

4.3.7 Low-E_T Electron Selection Efficiency and Scale Factor

We estimate the electron selection efficiency and scale factor for low-E_T electrons ($E_T < 30$ GeV) using Drell-Yan events ($\Delta\phi_{\ell_1\ell_2} > 2.8$), the events are provided by extracting LS dielectron events applied OSLS ratio from OS dielectron events with the invariant mass greater than 20 GeV/c^2. As mentioned before, the identification scale factor depends on the E_T of electron. The efficiencies and scale factors are shown in Tables A.9, A.11, A.13, A.15, and A.17

4.3.8 High-E_T Electron Selection Efficiency and Scale Factor

We estimate the electron selection efficiency and scale factor for high-E_T electrons ($E_T > 30$ GeV) using Drell-Yan events within Z mass window ($76 < M_{ee} < 106$) and the background subtraction is same as low-E_T electron selection efficiency study (see §4.3.7). The efficiencies and scale factors are shown in Tables A.10, A.12, A.14, A.16 and A.18

4.3.9 Muon Selection Efficiency and Scale Factor

We estimate the muon selection efficiency and scale factor using Drell-Yan events with OSLS ratio to subtract background events. In muon case, there is no clear muon p_T dependence for any muon selection variables. The efficiencies and scale factors are shown in Tables A.19-A.38.

4.3.10 Muon Reconstruction Efficiency and Scale Factor

We use Drell-Yan event passing $\Delta\phi_{\ell_1\ell_2}$ cut (> 2.8), the difference of z_0 position criterion for dimuon ($|z_0^{\ell_1} - z_0^{\ell_2}| < 2$cm) to estimate the muon reconstruction efficiency. we also

use OSLS ratio to subtract the background. We are using the high p_T muon trigger samples and Drell-Yan MC data produced by PYTHIA. The efficiencies and scale factors are shown in Tables A.39-A.43.

4.3.11 $Z/\gamma^* \to \ell^+\ell^-$ Cross Section

We measure the $Z/\gamma^* \to \ell^+\ell^-$ cross section for the invariant mass region 66-116 GeV/c^2 using the trigger efficiency and the scale factors to validate them. The cross section can be expressed by

$$\sigma(Z/\gamma^* \to \ell^+\ell^-) = \frac{N_{\rm obs}}{L \cdot \varepsilon}\,, \tag{4.27}$$

$$\varepsilon = \varepsilon_{\rm MC} \cdot \varepsilon_{\rm trig} \cdot {\rm SF}_{\rm pv} \cdot {\rm SF}_{\ell_1} \cdot {\rm SF}_{\ell_2}\,, \tag{4.28}$$

the $N_{\rm obs}$ is the number of observed events, the L is the integrated luminosity, the $\varepsilon_{\rm MC}$ is $Z/\gamma^* \to \ell^+\ell^-$ efficiency derived by Drell-Yan MC samples. the $\varepsilon_{\rm trig}$ means lepton trigger efficiency, the ${\rm SF}_{\rm pv}$ is the scale factor for the primary-vertex cut efficiency, and the ${\rm SF}_{\ell_{1,2}}$ mean the lepton selection and muon reconstruction efficiency scale factors. Tables 4.5-4.9 show the number of observed events, expected events and cross sections for each dilepton types. We see the maximum 8.0% difference in observed event and expected event for CMX-CMUP pair. We consider the overall difference (2.8%) as systematic uncertainty for our like-sign dilepton analysis.

Data Set	Observed (O)	Expected (E)	Significance for # of events	(E−O)/O	Cross-Secion (pb)	Significance for Cross-Section
0d	3781	3752.8 ± 238.9	−0.116	−0.008	256.2 ± 16.8	0.277
0h	4127	4285.4 ± 266.5	0.578	0.038	244.7 ± 15.7	−0.401
0i	6246	6304.5 ± 392.4	0.147	0.009	251.7 ± 16.0	0.022
0j	8528	9048.3 ± 560.8	0.916	0.061	239.6 ± 15.1	−0.738
0k	4696	4542.4 ± 281.7	−0.529	−0.033	262.8 ± 16.7	0.658
Overall	27378	27933.4 ± 822.1	0.663	0.020	250.3 ± 7.2	−0.111

Table 4.5: The number of $Z/\gamma^*(66 < M_{\ell\ell} < 116\ \mathrm{GeV}/c^2)$ events and the cross-section for CECE pair. (Note : Quote NNLO cross-section ($\sigma = 251.3 \pm 5$ pb) to estimate the significance for cross-section.)

Data Set	Observed (O)	Expected (E)	Significance for # of events	(E−O)/O	Cross-Secion (pb)	Significance for Cross-Section
0d	1141	1102.0 ± 78.0	−0.459	−0.034	263.3 ± 20.2	0.575
0h	1261	1233.5 ± 99.2	−0.261	−0.022	259.7 ± 22.1	0.372
0i	1971	1967.3 ± 144.3	−0.025	−0.002	254.7 ± 19.5	0.170
0j	2681	2845.9 ± 203.0	0.787	0.062	239.5 ± 17.7	−0.643
0k	1369	1320.0 ± 126.4	−0.372	−0.036	263.7 ± 26.2	0.462
Overall	8423	8468.7 ± 306.5	0.143	0.005	254.3 ± 9.2	0.289

Table 4.6: The number of $Z/\gamma^*(66 < M_{\ell\ell} < 116\ \mathrm{GeV}/c^2)$ events and the cross-section for UPUP pair. (Note : Quote NNLO cross-section ($\sigma = 251.3 \pm 5$ pb) to estimate the significance for cross-section.)

Data Set	Observed (O)	Expected (E)	Significance for # of events	(E−O)/O	Cross-Secion (pb)	Significance for Cross-Section
0d	548	575.3 ± 40.8	0.582	0.050	242.2 ± 20.0	−0.442
0h	884	880.1 ± 65.3	−0.054	−0.004	255.2 ± 20.8	0.182
0i	1315	1387.8 ± 117.3	0.594	0.055	240.9 ± 21.4	−0.473
0j	1875	2089.2 ± 148.5	1.382	0.114	228.2 ± 17.1	−1.301
0k	857	976.1 ± 81.3	1.378	0.139	223.2 ± 20.1	−1.356
Overall	5479	5908.5 ± 219.9	1.850	0.078	236.9 ± 8.8	−1.420

Table 4.7: The number of $Z/\gamma^*(66 < M_{\ell\ell} < 116\ \mathrm{GeV}/c^2)$ events and the cross-section for UPMX pair. (Note : Quote NNLO cross-section ($\sigma = 251.3 \pm 5$ pb) to estimate the significance for cross-section.)

Data Set	Observed (O)	Expected (E)	Significance for # of events	(E−O)/O	Cross-Secion (pb)	Significance for Cross-Section
0d	612	609.5 ± 42.1	−0.051	−0.004	255.3 ± 20.4	0.190
0h	821	822.1 ± 62.5	0.016	0.001	253.7 ± 21.2	0.112
0i	1214	1292.3 ± 112.6	0.664	0.064	238.8 ± 21.9	−0.554
0j	1722	1955.7 ± 140.8	1.592	0.136	223.8 ± 17.0	−1.550
0k	843	950.6 ± 80.8	1.252	0.128	225.4 ± 20.7	−1.215
Overall	5212	5630.1 ± 211.5	1.871	0.080	238.0 ± 8.9	−1.300

Table 4.8: The number of $Z/\gamma^*(66 < M_{\ell\ell} < 116$ GeV/$c^2)$ events and the cross-section for MXUP pair. (Note : Quote NNLO cross-section ($\sigma = 251.3 \pm 5$ pb) to estimate the significance for cross-section.)

Data Set	Observed (O)	Expected (E)	Significance for # of events	(E−O)/O	Cross-Secion (pb)	Significance for Cross-Section
0d	398	383.7 ± 26.5	−0.432	−0.036	263.8 ± 22.5	0.540
0h	607	587.3 ± 41.2	−0.410	−0.032	262.6 ± 21.3	0.516
0i	997	927.5 ± 88.1	−0.743	−0.070	273.3 ± 27.3	0.791
0j	1382	1438.8 ± 101.4	0.527	0.041	244.2 ± 18.4	−0.374
0k	694	697.7 ± 51.8	0.064	0.005	252.9 ± 21.1	0.072
Overall	4078	4035.1 ± 152.0	−0.260	−0.011	257.0 ± 9.7	0.526

Table 4.9: The number of $Z/\gamma^*(66 < M_{\ell\ell} < 116$ GeV/$c^2)$ events and the cross-section for MXMX pair. (Note : Quote NNLO cross-section ($\sigma = 251.3 \pm 5$ pb) to estimate the significance for cross-section.)

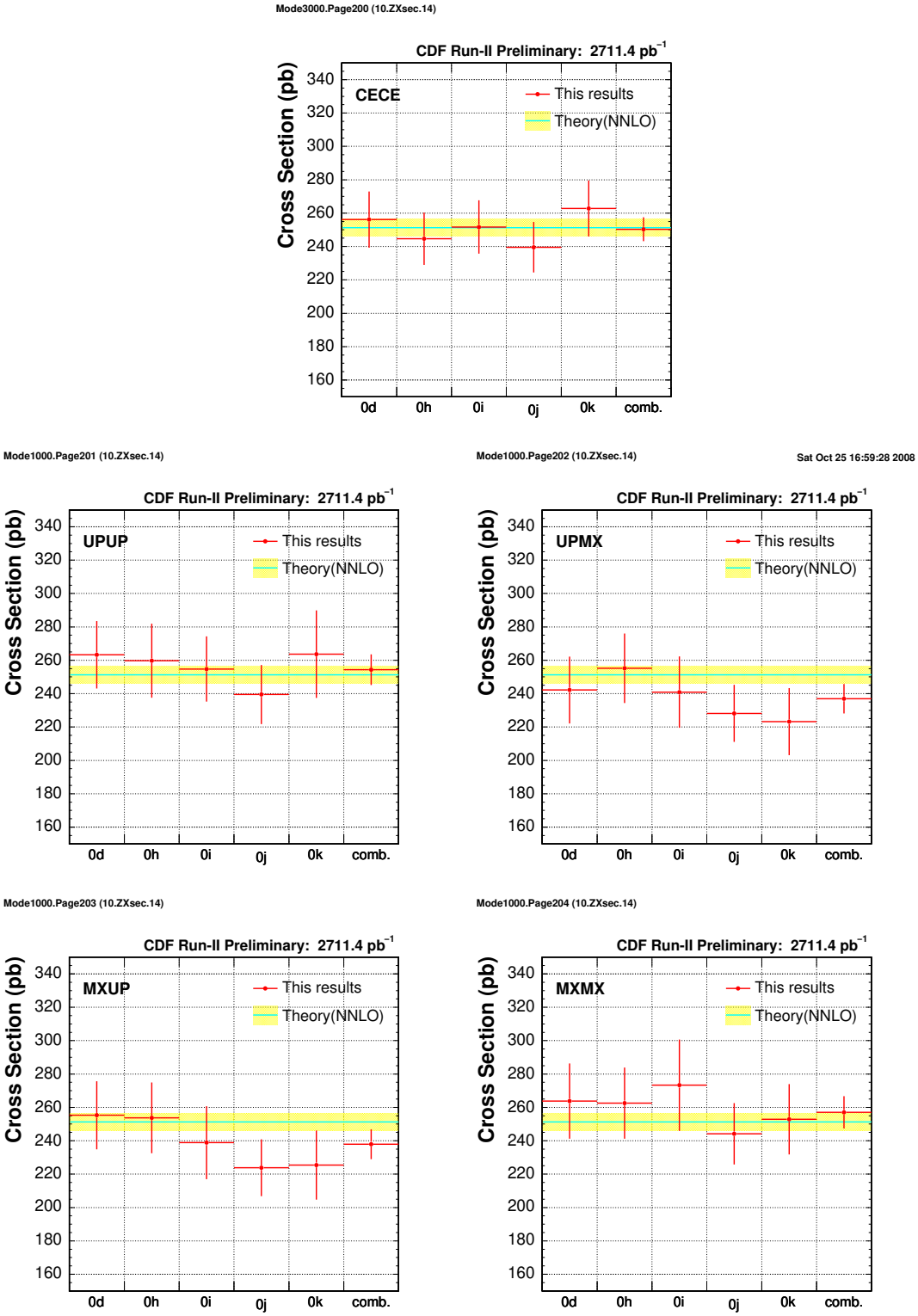

Figure 4.40: $Z/\gamma^* \to \ell^+\ell^-$ Cross Section for each dilepton type to validate the trigger efficiency and scale factors.

4.4 Expected Backgrounds

We show expected number of events passing our events selection cuts. We look into consistency between the data and background expectations by using a 2 dimensional plane (p_{T12} VS. p_{T2}), we divide the plane to 4 regions. The region definition is

- Region 1 : Dilepton system $p_T < 15$ GeV/c and 2nd lepton $p_T \geq 20$ GeV/c,
- Region 2 : Dilepton system $p_T < 15$ GeV/c and 2nd lepton $p_T < 20$ GeV/c,
- Region 3 : Dilepton system $p_T \geq 15$ GeV/c and 2nd lepton $p_T < 20$ GeV/c,
- Region 4 : Dilepton system $p_T \geq 15$ GeV/c and 2nd lepton $p_T \geq 20$ GeV/c.

The region 4 is most sensitive region for higgs (Wh) events comparing with other 3 regions, but unfortunately, also sensitive to WZ events due to the similar kinematics between Wh and WZ events in the final state. The observed and expected background events in region by region are shown in Table 4.10. There are no significant discrepancies between the data and the background expectations for each region. The total observed events are 172 events, while the background expectation are 188.3 events, the dominantly background component is fake lepton with 89.8%, and the residual photon-conversion with 8.3%.

	Regions				
	1	2	3	4	Total
Fakes	0.76	36.29	130.35	1.64	169.03
Photon-conversions	0.79	0.28	13.52	1.01	15.60
Total	1.54±0.65	36.57±6.15	143.87±16.70	2.65±1.26	184.62±24.25
(Stat.)	±0.29	±1.98	±4.16	±0.35	±4.65
(Syst.)	±0.59	±5.82	±16.18	±1.21	±23.80
$W \to e\nu$	0.000	0.000	0.000	0.000	0.000
$Z/\gamma^* \to ee$	0.000	0.000	0.000	0.000	0.000
$W \to \mu\nu$	0.000	0.000	0.000	0.000	0.000
$Z/\gamma^* \to \mu\mu$	0.000	0.000	0.000	0.000	0.000
$Z/\gamma^* \to \tau\tau$	0.000	0.000	0.000	0.000	0.000
$t\bar{t}$	0.000	0.000	0.000	0.000	0.000
WW	0.000	0.000	0.000	0.000	0.000
WZ	0.145	0.058	1.277	1.755	3.234
ZZ	0.025	0.019	0.313	0.283	0.641
Total MC	0.170±0.013	0.077±0.008	1.591±0.108	2.038±0.130	3.875±0.250
(Stat.)	±0.007	±0.005	±0.023	±0.024	±0.035
(Syst.)	±0.003	±0.003	±0.045	±0.037	±0.084
(Luminosity)	±0.010	±0.005	±0.095	±0.122	±0.223
Total expected	1.7±0.7	36.6±6.2	145.4±16.7	4.7±1.3	188.5±24.3
Data	3	26	137	6	172

Table 4.10: Background expectation and observed number of events for the like-sign dilepton events.

Chapter 5

Search for the Higgs Boson

This section describes the sensitivity for higgs search using LS-dilepton events. The higgs search is very challenging search due to low production cross section for higgs for instance $\sigma(p\bar{p}\rightarrow Wh) = 0.053$ pb for 160 GeV/c^2 higgs, while even so WZ production is $\sigma(p\bar{p}\rightarrow WZ) = 3.96$ pb. In order to gain the higgs search sensitivity, the multivariate analysis technique is employed. The technique can suppress background events, while keeping high signal detection efficiency. This search employs "Boosted Decision Trees" technique which is one of multivariate analyses to gain the higgs search sensitivity.

5.1 Detection Efficiency and Event Yield for Higgs

The detection efficiency and event yield after passing LS-dilepton selection are estimated by using higgs MCs which are generated by PYTHIA assuming higgs mass between from 110 to 200 GeV/c^2 in 10 GeV/c^2 steps, due to Standard Model does not tell us the higgs mass, but predicts the existence and other properties. The properties and the number of generated events for each higgs mass to be used in the higgs event estimation is shown in Table 5.1. The expected event yield for $Wh\rightarrow$LS-dilepton events are calculated by,

$$N_h = \varepsilon(Wh\rightarrow\ell^\pm\ell^\pm) \cdot L \cdot \sigma(p\bar{p}\rightarrow Wh) \cdot B_F(h\rightarrow WW) \tag{5.1}$$

where $\varepsilon(Wh\rightarrow\ell^\pm\ell^\pm)$ is the detection efficiency for $Wh\rightarrow\ell^\pm\ell^\pm$ that the denominator is $Wh\rightarrow WWW\rightarrow$LS-dilepton event, L is the integrated luminosity, $\sigma(p\bar{p}\rightarrow WH)$ means the production cross section, and $B_F(h\rightarrow WW)$ is the branching fraction. The detection efficiency is 2.16% for 110 GeV/c^2 higgs and 2.39% for 160 GeV/c^2 higgs. The expected event yield for 110 GeV/c^2 fermiophobic higgs is 1.32 events assuming the SM production cross section, and for 160 GeV/c^2 SM higgs is 0.38 events. The estimated values are taken into account relevant scale factors as described in §4.3. Table 5.2 shows the detection efficiency and the expected event yield for each higgs mass.

Mass (GeV/c^2)	$\sigma(p\bar{p}\to Wh)$ (fb)	$B_F(h_{\mathrm{FH}}\to WW)$	$B_F(h_{\mathrm{SM}}\to WW)$	Generated (Events)
110	216.0	0.87	0.04	4198567
120	159.0	0.88	0.12	4198567
130	119.0	0.88	0.27	4198567
140	90.2	0.89	0.47	4198567
150	68.9	0.90	0.68	4198567
160	53.1	0.97	0.92	4198567
170	41.3	0.98	0.97	4198567
180	32.4	0.94	0.94	4198567
190	25.5	0.94	0.94	4198567
200	20.3	0.94	0.94	4198567

Table 5.1: Higgs Monte Carlo samples. h_{FH} means fermiophobic higgs, while h_{SM} means Standard Model higgs.

Higgs Mass (GeV/c^2)	Efficiency (%)	Expected Events (Fermiophobic higgs)	Expected Events (SM higgs)
110	2.16 ± 0.08	1.318 ± 0.024	0.061 ± 0.001
120	2.27 ± 0.09	1.033 ± 0.018	0.141 ± 0.003
130	2.37 ± 0.09	0.808 ± 0.014	0.248 ± 0.004
140	2.48 ± 0.09	0.648 ± 0.011	0.342 ± 0.006
150	2.50 ± 0.09	0.504 ± 0.008	0.381 ± 0.006
160	2.39 ± 0.08	0.400 ± 0.006	0.380 ± 0.007
170	2.45 ± 0.08	0.323 ± 0.005	0.320 ± 0.005
180	2.57 ± 0.09	0.255 ± 0.004	0.255 ± 0.004
190	2.78 ± 0.09	0.217 ± 0.003	0.217 ± 0.003
200	2.91 ± 0.10	0.180 ± 0.003	0.180 ± 0.003

Table 5.2: Detection efficiency and expected event yeild for higgs passing LS-dilepton selection. MC statistic and MC scale factor uncertainty are included.

5.2 Boosted Decision Trees Discriminant

The background expectation is 188.3 events passing LS-dilepton selections. The S/B (ratio for signal and background) is 1.32/188.3 for fermiophobic higgs at 110 GeV/c^2. The search for smaller signal in larger data (background) such as this higgs search has become essential to use the available information from the data as possible to get more search sensitivity. The multivariate data analysis can extract the maximum of the information. In this search, "Boosted Decision Trees" (BDT) technique which is one of the multivariate data analyses is employed [53, 54]. Decision trees is a binary

tree structured classifier such as Figure 5.1. "S" means signal, "B" means background, terminal nodes are called "leaves". The naming for S or B is depending on the majority of events in the each node. The tree structure is built up by repeatedly splitting the given events to regions that are eventually classified as signal or background. A shortcoming of decision trees has instability for classifier response due to statistical fluctuation in the samples, derives the tree, called training samples, for example if two input variables such E_T and p_T exhibit similar separation power, the variables are handled as almost like one variables. In such a case the whole tree structure is altered below this node. This problem is overcame by "Boosting" algorithm. The Boosting constructs a forest of decision tree with modifies weights in event by event, as a result increases the statistical stability for the classifier and also improves the separation performance comparing with a single decision tree.

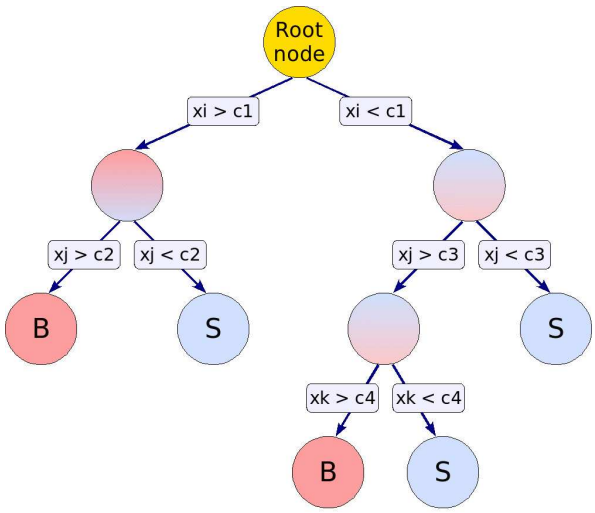

Figure 5.1: Schematic view of a decision tree.

5.2.1 Decision Trees

The Decision Trees are built up under the splitting criteria for each node. The splitting procedure is repeated until the whole tree is built. The split is determined by finding the variable and corresponding cut value that provides the best separation between signal and background. The node splitting is stopped at time that node is reached the required minimum number of events. The leaf nodes are classified as signal or background according to the majority of events in the node. The employed splitting criterion is "Gini-Index" to build the decision trees in this thesis. The Gini-Index is defined as

$$i_{\mathrm{G}} = p(1-p), \tag{5.2}$$

p is purity in a node defined as follows,

$$p = \frac{\sum_s W_s}{\sum_s W_s + \sum_b W_b} \tag{5.3}$$

where $\sum_s$ is the sum over signal events and $\sum_b$ is the sum over background events in a node, assuming the events are weighted with each events having W_i, so $p(1-p)$ is 0 if the samples is pure signal or pure background. The criterion is to maximize

$$i_{\mathrm{G}}(\text{parent}) - i_{\mathrm{G}}(\text{left-child}) - i_{\mathrm{G}}(\text{right-child}), \tag{5.4}$$

where i_G(parent) means Gini index of a node before splitting (parent node), and i_G(left-child, or right-child) means Gini index of a node after splitting from parent node.

The maximum constructed decision tree has some statistically insignificant nodes which leads to reduce the separation performance (overtrainig). Some "pruning" methods are used to avoid the overtrainig as possible. "Cost-complexity pruning" is used to perform the maximum separation. The cost-complexity in a tree T starting at node t is expressed by

$$R_\alpha(T_t) = R(T_t) + \alpha \cdot N(T_t) \tag{5.5}$$

where, $R(T_t)$ is the total error cost in the tree T, the error cost in each terminal node is given by multiplying the $1 - max(p, 1-p)$ by the proportion of data, α is the cost complexity parameter, and $N(T_t)$ is the number of terminal nodes in the tree T, while the cost-complexity at node t is

$$R_\alpha(t) = R(t) + \alpha. \tag{5.6}$$

As long as $R_\alpha(t) > R_\alpha(T_t)$ the tree T has a smaller cost-complexity than the single node t, in other words, it is worth to keep this node expanded. The inequality also expressed as the follows,

$$\alpha < \frac{R(t) - R(T_t)}{N(T_t) - 1}. \tag{5.7}$$

The node t with the α in the tree T is recursively pruned away as long as violating (5.7). Overtraing is managed by using the pruning method.

5.2.2 Boosting Algorithm

As described before, A single decision tree has instability for classifier response due to statistical fluctuation in the samples. In this thesis, "Adaboost" algorithm are used to overcome the problem, which is one of the some boosting algorithms. In general, the training events which were misclassified have their weights increased i.e. boosted, and new tree is formed. This procedure is then repeated for the new tree, as results many trees are built up. The score from the mth individual tree T_m is taken as +1 if the

events falls on a signal leaf and -1 if the event falls on a background leaf. The final score is taken as a weighted sum of the scores of the individual leaves. This section mentions in the boosting algorithm for "Adaboost".

Suppose that there are N events in the samples. The events are assigned the weight $1/N$ at first. Some notations are defined as the follows,

- x_i is the set of information (for example p_T or E_T) for the ith event
- $y_i = 1$ if the ith event is a signal event and $y_i = -1$ if the ith event is a background event
- w_i is the weight of the ith event
- $T_m(x_i) = 1$ if the set of information for the ith event lands that event on a signal leaf and $T_m(x_i) = -1$ if the set of information for that event lands it on a background leaf.
- $I(y_i \neq T_m(x_i)) = 1$ and $I(y_i = T_m(x_i)) = 0$

where m is index for Mth tree. Using the above notations, define the misclassification rate error,

$$err_m = \frac{\sum_{i=1}^{N} w_i I(y_i \neq T_m(x_i))}{\sum_{i=1}^{N} w_i} \tag{5.8}$$

The error is used to change the weight of each event

$$\alpha_m = \beta \times \ln\left(\frac{1 - err_m}{err_m}\right) \tag{5.9}$$

$$w_i \rightarrow w_i \times e^{\alpha_m I(y_i \neq T_m(x_i))}. \tag{5.10}$$

where $\beta = 1$ is the standard AdaBoost method. The changed weights are normalized to

$$w_i \rightarrow \frac{w_i}{\sum_{i=1}^{N} w_i}. \tag{5.11}$$

The score for a given event is

$$T(x) = \sum_{m=1}^{M} \alpha_m T_m(x) \tag{5.12}$$

which is the weighted sum of the scores of the individual trees. The boosting algorithm remedies the statistical fluctuation in the samples and improves the separation performance between signal and background. The BDT framework is implemented in TMVA package integrated in ROOT framework [55, 56], which is used in this search.

5.2.3 BDT Training Samples

From background estimation in §4, there are two main background events for like-sign dilepton events. One background event is residual-photon conversions event, which is electron originated from photon conversion with unobserved partner track. The other main background is fake leptons event. The components of the fake-lepton are interactive $\pi^{\pm}$, overlap of π^0 and a track, punch-through hadrons, and non-prompt leptons. The BDT discriminant is optimized to well separate between the higgs and the two main background, so-called "training". The signal training samples are higgs MC samples as shown in Table 5.1, while background samples are residual-photon conversion events, and fake lepton events, which are derived from data samples. The training are performed by using each higgs mass sample with the main backgrounds, independently. These samples are passing LS-dilepton selection criteria.

5.2.4 BDT Input Variables

The BDT is insensitive to including input variables with low separation powers, because the pruning procedure remove the spitting nodes under such variables, while the other multivariate techniques have to carefully select the input variables and deal with it, for example Artificial Neural Network. If a strongly correlated variables is selected as input variable, the performance should not be always good. We have selected 8 kinematics to be used the input variables to construct BDT discriminant.

- 1st lepton $p_T(p_{T1})$
- 2nd lepton $p_T(p_{T2})$
- Dilepton system $p_T(p_{T12})$
- Missing E_T
- Dilepton mass
- MetSpec : $\not\!\!E_T$ if $\Delta\phi(\not\!\!E_T, \ell \text{ or jet}) > \pi/2$ or
  . : $\not\!\!E_T \sin(\Delta\phi(\not\!\!E_T, \ell \text{ or jet}))$ if $\Delta\phi(\not\!\!E_T, \ell \text{ or jet}) < \pi/2$
- H_T (Sum of p_{T1}, p_{T2}, jets E_T ($E_T > 15$ GeV and $|\eta| < 2.0$), and Missing E_T)
- Number of Jets with $E_T > 15.0$ GeV

The normalized 8 input variables for LS-dilepton event are shown in Figure 5.2. The p_T relevant variables (p_{T2} and p_{T12}) well separate backgrounds from higgs, and H_T variable is growing the separation power as larger higgs mass. Figure 5.3 also show BDT input variables, but stacked histogram for expected background events and data.

5.2.5 BDT Optimization

The BDT in TMVA framework has some parameters to improve the sensitivity and to avoid overtraining. The "Prune-Strength" and "Number of trees" are used to optimize the BDT discriminant looking at reduced χ^2 for BDT output between the training and the test samples for both signal and background as shown in Figure 5.4. The reduced χ^2 is defined as multiplication with signal reduced χ^2 and background χ^2, so the value is best to be around 1 or less. Figure 5.5 show the reduced χ^2 in plane of Prune-Strength and Number of trees, and the projection plots using higgs mass 160 GeV/c^2 sample. We can see the reduced χ^2 is stable around from 20 Prune-Strength on any Number of trees, and the projection plot to Number of trees says 800 trees is minimum value. From this results, we set the values to 20.0 for Prune-Strength and 800 for Number of trees. We also performed this procedure for higgs mass samples 110 GeV/c^2 and 200 GeV/c^2. These samples also show similar values to 160 GeV/c^2 sample, so we decide to use the values got from 160 GeV/c^2 samples to other higgs mass samples training.

5.2.6 BDT Output and Cross Check

The BDT output is used to the discriminant between higgs and background. The trained BDT is validated by using three event samples which are OS dilepton, Low-MetSpec&High-Met event, and Zero-silicon event, before applying to LS-dilepton events. The OS dilepton events is passing lepton selection and dilepton selection but OS combination not LS combination, the event is used to check the validation for Monte Carlo based background expectation. The Low-MetSpec&High-Met events are defined as follows,

- OS dilepton passing lepton selection cuts
- Low-MetSpec : 15 < MetSpec < 50 GeV
- High-Met : $\not\!\!E_T$> 25 GeV
- Low Dilepton mass : 20 < $M_{\ell\ell}$ < 40 GeV/c^2

The sample events are fake-lepton rich (53%), to check the background estimation for fake leptons. The Zero-silicon hit events are defined as,

- LS dilepton passing lepton selection cuts, but
- The 1st lepton is not applied the silicon hit requirement
- The 2nd lepton is applied the zero-silicon hit requirement

The sample events are dominantly residual-photon conversion events (90%), to check the residual-photon conversion event expectation. There are no significant discrepancies between the data and the background expectations as shown in Table 5.3, 5.4, and 5.5, respectively, and the input variable also shows reasonable shapes shown in

Figure 5.6 for OS dilepton events, Figure 5.7 for Low-MetSpec&High-Met events, and Figure 5.8 for Zero-silicon hit events.

After looking background yield and the kinematic shape, The 3 samples are applied the trained BDT which is trained for LS-dilepton event. Figure 5.9, 5.10, and 5.11 show the BDT output in each 3 samples for 110 and 160 GeV/c^2 mass higgs. We can see reasonable agreement between the data distribution and expected events ones from these BDT outputs. From these results, we go to apply the trained BDT to LS dilepton events which is signal region in this search. Figure 5.12 shows the normalized BDT output for main backgrounds (Fake leptons and Residual photon-conversion) event and higgs event. The BDT well discriminate between background and higgs. Figure 5.13 shows the BDT output for LS dilepton events for 110 and 160 GeV/c^2 mass higgs.

	Regions				
	1	2	3	4	Total
Fakes	7.3	51.1	197.8	5.6	261.7
Photon-conversions	12.2	10.0	31.7	7.7	61.5
Total	19.5±4.8	61.1±9.8	229.4±26.8	13.3±4.0	323.2±44.7
(Stat.)	±1.2	±2.5	±5.3	±1.0	±6.1
(Syst.)	±4.7	±9.5	±26.2	±3.9	±44.3
$W \to e\nu$	0.0	0.0	0.0	0.0	0.0
$Z/\gamma^* \to ee$	2277.9	1723.4	1723.3	1183.6	6908.3
$W \to \mu\nu$	0.0	0.0	0.0	0.0	0.0
$Z/\gamma^* \to \mu\mu$	2855.0	1067.4	983.7	993.4	5899.4
$Z/\gamma^* \to \tau\tau$	247.7	419.7	482.0	72.8	1222.1
$t\bar{t}$	1.8	0.7	18.2	43.2	63.8
WW	8.4	2.9	39.9	64.4	115.6
WZ	0.4	0.2	2.8	3.8	7.2
ZZ	0.4	0.4	4.6	4.6	9.9
Total MC	5391.6±344.7	3214.6±253.8	3254.4±234.3	2365.7±149.6	14226.3±956.7
(Stat.)	±32.8	±25.3	±25.2	±21.5	±53.1
(Syst.)	±114.4	±163.0	±127.0	±42.0	±428.8
(Luminosity)	±323.5	±192.9	±195.3	±141.9	±853.6
Total expected	5411.0±344.7	3275.7±254.0	3483.8±235.8	2371.0±149.6	14549.5±957.7
Data	4648	2837	3795	2221	13501

Table 5.3: Background expectation and observed number of events for the opposite-sign dilepton events.

	Regions				
	1	2	3	4	Total
Fakes	0.00	0.11	40.85	0.23	41.20
Photon-conversions	0.00	0.00	3.48	0.00	3.47
Total	0.00±0.00	0.11±0.08	44.33±5.32	0.23±0.20	44.68±5.51
(Stat.)	±0.00	±0.08	±2.17	±0.08	±2.17
(Syst.)	±0.00	±0.02	±4.86	±0.18	±5.06
$W \to e\nu$	0.00	0.00	0.00	0.00	0.00
$Z/\gamma^* \to ee$	0.00	0.00	5.86	1.42	7.01
$W \to \mu\nu$	0.00	0.00	0.00	0.00	0.00
$Z/\gamma^* \to \mu\mu$	0.00	0.00	3.98	1.83	5.82
$Z/\gamma^* \to \tau\tau$	0.12	0.12	5.81	0.53	6.56
$t\bar{t}$	0.00	0.09	2.29	2.33	4.71
WW	0.00	0.08	9.03	2.42	11.53
WZ	0.00	0.01	0.42	0.10	0.52
ZZ	0.00	0.01	0.43	0.08	0.51
Total MC	0.12 ±0.12	0.30±0.12	27.82±2.60	8.42±1.01	36.66±3.17
(Stat.)	±0.12	±0.12	±1.70	±0.84	±1.91
(Syst.)	±0.01	±0.01	±1.03	±0.22	±1.24
(Luminosity)	±0.01	±0.02	±1.67	±0.51	±2.20
Total expected	0.12±0.12	0.42±0.15	72.15±5.92	8.66±1.02	81.34±6.36
Data	0	0	69	9	78

Table 5.4: Background expectation and observed number of event for Low-MetSpec & high-Met in low dilepton mass.

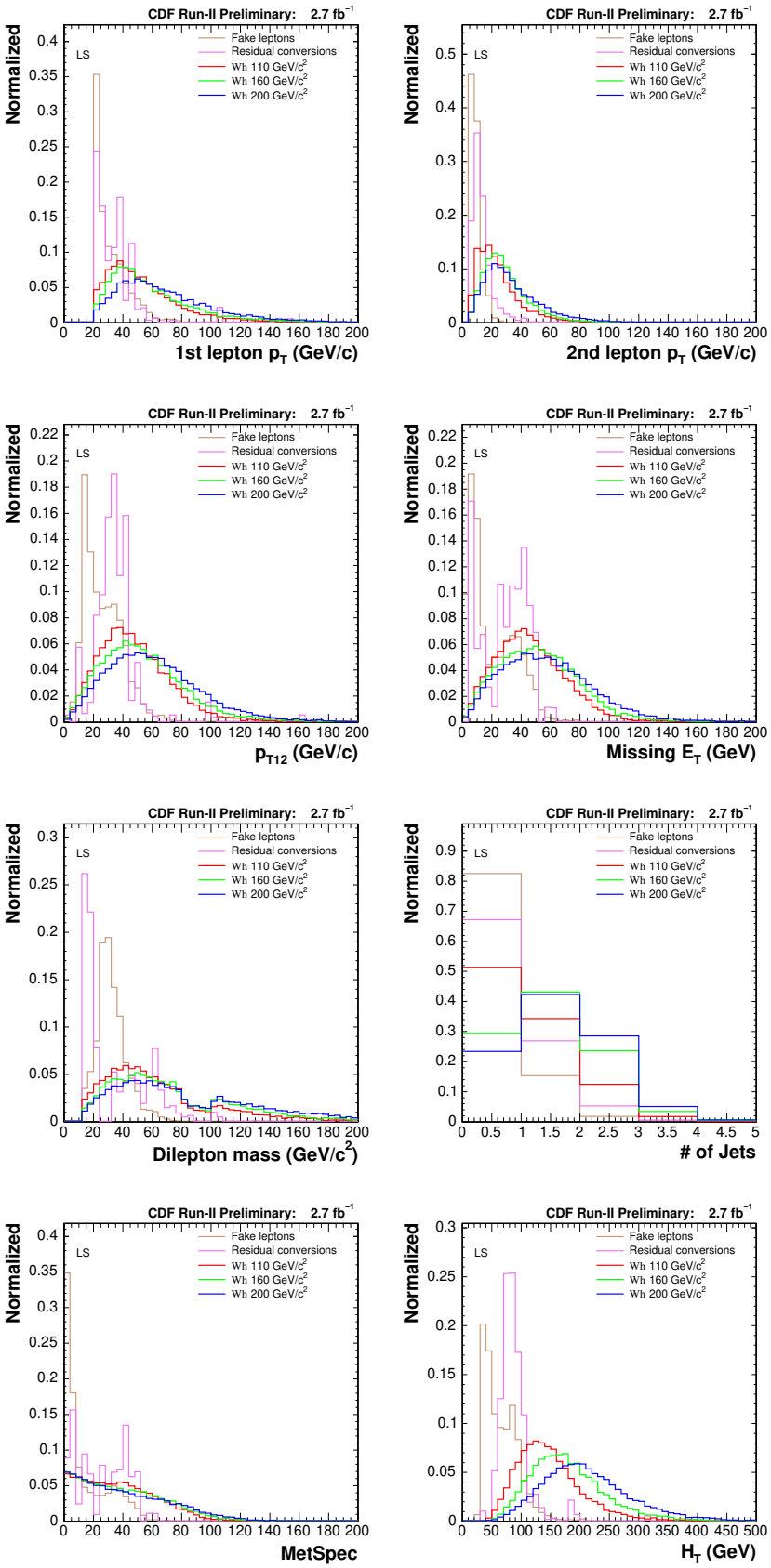

Figure 5.2: BDT input variables for like-sign dilepton (1st lepton $p_T(p_{T1})$, 2nd lepton $p_T(p_{T2})$, dilepton system $p_T(p_{T12})$, Missing E_T, Dilepton mass, number of jets, MetSpec, and H_T).

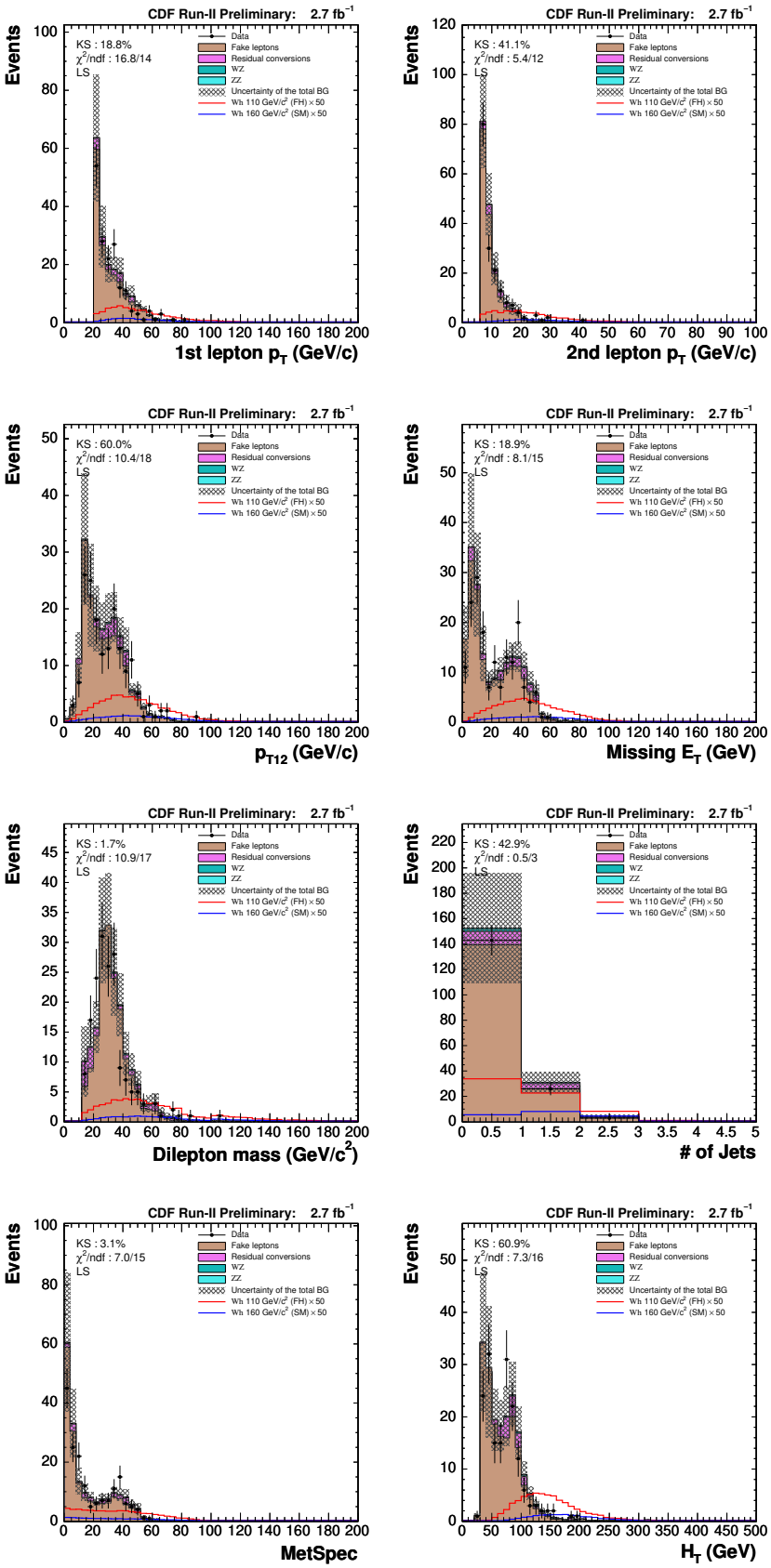

Figure 5.3: BDT input variables for like-sign dilepton (1st lepton $p_T(p_{T1})$, 2nd lepton $p_T(p_{T2})$, dilepton system $p_T(p_{T12})$, and Missing E_T, Dilepton mass, number of jets, MetSpec, and H_T).

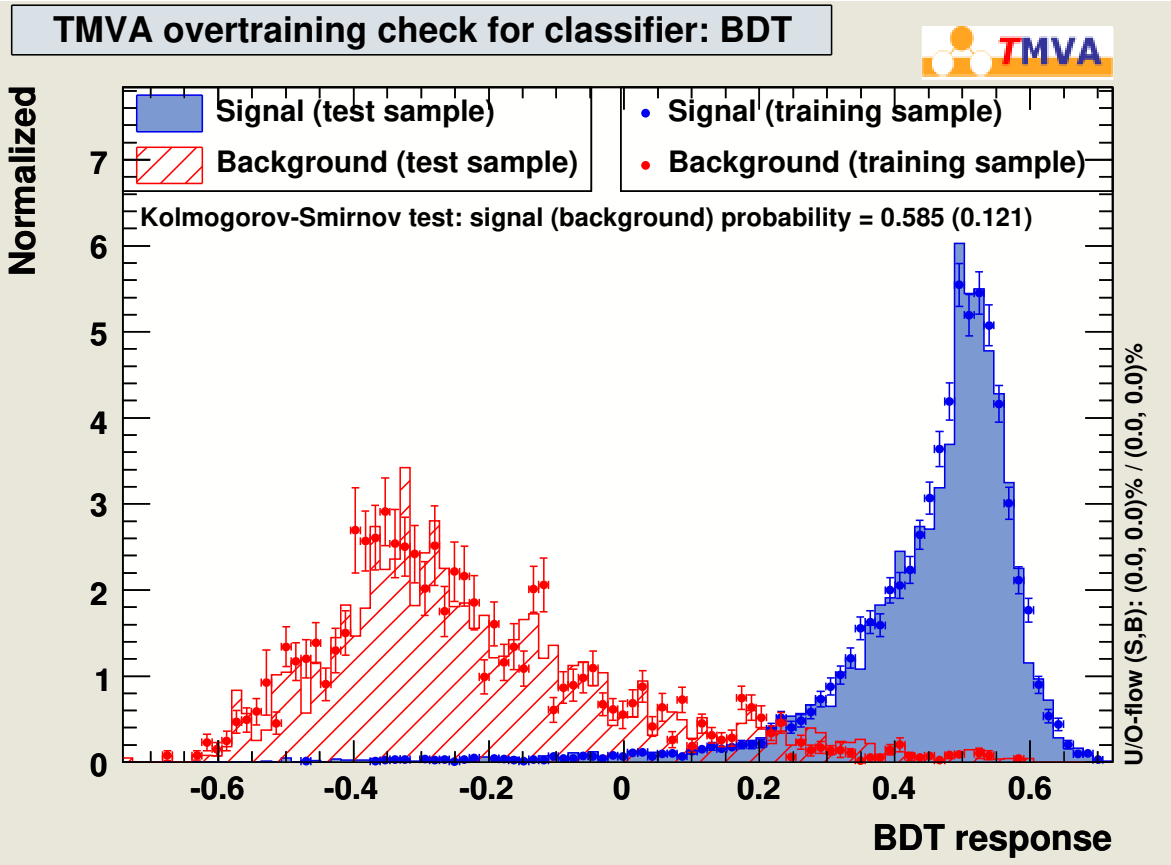

Figure 5.4: Expample of BDT output for training and test sample.

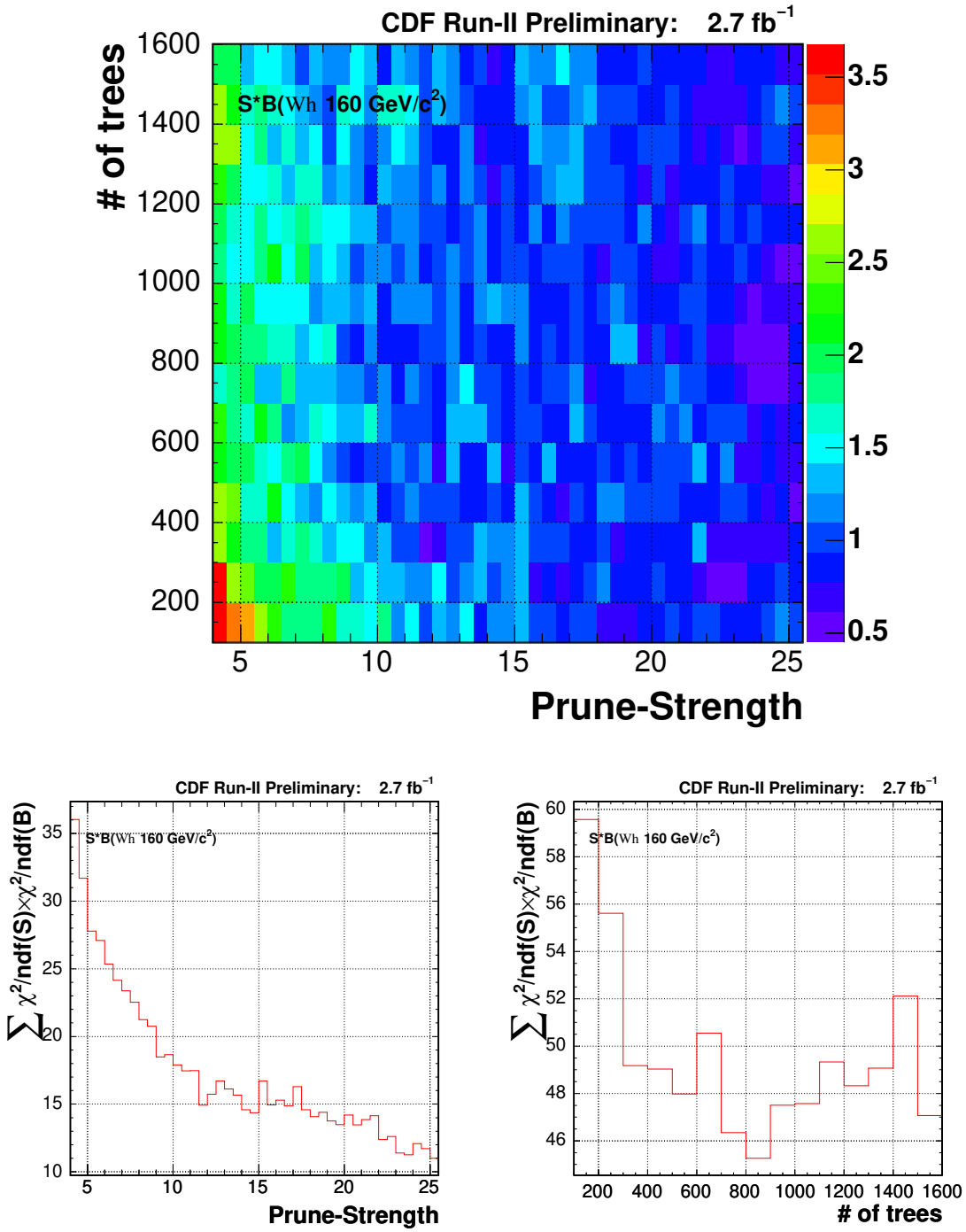

Figure 5.5: Reduced χ^2 test between training and test sample for signal and background (upper plot), and the projection plots to Prune-Strength and Number of trees (the lower left plot to Prune-Strength, lower right plot to Number of trees).

	Regions				
	1	2	3	4	Total
Fakes	0.03	1.29	4.77	0.03	6.12
Photon-conversions	1.60	3.32	27.23	3.79	35.94
Total	1.63±0.39	4.62±1.00	32.0±3.56	3.82±0.63	42.06±3.88
(Stat.)	±0.37	±0.96	±3.06	±0.59	±3.31
(Syst.)	±0.10	±0.27	±1.82	±0.22	±2.02
$W \to e\nu$	0.00	0.00	0.00	0.00	0.00
$Z/\gamma^* \to ee$	0.00	0.00	0.00	0.00	0.00
$W \to \mu\nu$	0.00	0.00	0.00	0.00	0.00
$Z/\gamma^* \to \mu\mu$	0.00	0.00	0.00	0.00	0.00
$Z/\gamma^* \to \tau\tau$	0.00	0.00	0.00	0.00	0.00
$t\bar{t}$	0.00	0.00	0.00	0.00	0.00
WW	0.00	0.00	0.00	0.00	0.00
WZ	0.00	0.00	0.00	0.00	0.00
ZZ	0.00	0.00	0.00	0.00	0.00
Total MC	0.00 ±0.00	0.00±0.00	0.00±0.00	0.00±0.00	0.00±0.00
(Stat.)	±0.00	±0.00	±0.00	±0.00	±0.00
(Syst.)	±0.00	±0.00	±0.00	±0.00	±0.00
(Luminosity)	±0.00	±0.00	±0.00	±0.00	±0.00
Total expected	1.63±0.39	4.62±1.00	32.00±3.56	3.82±0.63	42.06±3.88
Data	1	3	26	10	40

Table 5.5: Background expectation and observed number of event for Zero-silicon hit events.

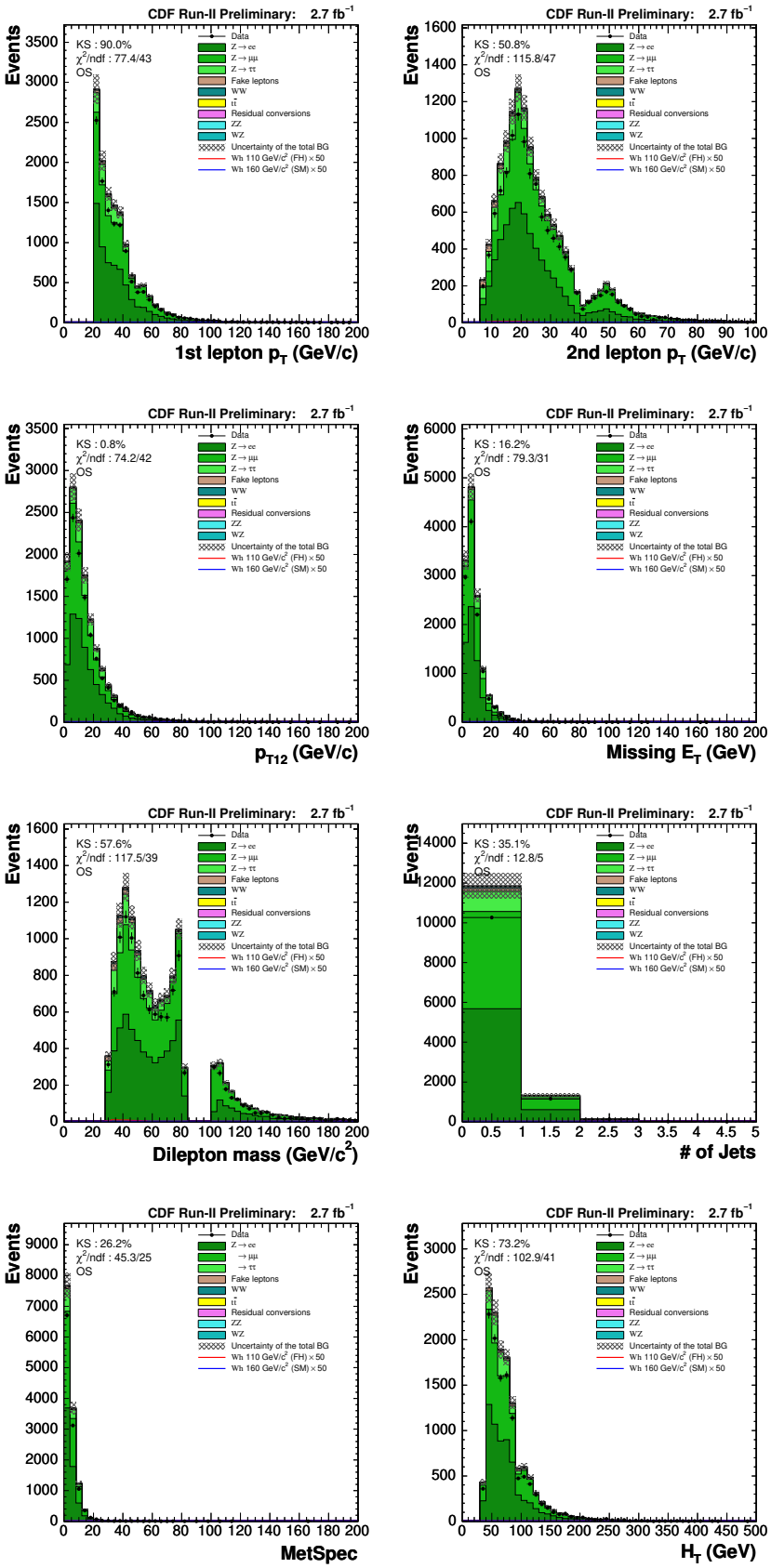

Figure 5.6: BDT input variables for opposite-sign dilepton (1st lepton $p_T(p_{T1})$, 2nd lepton $p_T(p_{T2})$, dilepton system $p_T(p_{T12})$, Missing E_T, Dilepton mass, number of jets, MetSpec, and H_T).

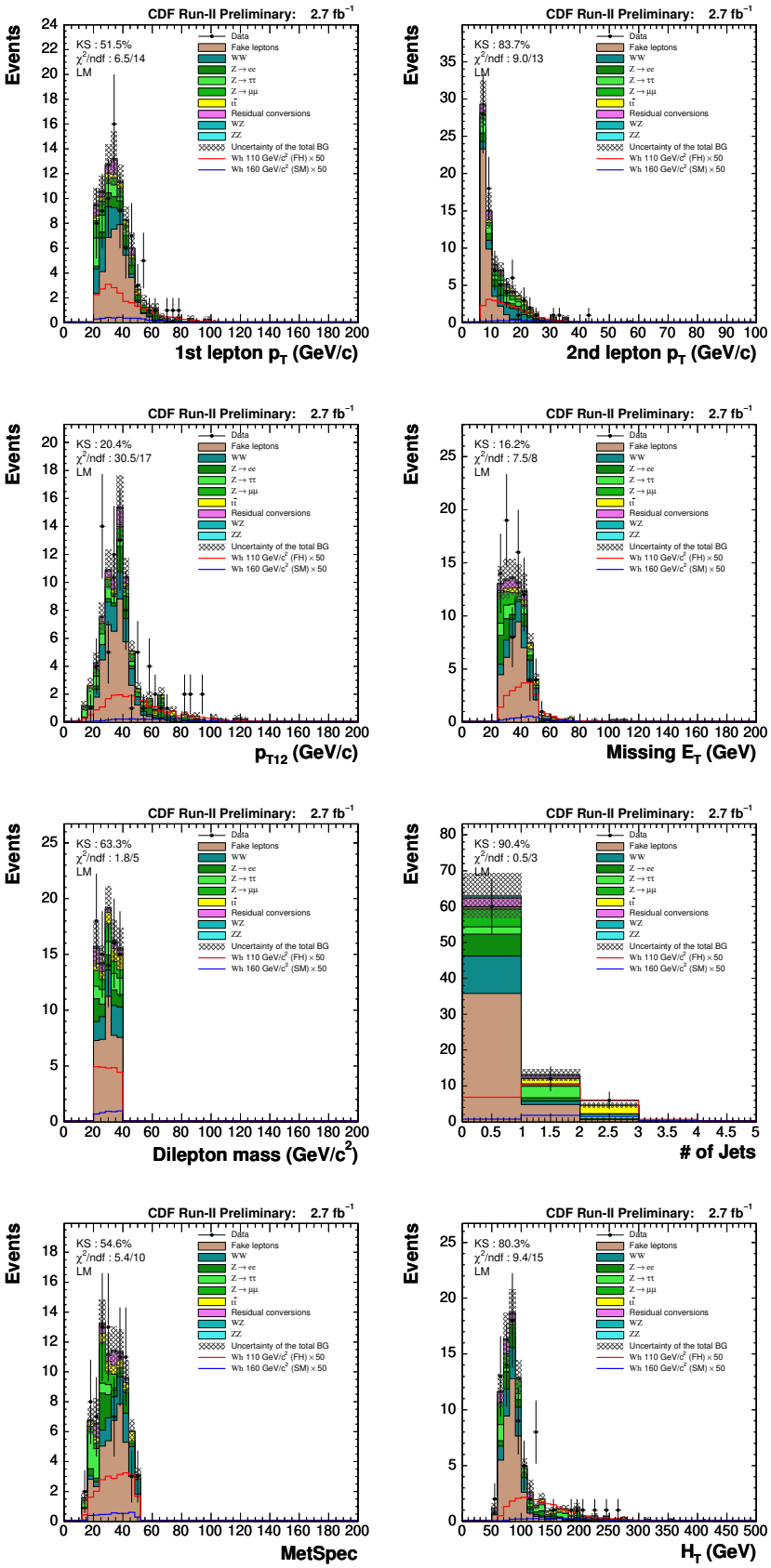

Figure 5.7: BDT input variables for LowMetSpec&HighMet event (1st lepton $p_T(p_{T1})$, 2nd lepton $p_T(p_{T2})$, dilepton system $p_T(p_{T12})$, Missing E_T, Dilepton mass, number of jets, MetSpec, and H_T).

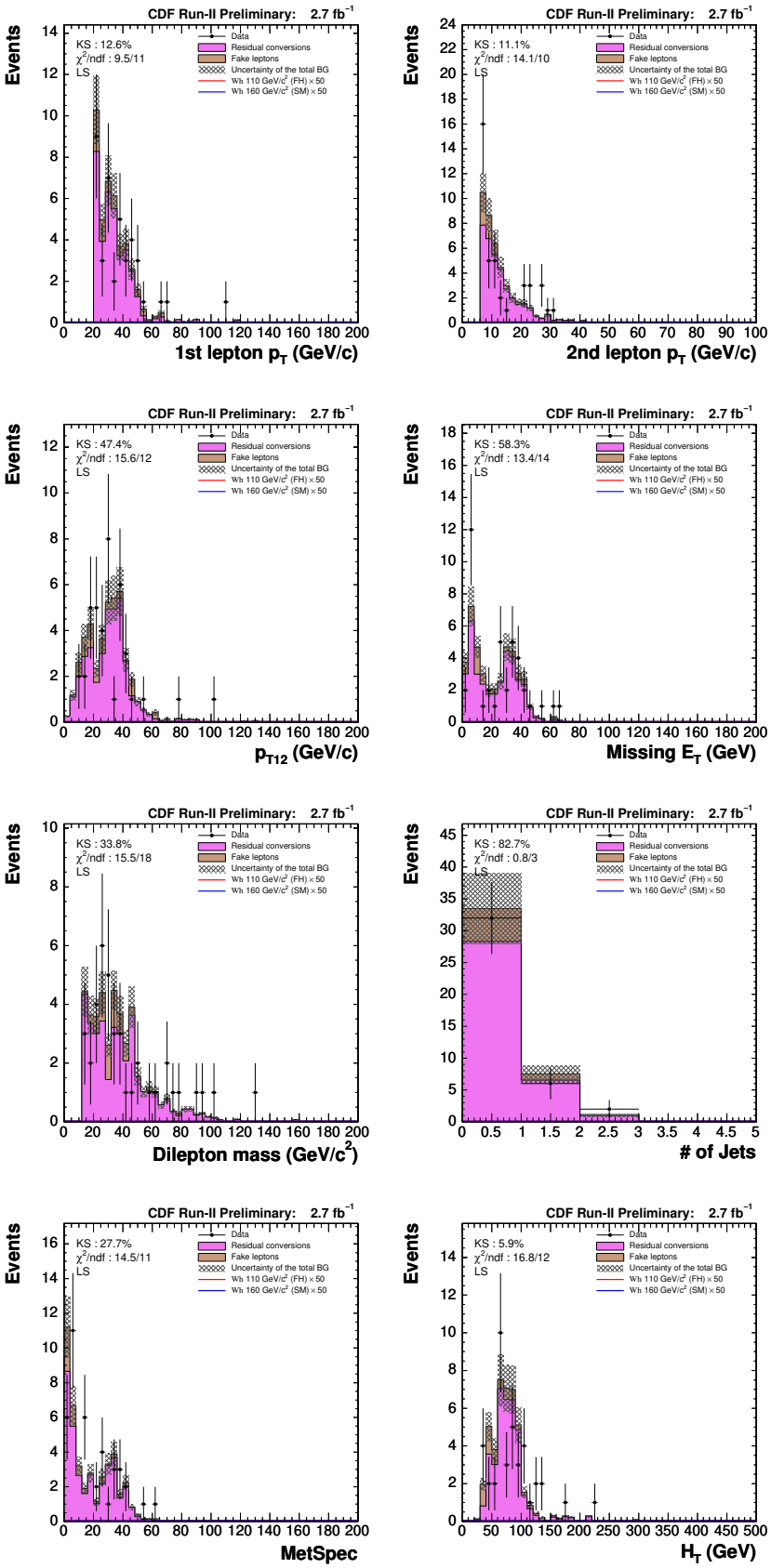

Figure 5.8: BDT input variables for Zero-silicon hit event (1st lepton $p_T(p_{T1})$, 2nd lepton $p_T(p_{T2})$, dilepton system $p_T(p_{T12})$, Missing E_T, Dilepton mass, number of jets, MetSpec, and H_T).

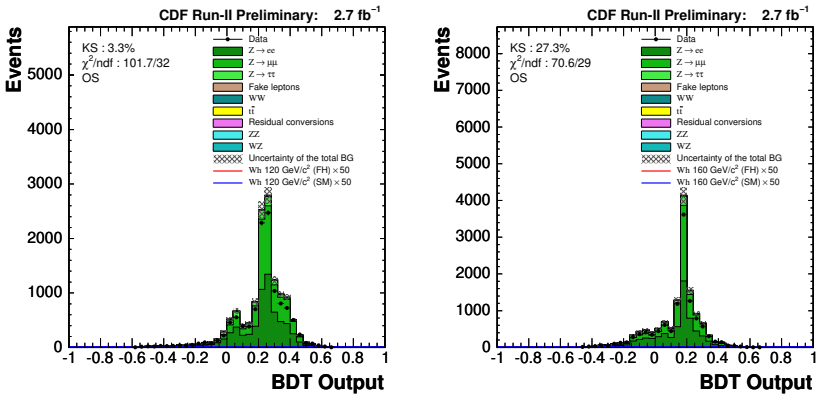

Figure 5.9: BDT output for opposite-sign dilepton (M_h : 110 and 160 GeV/c^2).

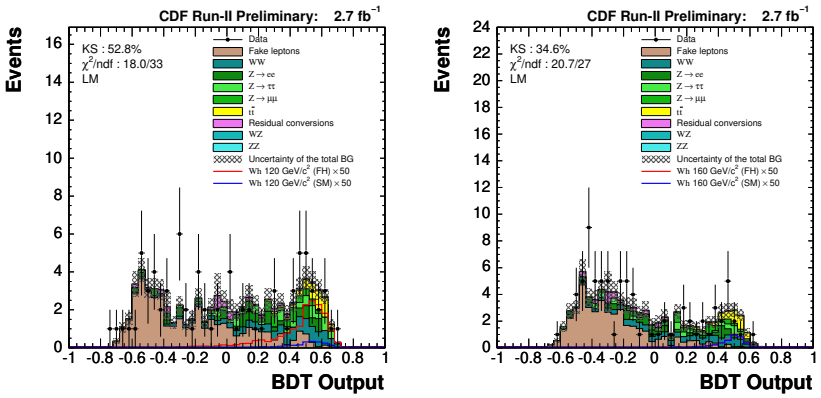

Figure 5.10: BDT output for LowMetSpec&HighMet event (M_h : 110 and 160 GeV/c^2).

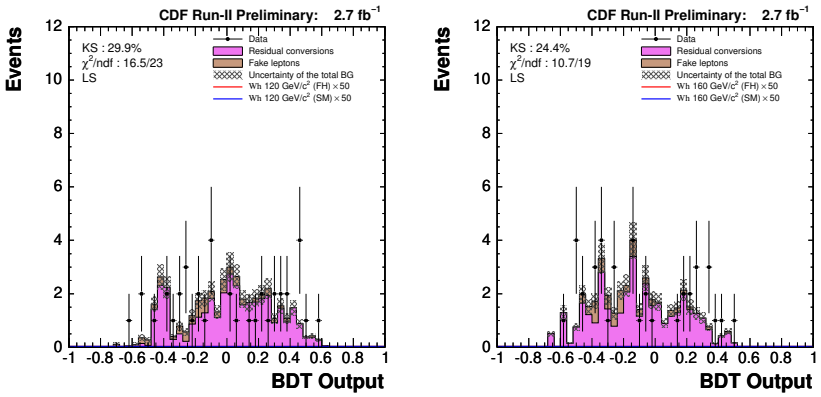

Figure 5.11: BDT output for Zero-silicon hit event (M_h : 110 and 160 GeV/c^2).

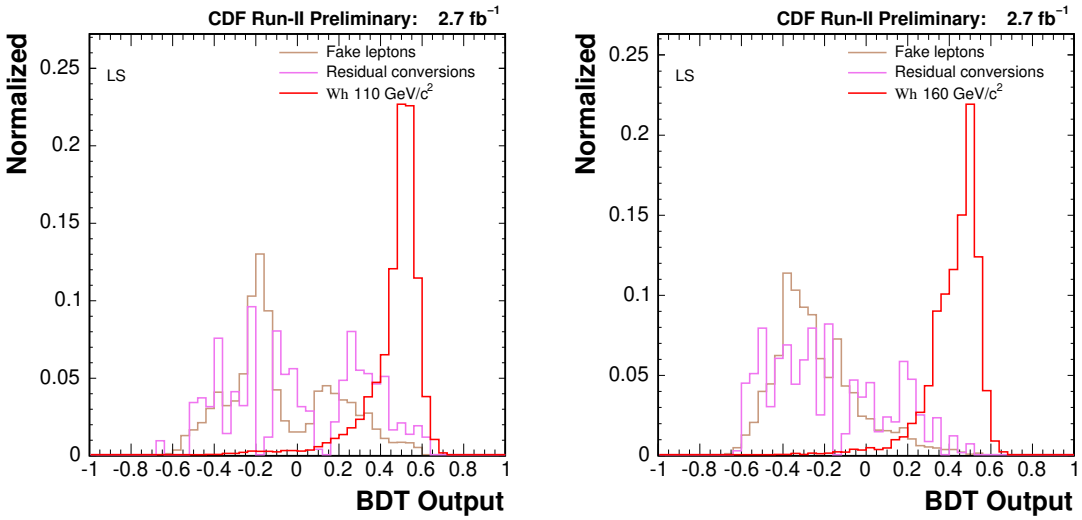

Figure 5.12: Normalized BDT output for like-sign dilepton (M_h : 110 and 160 GeV/c^2).

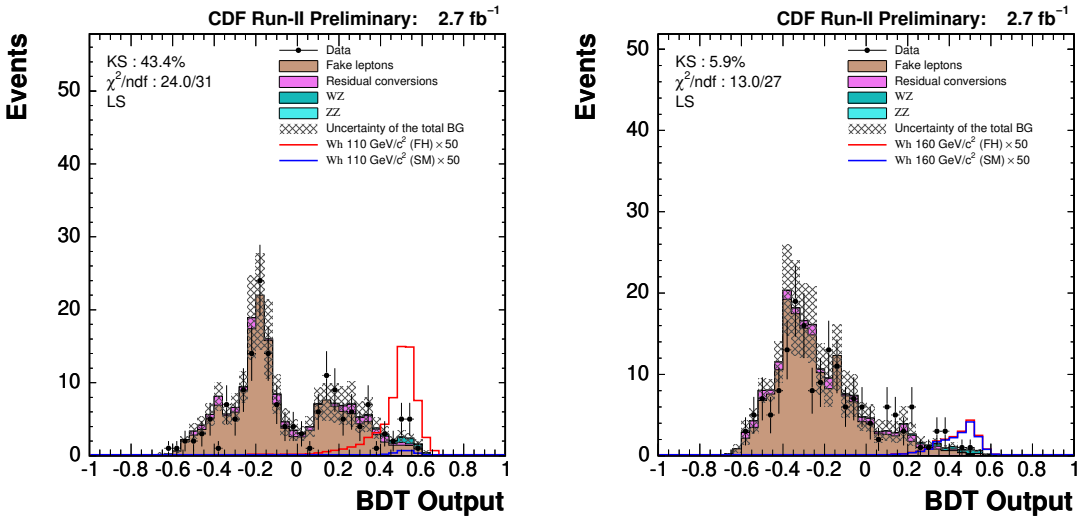

Figure 5.13: BDT output for like-sign dilepton (M_h : 110 and 160 GeV/c^2).

Chapter 6

Systematic Uncertainty

There are the systematic uncertainties arise from several sources in any study. The systematic uncertainties are classified to two types ones in this search. One is "Rate systematic uncertainty" which affects the event yield and acceptance, the other is "Shape systematic uncertainty" which changes the shape to the relevant kinematics. The both systematic strongly affects the search sensitivity, for example if larger systematic gains cross section upper limits, and give us poor observation chance for higgs. In this chapter, the several systematic uncertainties are shown in.

6.1 Rate Systematic Uncertainty

The rate systematic uncertainties affect the event yield (acceptance). The systematic uncertainties are taken into account for both signal and background for several systematic sources.

- Monte Carlo scale factors:
  The scale factor is to scale the MC based acceptance to realistic one by applying trigger efficiency and lepton identification efficiency scale factors, the systematic only affects MC based expectation, in this case, higgs, WZ, and ZZ event.

- Parton Distribution Function (PDF):
  Parton momentum in hadron is described by the PDF which is derived by theoretical calculations and measured by several experiments. Monte Carlo simulations use CTEQ5L as default PDF set in CDF. The PDF uncertainty are estimated by calculating acceptance using other PDF set with taking into account the difference of them. The other PDF are 2 CTEQ6Ls changing α_s value, 2 MRST set changing α_s and not, and 40 CTEQ6Ms changing eigenvector. The uncertainty is only taken into account for higgs samples.

- Initial and Final State Radiation (ISR and FSR):
  The gluon and photon radiation at initial and final state give correction to the event topology. The correction affect to acceptance is estimated as systematic

uncertainty using the MC changing the parameters related to the ISR and the FSR from default MC. The systematic estimation has been done on higgs samples.

- Production cross section:
  The several production cross sections are estimated by theoretical calculation taking into account experiment results. The uncertainty from the prediction calculation is concerned as systematic uncertain in acceptance. The uncertainty of higgs prediction cross section $\sigma(Wh \to p\bar{p})$ is noticed as 5% in [57]. The both WW and WZ uncertanity are mentioned in [58] as 10%.

- Z cross section:
  As described at §4.3.11, $Z/\gamma^* \to \ell^+\ell^-$cross sections are estimated to validate the trigger efficiency and lepton selection cut efficiency scale factors. The disagreement between data and expectation is taken into account systematic uncertainty, the systematic uncertainty is 2.8%.

- Luminosity:
  The luminosity measurement has been done by CLC detector as described in §2.7 in CDF experiment. The measurement has several considerable systematic uncertainties, that is, the uncertainty of the inelastic $p\bar{p}$ cross section and CLC acceptance. The systematic from the measurement is total 6%, which is for MC baced acceptance.

- Residual photon-conversion ratio and Fake lepton rate:
  The background expectation for fake lepton and residual photon-conversion are derived from data applying a weight, that is, fake lepton rate and residual photon-conversion ratio. The weight systematic uncertainty comes from used data/MC statistics and uncertainty between used samples, for example Jet samples for fake lepton rate.

The summaries of rate systematic uncertainties are shown in Table 6.1 for signal (higgs) and Table 6.2 for backgrounds.

6.2 Shape Systematic Uncertainty

The shape systematic uncertainty affects relevant kinematic distributions, especially BDT input and output distributions in this case. The considerable uncertainties are Jet energy scale uncertainty and weight uncertainties which are used to expect the residual photon-conversions and fake leptons which are main background in LS-dilepton event.

- Jet energy scale:
  As described at §3.2.3, the jet energy measured by calorimeters is collected by using data and MCs for detector effects and physics effects. The systematic uncertainties coming from the collections change the jet relevant kinematics, that

Mass(GeV/c^2)	110	120	130	140	150	160	170	180	190	200
MC statistics	1.01	0.98	0.96	0.94	0.93	0.96	0.94	0.92	0.88	0.86
MC scale factors	1.52	1.55	1.49	1.39	1.39	1.25	1.24	1.18	1.38	1.11
PDF	2.65	2.47	2.21	2.16	1.99	1.90	1.79	1.73	1.50	1.10
ISR	5.23	5.23	5.23	5.23	5.23	5.23	5.23	5.23	5.23	5.23
FSR	5.46	5.46	5.46	5.46	5.46	5.46	5.46	5.46	5.46	5.46
Cross Section	5.00	5.00	5.00	5.00	5.00	5.00	5.00	5.00	5.00	5.00
Z Cross Section	2.78	2.78	2.78	2.78	2.78	2.78	2.78	2.78	2.78	2.78
Luminosity	6.00	6.00	6.00	6.00	6.00	6.00	6.00	6.00	6.00	6.00
Total (%)	11.7	11.6	11.6	11.6	11.5	11.5	11.5	11.5	11.4	11.4

Table 6.1: Rate systematic uncertainty for signal.

	Fake leptons	Residual photon-conversion	WZ	ZZ
Statistics	2.27	16.90	0.80	3.59
Fake rate	14.08	-	-	-
Residual conversion rate	-	8.84	-	-
MC scale factors	-	-	2.22	2.65
Cross Section	-	-	10.00	10.00
Luminosity	-	-	6.00	6.00
Total (%)	14.3	19.1	11.9	12.5

Table 6.2: Rate systematic uncertainty for backgrounds.

is the jet transverse momentum, number of jet is passing central jet criteria, and H_T, as a results also varies the BDT output distribution as shown in Figure 6.1. The variation effects the search sensitivity.

- Residual photon-conversion ratio and Fake lepton rare:
  The each weights are formulated as a binned function of p_T for relevant objects as shown in §4.1 and §4.2. The systematic uncertainty in each bin affects the shape of kinematic distribution such as input variables. In this case, the effect also validates the BDT separation power. The systematic are estimated by simultaneously varying the all bins with 1 σ uncertainty. The shape systematic effect in the BDT output are shown in Figure 6.2 for the residual photon-conversion ratio and in Figure 6.3 for the fake lepton rate.

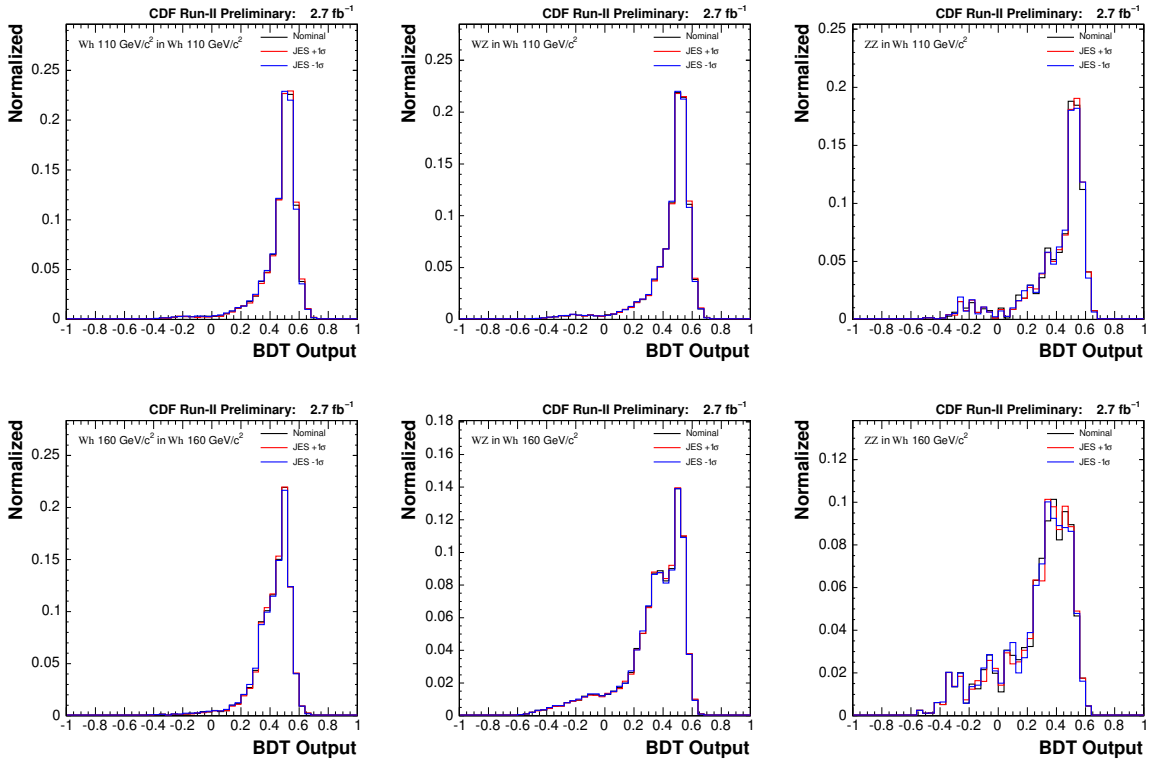

Figure 6.1: Shape systematic coming from jet energy scale in BDT output for higgs at 110 (top row) and 160 (bottom row) GeV/c^2 (from left to right : higgs, WZ, and ZZ).

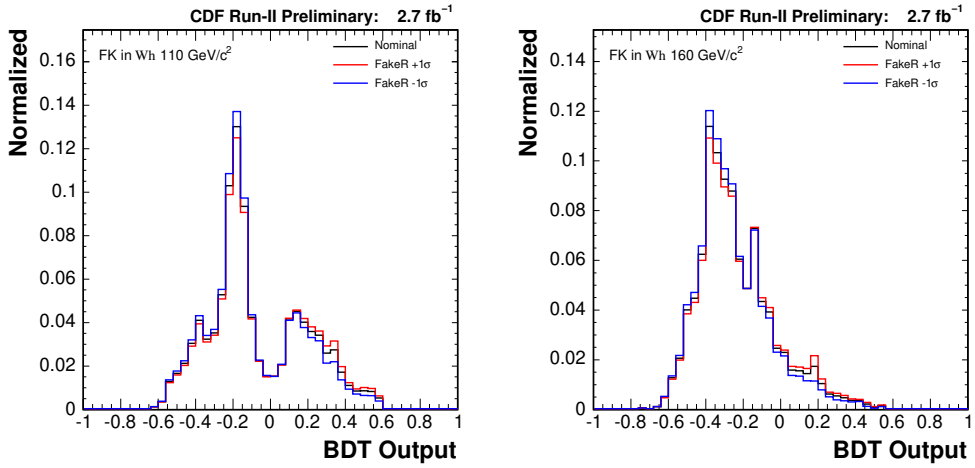

Figure 6.2: Shape systematic coming from fake lepton rate in BDT output for higgs at 110 (left) and 160 (right) GeV/c^2.

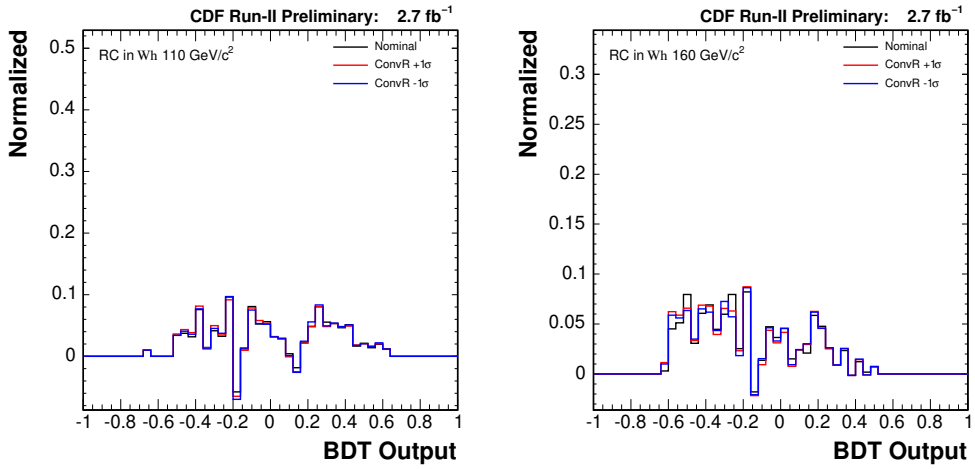

Figure 6.3: Shape systematic coming from residual conversion ratio in BDT output for higgs at 110 (left) and 160 (right) GeV/c^2.

Chapter 7

Upper Limit on Production Cross Section

As described above sections, there is no significance discrepancies between data and background expectation for number of events, several kinematics, and final discriminant i.e. BDT output. From this results, the upper limits on higgs production cross section is set by using binned likelihood function in Bayesian approach with the BDT output distribution. The binned likelihood function obeys the Poisson statics incorporating some information, that is, systematic uncertainties from several sources by the Gaussian. The following section shows the constriction for the binned likelihood function, and the upper limit on production cross section at a 95% confidence level by using the likelihood function.

7.1 Likelihood Function

The upper limit on production cross section is calculated by using Bayesian approach with fitting binned likelihood to the BDT output [60]. The likelihood is constructed under the Poisson statistics:

$$p(\mu, n) = \frac{\mu^n e^{-\mu}}{n!}, \ \mu = s + b \tag{7.1}$$

where n is number of observed events, μ is expected number of events, and $s(b)$ is expected number of events for signal(background). In this thesis, the binned likelihood fitting to N bins histogram is written down as the follows,

$$\mathcal{L} = \prod_{k}^{N_{\rm bin}} \frac{\mu_k^{n_k} e^{-\mu_k}}{n_k!}, \ \mu_k = s_k + b_k \tag{7.2}$$

In addition, the likelihood is taken some informations, the systematic uncertainties, into account by Gaussian,

$$\mathcal{L}(\sigma_1, \cdots, \sigma_{N_{\rm proc}}; \delta_1, \cdots, \delta_{N_{\rm syst}}) = \prod_{k=1}^{N_{\rm bin}} \frac{\mu_k^{n_k} \cdot e^{-\mu_k}}{n_k!} \cdot \prod_{i=1}^{N_{\rm proc}} G(\sigma_i | \sigma_i^{\rm SM}, \Delta\sigma_i^{\rm SM}) \cdot \prod_{j=1}^{N_{\rm syst}} G(\delta_j | 0, 1) \tag{7.3}$$

where $N_{\rm proc}$ is number of physics processes, $N_{\rm syst}$ is number of systematic sources. The expected event μ_k is taken both systematic uncertainties into account, expressed as the follows,

$$\mu_k = \sum_{i=1}^{N_{\rm proc}} \mu_{ik} \cdot \delta_i^{\rm rate} \cdot \delta_{ik}^{\rm shape}, \tag{7.4}$$

$$\delta_i^{\rm rate} = \prod_{j=1}^{N_{\rm syst}} [1 + |\delta_j| \cdot \{\varepsilon_{ij+} H(\delta_j) + \varepsilon_{ij-} H(-\delta_j)\}] \tag{7.5}$$

$$\delta_{ik}^{\rm shape} = \prod_{j=1}^{N_{\rm syst}} [1 + |\delta_j| \cdot \{\kappa_{ijk+} H(\delta_j) + \kappa_{ijk-} H(-\delta_j)\}]\,. \tag{7.6}$$

where ε_{ij} is the relative acceptance uncertainties from jth systematic source in ith process, κ_{ijk} is the relative uncertainty in the kth bin content from jth systematic source in ith process. Heaviside step function $H(\delta_j)$ is used in the above equations, defined as the follows,

$$H(\delta_j) = \begin{cases} 1 & (\delta_j > 0) \\ 0 & (\delta_j < 0) \end{cases} \tag{7.7}$$

The likelihood function (7.3) is used to calculate the upper limit on production cross section times branching fraction $\sigma(p\bar{p}\to Wh) \times B_F(h\to WW)$ at a 95% confidence level.

7.2 Upper Limit at a 95% Confidence Level

In this search, there is no significant excess in between data and background expectation, so the upper limits on production cross section times branching fraction $\sigma(p\bar{p}\to Wh) \times B_F(h\to WW)$ at a 95% confidence level (C.L.) is set by using the binned likelihood function (7.3) in Bayesian approach with BDT output distribution as the

following function,

$$95\% = \frac{\int_0^{\sigma_{95\%}} \mathcal{L}(\sigma)d\sigma}{\int_0^{\infty} \mathcal{L}(\sigma)d\sigma}. \tag{7.8}$$

The upper limits are calculated for both expected and observed ones corresponding to from 110 to 200 GeV/c^2 higgs. The expected upper limit calculations are performed with 10,000 pseudo-experiments. The expected limit are quoted the median in the distribution for 10,000 pseudo-experiment. As a results, the expected upper limit are

$$\sigma_{\rm exp}(p\bar{p}\to Wh) \times B_F(h\to WW) < 2.42 \text{ pb at } 110 \text{ GeV}/c^2,$$
$$\sigma_{\rm exp}(p\bar{p}\to Wh) \times B_F(h\to WW) < 1.23 \text{ pb at } 160 \text{ GeV}/c^2,$$

while the observed upper limits are

$$\sigma_{\rm obs}(p\bar{p}\to Wh) \times B_F(h\to WW) < 1.54 \text{ pb at } 110 \text{ GeV}/c^2,$$
$$\sigma_{\rm obs}(p\bar{p}\to Wh) \times B_F(h\to WW) < 0.98 \text{ pb at } 160 \text{ GeV}/c^2,$$

and the relative expected and observed upper limit to the fermiophobic higgs (FP) prediction at 110 GeV/c^2 are

$$\text{limit}_{\rm exp}/\sigma_{\rm FP110} < 8.2,$$
$$\text{limit}_{\rm obs}/\sigma_{\rm FP110} < 12.9,$$

and to the SM higgs ones at 160 GeV/c^2

$$\text{limit}_{\rm exp}/\sigma_{\rm SM160} < 20.1,$$
$$\text{limit}_{\rm obs}/\sigma_{\rm SM160} < 25.1.$$

Table 7.1 and Figure 7.1 show the expected and observed upper limits at a 95% C.L. for from 110 to 200 GeV/c^2 higgs. And the relative upper limits to higgs prediction cross section are also calculated, to the fermiophobic higgs shown in Table 7.2 and Figure 7.2 and to the SM higgs shown in Table 7.3 and Figure 7.3.

Higgs Mass (GeV/c^2)	Expected Median (pb)	Observed (pb)
110	$1.54^{+0.64}_{-0.44}$	2.42
120	$1.24^{+0.53}_{-0.34}$	1.80
130	$1.16^{+0.49}_{-0.32}$	1.97
140	$1.05^{+0.44}_{-0.29}$	1.73
150	$1.04^{+0.42}_{-0.29}$	1.82
160	$0.98^{+0.42}_{-0.27}$	1.23
170	$0.97^{+0.40}_{-0.27}$	1.48
180	$0.88^{+0.37}_{-0.24}$	1.23
190	$0.82^{+0.34}_{-0.23}$	1.18
200	$0.76^{+0.31}_{-0.21}$	0.89

Table 7.1: The expected and observed upper limit on production cross section times branching fraction $\sigma(p\bar{p}\to Wh) \times B_F(h\to WW)$ at a 95% confidence level in each higgs mass.

Higgs Mass (GeV/c^2)	Expected Median (Limit/σ_{FH})	Observed (Limit/σ_{FH})
110	$8.2^{+3.4}_{-2.3}$	12.9
120	$8.8^{+3.8}_{-2.4}$	12.9
130	$11.1^{+4.6}_{-3.1}$	18.8
140	$13.0^{+5.5}_{-3.6}$	21.6
150	$16.7^{+6.8}_{-4.7}$	29.4
160	$19.1^{+8.2}_{-5.3}$	23.8
170	$24.0^{+9.8}_{-6.8}$	36.7
180	29^{+12}_{-8}	40.4
190	34^{+14}_{-10}	49.2
200	40^{+17}_{-11}	46.5

Table 7.2: The relative upper limits on $\sigma(p\bar{p}\to Wh) \times B_F(h\to WW)$ to fermiophobic higgs prediction at a 95% confidence level in each higgs mass.

Higgs Mass (GeV/c^2)	Expected Median (Limit/σ_{SM})	Observed (Limit/σ_{SM})
110	180^{+74}_{-52}	283.0
120	65^{+28}_{-18}	94.9
130	36^{+15}_{-10}	60.9
140	25^{+11}_{-7}	41.2
150	$22.0^{+8.9}_{-6.2}$	38.7
160	$20.1^{+8.6}_{-5.5}$	25.1
170	$24.0^{+9.8}_{-6.8}$	36.7
180	29^{+12}_{-8}	40.4
190	34^{+14}_{-10}	49.2
200	40^{+17}_{-11}	46.5

Table 7.3: The relative upper limits on $\sigma(p\bar{p}\rightarrow Wh) \times B_F(h\rightarrow WW)$ to SM higgs prediction at a 95% confidence level in each higgs mass.

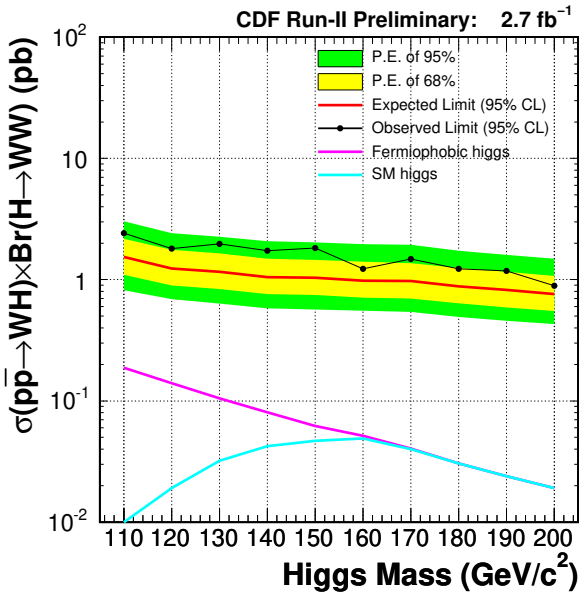

Figure 7.1: The upper limits on the production cross section times branching fraction $\sigma(p\bar{p}\rightarrow Wh) \times B_F(h\rightarrow WW)$ at a 95% confidence level as a function of higgs mass together with the cross sections of the benchmark senario for the fermiophobic higgs and of the Standard Model.

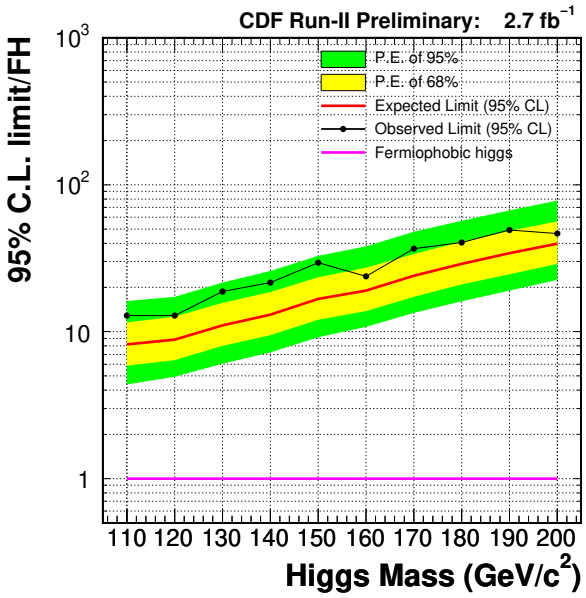

Figure 7.2: The relative upper limits on the production cross section times branching fraction $\sigma(p\bar{p}\rightarrow Wh) \times B_F(h\rightarrow WW)$ to fermiophobic higgs prediction at a 95% confidence level as a function of higgs mass.

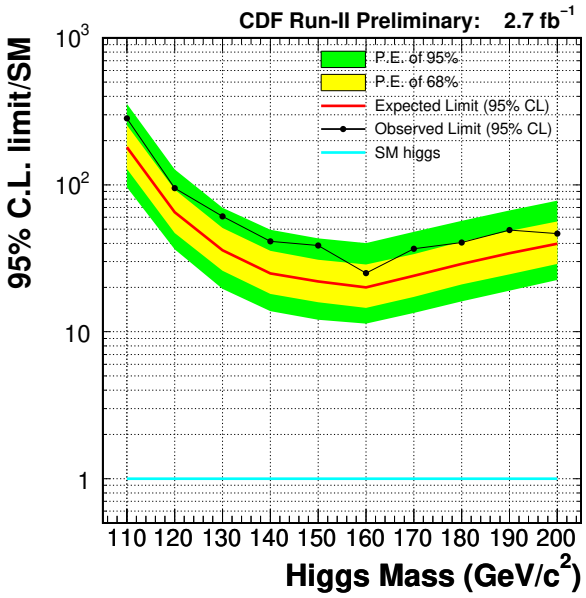

Figure 7.3: The relative upper limits on the production cross section times branching fraction $\sigma(p\bar{p}\rightarrow Wh) \times B_F(h\rightarrow WW)$ to SM higgs prediction at a 95% confidence level as a function of higgs mass.

Chapter 8

Conclusion

This thesis has described the search for the neutral higgs production associated W boson using high-p_T like-sign dilepton events with the data corresponding to an integrated luminosity of 2.7 fb^{-1}. The background expectation in the final selected like-sign event was 188 events, while the observed event was 172, so there was no significant discrepancies between data and the expectation within the uncertainties, also well matched the several kinematic distributions. The expected number of signal events was 1.31 for the fermiophobic higgs of the mass 110 GeV/c^2 assuming the Standard Model production cross section and 0.38 for the Standard Model higgs of 160 GeV/c^2. The Boosted Decision Tree technique was used to give more separation power between backgrounds and signal events in the final sample. The BDT output distribution also have shown no significant excess between the data and background expectation. From this results, the upper limits on the production cross section times the branching fraction $\sigma(p\bar{p}\rightarrow Wh) \times B_F(h\rightarrow WW)$ at a 95% confidence level was set by using the binned likelihood function in Bayesian approach with the BDT output distribution. The observed limit was for higgs mass at 110 and 160 GeV/c^2 respectively,

$$\sigma(p\bar{p}\rightarrow Wh) \times B_F(h\rightarrow WW) < 2.42 \text{ pb at } 110 \text{ GeV}/c^2,$$
$$\sigma(p\bar{p}\rightarrow Wh) \times B_F(h\rightarrow WW) < 1.23 \text{ pb at } 160 \text{ GeV}/c^2.$$

The CDF experiment is also searching the neutral higgs boson using the other channels (total 7 channels) with several analysis techniques (Artificial Neural Network and Matrix Element) [24, 61, 62, 63, 65, 64]. The channels also set the upper limits on cross section, respectively. And the combined upper limits with the 7 channels using from 2.0 to 3.6 fb^{-1} data show more sensitivity to the Standard Model higgs comparing with the upper limit in the individual channel. In addition, the other experiment, so-called the DØ, in the Tevatron is also searching the SM higgs boson using 9 channels from 0.9 to 4.2 fb^{-1} data [27, 28, 31, 66, 67, 68, 68, 69, 70]. The both collaboration have reported the combined upper limits from 110 to 200 GeV/c^2 [71]. In that report, The SM higgs with 160-170 GeV/c^2 was excluded at 95% confidence level as shown in Figure 8.1. The results has been updated since LEP results for the first time in about 5 years [19], and give us new knowledge for the SM higgs. The Tevatron will

run in FY2010 and it will give us total the 6-8 fb^{-1} data, that also give us the hope to "discover" the higgs in the Tevatron.

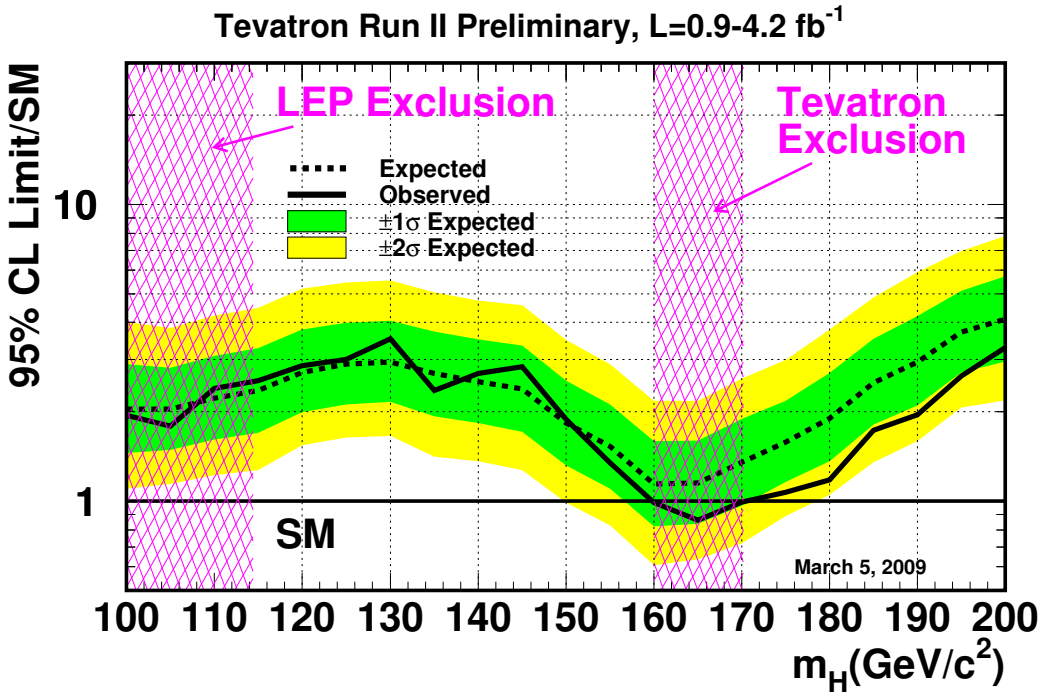

Figure 8.1: The ralative observed and expected upper limit on production cross section to SM prediction as a function of the higgs mass for the combined CDF and DØ results.

Appendix A

Events Selection Effciency and Scale Factor

A.1 Trigger Efficiency

Period	Efficiency
0	0.9635 ± 0.0005
1	0.9780 ± 0.0007
2	0.9788 ± 0.0007
3	0.9750 ± 0.0008
4	0.9796 ± 0.0008
5	0.9672 ± 0.0113
6	0.9777 ± 0.0007
7	0.9687 ± 0.0016
8	0.9677 ± 0.0030
9	0.9610 ± 0.0008
10	0.9630 ± 0.0006
11	0.9638 ± 0.0006
12	0.9609 ± 0.0008
13	0.9588 ± 0.0007
14	0.9643 ± 0.0017
15	0.9660 ± 0.0008
16	0.9632 ± 0.0010
17	0.9659 ± 0.0007

Table A.1: `ELECTRON_CENTRAL_18` trigger efficiency for each period.

Period	Efficiency
0	0.9017 ± 0.0090
1	0.9118 ± 0.0142
2	0.9242 ± 0.0121
3	0.9314 ± 0.0130
4	0.9399 ± 0.0141
5	0.9102 ± 0.0121
6	0.9171 ± 0.0136
7	0.9337 ± 0.0178
8	0.9176 ± 0.0062
9	0.9192 ± 0.0106
10	0.9313 ± 0.0082
11	0.9263 ± 0.0089
12	0.9141 ± 0.0116
13	0.9174 ± 0.0095
14	0.9209 ± 0.0229
15	0.9203 ± 0.0118
16	0.8826 ± 0.0187
17	0.9212 ± 0.0109

Table A.2: `MUON_CMUP18` trigger efficiency for each period.

Period	Efficiency
0	0.9687 ± 0.0054
1	0.9005 ± 0.0149
2	0.8780 ± 0.0146
3	0.8738 ± 0.0165
4	0.9078 ± 0.0169
5	0.8833 ± 0.0134
6	0.8644 ± 0.0164
7	0.8927 ± 0.0216
8	0.8768 ± 0.0073
9	0.8529 ± 0.0133
10	0.9274 ± 0.0084
11	0.9093 ± 0.0097
12	0.8764 ± 0.0134
13	0.8595 ± 0.0116
14	0.8889 ± 0.0262
15	0.8755 ± 0.0140
16	0.9228 ± 0.0158
17	0.9167 ± 0.0112

Table A.3: `MUON_CMX18` trigger efficiency for each period.

A.2 Primary-Vertex Cut Efficiency and Scale Factor

MC samples	Efficiency(Data)	Efficiency(MC)	Scale Factor
Drell-Yan ($Z/\gamma^* \to e^+e^-$)	0.9488 ± 0.0127	0.9531 ± 0.0001	0.9955 ± 0.0133
Drell-Yan ($Z/\gamma^* \to \mu^+\mu^-$)	0.9488 ± 0.0127	0.9528 ± 0.0001	0.9958 ± 0.0133
higgs : $M_{\text{higgs}} = 110(\text{GeV}/c^2)$	0.9488 ± 0.0127	0.9486 ± 0.0004	1.0002 ± 0.0134
higgs : $M_{\text{higgs}} = 120(\text{GeV}/c^2)$	0.9488 ± 0.0127	0.9479 ± 0.0004	1.0010 ± 0.0134
higgs : $M_{\text{higgs}} = 130(\text{GeV}/c^2)$	0.9488 ± 0.0127	0.9488 ± 0.0004	1.0000 ± 0.0134
higgs : $M_{\text{higgs}} = 140(\text{GeV}/c^2)$	0.9488 ± 0.0127	0.9494 ± 0.0003	0.9994 ± 0.0134
higgs : $M_{\text{higgs}} = 150(\text{GeV}/c^2)$	0.9488 ± 0.0127	0.9492 ± 0.0003	0.9996 ± 0.0134
higgs : $M_{\text{higgs}} = 160(\text{GeV}/c^2)$	0.9488 ± 0.0127	0.9497 ± 0.0003	0.9991 ± 0.0134
higgs : $M_{\text{higgs}} = 170(\text{GeV}/c^2)$	0.9488 ± 0.0127	0.9485 ± 0.0003	1.0004 ± 0.0134
higgs : $M_{\text{higgs}} = 180(\text{GeV}/c^2)$	0.9488 ± 0.0127	0.9501 ± 0.0003	0.9987 ± 0.0134
higgs : $M_{\text{higgs}} = 190(\text{GeV}/c^2)$	0.9488 ± 0.0127	0.9491 ± 0.0003	0.9997 ± 0.0134
higgs : $M_{\text{higgs}} = 200(\text{GeV}/c^2)$	0.9488 ± 0.0127	0.9486 ± 0.0003	1.0003 ± 0.0134
Overall	0.9488 ± 0.0127	0.9497 ± 0.0016	0.9991 ± 0.0135

Table A.4: Primary vertex cut efficiency and scale factor for `0d` data set.

MC samples	Efficiency(Data)	Efficiency(MC)	Scale Factor
Drell-Yan ($Z/\gamma^* \to e^+e^-$)	0.9565 ± 0.0058	0.9614 ± 0.0001	0.9949 ± 0.0061
Drell-Yan ($Z/\gamma^* \to \mu^+\mu^-$)	0.9565 ± 0.0058	0.9606 ± 0.0001	0.9957 ± 0.0061
higgs : $M_{\text{higgs}} = 110(\text{GeV}/c^2)$	0.9565 ± 0.0058	0.9595 ± 0.0003	0.9969 ± 0.0061
higgs : $M_{\text{higgs}} = 120(\text{GeV}/c^2)$	0.9565 ± 0.0058	0.9584 ± 0.0003	0.9980 ± 0.0061
higgs : $M_{\text{higgs}} = 130(\text{GeV}/c^2)$	0.9565 ± 0.0058	0.9586 ± 0.0003	0.9979 ± 0.0061
higgs : $M_{\text{higgs}} = 140(\text{GeV}/c^2)$	0.9565 ± 0.0058	0.9586 ± 0.0003	0.9978 ± 0.0061
higgs : $M_{\text{higgs}} = 150(\text{GeV}/c^2)$	0.9565 ± 0.0058	0.9591 ± 0.0003	0.9973 ± 0.0061
higgs : $M_{\text{higgs}} = 160(\text{GeV}/c^2)$	0.9565 ± 0.0058	0.9594 ± 0.0003	0.9970 ± 0.0061
higgs : $M_{\text{higgs}} = 170(\text{GeV}/c^2)$	0.9565 ± 0.0058	0.9581 ± 0.0003	0.9984 ± 0.0061
higgs : $M_{\text{higgs}} = 180(\text{GeV}/c^2)$	0.9565 ± 0.0058	0.9580 ± 0.0003	0.9984 ± 0.0061
higgs : $M_{\text{higgs}} = 190(\text{GeV}/c^2)$	0.9565 ± 0.0058	0.9577 ± 0.0003	0.9987 ± 0.0061
higgs : $M_{\text{higgs}} = 200(\text{GeV}/c^2)$	0.9565 ± 0.0058	0.9577 ± 0.0003	0.9988 ± 0.0061
Overall	0.9565 ± 0.0058	0.9589 ± 0.0011	0.9975 ± 0.0062

Table A.5: Primary vertex cut efficiency and scale factor for `0h` data set.

MC samples	Efficiency(Data)	Efficiency(MC)	Scale Factor
Drell-Yan ($Z/\gamma^* \to e^+e^-$)	0.9598 ± 0.0066	0.9646 ± 0.0001	0.9950 ± 0.0069
Drell-Yan ($Z/\gamma^* \to \mu^+\mu^-$)	0.9598 ± 0.0066	0.9639 ± 0.0001	0.9957 ± 0.0069
higgs : $M_{\text{higgs}} = 110(\text{GeV}/c^2)$	0.9598 ± 0.0066	0.9643 ± 0.0002	0.9953 ± 0.0069
higgs : $M_{\text{higgs}} = 120(\text{GeV}/c^2)$	0.9598 ± 0.0066	0.9641 ± 0.0002	0.9955 ± 0.0069
higgs : $M_{\text{higgs}} = 130(\text{GeV}/c^2)$	0.9598 ± 0.0066	0.9641 ± 0.0002	0.9955 ± 0.0069
higgs : $M_{\text{higgs}} = 140(\text{GeV}/c^2)$	0.9598 ± 0.0066	0.9640 ± 0.0002	0.9957 ± 0.0069
higgs : $M_{\text{higgs}} = 150(\text{GeV}/c^2)$	0.9598 ± 0.0066	0.9639 ± 0.0002	0.9958 ± 0.0069
higgs : $M_{\text{higgs}} = 160(\text{GeV}/c^2)$	0.9598 ± 0.0066	0.9651 ± 0.0002	0.9945 ± 0.0069
higgs : $M_{\text{higgs}} = 170(\text{GeV}/c^2)$	0.9598 ± 0.0066	0.9651 ± 0.0002	0.9944 ± 0.0069
higgs : $M_{\text{higgs}} = 180(\text{GeV}/c^2)$	0.9598 ± 0.0066	0.9642 ± 0.0002	0.9954 ± 0.0069
higgs : $M_{\text{higgs}} = 190(\text{GeV}/c^2)$	0.9598 ± 0.0066	0.9647 ± 0.0002	0.9949 ± 0.0069
higgs : $M_{\text{higgs}} = 200(\text{GeV}/c^2)$	0.9598 ± 0.0066	0.9644 ± 0.0002	0.9952 ± 0.0069
Overall	0.9598 ± 0.0066	0.9644 ± 0.0004	0.9952 ± 0.0069

Table A.6: Primary vertex cut efficiency and scale factor for `0i` data set.

MC samples	Efficiency(Data)	Efficiency(MC)	Scale Factor
Drell-Yan ($Z/\gamma^* \to e^+e^-$)	0.9577 ± 0.0068	0.9694 ± 0.0001	0.9880 ± 0.0071
Drell-Yan ($Z/\gamma^* \to \mu^+\mu^-$)	0.9577 ± 0.0068	0.9691 ± 0.0001	0.9882 ± 0.0071
higgs : $M_{\text{higgs}} = 110(\text{GeV}/c^2)$	0.9577 ± 0.0068	0.9683 ± 0.0002	0.9891 ± 0.0071
higgs : $M_{\text{higgs}} = 120(\text{GeV}/c^2)$	0.9577 ± 0.0068	0.9673 ± 0.0002	0.9902 ± 0.0071
higgs : $M_{\text{higgs}} = 130(\text{GeV}/c^2)$	0.9577 ± 0.0068	0.9680 ± 0.0002	0.9894 ± 0.0071
higgs : $M_{\text{higgs}} = 140(\text{GeV}/c^2)$	0.9577 ± 0.0068	0.9685 ± 0.0002	0.9889 ± 0.0071
higgs : $M_{\text{higgs}} = 150(\text{GeV}/c^2)$	0.9577 ± 0.0068	0.9685 ± 0.0002	0.9889 ± 0.0071
higgs : $M_{\text{higgs}} = 160(\text{GeV}/c^2)$	0.9577 ± 0.0068	0.9686 ± 0.0002	0.9888 ± 0.0071
higgs : $M_{\text{higgs}} = 170(\text{GeV}/c^2)$	0.9577 ± 0.0068	0.9679 ± 0.0002	0.9895 ± 0.0071
higgs : $M_{\text{higgs}} = 180(\text{GeV}/c^2)$	0.9577 ± 0.0068	0.9682 ± 0.0002	0.9892 ± 0.0071
higgs : $M_{\text{higgs}} = 190(\text{GeV}/c^2)$	0.9577 ± 0.0068	0.9682 ± 0.0002	0.9892 ± 0.0071
higgs : $M_{\text{higgs}} = 200(\text{GeV}/c^2)$	0.9577 ± 0.0068	0.9675 ± 0.0002	0.9899 ± 0.0071
Overall	0.9577 ± 0.0068	0.9683 ± 0.0006	0.9891 ± 0.0071

Table A.7: Primary vertex cut efficiency and scale factor for `0j` data set.

MC samples	Efficiency(Data)	Efficiency(MC)	Scale Factor
Drell-Yan ($Z/\gamma^* \to e^+e^-$)	0.9679 ± 0.0049	0.9707 ± 0.0001	0.9971 ± 0.0050
Drell-Yan ($Z/\gamma^* \to \mu^+\mu^-$)	0.9679 ± 0.0049	0.9707 ± 0.0001	0.9971 ± 0.0050
higgs : $M_{\text{higgs}} = 110(\text{GeV}/c^2)$	0.9679 ± 0.0049	0.9683 ± 0.0001	0.9996 ± 0.0050
higgs : $M_{\text{higgs}} = 120(\text{GeV}/c^2)$	0.9679 ± 0.0049	0.9685 ± 0.0001	0.9994 ± 0.0050
higgs : $M_{\text{higgs}} = 130(\text{GeV}/c^2)$	0.9679 ± 0.0049	0.9678 ± 0.0001	1.0001 ± 0.0050
higgs : $M_{\text{higgs}} = 140(\text{GeV}/c^2)$	0.9679 ± 0.0049	0.9677 ± 0.0001	1.0002 ± 0.0050
higgs : $M_{\text{higgs}} = 150(\text{GeV}/c^2)$	0.9679 ± 0.0049	0.9682 ± 0.0001	0.9997 ± 0.0050
higgs : $M_{\text{higgs}} = 160(\text{GeV}/c^2)$	0.9679 ± 0.0049	0.9685 ± 0.0001	0.9994 ± 0.0050
higgs : $M_{\text{higgs}} = 170(\text{GeV}/c^2)$	0.9679 ± 0.0049	0.9684 ± 0.0001	0.9995 ± 0.0050
higgs : $M_{\text{higgs}} = 180(\text{GeV}/c^2)$	0.9679 ± 0.0049	0.9683 ± 0.0001	0.9996 ± 0.0050
higgs : $M_{\text{higgs}} = 190(\text{GeV}/c^2)$	0.9679 ± 0.0049	0.9680 ± 0.0001	0.9999 ± 0.0050
higgs : $M_{\text{higgs}} = 200(\text{GeV}/c^2)$	0.9679 ± 0.0049	0.9682 ± 0.0001	0.9997 ± 0.0050
Overall	0.9679 ± 0.0049	0.9686 ± 0.0010	0.9993 ± 0.0051

Table A.8: Primary vertex cut efficiency and scale factor for `0k` data set.

A.3 Lepton Selection Efficiency and Scale Factor

cuts	Data Efficiency	MC Efficiency	Scale Factor
COT hit	0.9880 ± 0.0158	0.9915 ± 0.0005	0.9966 ± 0.0159
$z_0 - z_{\text{pv}}$	0.9853 ± 0.0074	0.9953 ± 0.0004	0.9900 ± 0.0075
d_0	0.9752 ± 0.0137	0.9768 ± 0.0008	0.9984 ± 0.0140
Silicon hit	0.8712 ± 0.0337	0.8700 ± 0.0019	1.0014 ± 0.0388
$\text{ISO}^{\text{cal}}_{0.4}$	0.7901 ± 0.0346	0.8050 ± 0.0023	0.9814 ± 0.0430
EM	0.9772 ± 0.0308	0.9847 ± 0.0007	0.9925 ± 0.0312
L_{shr}	0.9584 ± 0.0319	0.9712 ± 0.0009	0.9869 ± 0.0328
E/p	0.9627 ± 0.0171	0.9601 ± 0.0011	1.0027 ± 0.0179
χ^2_{srtip}	0.9268 ± 0.0284	0.9609 ± 0.0010	0.9645 ± 0.0296
Δz_{CES}	0.9679 ± 0.0244	0.9793 ± 0.0008	0.9883 ± 0.0250
$Q \times \Delta x_{\text{CES}}$	0.9166 ± 0.0241	0.9519 ± 0.0012	0.9629 ± 0.0254
Conversion removal	0.9633 ± 0.0208	0.9308 ± 0.0014	1.0349 ± 0.0224
Overall	0.6036 ± 0.0321	0.6290 ± 0.0030	0.9596 ± 0.0513

Table A.9: Low E_T electron selection cut efficiencies and scale factors for `0d` data set.

cuts	Data Efficiency	MC Efficiency	Scale Factor
COT hit	0.9771 ± 0.0018	0.9937 ± 0.0002	0.9832 ± 0.0018
$z_0 - z_{\rm pv}$	0.9967 ± 0.0008	0.9966 ± 0.0001	1.0001 ± 0.0008
d_0	0.9865 ± 0.0016	0.9834 ± 0.0003	1.0032 ± 0.0016
Silicon hit	0.9256 ± 0.0033	0.9325 ± 0.0006	0.9925 ± 0.0036
$\mathrm{ISO}^{\rm cal}_{0.4}$	0.9115 ± 0.0035	0.8994 ± 0.0008	1.0134 ± 0.0040
EM	0.9929 ± 0.0013	0.9912 ± 0.0002	1.0017 ± 0.0013
$L_{\rm shr}$	0.9920 ± 0.0013	0.9912 ± 0.0002	1.0008 ± 0.0013
E/p	0.9318 ± 0.0031	0.9233 ± 0.0007	1.0092 ± 0.0034
$\chi^2_{\rm srtip}$	0.9753 ± 0.0019	0.9854 ± 0.0003	0.9898 ± 0.0020
$\Delta z_{\rm CES}$	0.9939 ± 0.0010	0.9960 ± 0.0002	0.9979 ± 0.0011
$Q \times \Delta x_{\rm CES}$	0.9855 ± 0.0015	0.9862 ± 0.0003	0.9993 ± 0.0016
Conversion removal	0.9519 ± 0.0028	0.9431 ± 0.0006	1.0093 ± 0.0031
Overall	0.7200 ± 0.0057	0.7099 ± 0.0013	1.0142 ± 0.0082

Table A.10: High E_T electron selection cut efficiencies and scale factors for `0d` data set.

cuts	Data Efficiency	MC Efficiency	Scale Factor
COT hit	0.9935 ± 0.0156	0.9896 ± 0.0005	1.0039 ± 0.0158
$z_0 - z_{\rm pv}$	0.9976 ± 0.0078	0.9952 ± 0.0003	1.0024 ± 0.0079
d_0	0.9857 ± 0.0163	0.9769 ± 0.0007	1.0090 ± 0.0167
Silicon hit	0.9081 ± 0.0389	0.8716 ± 0.0017	1.0418 ± 0.0447
$\mathrm{ISO}^{\rm cal}_{0.4}$	0.8329 ± 0.0401	0.7943 ± 0.0022	1.0486 ± 0.0506
EM	0.9893 ± 0.0362	0.9838 ± 0.0006	1.0056 ± 0.0368
$L_{\rm shr}$	0.9705 ± 0.0368	0.9703 ± 0.0008	1.0001 ± 0.0379
E/p	0.9651 ± 0.0191	0.9618 ± 0.0010	1.0034 ± 0.0198
$\chi^2_{\rm srtip}$	0.9441 ± 0.0327	0.9590 ± 0.0010	0.9845 ± 0.0341
$\Delta z_{\rm CES}$	0.9713 ± 0.0276	0.9799 ± 0.0007	0.9912 ± 0.0282
$Q \times \Delta x_{\rm CES}$	0.9491 ± 0.0285	0.9522 ± 0.0011	0.9967 ± 0.0299
Conversion removal	0.9709 ± 0.0240	0.9290 ± 0.0013	1.0452 ± 0.0259
Overall	0.6371 ± 0.0373	0.6208 ± 0.0028	1.0263 ± 0.0603

Table A.11: Low E_T electron selection cut efficiencies and scale factors for `0h` data set.

cuts	Data Efficiency	MC Efficiency	Scale Factor
COT hit	0.9851 ± 0.0014	0.9915 ± 0.0002	0.9936 ± 0.0014
$z_0 - z_{\rm pv}$	0.9944 ± 0.0009	0.9966 ± 0.0001	0.9977 ± 0.0009
d_0	0.9865 ± 0.0017	0.9841 ± 0.0003	1.0025 ± 0.0017
Silicon hit	0.9420 ± 0.0028	0.9370 ± 0.0006	1.0053 ± 0.0031
$\mathrm{ISO}^{\rm cal}_{0.4}$	0.9081 ± 0.0034	0.8917 ± 0.0008	1.0183 ± 0.0039
EM	0.9946 ± 0.0012	0.9912 ± 0.0002	1.0034 ± 0.0013
$L_{\rm shr}$	0.9920 ± 0.0013	0.9916 ± 0.0002	1.0005 ± 0.0013
E/p	0.9375 ± 0.0030	0.9249 ± 0.0006	1.0136 ± 0.0033
$\chi^2_{\rm srtip}$	0.9752 ± 0.0019	0.9853 ± 0.0003	0.9897 ± 0.0020
$\Delta z_{\rm CES}$	0.9958 ± 0.0010	0.9960 ± 0.0001	0.9999 ± 0.0011
$Q \times \Delta x_{\rm CES}$	0.9873 ± 0.0013	0.9865 ± 0.0003	1.0008 ± 0.0014
Conversion removal	0.9557 ± 0.0027	0.9456 ± 0.0005	1.0107 ± 0.0029
Overall	0.7291 ± 0.0054	0.7113 ± 0.0012	1.0250 ± 0.0078

Table A.12: High E_T electron selection cut efficiencies and scale factors for `0h` data set.

cuts	Data Efficiency	MC Efficiency	Scale Factor
COT hit	0.9803 ± 0.0146	0.9879 ± 0.0004	0.9923 ± 0.0148
$z_0 - z_{\rm pv}$	0.9970 ± 0.0081	0.9950 ± 0.0003	1.0021 ± 0.0082
d_0	0.9905 ± 0.0156	0.9753 ± 0.0006	1.0156 ± 0.0160
Silicon hit	0.9123 ± 0.0361	0.8730 ± 0.0014	1.0449 ± 0.0414
$\mathrm{ISO}^{\rm cal}_{0.4}$	0.8041 ± 0.0367	0.7910 ± 0.0017	1.0165 ± 0.0464
EM	0.9981 ± 0.0336	0.9839 ± 0.0005	1.0144 ± 0.0342
$L_{\rm shr}$	0.9812 ± 0.0344	0.9709 ± 0.0007	1.0106 ± 0.0354
E/p	0.9674 ± 0.0173	0.9619 ± 0.0008	1.0057 ± 0.0180
$\chi^2_{\rm srtip}$	0.9495 ± 0.0306	0.9603 ± 0.0008	0.9888 ± 0.0318
$\Delta z_{\rm CES}$	0.9905 ± 0.0265	0.9798 ± 0.0006	1.0110 ± 0.0270
$Q \times \Delta x_{\rm CES}$	0.9244 ± 0.0264	0.9521 ± 0.0009	0.9709 ± 0.0277
Conversion removal	0.9685 ± 0.0234	0.9277 ± 0.0010	1.0440 ± 0.0253
Overall	0.6069 ± 0.0334	0.6198 ± 0.0022	0.9792 ± 0.0539

Table A.13: Low E_T electron selection cut efficiencies and scale factors for `0i` data set.

cuts	Data Efficiency	MC Efficiency	Scale Factor
COT hit	0.9818 ± 0.0013	0.9904 ± 0.0002	0.9914 ± 0.0013
$z_0 - z_{\rm pv}$	0.9952 ± 0.0007	0.9964 ± 0.0001	0.9988 ± 0.0007
d_0	0.9851 ± 0.0013	0.9837 ± 0.0002	1.0014 ± 0.0013
Silicon hit	0.9408 ± 0.0023	0.9338 ± 0.0005	1.0075 ± 0.0025
$\mathrm{ISO}^{\rm cal}_{0.4}$	0.8936 ± 0.0029	0.8839 ± 0.0006	1.0110 ± 0.0034
EM	0.9943 ± 0.0011	0.9913 ± 0.0002	1.0031 ± 0.0011
$L_{\rm shr}$	0.9920 ± 0.0011	0.9916 ± 0.0002	1.0004 ± 0.0011
E/p	0.9326 ± 0.0025	0.9242 ± 0.0005	1.0090 ± 0.0027
$\chi^2_{\rm srtip}$	0.9729 ± 0.0016	0.9859 ± 0.0002	0.9868 ± 0.0017
$\Delta z_{\rm CES}$	0.9951 ± 0.0009	0.9959 ± 0.0001	0.9992 ± 0.0009
$Q \times \Delta x_{\rm CES}$	0.9858 ± 0.0012	0.9860 ± 0.0002	0.9998 ± 0.0012
Conversion removal	0.9513 ± 0.0023	0.9453 ± 0.0004	1.0063 ± 0.0024
Overall	0.7064 ± 0.0044	0.7014 ± 0.0010	1.0072 ± 0.0065

Table A.14: High E_T electron selection cut efficiencies and scale factors for `0i` data set.

cuts	Data Efficiency	MC Efficiency	Scale Factor
COT hit	0.9842 ± 0.0143	0.9842 ± 0.0004	1.0000 ± 0.0145
$z_0 - z_{\rm pv}$	0.9981 ± 0.0085	0.9951 ± 0.0002	1.0031 ± 0.0086
d_0	0.9877 ± 0.0148	0.9760 ± 0.0005	1.0120 ± 0.0152
Silicon hit	0.9062 ± 0.0335	0.8657 ± 0.0011	1.0467 ± 0.0387
$\mathrm{ISO}^{\rm cal}_{0.4}$	0.7858 ± 0.0335	0.7789 ± 0.0014	1.0088 ± 0.0430
EM	0.9991 ± 0.0312	0.9836 ± 0.0004	1.0158 ± 0.0318
$L_{\rm shr}$	0.9598 ± 0.0316	0.9691 ± 0.0006	0.9904 ± 0.0326
E/p	0.9624 ± 0.0168	0.9623 ± 0.0006	1.0001 ± 0.0174
$\chi^2_{\rm srtip}$	0.9543 ± 0.0286	0.9602 ± 0.0006	0.9939 ± 0.0298
$\Delta z_{\rm CES}$	0.9788 ± 0.0249	0.9795 ± 0.0005	0.9993 ± 0.0254
$Q \times \Delta x_{\rm CES}$	0.9263 ± 0.0249	0.9501 ± 0.0007	0.9749 ± 0.0262
Conversion removal	0.9653 ± 0.0212	0.9288 ± 0.0008	1.0392 ± 0.0228
Overall	0.6115 ± 0.0305	0.6016 ± 0.0018	1.0164 ± 0.0508

Table A.15: Low E_T electron selection cut efficiencies and scale factors for `0j` data set.

cuts	Data Efficiency	MC Efficiency	Scale Factor
COT hit	0.9813 ± 0.0011	0.9870 ± 0.0002	0.9943 ± 0.0011
$z_0 - z_{\rm pv}$	0.9957 ± 0.0006	0.9964 ± 0.0001	0.9993 ± 0.0006
d_0	0.9868 ± 0.0011	0.9848 ± 0.0002	1.0020 ± 0.0012
Silicon hit	0.9356 ± 0.0021	0.9268 ± 0.0004	1.0095 ± 0.0023
$\mathrm{ISO}^{\rm cal}_{0.4}$	0.8791 ± 0.0026	0.8686 ± 0.0005	1.0122 ± 0.0031
EM	0.9938 ± 0.0009	0.9915 ± 0.0001	1.0023 ± 0.0010
$L_{\rm shr}$	0.9914 ± 0.0010	0.9912 ± 0.0001	1.0002 ± 0.0010
E/p	0.9316 ± 0.0021	0.9264 ± 0.0004	1.0057 ± 0.0023
$\chi^2_{\rm srtip}$	0.9740 ± 0.0014	0.9855 ± 0.0002	0.9883 ± 0.0014
$\Delta z_{\rm CES}$	0.9946 ± 0.0008	0.9959 ± 0.0001	0.9987 ± 0.0008
$Q \times \Delta x_{\rm CES}$	0.9864 ± 0.0010	0.9863 ± 0.0002	1.0001 ± 0.0010
Conversion removal	0.9528 ± 0.0019	0.9459 ± 0.0003	1.0073 ± 0.0020
Overall	0.6809 ± 0.0038	0.6842 ± 0.0008	0.9951 ± 0.0057

Table A.16: High E_T electron selection cut efficiencies and scale factors for `0j` data set.

cuts	Data Efficiency	MC Efficiency	Scale Factor
COT hit	0.9763 ± 0.0142	0.9804 ± 0.0005	0.9958 ± 0.0145
$z_0 - z_{\rm pv}$	0.9979 ± 0.0089	0.9949 ± 0.0003	1.0031 ± 0.0090
d_0	0.9809 ± 0.0152	0.9765 ± 0.0005	1.0045 ± 0.0156
Silicon hit	0.8746 ± 0.0335	0.8661 ± 0.0013	1.0098 ± 0.0387
$\mathrm{ISO}^{\rm cal}_{0.4}$	0.7669 ± 0.0341	0.7653 ± 0.0017	1.0022 ± 0.0446
EM	0.9697 ± 0.0312	0.9830 ± 0.0005	0.9864 ± 0.0317
$L_{\rm shr}$	0.9581 ± 0.0314	0.9685 ± 0.0006	0.9892 ± 0.0325
E/p	0.9663 ± 0.0170	0.9628 ± 0.0007	1.0036 ± 0.0177
$\chi^2_{\rm srtip}$	0.9272 ± 0.0284	0.9600 ± 0.0007	0.9658 ± 0.0296
$\Delta z_{\rm CES}$	0.9812 ± 0.0253	0.9789 ± 0.0005	1.0024 ± 0.0259
$Q \times \Delta x_{\rm CES}$	0.9271 ± 0.0249	0.9502 ± 0.0008	0.9757 ± 0.0262
Conversion removal	0.9575 ± 0.0220	0.9274 ± 0.0009	1.0324 ± 0.0237
Overall	0.5980 ± 0.0315	0.5911 ± 0.0020	1.0117 ± 0.0534

Table A.17: Low E_T electron selection cut efficiencies and scale factors for `0k` data set.

cuts	Data Efficiency	MC Efficiency	Scale Factor
COT hit	0.9780 ± 0.0014	0.9827 ± 0.0002	0.9952 ± 0.0015
$z_0 - z_{\rm pv}$	0.9953 ± 0.0007	0.9963 ± 0.0001	0.9989 ± 0.0007
d_0	0.9862 ± 0.0013	0.9844 ± 0.0002	1.0018 ± 0.0013
Silicon hit	0.9378 ± 0.0025	0.9292 ± 0.0004	1.0092 ± 0.0028
$\mathrm{ISO}^{\rm cal}_{0.4}$	0.8714 ± 0.0035	0.8540 ± 0.0006	1.0203 ± 0.0042
EM	0.9928 ± 0.0011	0.9912 ± 0.0002	1.0016 ± 0.0011
$L_{\rm shr}$	0.9918 ± 0.0012	0.9912 ± 0.0002	1.0007 ± 0.0012
E/p	0.9357 ± 0.0026	0.9262 ± 0.0004	1.0102 ± 0.0029
$\chi^2_{\rm srtip}$	0.9743 ± 0.0017	0.9855 ± 0.0002	0.9886 ± 0.0018
$\Delta z_{\rm CES}$	0.9952 ± 0.0010	0.9959 ± 0.0001	0.9993 ± 0.0010
$Q \times \Delta x_{\rm CES}$	0.9849 ± 0.0013	0.9865 ± 0.0002	0.9984 ± 0.0013
Conversion removal	0.9508 ± 0.0024	0.9457 ± 0.0004	1.0054 ± 0.0026
Overall	0.6826 ± 0.0051	0.6704 ± 0.0009	1.0183 ± 0.0077

Table A.18: High E_T electron selection cut efficiencies and scale factors for `0k` data set.

cuts	Data Efficiency	MC Efficiency	Scale Factor
COT hit	0.9604 ± 0.0050	0.9932 ± 0.0004	0.9670 ± 0.0051
$z_0 - z_{\rm pv}$	1.0000 ± 0.0000	0.9992 ± 0.0002	1.0008 ± 0.0002
d_0	0.9976 ± 0.0026	0.9987 ± 0.0002	0.9990 ± 0.0026
Silicon hit	0.9037 ± 0.0092	0.9096 ± 0.0016	0.9935 ± 0.0103
$\mathrm{ISO}^{\rm cal}_{0.4}$	0.9004 ± 0.0093	0.9222 ± 0.0014	0.9764 ± 0.0102
EM	0.9453 ± 0.0071	0.9305 ± 0.0014	1.0158 ± 0.0078
HAD	0.9773 ± 0.0052	0.9842 ± 0.0007	0.9930 ± 0.0053
$r \times \Delta\phi$	0.9310 ± 0.0079	0.9845 ± 0.0007	0.9457 ± 0.0080
Overall	0.7201 ± 0.0123	0.7774 ± 0.0023	0.9263 ± 0.0161

Table A.19: Muon selection cut efficiencies and scale factors from CMUP-CMUP for `0d` data set.

cuts	Data Efficiency	MC Efficiency	Scale Factor
COT hit	0.9779 ± 0.0067	0.9922 ± 0.0007	0.9856 ± 0.0068
$z_0 - z_{\rm pv}$	0.9969 ± 0.0022	0.9990 ± 0.0003	0.9979 ± 0.0022
d_0	0.9985 ± 0.0015	0.9991 ± 0.0002	0.9994 ± 0.0016
Silicon hit	0.9080 ± 0.0134	0.9305 ± 0.0021	0.9758 ± 0.0145
$\mathrm{ISO}^{\rm cal}_{0.4}$	0.9106 ± 0.0136	0.9281 ± 0.0021	0.9812 ± 0.0148
EM	0.9540 ± 0.0115	0.9332 ± 0.0020	1.0223 ± 0.0125
HAD	0.9724 ± 0.0087	0.9782 ± 0.0012	0.9940 ± 0.0090
$r \times \Delta\phi$	0.9974 ± 0.0086	0.9935 ± 0.0007	1.0039 ± 0.0087
Overall	0.7960 ± 0.0172	0.8039 ± 0.0032	0.9902 ± 0.0218

Table A.20: Muon selection cut efficiencies and scale factors from CMUP-CMX for `0d` data set.

cuts	Data Efficiency	MC Efficiency	Scale Factor
COT hit	0.9702 ± 0.0082	0.9941 ± 0.0006	0.9760 ± 0.0083
$z_0 - z_{\rm pv}$	1.0000 ± 0.0000	0.9995 ± 0.0002	1.0005 ± 0.0002
d_0	0.9975 ± 0.0017	0.9985 ± 0.0003	0.9990 ± 0.0018
Silicon hit	0.8667 ± 0.0136	0.8895 ± 0.0025	0.9743 ± 0.0156
$\mathrm{ISO}^{\rm cal}_{0.4}$	0.8986 ± 0.0135	0.9218 ± 0.0021	0.9749 ± 0.0148
EM	0.9482 ± 0.0106	0.9354 ± 0.0020	1.0137 ± 0.0115
HAD	0.9813 ± 0.0074	0.9852 ± 0.0010	0.9961 ± 0.0076
$r \times \Delta\phi$	0.9371 ± 0.0111	0.9825 ± 0.0010	0.9538 ± 0.0113
Overall	0.7048 ± 0.0173	0.7630 ± 0.0034	0.9238 ± 0.0231

Table A.21: Muon selection cut efficiencies and scale factors from CMX-CMUP for `0d` data set.

cuts	Data Efficiency	MC Efficiency	Scale Factor
COT hit	0.9660 ± 0.0098	0.9924 ± 0.0009	0.9734 ± 0.0100
$z_0 - z_{\rm pv}$	0.9978 ± 0.0022	0.9992 ± 0.0003	0.9986 ± 0.0022
d_0	0.9978 ± 0.0022	0.9990 ± 0.0003	0.9988 ± 0.0022
Silicon hit	0.9130 ± 0.0161	0.9202 ± 0.0029	0.9921 ± 0.0178
$\mathrm{ISO}^{\rm cal}_{0.4}$	0.8895 ± 0.0183	0.9283 ± 0.0028	0.9581 ± 0.0199
EM	0.9454 ± 0.0127	0.9344 ± 0.0026	1.0118 ± 0.0139
HAD	0.9800 ± 0.0066	0.9753 ± 0.0017	1.0048 ± 0.0070
$r \times \Delta\phi$	0.9914 ± 0.0096	0.9952 ± 0.0007	0.9962 ± 0.0097
Overall	0.7983 ± 0.0212	0.7935 ± 0.0043	1.0060 ± 0.0273

Table A.22: Muon selection cut efficiencies and scale factors from CMX-CMX for `0d` data set.

cuts	Data Efficiency	MC Efficiency	Scale Factor
COT hit	0.9818 ± 0.0040	0.9905 ± 0.0005	0.9912 ± 0.0041
$z_0 - z_{\rm pv}$	0.9980 ± 0.0020	0.9993 ± 0.0001	0.9987 ± 0.0020
d_0	1.0000 ± 0.0000	0.9987 ± 0.0002	1.0013 ± 0.0002
Silicon hit	0.9032 ± 0.0097	0.9179 ± 0.0014	0.9840 ± 0.0106
$\mathrm{ISO}^{\rm cal}_{0.4}$	0.8907 ± 0.0100	0.9156 ± 0.0014	0.9729 ± 0.0110
EM	0.9542 ± 0.0077	0.9307 ± 0.0013	1.0253 ± 0.0084
HAD	0.9850 ± 0.0054	0.9841 ± 0.0006	1.0009 ± 0.0055
$r \times \Delta\phi$	0.9464 ± 0.0079	0.9854 ± 0.0006	0.9604 ± 0.0080
Overall	0.7392 ± 0.0122	0.7774 ± 0.0021	0.9509 ± 0.0159

Table A.23: Muon selection cut efficiencies and scale factors from CMUP-CMUP for `0h` data set.

cuts	Data Efficiency	MC Efficiency	Scale Factor
COT hit	0.9863 ± 0.0056	0.9896 ± 0.0007	0.9967 ± 0.0057
$z_0 - z_{\rm pv}$	1.0000 ± 0.0000	0.9990 ± 0.0002	1.0010 ± 0.0002
d_0	0.9992 ± 0.0043	0.9990 ± 0.0002	1.0001 ± 0.0044
Silicon hit	0.9420 ± 0.0109	0.9373 ± 0.0016	1.0051 ± 0.0117
$\mathrm{ISO}^{\rm cal}_{0.4}$	0.9128 ± 0.0121	0.9172 ± 0.0018	0.9951 ± 0.0134
EM	0.9554 ± 0.0100	0.9347 ± 0.0016	1.0222 ± 0.0108
HAD	0.9879 ± 0.0076	0.9794 ± 0.0009	1.0086 ± 0.0078
$r \times \Delta\phi$	0.9959 ± 0.0081	0.9947 ± 0.0005	1.0013 ± 0.0082
Overall	0.8045 ± 0.0147	0.8045 ± 0.0026	1.0001 ± 0.0185

Table A.24: Muon selection cut efficiencies and scale factors from CMUP-CMX for `0h` data set.

cuts	Data Efficiency	MC Efficiency	Scale Factor
COT hit	0.9773 ± 0.0056	0.9901 ± 0.0006	0.9871 ± 0.0057
$z_0 - z_{\rm pv}$	1.0023 ± 0.0029	0.9998 ± 0.0001	1.0025 ± 0.0029
d_0	0.9968 ± 0.0029	0.9986 ± 0.0002	0.9983 ± 0.0029
Silicon hit	0.9092 ± 0.0114	0.8973 ± 0.0020	1.0133 ± 0.0128
$\mathrm{ISO}^{\rm cal}_{0.4}$	0.9039 ± 0.0118	0.9099 ± 0.0018	0.9933 ± 0.0131
EM	0.9540 ± 0.0094	0.9319 ± 0.0016	1.0238 ± 0.0102
HAD	0.9901 ± 0.0071	0.9839 ± 0.0008	1.0063 ± 0.0072
$r \times \Delta\phi$	0.9393 ± 0.0102	0.9842 ± 0.0008	0.9544 ± 0.0104
Overall	0.7164 ± 0.0152	0.7587 ± 0.0028	0.9442 ± 0.0203

Table A.25: Muon selection cut efficiencies and scale factors from CMX-CMUP for `0h` data set.

cuts	Data Efficiency	MC Efficiency	Scale Factor
COT hit	0.9871 ± 0.0053	0.9891 ± 0.0009	0.9980 ± 0.0054
$z_0 - z_{\rm pv}$	0.9996 ± 0.0033	0.9992 ± 0.0002	1.0004 ± 0.0033
d_0	0.9972 ± 0.0020	0.9990 ± 0.0003	0.9982 ± 0.0020
Silicon hit	0.9299 ± 0.0116	0.9316 ± 0.0021	0.9982 ± 0.0127
$\mathrm{ISO}^{\rm cal}_{0.4}$	0.8996 ± 0.0138	0.9144 ± 0.0023	0.9838 ± 0.0153
EM	0.9563 ± 0.0102	0.9353 ± 0.0020	1.0225 ± 0.0112
HAD	0.9807 ± 0.0075	0.9805 ± 0.0011	1.0002 ± 0.0077
$r \times \Delta\phi$	0.9901 ± 0.0073	0.9940 ± 0.0006	0.9961 ± 0.0074
Overall	0.7922 ± 0.0169	0.7992 ± 0.0033	0.9911 ± 0.0215

Table A.26: Muon selection cut efficiencies and scale factors from CMX-CMX for `0h` data set.

cuts	Data Efficiency	MC Efficiency	Scale Factor
COT hit	0.9750 ± 0.0040	0.9879 ± 0.0004	0.9869 ± 0.0041
$z_0 - z_{\rm pv}$	0.9976 ± 0.0026	0.9993 ± 0.0001	0.9983 ± 0.0026
d_0	0.9971 ± 0.0034	0.9987 ± 0.0001	0.9984 ± 0.0034
Silicon hit	0.9153 ± 0.0074	0.9123 ± 0.0011	1.0034 ± 0.0082
$\mathrm{ISO}^{\rm cal}_{0.4}$	0.8874 ± 0.0081	0.9052 ± 0.0012	0.9804 ± 0.0091
EM	0.9499 ± 0.0063	0.9295 ± 0.0010	1.0219 ± 0.0069
HAD	0.9869 ± 0.0046	0.9839 ± 0.0005	1.0031 ± 0.0047
$r \times \Delta\phi$	0.9457 ± 0.0059	0.9838 ± 0.0005	0.9613 ± 0.0061
Overall	0.7204 ± 0.0098	0.7663 ± 0.0017	0.9401 ± 0.0130

Table A.27: Muon selection cut efficiencies and scale factors from CMUP-CMUP for `0i` data set.

cuts	Data Efficiency	MC Efficiency	Scale Factor
COT hit	0.9804 ± 0.0058	0.9874 ± 0.0006	0.9929 ± 0.0059
$z_0 - z_{\rm pv}$	0.9957 ± 0.0024	0.9990 ± 0.0002	0.9967 ± 0.0025
d_0	0.9983 ± 0.0027	0.9991 ± 0.0002	0.9991 ± 0.0027
Silicon hit	0.9483 ± 0.0090	0.9338 ± 0.0013	1.0155 ± 0.0097
$\mathrm{ISO}^{\rm cal}_{0.4}$	0.9169 ± 0.0103	0.9130 ± 0.0015	1.0042 ± 0.0114
EM	0.9643 ± 0.0082	0.9332 ± 0.0013	1.0333 ± 0.0089
HAD	0.9808 ± 0.0052	0.9792 ± 0.0007	1.0016 ± 0.0054
$r \times \Delta\phi$	0.9960 ± 0.0065	0.9942 ± 0.0004	1.0018 ± 0.0066
Overall	0.8085 ± 0.0122	0.7943 ± 0.0021	1.0178 ± 0.0156

Table A.28: Muon selection cut efficiencies and scale factors from CMUP-CMX for `0i` data set.

cuts	Data Efficiency	MC Efficiency	Scale Factor
COT hit	0.9623 ± 0.0053	0.9880 ± 0.0006	0.9739 ± 0.0053
$z_0 - z_{\rm pv}$	0.9954 ± 0.0023	0.9989 ± 0.0002	0.9965 ± 0.0023
d_0	0.9948 ± 0.0024	0.9982 ± 0.0002	0.9965 ± 0.0024
Silicon hit	0.9142 ± 0.0089	0.8995 ± 0.0015	1.0163 ± 0.0101
$\mathrm{ISO}^{\rm cal}_{0.4}$	0.8961 ± 0.0095	0.9069 ± 0.0015	0.9880 ± 0.0106
EM	0.9651 ± 0.0067	0.9333 ± 0.0013	1.0341 ± 0.0073
HAD	0.9829 ± 0.0052	0.9837 ± 0.0006	0.9992 ± 0.0053
$r \times \Delta\phi$	0.9453 ± 0.0076	0.9837 ± 0.0006	0.9609 ± 0.0077
Overall	0.7289 ± 0.0121	0.7579 ± 0.0022	0.9617 ± 0.0162

Table A.29: Muon selection cut efficiencies and scale factors from CMX-CMUP for `0i` data set.

cuts	Data Efficiency	MC Efficiency	Scale Factor
COT hit	0.9757 ± 0.0057	0.9863 ± 0.0007	0.9892 ± 0.0058
$z_0 - z_{\rm pv}$	1.0000 ± 0.0000	0.9987 ± 0.0002	1.0013 ± 0.0002
d_0	0.9974 ± 0.0044	0.9990 ± 0.0002	0.9984 ± 0.0044
Silicon hit	0.9381 ± 0.0096	0.9276 ± 0.0017	1.0113 ± 0.0105
$\mathrm{ISO}^{\rm cal}_{0.4}$	0.8863 ± 0.0113	0.9119 ± 0.0018	0.9719 ± 0.0126
EM	0.9510 ± 0.0089	0.9368 ± 0.0016	1.0152 ± 0.0097
HAD	0.9817 ± 0.0063	0.9802 ± 0.0009	1.0016 ± 0.0065
$r \times \Delta\phi$	1.0000 ± 0.0000	0.9933 ± 0.0005	1.0067 ± 0.0005
Overall	0.7752 ± 0.0136	0.7913 ± 0.0026	0.9797 ± 0.0175

Table A.30: Muon selection cut efficiencies and scale factors from CMX-CMX for `0i` data set.

cuts	Data Efficiency	MC Efficiency	Scale Factor
COT hit	0.9630 ± 0.0035	0.9815 ± 0.0004	0.9812 ± 0.0036
$z_0 - z_{\rm pv}$	0.9946 ± 0.0018	0.9987 ± 0.0001	0.9959 ± 0.0018
d_0	0.9970 ± 0.0018	0.9984 ± 0.0001	0.9986 ± 0.0018
Silicon hit	0.9084 ± 0.0061	0.9012 ± 0.0010	1.0080 ± 0.0068
$\mathrm{ISO}^{\rm cal}_{0.4}$	0.8644 ± 0.0068	0.8898 ± 0.0010	0.9715 ± 0.0077
EM	0.9426 ± 0.0049	0.9279 ± 0.0008	1.0159 ± 0.0054
HAD	0.9880 ± 0.0031	0.9837 ± 0.0004	1.0043 ± 0.0032
$r \times \Delta\phi$	0.9410 ± 0.0055	0.9845 ± 0.0004	0.9558 ± 0.0056
Overall	0.6937 ± 0.0082	0.7405 ± 0.0014	0.9367 ± 0.0112

Table A.31: Muon selection cut efficiencies and scale factors from CMUP-CMUP for `0j` data set.

cuts	Data Efficiency	MC Efficiency	Scale Factor
COT hit	0.9748 ± 0.0044	0.9812 ± 0.0006	0.9934 ± 0.0045
$z_0 - z_{\rm pv}$	0.9934 ± 0.0027	0.9986 ± 0.0002	0.9948 ± 0.0027
d_0	0.9955 ± 0.0028	0.9988 ± 0.0001	0.9966 ± 0.0028
Silicon hit	0.9322 ± 0.0078	0.9253 ± 0.0011	1.0075 ± 0.0085
$\mathrm{ISO}^{\rm cal}_{0.4}$	0.8847 ± 0.0088	0.9037 ± 0.0012	0.9789 ± 0.0098
EM	0.9565 ± 0.0063	0.9333 ± 0.0010	1.0248 ± 0.0069
HAD	0.9812 ± 0.0044	0.9794 ± 0.0006	1.0018 ± 0.0046
$r \times \Delta\phi$	0.9853 ± 0.0051	0.9942 ± 0.0003	0.9911 ± 0.0051
Overall	0.7759 ± 0.0101	0.7771 ± 0.0017	0.9985 ± 0.0132

Table A.32: Muon selection cut efficiencies and scale factors from CMUP-CMX for `0j` data set.

cuts	Data Efficiency	MC Efficiency	Scale Factor
COT hit	0.9664 ± 0.0041	0.9813 ± 0.0005	0.9848 ± 0.0043
$z_0 - z_{\rm pv}$	0.9951 ± 0.0021	0.9989 ± 0.0001	0.9962 ± 0.0021
d_0	0.9949 ± 0.0027	0.9980 ± 0.0002	0.9969 ± 0.0027
Silicon hit	0.8925 ± 0.0075	0.8855 ± 0.0013	1.0079 ± 0.0086
$\mathrm{ISO}^{\rm cal}_{0.4}$	0.8626 ± 0.0083	0.8892 ± 0.0013	0.9702 ± 0.0095
EM	0.9504 ± 0.0058	0.9297 ± 0.0010	1.0223 ± 0.0063
HAD	0.9858 ± 0.0036	0.9847 ± 0.0005	1.0011 ± 0.0037
$r \times \Delta\phi$	0.9383 ± 0.0064	0.9842 ± 0.0005	0.9534 ± 0.0065
Overall	0.6789 ± 0.0102	0.7276 ± 0.0018	0.9331 ± 0.0142

Table A.33: Muon selection cut efficiencies and scale factors from CMX-CMUP for `0j` data set.

cuts	Data Efficiency	MC Efficiency	Scale Factor
COT hit	0.9655 ± 0.0050	0.9813 ± 0.0007	0.9838 ± 0.0051
$z_0 - z_{\rm pv}$	0.9963 ± 0.0034	0.9985 ± 0.0002	0.9978 ± 0.0035
d_0	0.9987 ± 0.0032	0.9989 ± 0.0002	0.9998 ± 0.0032
Silicon hit	0.9158 ± 0.0090	0.9203 ± 0.0014	0.9951 ± 0.0099
$\mathrm{ISO}^{\rm cal}_{0.4}$	0.8670 ± 0.0101	0.8991 ± 0.0015	0.9643 ± 0.0113
EM	0.9519 ± 0.0071	0.9343 ± 0.0013	1.0188 ± 0.0077
HAD	0.9873 ± 0.0057	0.9806 ± 0.0007	1.0069 ± 0.0058
$r \times \Delta\phi$	0.9952 ± 0.0059	0.9937 ± 0.0004	1.0015 ± 0.0059
Overall	0.7554 ± 0.0118	0.7729 ± 0.0021	0.9773 ± 0.0155

Table A.34: Muon selection cut efficiencies and scale factors from CMX-CMX for `0j` data set.

cuts	Data Efficiency	MC Efficiency	Scale Factor
COT hit	0.9582 ± 0.0056	0.9740 ± 0.0006	0.9837 ± 0.0058
$z_0 - z_{\rm pv}$	0.9903 ± 0.0026	0.9985 ± 0.0001	0.9918 ± 0.0026
d_0	0.9939 ± 0.0026	0.9981 ± 0.0002	0.9957 ± 0.0026
Silicon hit	0.9158 ± 0.0082	0.9030 ± 0.0011	1.0142 ± 0.0092
$\mathrm{ISO}^{\rm cal}_{0.4}$	0.8623 ± 0.0094	0.8753 ± 0.0012	0.9852 ± 0.0108
EM	0.9561 ± 0.0061	0.9291 ± 0.0009	1.0291 ± 0.0066
HAD	0.9885 ± 0.0046	0.9840 ± 0.0004	1.0046 ± 0.0047
$r \times \Delta\phi$	0.9254 ± 0.0076	0.9854 ± 0.0004	0.9391 ± 0.0078
Overall	0.6900 ± 0.0114	0.7296 ± 0.0016	0.9457 ± 0.0158

Table A.35: Muon selection cut efficiencies and scale factors from CMUP-CMUP for `0k` data set.

cuts	Data Efficiency	MC Efficiency	Scale Factor
COT hit	0.9710 ± 0.0057	0.9727 ± 0.0007	0.9983 ± 0.0059
$z_0 - z_{\text{pv}}$	0.9966 ± 0.0039	0.9977 ± 0.0002	0.9989 ± 0.0039
d_0	0.9940 ± 0.0034	0.9983 ± 0.0002	0.9957 ± 0.0034
Silicon hit	0.9282 ± 0.0115	0.9281 ± 0.0012	1.0002 ± 0.0124
$\text{ISO}^{\text{cal}}_{0.4}$	0.8758 ± 0.0137	0.8927 ± 0.0014	0.9811 ± 0.0154
EM	0.9468 ± 0.0113	0.9309 ± 0.0011	1.0172 ± 0.0122
HAD	0.9861 ± 0.0080	0.9809 ± 0.0006	1.0053 ± 0.0082
$r \times \Delta\phi$	0.9952 ± 0.0091	0.9946 ± 0.0003	1.0006 ± 0.0091
Overall	0.7621 ± 0.0156	0.7664 ± 0.0019	0.9943 ± 0.0205

Table A.36: Muon selection cut efficiencies and scale factors from CMUP-CMX for `0k` data set.

cuts	Data Efficiency	MC Efficiency	Scale Factor
COT hit	0.9653 ± 0.0059	0.9748 ± 0.0007	0.9903 ± 0.0061
$z_0 - z_{\text{pv}}$	0.9956 ± 0.0027	0.9984 ± 0.0002	0.9971 ± 0.0027
d_0	0.9916 ± 0.0026	0.9976 ± 0.0002	0.9940 ± 0.0026
Silicon hit	0.8931 ± 0.0100	0.8927 ± 0.0014	1.0004 ± 0.0113
$\text{ISO}^{\text{cal}}_{0.4}$	0.8296 ± 0.0116	0.8749 ± 0.0015	0.9482 ± 0.0134
EM	0.9444 ± 0.0071	0.9317 ± 0.0011	1.0136 ± 0.0077
HAD	0.9770 ± 0.0051	0.9837 ± 0.0006	0.9931 ± 0.0052
$r \times \Delta\phi$	0.9249 ± 0.0082	0.9842 ± 0.0005	0.9398 ± 0.0084
Overall	0.6491 ± 0.0142	0.7209 ± 0.0020	0.9004 ± 0.0198

Table A.37: Muon selection cut efficiencies and scale factors from CMX-CMUP for `0k` data set.

cuts	Data Efficiency	MC Efficiency	Scale Factor
COT hit	0.9860 ± 0.0093	0.9742 ± 0.0009	1.0120 ± 0.0096
$z_0 - z_{\rm pv}$	1.0000 ± 0.0000	0.9985 ± 0.0002	1.0015 ± 0.0002
d_0	1.0000 ± 0.0000	0.9987 ± 0.0002	1.0013 ± 0.0002
Silicon hit	0.9332 ± 0.0133	0.9236 ± 0.0015	1.0103 ± 0.0145
$\mathrm{ISO}^{\rm cal}_{0.4}$	0.8685 ± 0.0154	0.8852 ± 0.0018	0.9811 ± 0.0175
EM	0.9636 ± 0.0118	0.9349 ± 0.0014	1.0307 ± 0.0127
HAD	0.9811 ± 0.0089	0.9804 ± 0.0008	1.0007 ± 0.0091
$r \times \Delta\phi$	1.0000 ± 0.0000	0.9940 ± 0.0004	1.0060 ± 0.0004
Overall	0.7438 ± 0.0171	0.7604 ± 0.0024	0.9781 ± 0.0226

Table A.38: Muon selection cut efficiencies and scale factors from CMX-CMX for `0k` data set.

cuts	Data Efficiency	MC Efficiency	Scale Factor
CMUP-CMUP	0.9650 ± 0.0050	0.9860 ± 0.0005	0.9787 ± 0.0051
CMUP-CMX	0.9800 ± 0.0078	0.9935 ± 0.0007	0.9864 ± 0.0079
CMUP-CMX(AR)	0.9800 ± 0.0078	0.9935 ± 0.0007	0.9864 ± 0.0079
CMUP-CMX(KS)	1.0000 ± 0.0000	1.0000 ± 0.0000	1.0000 ± 0.0000
CMUP-CMX(MS)	1.0000 ± 0.0000	1.0000 ± 0.0000	1.0000 ± 0.0000
CMX-CMUP	0.9407 ± 0.0129	0.9732 ± 0.0013	0.9666 ± 0.0133
CMX-CMX	0.9956 ± 0.0045	0.9967 ± 0.0005	0.9990 ± 0.0045
CMX-CMX(AR)	0.9956 ± 0.0045	0.9967 ± 0.0005	0.9990 ± 0.0045
CMX-CMX(KS)	1.0000 ± 0.0000	1.0000 ± 0.0000	1.0000 ± 0.0000
CMX-CMX(MS)	1.0000 ± 0.0000	1.0000 ± 0.0000	1.0000 ± 0.0000

Table A.39: Muon reconstruction efficiencies and scale factors for `0d` data set. (AR : Arch, MS : Miniskirt, KS : Keystone)

cuts	Data Efficiency	MC Efficiency	Scale Factor
CMUP-CMUP	0.9553 ± 0.0052	0.9857 ± 0.0005	0.9691 ± 0.0053
CMUP-CMX	0.9785 ± 0.0093	0.9924 ± 0.0006	0.9860 ± 0.0094
CMUP-CMX(AR)	0.9992 ± 0.0100	0.9945 ± 0.0006	1.0047 ± 0.0101
CMUP-CMX(KS)	0.9173 ± 0.0460	0.9849 ± 0.0038	0.9314 ± 0.0468
CMUP-CMX(MS)	0.9118 ± 0.0235	0.9866 ± 0.0018	0.9242 ± 0.0239
CMX-CMUP	0.9081 ± 0.0123	0.9726 ± 0.0011	0.9337 ± 0.0127
CMX-CMX	0.9972 ± 0.0055	0.9961 ± 0.0004	1.0012 ± 0.0056
CMX-CMX(AR)	1.0000 ± 0.0000	0.9970 ± 0.0004	1.0030 ± 0.0004
CMX-CMX(KS)	0.9933 ± 0.0525	0.9928 ± 0.0025	1.0005 ± 0.0529
CMX-CMX(MS)	0.9508 ± 0.0169	0.9928 ± 0.0013	0.9577 ± 0.0170

Table A.40: Muon reconstruction efficiencies and scale factors for `0h` data set. (AR : Arch, MS : Miniskirt, KS : Keystone)

cuts	Data Efficiency	MC Efficiency	Scale Factor
CMUP-CMUP	0.9572 ± 0.0043	0.9856 ± 0.0004	0.9712 ± 0.0043
CMUP-CMX	0.9482 ± 0.0084	0.9918 ± 0.0005	0.9561 ± 0.0085
CMUP-CMX(AR)	0.9842 ± 0.0088	0.9934 ± 0.0005	0.9908 ± 0.0089
CMUP-CMX(KS)	0.9697 ± 0.0211	0.9845 ± 0.0030	0.9850 ± 0.0216
CMUP-CMX(MS)	0.8097 ± 0.0240	0.9877 ± 0.0014	0.8198 ± 0.0244
CMX-CMUP	0.9164 ± 0.0104	0.9701 ± 0.0009	0.9447 ± 0.0107
CMX-CMX	0.9879 ± 0.0042	0.9959 ± 0.0003	0.9920 ± 0.0042
CMX-CMX(AR)	0.9959 ± 0.0046	0.9968 ± 0.0003	0.9991 ± 0.0047
CMX-CMX(KS)	1.0000 ± 0.0000	0.9951 ± 0.0017	1.0049 ± 0.0017
CMX-CMX(MS)	0.9459 ± 0.0121	0.9920 ± 0.0010	0.9535 ± 0.0122

Table A.41: Muon reconstruction efficiencies and scale factors for `0i` data set. (AR : Arch, MS : Miniskirt, KS : Keystone)

cuts	Data Efficiency	MC Efficiency	Scale Factor
CMUP-CMUP	0.9557 ± 0.0040	0.9858 ± 0.0003	0.9694 ± 0.0041
CMUP-CMX	0.9690 ± 0.0076	0.9921 ± 0.0004	0.9767 ± 0.0077
CMUP-CMX(AR)	0.9948 ± 0.0078	0.9940 ± 0.0004	1.0008 ± 0.0079
CMUP-CMX(KS)	0.9368 ± 0.0250	0.9796 ± 0.0028	0.9563 ± 0.0256
CMUP-CMX(MS)	0.8636 ± 0.0218	0.9882 ± 0.0011	0.8739 ± 0.0221
CMX-CMUP	0.9189 ± 0.0089	0.9724 ± 0.0007	0.9449 ± 0.0092
CMX-CMX	0.9863 ± 0.0045	0.9960 ± 0.0002	0.9902 ± 0.0046
CMX-CMX(AR)	0.9971 ± 0.0048	0.9966 ± 0.0002	1.0004 ± 0.0048
CMX-CMX(KS)	0.9890 ± 0.0109	0.9936 ± 0.0016	0.9954 ± 0.0111
CMX-CMX(MS)	0.9299 ± 0.0132	0.9937 ± 0.0007	0.9358 ± 0.0133

Table A.42: Muon reconstruction efficiencies and scale factors for `0j` data set. (AR : Arch, MS : Miniskirt, KS : Keystone)

cuts	Data Efficiency	MC Efficiency	Scale Factor
CMUP-CMUP	0.9479 ± 0.0048	0.9855 ± 0.0003	0.9618 ± 0.0049
CMUP-CMX	0.9529 ± 0.0099	0.9914 ± 0.0004	0.9612 ± 0.0100
CMUP-CMX(AR)	0.9658 ± 0.0112	0.9940 ± 0.0004	0.9717 ± 0.0112
CMUP-CMX(KS)	0.9933 ± 0.0525	0.9838 ± 0.0028	1.0096 ± 0.0534
CMUP-CMX(MS)	0.8909 ± 0.0231	0.9837 ± 0.0014	0.9057 ± 0.0235
CMX-CMUP	0.9035 ± 0.0128	0.9730 ± 0.0007	0.9286 ± 0.0132
CMX-CMX	0.9796 ± 0.0056	0.9966 ± 0.0002	0.9830 ± 0.0057
CMX-CMX(AR)	0.9910 ± 0.0062	0.9969 ± 0.0003	0.9940 ± 0.0062
CMX-CMX(KS)	0.9524 ± 0.0268	0.9955 ± 0.0014	0.9567 ± 0.0270
CMX-CMX(MS)	0.9325 ± 0.0150	0.9951 ± 0.0007	0.9371 ± 0.0151

Table A.43: Muon reconstruction efficiencies and scale factors for `0k` data set. (AR : Arch, MS : Miniskirt, KS : Keystone)

Bibliography

[1] I. Newton, "Philosophiae naturalis principia mathematica", ISBN 0674664752 (1833).

[2] A. Einstein, "On the Electrodynamics of Moving Bodies", Annalen der Physik **17** (1905) 891.

[3] A.Einstein, "Does the Inertia of a Body Depend upon its Energy-Content", Annalen der Physik **18** (1905) 639.

[4] C. Amsler *et al* (Particle Data Group), "Review of Particle Physics", Phys. Lett. B **667**, 1 (2008).

[5] F. Halzen and A.D. Martin, "Quarks and Leptons: An Introductory Course in Modern Particle Physics", ISBN 0-471-88741-2 (1984)

[6] S. Glashow, "Partial Symmetries of Weak Interactions", Nucl. Phys. 22 (1961) 579.

[7] S. Weinberg, "A Model of Leptons", Phys. Rev. Lett. **19** (1967) 1264.

[8] A. Salam, in "Elementary Particle Theory", ed N. Svartholm, Almqvist and Wiksells, Stockholm (1969) p.367.

[9] P.W. Higgs, "Broken Symmetries, Massless Particles and Gauge Fields", Phys. Lett. **12** (1964) 132-133.

[10] P.W. Higgs, "Broken Symmetries and The Masses of Gauge Bosons", Phys. Rev. **13** (1964) 508-509.

[11] P.W. Higgs, "Spontaneous Symmetry Breakdown without Massless Bosons", Phys. Rev. **145** (1966) 1156-1163.

[12] H.E. Haber, G.L. Kane, and T. Sterling, "THE FERMION MASS SCALE POSSIBLE EFFECTS OF HIGGS BOSONS ON EXPERIMENTAL OBSERVABLES", Nucl. Phys. B**161** (1979) 493-532.

[13] J.F. Gunion, H.E. Haber, G. Kane, and S. Dawson, "The Higgs Hunter's Guide", ISBN: 0-7382-0305-X (2000)

[14] J.F. Gunion and H.E. Haber, "CP-conserving two-Higgs-doublets model: The approach to the decoupling limit", Phys. Rev. D **67** (2003) 075019.

[15] M. Carena, J.S. Conway, H.E. Havber, and J.D. Hobbs, "Report of the Tevatron Higgs Working Group", arXiv:hep-ph/0010338.

[16] A. Djouadi, "The Anatomy of Electro-Weak Symmetry Breaking TomeI: The Higgs boson in the Standard Model", arXiv:hep-ph/0503172.

[17] P.C. Bhat, H.B. Prosper, and S.S. Snyder, "Top Quark Physics At The Tevatron", arXiv:hep-ex/9809011.

[18] The ALEPH, CDF, DØ, DELPHI, L3, OPAL, SLD Collaboration, the LEP Electroweak working Group, the Tevatron Electroweak Group, and the SLD electroweak ans heavy flavour groups, "Precision Electroweak Measurements and Constraints on the Standard Model", arXiv:0811.4682 [hep-ex]

[19] The LEP Higgs Working Group, ALEPH Collaboration, DELPHI Collaboration, L3 Collaboration, and OPAL Collaboration, "Search for the Standard Model Higgs boson at LEP", Phys. Lett. B **565** (2003) 61-75.

[20] The LEP Higgs Working Group, ALEPH Collaboration, DELPHI Collaboration, L3 Collaboration, and OPAL Collaboration, "Searches for Higgs Bosons Decaying into Photons: Combined Results from the LEP Experiments", LHWG Note 2002-02.

[21] CDF Collaboration, "Combined $WH \to \ell\nu b\bar{b}$ search with 2.7 fb^{-1} of CDF data", CDF Public Note 9596 (2008).

[22] CDF Collaboration, "A Search for $ZH \to \ell^+\ell^- b\bar{b}$ in 2.7 fb^{-1} using a Neural Network discriminant", CDF Public Note 9665 (2008).

[23] CDF Collaboration, "Search for the Standard Model Higgs boson in the $\not\!\!E_T$ plus jets sample", CDF Public Note 9642 (2008).

[24] CDF Collaboration, "Search for the Standard Model Higgs Boson in $H \to \tau\tau$ Channel at CDF Run II $\sim$ Simultaneous Search for $WH/ZH/\mathrm{VBF}/H$ Processes $\sim$", CDF Public Note 9248 (2008).

[25] CDF Collaboration, "Search for $H \to WW^*$ Production at CDF Using 3.0 fb^{-1} of Data", CDF Public Note 9500 (2008).

[26] CDF Collaboration, "Search for the Wh Production Using High-p_T Isolated Like-Sign Dilepton events in Run-II with 2.7 fb^{-1}", CDF Public Note 7307 (2008).

[27] DØ Collaboration, "Search for WH associated production using a combined Neural Network and Matrix Element Approach with 2.7 fb^{-1} Run II data", DØ Note 5828-CONF (2009).

[28] DØ Collaboration, "A Search for $ZH(\rightarrow e^+e^-b\bar{b})$ and $ZH(\rightarrow \mu^+\mu^-b\bar{b})$ Production with the DØ Detector in $p\bar{p}$ Collisions at $\sqrt{s} = 1.96$ TeV", DØ Note 5570-CONF (2008).

[29] DØ Collaboration, "A Search for the Standard Model Higgs Boson in the Channel $ZH\rightarrow\nu\bar{\nu}b\bar{b}$ at $\sqrt{s} = 1.96$ TeV", DØ Note 5506-CONF (2007).

[30] DØ Collaboration, "Search for the Higgs boson in $H\rightarrow WW(*)\rightarrow\ell\ell'\nu\nu$ $(\ell, \ell' = e, \mu)$ decays with 3.0 fb^{-1} at DØ in Run II", DØ Note 5757-CONF (2008).

[31] DØ Collaboration, "Search for the Associated Higgs Boson Production $p\bar{p}\rightarrow WH\rightarrow WWW^*\rightarrow\ell^{\pm}\nu\ell'^{\pm}\nu' + X$ at $\sqrt{s} = 1.96$ TeV", DØ Note 5485-CONF (2007).

[32] DØ Collaboration, "Search for the standard model Higgs boson in $\gamma\gamma$ final states at $D\emptyset$" DØ Note 5737-CONF (2008).

[33] Tevatron New Phenomena, Higgs working group, CDF Collaboration, DØ Collaboration, "Combined CDF and DØ Upper Limits on Standard Model Higgs Boson Production at High Mass (155-200 GeV/c^2) with 3 fb^{-1}" arXiv:hep-ex/0808.0534 (2008)

[34] T. Affolder, *et al*, The CDF Collaboration, "Search for narrow diphoton resonances and for $\gamma\gamma + WZ$ signatures in $p\bar{p}$ collisions at $\sqrt{s} = 1.8$ TeV", Phys. Rev. D **64** (2001) 092002.

[35] B. Abbott, *et al*, The DØ Collaboration, "Search for Nonstandard Higgs Bosons Using High Mass Photon Pairs in $p\bar{p}\rightarrow\gamma\gamma + 2$ Jets at $\sqrt{s} = 1.8$ TeV", Phys. Rev. Lett. **82** (1999) 11.

[36] CDF Collaboration, "Search for a Fermiophobic Higgs Boson with the Diphoton Final State at CDF", CDF Public Note 9586 (2008),

[37] DØ Collaboration, "Search for Fermiophobic Higgs Boson in $3\gamma + X$ Events", DØ Note 5067-CONF (2007).

[38] The CDF II Collaboration, "The CDF II Detector Technical Design Report", FERMILAB-Pub-96/390-E (1996).

[39] T.K. Nelson *et al*, "The CDF Layer 00 Detector", FERMILAB-CONF-01/357-E (2001).

[40] C.S. Hill *et al*, "Initial experience with the CDF layer 00 silicon detector", Nucl. Instrum. and Meth. A **511** (2003) 118-120.

[41] A. Sill *et al*, "CDF Run II silicon tracking projects", Nucl. Instrum. and Meth. A **447** (200) 1-8.

[42] W. Ashmanskas *et al*, "The CDF silicon vertex trigger", Nucl. Instrum. and Meth. A **518** (2004) 532-636.

[43] A. Affolder *et al*, "Status report of the Intermediate Silicon Layers detector at CDFII", CDF Public Note 5687 (2001).

[44] A. Affolder *et al*, "Intermediate silicon layers detector for the CDF experiment", Nucl. Instrum. and Meth. A **453** (2000) 84-88.

[45] T. Affolder *et al*, "CDF Central Outer Tracker", CDF Public Note 6267 (2003).

[46] L. Balka *et al*, "The CDF Central Electromagnetic Calorimeter", Nucl. Instrum. Meth. A **267**, 272 (1988).

[47] S. Bertolucci *et al*, "The CDF Central and Endwall Hadron Calorimeter", Nucl. Instrum. Meth. A **267**, 301 (1988).

[48] S. Lami *et al* "The CDF calorimeter upgrade for Run IIb", Nucl. Instrum. Meth. A **518** (2004) 39-41.

[49] Y. Seiya *et al*, "The CDF plug upgrade electromagnetic calorimeter test beam results", Nucl. Instrum. Meth. A **480** (2002) 524-546.

[50] D. Acosta *et al*, "The CDF Cherenkov luminosity monitor", Nucl. Instrum. Meth. A **461** (2001) 540-544.

[51] D. Acosta *et al*, "The performance of the CDF luminosity monitor", Nucl. Instrum. Meth. A **494** (2002) 57-62.

[52] B. Rossi, High-Energy Particles, Prentice-Hall.

[53] L.Breiman, J.H.Friedman, R.A.Olshen and C.J.Stone "Classification and regression trees", ISBN: 0-412-04841-8

[54] H.Yang, B.P.Roe and J.Zhu. "Studies of Boosted Decision Trees for MiniBooNE Particle Identification", arXiv:physics/0508045

[55] R.Brun *et al*, "ROOT An Object-Oriented Data Analysis Framework: Users Guide 5.20", (2008)

[56] A.Hocker, P.Speckmayer, J.Stelzer, F.Tegenfeldt, H.Voss, and K,Voss, "TMVA Toolkit for Multivariate Data Analysis with ROOT Users Guide".

[57] K.A.Assamgan *et al*, "THE HIGGS WORKING GROUP: Summary Report", hep-ph/0406152v1.

[58] J.M. Campbell and R.K. Ellis, "An update on vector boson pair production at hadron colliders", Phys. Rev. D **60** 113006 (1999).

[59] A. Bhatti *et al*, "Determination of the Jet Energy Scale as the Collider Detector at Fermilab", hep-ex/0510047v1.

[60] CDF Collaboration, D. Acosta, *et al*, "Search for Electroweak single-top-quark production in $p\bar{p}$ collisions at $\sqrt{s} = 1.96$ TeV", Phys. Rev. D **71**, 012005 (2005).

[61] CDF Collaboration, "Combined $WH \to \ell\nu b\bar{b}$ search with 2.7 fb^{-1} of Data", CDF Public Note 9596 (2008).

[62] CDF Collaboration, "Search fof the Standard Model Higgs Boson in the $\not\!\!E_T$ Plus Jets Sample", CDF Public Note 9642 (2008).

[63] CDF Collaboration, "Search for $ZH \to \ell^+\ell^- b\bar{b}$ in 2.7 fb^{-1} using Neural Network Discriminant", CDF Public Note 9665 (2009).

[64] CDF Collaborationn, "Search for $H \to WW^*$ Production Using 3.6 fb^{-1} of Data", CDF Public Note 9500 (2009).

[65] CDF Collaboration, "A Search for the Standard Model Higgs Boson in the All-Hadronic channel using a Matrix Element Method", CDF Public Note 9366 (2008).

[66] DØ Collaboration, "Search for the standard model Higgs boson τ final states", DØ Note 5883-CONF (2009).

[67] DØ Collaboration, "Search for the standard model Higgs boson in the $HZ \to b\bar{b}\nu\bar{\nu}$ channel in 2.1 fb^{-1} of $p\bar{p}$ collision at $\sqrt{s} = 1.96$ TeV", DØ Note 5586-CONF (2008).

[68] DØ Collaboration, "Search for Higgs production in dilepton plus missing energy final states with 3.0-4.2 fb^{-1} of $p\bar{p}$ collisions at $\sqrt{s} = 1.96$", DØ Note 5871-CONF (2009).

[69] DØ Collaboration, "Search for the standard model Higgs boson in $\gamma\gamma$ final states at DØ with $L = 4.2$ fb^{-1}", DØ Note 5846-CONF (2009).

[70] DØ Collaboration, "Search for the Standard Model Higgs boson in the $t\bar{t}H \to t\bar{t}b\bar{b}$ channel", DØ Note 5739-CONF (2009).

[71] The TEVNPH Working Group, CDF Collaboration and DØ Collaboration, "Combined CDF and DØ Upper Limits on Standard-Model Higgs-Boson Production with up to 4.2 fb^{-1} of Data", CDF Public Note 9713 (2009).